

Utilisation of Ventilation Air Methane in Chemical Looping Systems

Yongxing Zhang

(BEng)

A thesis submitted in fulfilment of
the requirements for the degree

Doctor of Philosophy

Department of Chemical Engineering
University of Newcastle
Callaghan, New South Wales 2308
Australia

Date of Submission: April 2014

DECLARATION

I hereby certify the work embodied in this thesis is the result of original research and has not been submitted for a higher degree to any other University or Institute and, to the best of my knowledge and belief, contains no material previously published or written by another person, except where due reference has been made in the text.

Signed: _____

Date: _____

University of Newcastle
March 2013

Acknowledgements

I owe my gratitude to Prof Behdad Moghtaderi for being a kind, sincere, caring, cooperative, rational, practical, appreciative, and friendly supervisor. I find myself exceptionally fortunate to have a supervisor like Behdad. I thank him for always being there when I needed his guidance, inciting professional thoughts in me and making me utilise my capabilities in the best possible ways. Behdad not only guided me through to achieve this PhD but also inspired me both professionally and personally, which will help me throughout my career. Thanks also go to my co-supervisor Dr Elham Doroodchi for her encouragement and guidance.

Acknowledgement is also given to the staff at the Centre for Energy as they have offered tremendous technical support during my research. Thanks in particular to Jane Hamson for her assistance in the beginning of my experimental work.

The Chinese Scholarship Council must also be acknowledged as they provided most of the financial support during my PhD study.

The kind support supplied by the staff of Central Scientific Services is acknowledged, and in particular, thanks are given to David Phelan and Victor Wang with the SEM analysis.

I would also like to thank my fellow postgraduate students from the Centre for their own unique brand of encouragement, and in particular, thanks are given to Hui Song, Kai Chen, and Sazal Kundu for assistance in my experiments.

Last, but not least, I wish to thank my family and friends. My family, in particular my parents and my wife, for all the encouragement and support they have given me during my studies. My friends have been more than happy to share both the study and life. To them I am deeply indebted.

Executive Summary

A major source of greenhouse gas emissions from the mining sector is the release of fugitive methane emissions (CH_4 with a global warming potential 25 times greater than that of CO_2) from the ventilation air systems in coalmines. Abatement of ventilation air methane (VAM) has been a priority for the coal industry in recent years and has become an even higher priority following the introduction of a carbon price in many parts of the world including Australia. Capture and use of VAM (i.e. utilisation) is considered the most effective means of abating fugitive methane emissions from coal mining. The key challenge though is to develop abatement platforms which can effectively deal with (i) high gas volumes; as high as $600 \text{ m}^3/\text{s}$; (ii) low methane concentrations; typically 0.1-1 % V/V; and (iii) the highly variable nature of VAM both in terms of the flow rate and concentration.

This PhD thesis has been motivated by the desire to overcome the above challenge and has resulted in the development of three chemical looping based alternative pathways to utilise VAM. These are:

1. Conversion of VAM to hydrogen as a value added product using a dual loop chemical looping process.
2. Thermal oxidation of hydrogen enriched VAM using H_2 produced by a novel Integrated Gasification Chemical Looping Combustion (IGCLC) process.
3. Ancillary use of VAM as an oxidizing agent in chemical looping combustion of synthesis gas.

In the first option a Cu-based chemical loop for air separation process is integrated with a Fe-based chemical loop (i.e. dual loop) where VAM is used as a feedstock to produce pure hydrogen. It was proved that oxygen in VAM can be removed with Cu_2O at temperatures between 573K and 673K without the occurrence of methane oxidation. With a moderate iron oxide circulation rate, pure hydrogen can be produced with methane concentration as low as 0.4 vol%, and a hydrogen efficiency of 60% was obtained with methane concentration of 1 vol%. The reduction of $\text{Fe}_2\text{O}_3/\text{Al}_2\text{O}_3$ by ultra-low concentration methane was investigated experimentally in TGA and fixed bed setup, showing that 45 wt%

$\text{Fe}_2\text{O}_3/\text{Al}_2\text{O}_3$ was the most suitable oxygen carrier for chemical looping hydrogen production with methane concentration as low as 0.1 vol%. Reduction of Fe_2O_3 with ultra-low concentration methane was found to be a two-step process. The first step of Fe_2O_3 to Fe_3O_4 was controlled by a phase change mechanism followed by the step of Fe_3O_4 to FeO by a diffusion controlled mechanism.

In the second option the thermal oxidation of VAM takes place in a VAM combustor (VC) along with hydrogen as a supplementary fuel. The hydrogen in this process is produced from the integrated gasification chemical looping combustion (IGCLC) of coal. With a moderate VAM flow rate (~25 kg/kg coal), the temperature in VC was found to be higher than 1188 K even with methane concentration as low as 0.1 vol%. In most cases, the overall efficiency for the whole system was higher than 45% and CO_2 capture rate higher than 80%. However, the variation in VAM flow rate and methane concentration led to a significant change in the VC temperature. In particular, the temperature was increasing linearly with the increase in methane concentration, which increased by 200K from the methane concentration of 0.1 vol% to 1 vol%.

Similarly in Option 3, VAM was utilised as an oxidation agent in chemical looping combustion of synthesis gas where methane was oxidised in an air reactor in the presence of oxygen carriers. Due to the circulation of oxygen carriers between the fuel and air reactors, the temperature difference was decreased to 34 K when methane concentration varied from 0.1 vol% to 1 vol%. Moreover, the process delivered a higher CO_2 capture rate of over 90% and similar overall system efficiency compared with the abovementioned process. The methane conversion with reaction temperature was reported for the oxidation of VAM in the presence of iron oxide as an oxygen carrier. Complete methane conversion can be achieved at temperatures around 873 K even with the methane concentration as low as 0.23 vol% and iron oxide content as low as 1 wt%.

Overall, we found that the above chemical looping processes are quite suitable for applications involving utilisation of methane. However, selection of one technology over the others for a given applications hinges upon a careful analysis of the pros and cons of the three technology options discussed earlier.

Publications Arise from this Thesis

1. **Y. Zhang**, E. Doroodchi, and B. Moghtaderi. Thermodynamic Assessment of a Novel Concept for Integrated Gasification Chemical Looping Combustion of Solid Fuels. *Energy & Fuels*, **2012** 26 (1), 287-295.
2. **Y. Zhang**, E. Doroodchi, and B. Moghtaderi. Chemical Looping Combustion of Ultra Low Concentration of Methane with $\text{Fe}_2\text{O}_3/\text{Al}_2\text{O}_3$ and CuO/SiO_2 . *Applied Energy*, **2014** 113, 1916-1923.
3. **Y. Zhang**, E. Doroodchi, and B. Moghtaderi. Utilization of Ventilation Air Methane as an Oxidizing Agent in Chemical Looping Combustion. *Energy Conversion and Management*, Accepted.
4. **Y. Zhang**, E. Doroodchi, and B. Moghtaderi. Comprehensive Study on the Reduction of $\text{Fe}_2\text{O}_3/\text{Al}_2\text{O}_3$ with Ultra Low Concentration Methane in Chemical Looping Combustion. *In Submission*.
5. **Y. Zhang**, E. Doroodchi, and B. Moghtaderi. Reduction Kinetics of $\text{Fe}_2\text{O}_3/\text{Al}_2\text{O}_3$ with Low Concentration Methane in Chemical Looping Combustion. *In Submission*.
6. **Y. Zhang**, B. Moghtaderi and K. Shah. Investigation on a Novel Integrated Gasification Chemical Looping Combustion for Solid Fuels. Proceedings of the Australian Combustion Symposium, 2011, Newcastle, Australia.
7. **Y. Zhang**, E. Doroodchi, and B. Moghtaderi. The Application of Chemical Looping Principles in Mitigating Ventilation Air Methane (VAM) Emissions. 2nd International Conference on Chemical Looping, 2012, Darmstadt, Germany.
8. **Y. Zhang**, E. Doroodchi, and B. Moghtaderi. A Novel Ancillary Utilization of Ventilation Air Methane as the Substitute of Air in Chemical Looping Combustion. 26th International Conference on Efficiency, Cost, Optimization, Simulation and Environmental Impact of Energy Systems, 2013, Guilin, China.

Table of Contents

Chapter 1: INTRODUCTION.....	1
1.1 Background.....	1
1.1.1 Global Warming and GHG Emissions.....	1
1.1.2 The Sources of Methane Emissions	4
1.1.3 Utilisation of Ventilation Air Methane	6
1.1.4 Chemical Looping Technology.....	7
1.2 Motivation.....	9
1.3 Aims and Objectives	10
1.4 Structure of the Thesis	12
Chapter 2: LITERATURE REVIEW.....	14
2.1 Conventional Techniques for VAM Treatment	14
2.1.1 Principle Use of VAM	14
2.1.2 Ancillary Use of VAM.....	21
2.2 Chemical Looping Processes	22
2.2.1 Chemical Looping Combustion	22
2.2.2 Chemical Looping Hydrogen Generation	23
2.2.3 Other Chemical Looping Processes	27
2.2.4 Oxygen Carriers in Chemical Looping Processes.....	28
Chapter 3: METHODS AND TECHNIQUES.....	36
3.1 Theoretical	36
3.1.1 Selection of Reactors	36
3.1.2 Selection of Property Method	38
3.2 Experimental	38
3.2.1 Thermogravimetric Analysis.....	38
3.2.2 Fixed Bed Reactor Rig.....	40
3.2.3 Samples Preparation.....	49
3.2.4 Scanning Electron Microscope (SEM).....	49
Chapter 4: REDUCTION OF Fe₂O₃ BY ULTRA-LOW CH₄.....	50
4.1 Introduction.....	50

4.2	Experimental Studies	50
4.3	Results and Discussions	51
4.3.1	Reduction of Pure Fe ₂ O ₃ with CH ₄	51
4.3.2	Reduction of Alumina-supported Fe ₂ O ₃ with CH ₄	55
4.3.3	Gas Analysis for the Reduction of Alumina-supported Fe ₂ O ₃ with CH ₄	64
4.3.4	The Influential Factors on Reduction Reactivity of Fe ₂ O ₃ to FeO.....	68
4.4	Conclusions.....	75
Chapter 5: REDUCTION KINETICS OF Fe₂O₃ BY ULTRA-LOW CH₄		76
5.1	Introduction.....	76
5.2	Experimental Studies	76
5.3	Kinetic Model	76
5.4	Results.....	80
5.4.1	Reduction of Fe ₂ O ₃ /Al ₂ O ₃ by CH ₄	80
5.4.2	Reduction Kinetics of Fe ₂ O ₃ to Fe ₃ O ₄	82
5.4.3	Reduction Kinetics of Fe ₃ O ₄ to FeAl ₂ O ₄	86
5.5	Discussion	93
5.6	Conclusions.....	97
Chapter 6: CONVERSION OF VAM INTO HYDROGEN IN A DUAL-LOOP SYSTEM		98
6.1	Introduction.....	98
6.2	Description of the Dual-Loop Chemical Looping Process	98
6.3	Process Simulation and Model.....	102
6.4	Case Study	104
6.5	Parametric Study.....	105
6.5.1	Impact of Excess Rate of Oxygen Carrier Circulation.....	105
6.5.2	Impact of Al ₂ O ₃ Content	108
6.5.3	Impact of VAM Concentration	111
6.5.4	Impact of Oxygen Partial Pressure in Reduction Reactor.....	113
6.5.5	Impact of System Configurations	115
6.6	Conclusions.....	116
Chapter 7: THERMAL OXIDATION OF HYDROGEN ENRICHED VAM		117
7.1	Introduction.....	117

7.2	A Novel IGCLC System for Producing Hydrogen	118
7.2.1	The Working Principle.....	118
7.2.2	Key Reactions	119
7.2.3	Process Simulation and Model.....	121
7.2.4	Gasification Reactor (GR) Unit	123
7.2.5	Fuel Reactor (FR) Unit	127
7.2.6	Hydrogen Generator (SR) Unit.....	129
7.3	Performance Characteristics of the System Integrated with VAM Combustor	130
7.3.1	Effect of SHTCR.....	132
7.3.2	Effect of Oxygen Carrier Circulation Rate	135
7.3.3	Effect of Air Flow Rate.....	136
7.3.4	Effect of Steam Conversion	137
7.3.5	Effect of VAM Flow Rate and VAM Concentration	139
7.4	Conclusions.....	141
Chapter 8: USE OF VAM AS AN OXIDISING AGENT IN CHEMICAL LOOPING COMBUSTION OF SYNTHESIS GAS.....		143
8.1	Introduction.....	143
8.2	Thermodynamics Analysis.....	144
8.2.1	The Optimisation of the System Performance	146
8.2.2	Effect of VAM Flow Rate.....	149
8.2.3	Effect of Methane Concentration in VAM.....	150
8.3	Experimental Study.....	152
8.3.1	Oxidation of VAM in the Empty Reactor	153
8.3.2	Oxidation of VAM with the Presence of Oxygen Carriers	158
8.3.3	Effect of Fe ₂ O ₃ Loading Content on Al ₂ O ₃	161
8.4	Discussion	163
8.5	Conclusions.....	165
Chapter 9: CONCLUSIONS AND RECOMMENDATIONS.....		167
9.1	Conclusions.....	167
9.1.1	The Use of VAM to Produce Pure Hydrogen	167
9.1.2	Thermal Oxidation of Hydrogen Enriched VAM	170
9.1.3	The use of VAM as oxidation agent in a CLC process.....	171

9.2 Recommendations for Future Work.....172

List of Figures

Figure 1.1: The change in global atmosphere concentration of CO ₂ and CH ₄ [source: US EPA, 2013 [3]].	2
Figure 1.2: The radiative forcing from various greenhouse gases [source: NOAA, 2012 [4]].	3
Figure 1.3: The global GHG emissions distribution by gases and sectors [source: World Resources Institute, 2012 [5]].	3
Figure 1.4: The expectation of future temperature and sea level change [source: US EPA, 2006 [8]].	4
Figure 1.5: The sources of anthropogenic methane emissions [source: US EPA, 2006 [8]].	5
Figure 1.6: Scheme of chemical looping combustion.	8
Figure 1.7: Fe-based chemical looping processes for VAM treatment.	11
Figure 2.1: Schematic of the TFRR reactor.	14
Figure 2.2: Schematic of the CFRR reactor.	16
Figure 2.3: Schematic of three reactors CLHG process [61].	24
Figure 2.4: Flow sheet of four reactors CLHG process [62].	25
Figure 2.5: Diagram of the BDCL process for hydrogen production [64].	26
Figure 2.6: Schematic of CLAS [67].	27
Figure 2.7: Schematic of ICLAS [68].	28
Figure 3.1: Scheme of TGA experiments.	40
Figure 3.2: Schematic of the fixed bed reactor rig.	41
Figure 3.3: Calibration of MFC-CO ₂ -5 using CH ₄ .	42
Figure 3.4: Calibration of MFC-CO-50 using instrument air.	43
Figure 3.5: Calibration of MFC-CH ₄ -100 using N ₂ .	43
Figure 3.6: Calibration of MFC-N ₂ -100 using N ₂ .	44
Figure 3.7: Calibration for temperature at 875°C.	45
Figure 3.8: Calibration for temperature at 800°C.	45
Figure 3.9: Calibration for temperature at 750°C.	46
Figure 3.10: Plots of peak area vs. H ₂ concentration.	47
Figure 3.11: Plots of peak area vs. CO concentration.	47
Figure 3.12: Plots of peak area vs. CH ₄ concentration.	48
Figure 3.13: Plots of peak area vs. CO ₂ concentration.	48
Figure 4.1: Reduction of pure Fe ₂ O ₃ with 1 vol% CH ₄ at: (a) 1073 K, (b) 1023 K, and (c) 973 K in 5 cycles and (d) 1023 K in 30 cycles.	54
Figure 4.2: SEM images at 6000× magnification for unsupported iron oxide, after 5 cycles at: (a) 973 K, (b) 1023 K, and (c) 1073 K; (d) after 30 cycles at 1023 K.	55
Figure 4.3: The variations of the temperature in fuel reactor with Al ₂ O ₃ content.	57
Figure 4.4: Mass loss at 1023 K in 30 cycles for pure Fe ₂ O ₃ , Fe ₄₅ Al, Fe ₂₅ Al and Fe ₁₀ Al.	58

Figure 4.5: Reduction conversion and reaction rate for the 5 th cycle at 1023 K for pure (2 nd cycle), Fe45Al, Fe25Al and Fe10Al.	58
Figure 4.6: Reactivity variations with cycles at different conversions for: (a) pure Fe ₂ O ₃ , (b) Fe45Al, (c) Fe25Al, and (d) Fe10Al.	61
Figure 4.7: The effect of loading content on reaction rate (solid) and <i>ROT</i> (open): $X=0.5$ (○); $X=1$ (□); $X=1.5$ (Δ).	64
Figure 4.8: Gas concentration profile for: (a) Fe10Al, (b) Fe25Al (c) Fe45Al with 1 vol% CH ₄ at 1023 K, and (d) CH ₄ conversion as well as the duration on high conversion.	67
Figure 4.9: The effect of temperature on: (a) the conversion and (b) reactivity.	70
Figure 4.10: The effect of temperatures (◇ 873 K, ▽ 923 K, □ 973 K, ○ 1023 K and △ 1073 K) on the product gas concentration, (a) CO ₂ (solid line) and CH ₄ (dash line); and (b) methane conversion and duration on high level conversion.	71
Figure 4.11: The effect of gas concentrations on: (a) the conversion and (b) reactivity. ...	73
Figure 4.12: The effect of CO ₂ composition in the reducing gas on: (a) the conversion and (b) reactivity.	74
Figure 5.1: Reduction of: (a) Fe25Al and (b) Fe45Al with CH ₄ at different temperatures.	81
Figure 5.2: Plots of $\ln(-\ln(1-X))$ vs $\ln t$ for the reduction of Fe ₂ O ₃ to Fe ₃ O ₄ for samples: (a) Fe25Al and (b) Fe45Al.	83
Figure 5.3: Comparison of experimental data (symbol) with calculation results (line) for the reduction of Fe ₂ O ₃ to Fe ₃ O ₄ with samples: (a) Fe25Al and (b) Fe45Al, (□:1073 K, △:1048 K, ○:998 K, ◇:973 K).	84
Figure 5.4: Plots of $\ln K$ vs $1000/T$ for the reduction of Fe ₂ O ₃ to Fe ₃ O ₄ with samples (○:Fe25Al and □:Fe45Al).	86
Figure 5.5: Plots of $\ln(-\ln(1-X))$ vs $\ln t$ for the reduction of Fe ₃ O ₄ to FeAl ₂ O ₄ for samples: (a) Fe25Al, and (b) Fe45Al.	89
Figure 5.6: <i>RMSD</i> values for different reaction models.	90
Figure 5.7: Comparison of experimental data (symbol) with calculation results (line) for the reduction of Fe ₃ O ₄ to FeAl ₂ O ₄ with samples: (a) Fe25Al and (b) Fe45Al, (□:1073 K, △:1048 K, ▽:1023 K, ○:998 K, ◇:973 K)	91
Figure 5.8: Plots of $\ln k$ vs $1000/T$ for the reduction of Fe ₃ O ₄ to FeAl ₂ O ₄ with samples (○:Fe25Al and □:Fe45Al).	92
Figure 5.9: Comparison of experimental data with A2 model and A3 model results for the reduction of Fe ₂ O ₃ to Fe ₃ O ₄ with samples: (a) Fe25Al and (b) Fe45Al at temperature 1073 K.	95
Figure 6.1: Flow sheet of a dual loops CLC system for reforming VAM into H ₂	99
Figure 6.2: Combustion of 1 vol% methane in O ₂ over CuO/MgAl ₂ O ₄ (refer to Artizzu et al. [34]).	101
Figure 6.3: Non-isothermal oxidation of Cu ₂ O in air.	101
Figure 6.4: The impact of oxygen carrier circulation rate.	108
Figure 6.5: The impact of Al ₂ O ₃ content on: (a) temperature and (b) H ₂ efficiency.	110

Figure 6.6: The impact of methane concentration in VAM stream.	113
Figure 6.7: The effect of oxygen partial pressure on: (a) H ₂ efficiency and (b) energy consumption.	114
Figure 6.8: The difference in H ₂ efficiency between the configurations with and without O ₂ product.	115
Figure 7.1: Diagram of a novel IGCLC-VC system.	117
Figure 7.2: Gasification temperature and carbon conversion in the GR unit.	126
Figure 7.3: Plots of product selectivity as a function of SHTCR and T _{Feed}	126
Figure 7.4: Variations of the FR and AR temperatures with the SHTCR and T _{Feed}	128
Figure 7.5: Production of H ₂ and consumption of hematite as a function of SHTCR and T _{Feed}	128
Figure 7.6: The effect of SHTCR on the fuel conversion in the fuel reactor.	133
Figure 7.7: The effect of SHTCR on system performance.	133
Figure 7.8: The effect of oxygen carrier circulation rate on H ₂ production.	134
Figure 7.9: The effect of oxygen carrier circulation rate on system performance.	134
Figure 7.10: The effect of airflow rate in AR.	136
Figure 7.11: The effect of steam conversion in SR.	138
Figure 7.12: The effect of: (a) VAM flow rate and (b) VAM concentration on VC temperature.	139
Figure 7.13: The effect of VAM flow rate on system performance.	140
Figure 7.14: The effect of VAM concentration on system performance.	140
Figure 8.1: Flow sheet of the proposed combustion method of VAM.	145
Figure 8.2: The optimisation of: (a) CGE and (b) the overall efficiency and CO ₂ capture rate.	148
Figure 8.3: The effect of VAM flow rate on the air reactor temperature (■), CO ₂ capture rate (○) and overall efficiency (▲).	150
Figure 8.4: The effect of CH ₄ concentration on system performance.	151
Figure 8.5: The profiles of outlet gas concentration with inlet methane concentrations in: (a) 0.23 vol%, (b) 0.51 vol%, and (c) 0.95 vol% in empty reactor.	156
Figure 8.6: The variation of methane conversion with temperatures in empty reactor. ...	157
Figure 8.7: The profiles of outlet gas concentration with inlet methane concentrations in: (a) 0.23 vol%, (b) 0.51 vol%, (c) 0.95 vol% in a packed reactor with Fe ₂ O ₃ /Al ₂ O ₃ , and (d) methane conversion in packed reactor with Fe ₂ O ₃ /Al ₂ O ₃	160
Figure 8.8: The profiles of outlet gas concentration with 0.95% inlet methane concentrations in a packed reactor with different loading content Fe ₂ O ₃ /Al ₂ O ₃ , (a) 1% and (b) 5%-50%.	162
Figure 8.9: Methane conversion in packed reactor with different loading content Fe ₂ O ₃ /Al ₂ O ₃	163

List of Tables

Table 4.1: Fixed bed reactor experiments matrix.....	51
Table 4.2: TGA experiments matrix.	51
Table 4.3: Detailed deviations on reaction rates for different conversion values.	62
Table 5.1: Kinetic equations for different reaction mechanisms.	78
Table 5.2: m value for $\text{Fe}_2\text{O}_3\text{-Fe}_3\text{O}_4$	85
Table 5.3: Fitting correlation coefficient r for different diffusion model ($\text{Fe}_2\text{O}_3\text{-Fe}_3\text{O}_4$). ..	85
Table 5.4: Kinetic parameters using 2-D nuclei growth model A2.	85
Table 5.5: m value for $\text{Fe}_3\text{O}_4\text{-FeAl}_2\text{O}_4$	88
Table 5.6: Fitting correlation coefficient r for different diffusion controlled models.	88
Table 5.7: Kinetic parameters for diffusion controlled model $D3$	88
Table 5.8: m value for $\text{Fe}_2\text{O}_3\text{-Fe}_3\text{O}_4$ within the conversion range of 0.6-0.9.....	94
Table 5.9: Summary of activation energy in this study and literature.	96
Table 6.1: Oxygen partial pressure at various temperatures.	100
Table 6.2: Assumptions and operation parameters.	104
Table 6.3: Case study results.....	104
Table 7.1: Coal analysis	122
Table 7.2: The comparison of IGCLC with conventional coal gasification CLC.....	130
Table 8.1: Assumptions and operation parameters.	146

Chapter 1: INTRODUCTION

1.1 Background

1.1.1 Global Warming and GHG Emissions

Global warming is perhaps one of the most challenging issues faced by mankind at present. The most likely reason for the resultant climate changes is the increase in anthropogenic greenhouse gas (GHG) concentrations, including CO₂, CH₄, NO_x, and F-gases. The emissions of carbon dioxide (CO₂) and methane (CH₄) account for the largest part of the anthropogenic GHG, which imposes the most significant influence on the global warming issue. The concentrations of carbon dioxide and methane in the atmosphere from hundreds of thousands of years ago through 2012 are shown in Figure 1.1. Global atmospheric concentrations of carbon dioxide and methane have been rising over the last century. Before the industrial era began in the late 1700s, carbon dioxide concentrations were measured to be approximately 280 ppm. Since then it has risen steadily and reach an annual average of 394 ppm in 2012, equivalent to a 41% increase. Almost all of this increase is resulting from human activities [1]. The concentration of methane in the atmosphere has more than double increase and reaches about 1,826 ppb in 2012. It is very likely due to agricultural industry expansion and fossil fuel use [2].

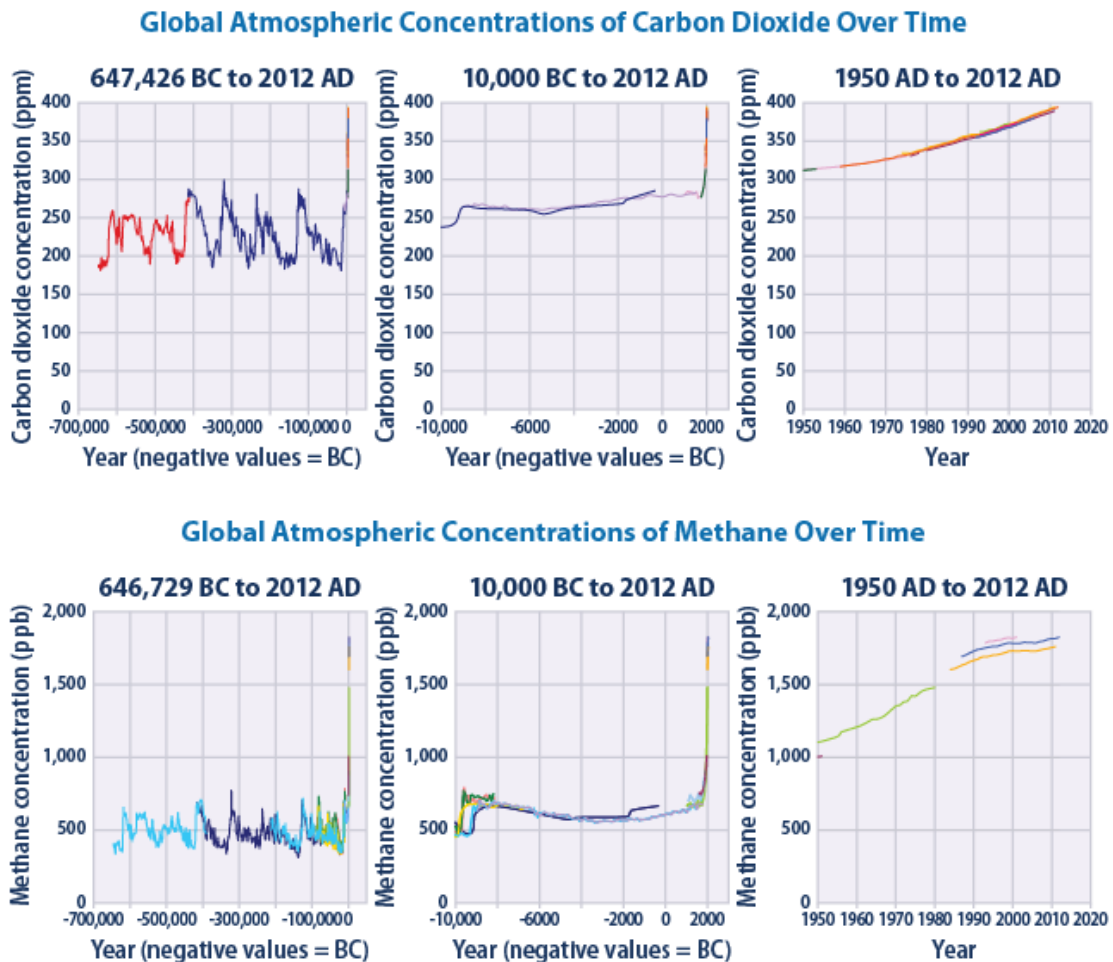


Figure 1.1: The change in global atmosphere concentration of CO_2 and CH_4 [source: US EPA, 2013 [3]].

Figure 1.2 shows the amount of radiative forcing caused by various greenhouse gases, based on the annual average concentrations in the atmosphere. The radiative forcing has also been indicated by the Annual Greenhouse Gas Index, which is set to a value of 1.0 for 1990. In 2011 the Annual Greenhouse Gas Index was 1.30, equivalent to an increase of 30% since 1990. Furthermore, carbon dioxide accounts for by far the largest amount of radiative forcing followed by methane. It should be noted that the methane concentrations have remained relatively steady since 1990, resulting in a slow increase in the overall Annual Greenhouse Gas Index.

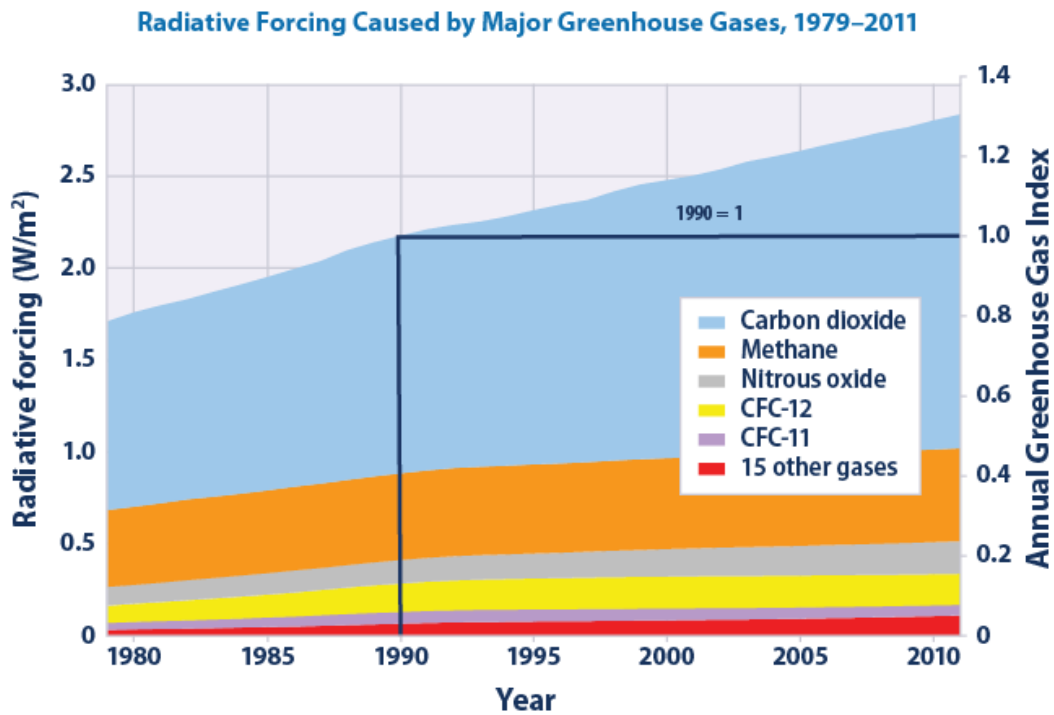


Figure 1.2: The radiative forcing from various greenhouse gases [source: NOAA, 2012 [4]].

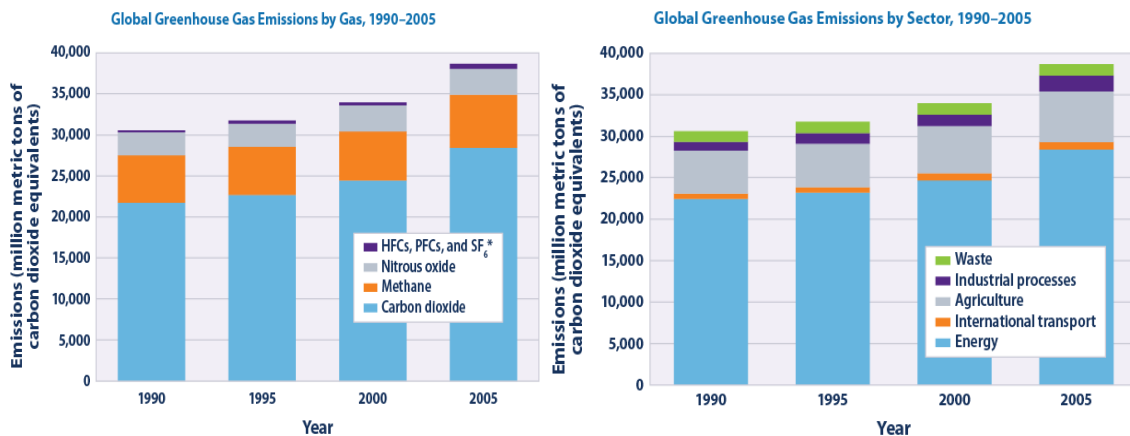


Figure 1.3: The global GHG emissions distribution by gases and sectors [source: World Resources Institute, 2012 [5]].

Figure 1.3 shows worldwide emissions resulting from various gases (carbon dioxide, methane, nitrous oxide, and several fluorinated gases) and sectors from 1990 to 2005. In 2005, the worldwide emissions were estimated to be nearly 39 billion metric tons of greenhouse gases expressed as carbon dioxide equivalents, representing a 26% increase from 1990. Between 1990 and 2005, all major greenhouse gases emissions increased. This increase was mainly contributed by the energy sector, which is the largest source of

greenhouse gas emissions worldwide (about 73% of the total), followed by agriculture (16 to 17%). It can be inferred that the increase in energy-related emissions is driven by the economic growth of emerging economies and the availability of fossil fuel resources since 1990.

Further climate changes can be expected if emissions of greenhouse gases continued, including a warmer atmosphere, a warmer and more acidic ocean, higher sea levels, and larger changes in precipitation patterns. For instance, the rise in the average global temperatures are expected to be from 2 °F to 11.5 °F by 2100 as shown in Figure 1.4, depending on the level of future greenhouse gas emissions and the expectations from various models [6]. By 2100, it is expected to warm at least twice compared with the last 100 years [1]. Warming temperatures lead to sea level rise by several ways: expanding ocean water; melting mountain glaciers and ice caps; and causing portions of the Greenland and Antarctic ice sheets to melt [7]. The global sea levels for the decades is therefore expected to rise at a greater rate than the past 50 years [2].

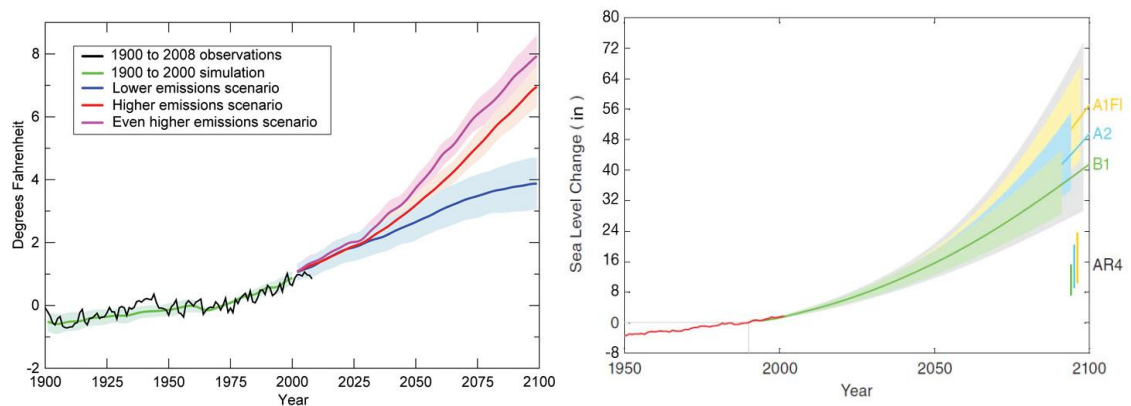


Figure 1.4: The expectation of future temperature and sea level change [source: US EPA, 2006 [8]].

1.1.2 The Sources of Methane Emissions

Regarding the topic of global warming, most of the concern has focused on emissions of carbon dioxide (CO₂) from the energy sector, which contribute over 61% of total manmade GHG emissions. However, a closer look should be taken to methane emissions from the energy and resources sectors to create an effective and efficient solution to climate change.

Methane is reported to be a potent greenhouse gas: 25 times more powerful than CO₂ over a 100-year time period. As a result, reductions in methane emissions is of great significance to not only stabilise the climate in the near term but also buying time for longer term energy technology solutions to be implemented [9].

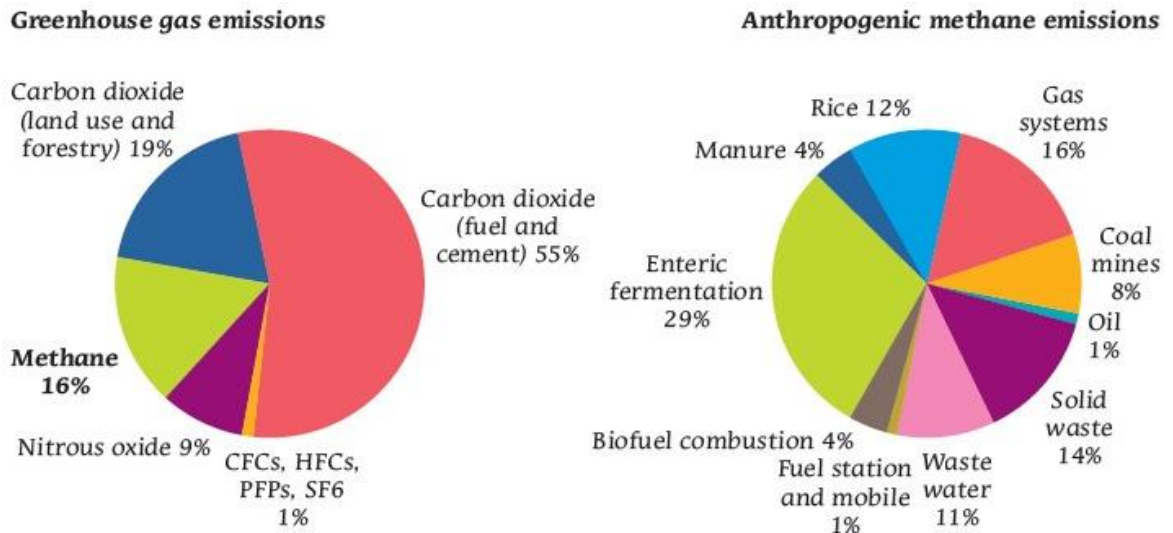


Figure 1.5: The sources of anthropogenic methane emissions [source: US EPA, 2006 [8]].

Methane emissions can be from a variety of anthropogenic and natural activities, accounting for 16% of global GHG emissions (see Figure 1.5). In 2005, Over 44 Gt CO₂-equivalent emissions (CO₂-eq) were emitted globally and methane accounts for 7 Gt CO₂-eq. Anthropogenic activities account for 70% of methane emissions and the rest from natural sources. Approximately 25% of anthropogenic methane emissions are due to energy and resources sectors, such as coalmining and natural gas and oil recovery activities, in the form of low concentration methane.

Coalmine methane (CMM) refers to methane released from the coal mine due to mining activities. In underground mines, it creates an explosive hazard to coalminers. Hence, it is typically removed using ventilation systems. Coalmining is estimated to contribute 8% of total global anthropogenic methane emissions [8]. Driven by the growth in coal production, combined with technology improvements on deeper coal extraction, 20% growth in CMM emissions is expected in the time frame of 2000 to 2020 [10]. For occupational health and safety reasons, methane concentrations in ventilation systems of underground coalmines are

kept typically less than 1% methane in air. This gas mixture which primarily contains air along with a dilute concentration of methane is commonly known as ventilation air methane (VAM). It is reported that approximately 64% of methane emissions in underground coalmine operations are the result of ventilation air methane (VAM).

1.1.3 Utilisation of Ventilation Air Methane

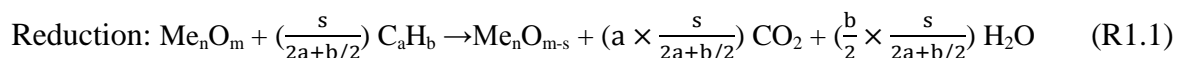
To lower and maintain the anthropogenic greenhouse gas emissions at desired levels, the emissions of ventilation air methane should be mitigated. One option (maybe the most effective one) is to reduce global energy consumption, especially electricity energy from fossil fuels. This can be accomplished by replacing fossil fuels with renewable energy sources like hydropower, wind power or solar energy or alternatively with nuclear power. However, the large-scale utilisation of these energy sources is restricted by the cost and conversion efficiency. Another option which is more cost effective in the near term is to develop advanced technologies for utilisation of VAM emissions.

It is difficult to utilise of VAM in conventional combustion methods primarily because: (i) the volume of VAM is large (as high as 600m³/s); (ii) the methane concentration in VAM is dilute (0.1-1 % V/V); and (iii) the concentration of methane and the flow rate of the gas mixture varied over time (iv) dust presents in the gas mixture. Currently VAM is more of being mitigated through systems based on principal use of methane (as opposed to ancillary use) other than being utilised. Examples of such systems include: TFRR [11] (thermal flow reversal reactors), CFRR [12] (catalytic flow reversal reactors), CMR [13] (catalytic monolith reactors), and CLBGT [14] (catalytic lean-burn gas turbines). The above technologies suffer from a range of shortcomings including: (a) unstable performance due to frequent variations in the VAM flow rate and concentration; (b) unable to work with VAM concentrations below 0.3 vol%; (c) high extra energy demand for ignition; (d) inherent safety and heat management issues; and (e) limitations on integration with other technology options at mine sites for combined heat and power generation. Chemical looping based processes have the potential to resolve these shortcomings in an effective manner and, as such, are the focus of this study.

1.1.4 Chemical Looping Technology

Chemical looping is a versatile and robust reaction concept that can be used in a variety of different applications with the added benefit of avoiding unwanted emissions or by-products. The chemical looping concept was first proposed by Richter and Knoche [15] in the 1980s for increasing power plant efficiency as this system enhances the reversibility through the two redox reactions. Nevertheless, during recent decades, research interest has focussed on its inherent carbon capture ability. In this process, the undiluted CO₂ stream from the reducer is stored after condensing water without any separation penalty while the oxidiser exit gas can be discharged to the atmosphere causing minimal greenhouse gas pollution.

The first use of chemical looping concept was for combustion (the so-called chemical looping combustion) of gaseous fuels. In this oxy-firing approach (as illustrated in Figure 1.6), carbon dioxide is inherently separated from nitrogen thus saving the cost for separation using membrane or carbonation, and improving the energy utilisation efficiency as the irreversibility is decreased. This approach eliminates the need for expensive post-combustion capture options which are being considered in the broader context of carbon capture and sequestration. The CLC process is commonly carried out in a two-step reduction/oxidation (redox) reaction by circulating metal oxide particles between two connected reactors (see reactions R1.1 to R1.3). Fuel is burnt with oxygen carrier particles, e.g. metal oxide (Me_nO_m), in a fuel reactor (FR) while oxygen carrier particles are reduced to Me_nO_{m-s}. The oxygen carriers are then transferred to an air reactor (AR) to react with air and oxidise to their original oxidation state (this is commonly referred to as regeneration). CO₂ and steam are the main products from the fuel reactor although minute quantities of CO, CH₄, H₂ and other hydrocarbons can also form. The product gas from the air reactor primarily consists of N₂ and excess oxygen. As noted, CO₂ and N₂ do not mix in the CLC process and as such the operational costs and energy efficiency are both improved dramatically compared with conventional combustion.



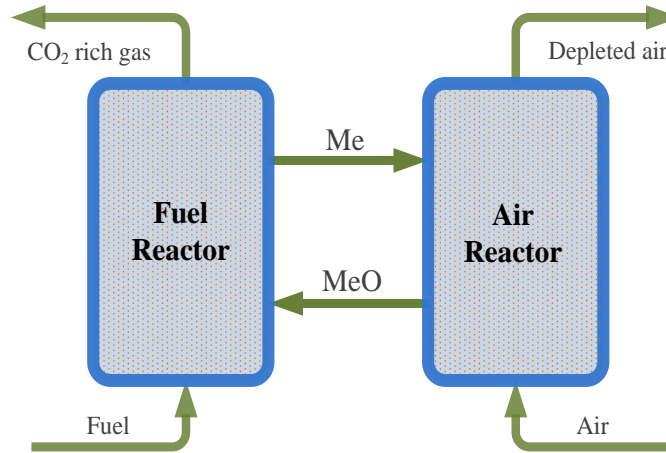
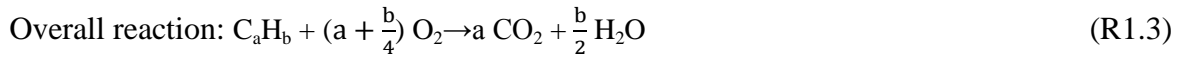
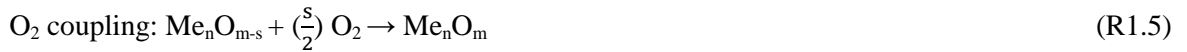


Figure 1.6: Scheme of chemical looping combustion.

Apart from the power generation, chemical looping schemes are proposed to produce pure hydrogen which are so-called “chemical looping hydrogen generation (CLHG)” processes. Typically, the produced hydrogen can be subsequently used for power generation as a clean fuel or alternatively as a feedstock for other chemical manufacturing processes. Most of CLHG processes are devised based on the well-known steam/iron process and employed three-reactor layout to achieve the goal of polygeneration of hydrogen and power. The principle of the three-reactor processes is first reducing Fe_2O_3 to FeO and/or Fe in the fuel reactor which is similar to the CLC process. The reduced iron oxides (FeO and/or Fe) are then partially oxidised to Fe_3O_4 by steam in the steam reactor and finally to Fe_2O_3 by O_2 in air reactor. The detailed information for CLHG is referred to Section 2.2.2.

The chemical looping based methods are also developed for air separation by our group, known as chemical looping air separation (CLAS). The scheme of this process is similar with the CLC process. The difference is that there is no need for fuel in the fuel reactor of CLAS and instead steam is introduced as the atmosphere of decomposition of metal oxides. The principle of CLAS is based on the assumption that metal oxides can decouple oxygen at high temperatures in one reactor (R1.4) and re-oxidised by air in second reactor (R1.5).



1.2 Motivation

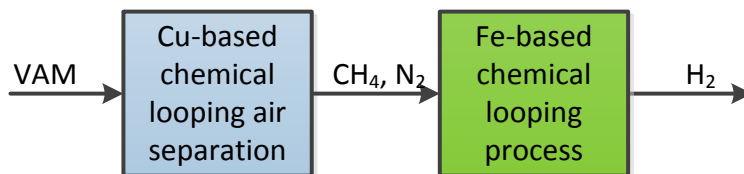
The Environmental Protection Agency [16] and the Intergovernmental Panel on Climate Change [17] have suggested that methane has the second largest portions of greenhouse gas emitted by human activities after carbon dioxide and has a much greater short-term global warming potential [2]. This means that increasing methane emissions has a significant impact on aggravate the issue of global warming, particularly over the short-term, while reducing methane emissions is regarded as a effective solution in slowing down the rate of climate change [18]. Reducing the emission of VAM has the potential to serve as an efficient and economical manner to achieve the aim of reducing methane emissions.

Methane emissions mitigation provides a great deal of important energy, safety, economic, and environmental benefits. First of all, considering the fact that methane is a potent GHG (25 times more potent than CO₂ on a 100-year basis), and has a short atmospheric lifetime, reductions of methane emissions are able to create important near term progress toward climate change mitigation. In addition, methane is known as a valuable, clean-burning energy source that benefits to local economic development and local environmental pollution reduction. Methane recovery enables the reduction on coal supply in power plant for power generation and as such reduces emissions of CO₂ and air pollutants. Finally, it is also able to improve safety conditions by reducing the exposure of methane in air. Thus coalmine methane should be recovered and used as an important source of energy for their own use or for local gas or electricity networks [9].

1.3 Aims and Objectives

The present thesis is concerned with the development of chemical looping based processes for utilisation and/or mitigation of VAM. The focus on chemical looping approach is primarily driven by the fact that such processes can overcome the shortcomings of conventional technologies (see Chapter 2 for more details) and can be deployed to a diverse range of mine settings. The thesis specifically examines three novel iron oxide based chemical looping processes for utilisation and/or mitigation of VAM with the aim of determining the science underpinning these alternative process options. The processes examined in this study are:

1. A dual loop chemical looping process for conversion of VAM to hydrogen as a value added product (see Figure 1.7a).
2. An integrated gasification chemical looping combustion (IGCLC) process for hydrogen enrichment of VAM followed by the thermal oxidation of the resultant mixture (see Figure 1.7b).
3. Ancillary use of VAM as an oxidizing agent in chemical looping combustion of synthesis gas (see Figure 1.7c).



(a)

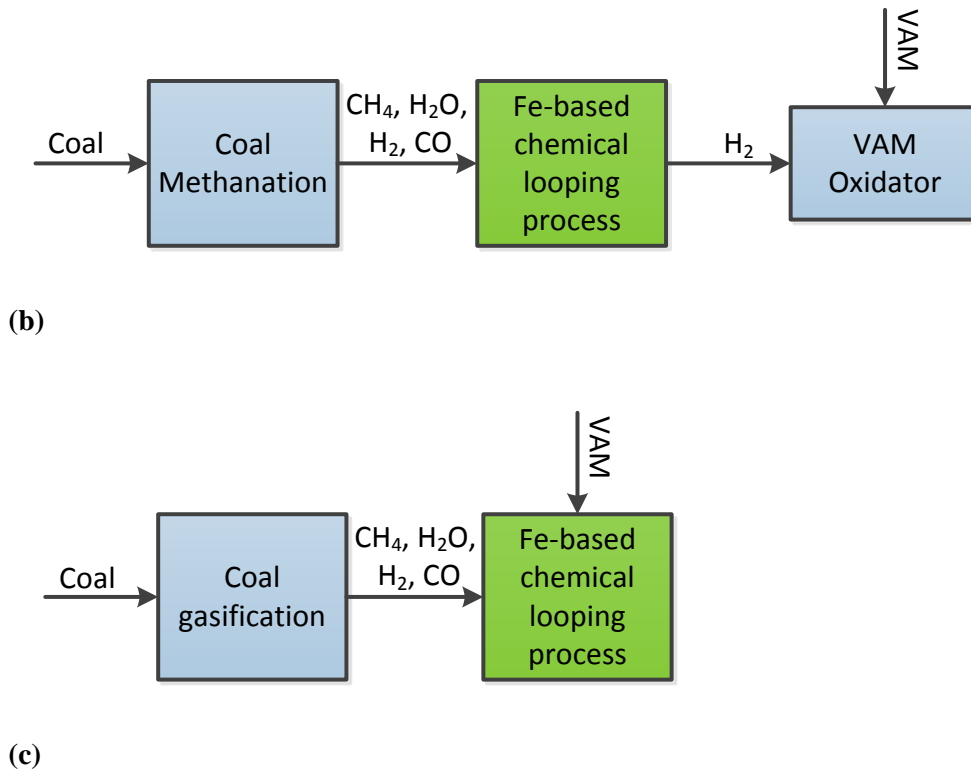


Figure 1.7: Fe-based chemical looping processes for VAM treatment.

To achieve the broad objectives of the study, the following key research tasks were undertaken:

- Evaluation of the thermodynamics feasibility of the three alternative options,
- Investigation of the impact of the process parameters on the overall efficiency for each process option,
- Experimental investigation of the oxidation of VAM as oxidation agent in chemical looping combustion process,
- Examination of the reduction reactivity of Fe_2O_3 to FeO by ultra-low CH_4 for hydrogen production,
- Identification of the most suitable $\text{Fe}_2\text{O}_3/\text{Al}_2\text{O}_3$ and reduction temperature for oxidising ultra-low CH_4 and producing hydrogen,
- Development of a kinetics model which can be used to mathematically describe the reduction mechanism of Fe_2O_3 to FeO with ultra-low CH_4 .

1.4 Structure of the Thesis

This thesis comprises 9 chapters including the present chapter that focuses on introducing the project and its aims and objectives.

In Chapter 2, the conventional techniques for mitigating VAM emission are critically reviewed and the technical backgrounds of these approaches are described along with more detailed information about the previous work on CLC and other relevant chemical looping processes.

Chapter 3 gives an introduction to the theoretical and experimental methods and techniques employed in this thesis for examination of the feasibility and performance of the three proposed chemical looping processes. The theoretical studies were carried out using the process modelling/simulation software, ASPEN PLUS, while the experimental studies were conducted in a TGA (thermogravimetric Analyser) and a fixed bed setup. With the combination of theoretical and experimental studies, both the thermodynamics and kinetics analysis were accomplished.

Chapter 4 provides the results of an experimental study on the reduction of Fe_2O_3 to FeO by ultra-low concentration methane. The motivation behind this study was that the reduction of Fe_2O_3 to FeO constitutes a key step in reforming VAM into pure hydrogen and, hence, is of particular importance in the first process option proposed here (i.e. dual chemical loop).

Chapter 5 complements Chapter 4 and presents the reduction kinetics of Fe_2O_3 to FeO under an environment of ultra-low methane concentration.

Chapter 6 presents the results of the study on dual chemical looping process for reforming VAM into pure hydrogen. The process consists of a Cu-based chemical looping air separation process coupled with a Fe-based chemical looping hydrogen generation process. In this chapter the feasibility of the dual chemical looping process is analysed both thermodynamically and experimentally. The performance characteristics of the process are studied thermodynamically by a case study while the parametric study is conducted to understand the effect of the key controlling parameters on the system performance.

Chapter 7 focuses on the second chemical looping process option outlined earlier in this chapter (i.e. thermal oxidation of hydrogen enriched VAM where H_2 is produced using a novel Integrated Gasification Chemical Looping Combustion (IGCLC) process). The feasibility of this novel process was analysed thermodynamically. A parametric study was also conducted to determine the influence of operating parameters (especially the VAM flow rate and methane concentration) on the overall system performance.

Chapter 8 presents the results of the study on the ancillary use a VAM in the chemical looping combustion process (process option 3 outlined earlier in this chapter). In this process, VAM is used as the oxidation agent in AR where the energy for coal gasification to syngas is supplied by the combination of oxidation of oxygen carrier medium and oxidation of VAM. The potential efficiency of this process for combustion of coal and VAM using the CLC system was investigated thermodynamically while the oxidation of VAM in the presence of oxygen carriers was studied experimentally in a fixed bed reactor setup.

Chapter 9 provides the conclusions reached by this work. Some recommendations are also given for further research in this field of study.

Chapter 2: LITERATURE REVIEW

2.1 Conventional Techniques for VAM Treatment

2.1.1 Principle Use of VAM

Several methods have been developed to reduce the emissions of VAM, which can be categorised into principle use and ancillary use. The principle utilisation technology refers to the use of methane in VAM as the energy source and no additional fuel in assistance to the ignition of methane. In terms of the reaction kinetic mechanism, it can be classified into thermal oxidation and catalytic oxidation [14]. The only difference between them is the use of catalyst. Based on the thermal oxidation principle, a thermal flow reversal reactor (TFRR) was offered by MEGTEC. But it suffers from an extremely high auto-ignition temperature (above 1273K) which causes plenty of energy loss to start-up the operation [19]. It is also a challenge to maintain such a high temperature level for a long-term run as far as the huge flow rate is concerned. It is a modification of a commercially proven process for the thermal oxidation of volatile organic compounds (VOCs).

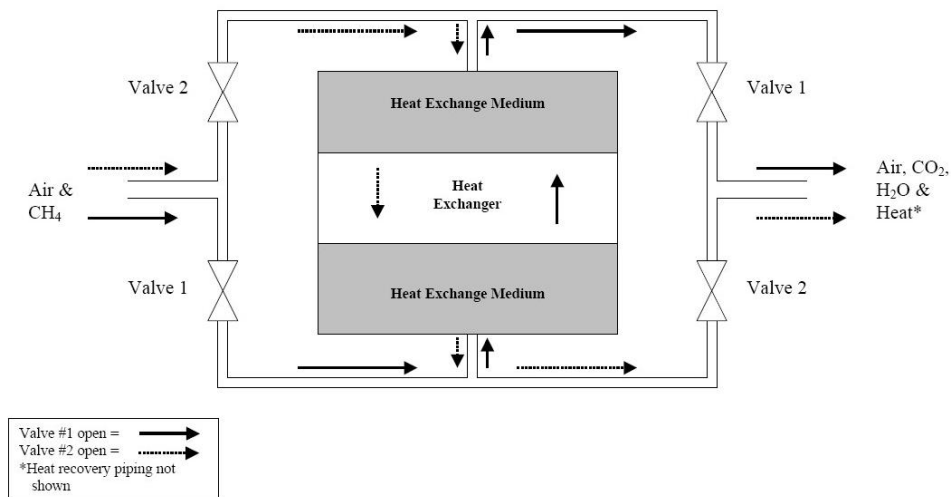


Figure 2.1: Schematic of the TFRR reactor.

Figure 2.1 shows a schematic of the TFRR reactor. A large bed of heat exchange medium was located in the centre. The efficient heat exchange between the gas stream of ventilation air methane and the solid heat exchange medium is able to maintain the reaction temperature in the reaction zone. One cycle of the process consists of two flow reversals, so each flow reversal is a half-cycle. At the beginning, the heat is provided by the use of electrical heating element to initiate the oxidation. During the first half-cycle, ventilation air methane at ambient temperature comes to the reactor and is preheated to the desired oxidation temperature before the methane oxidation takes place. Maintaining this temperature, theoretically speaking, complete conversion of methane (to carbon dioxide and water) can be achieved. If the temperature is lower than required value, the reaction will not occur. As a result, the heat exchange medium is slowly cooled by the incoming cold gas as no heat source is provided. Finally, both solid and gas constituents are cooled down to the ambient temperature. If it is observed over a number of cycles, this situation is called a blow-out [19].

MEGTEC claims that if the methane concentration in the incoming air is consistently 0.15% or more, the auto-thermic operation can be fulfilled (i.e. no need for additional heat or fuel). This means that the oxidation of this quantity of methane can produce enough heat to compensate for an approximate 40 K temperature rise in the exit gas flow (relative to incoming gas temperature), which represents a heat loss from the process. Li studied the potential of using TFRR for reducing VAM emissions in a thermal reverse flow reactor packed with the ceramic honeycomb monoliths and started up with a burner. The methane thermal oxidation characteristics were studied experimentally with different methane concentrations (0.3–1 vol%). The results show that the lean methane oxidation can be run auto-thermally and sustained in the reverse flow reactor; the methane conversion efficiency achieved is over 95%; the lowest methane concentration limit at which methane will oxidise reliably is approximately 0.3 vol% [20]. Gosiewski studied the homogeneous, thermal combustion of lean methane mixtures in pelletised bed. It can be expected that complete thermal combustion will be obtained at reasonable operating temperatures. Complete combustion can be expected above 1023K, but heat accumulation in the reverse flow reactor leads to a much higher maximum temperature. However, for optimised process

parameters the maximum temperature for the combustion of coalmine ventilation air will not exceed 1473K. On the other hand, with the higher temperature of the hot gas withdrawn from the TFRR the efficiency of heat recovery should also be higher [11]. He also suggested that the ignition temperature for the homogeneous combustion of methane strongly depends on the area of the surface in contact with the gas phase. That is, the lower the surface area, the higher the auto-ignition temperature. Wang claimed that the ignition temperature is about 992K for homogeneous thermal oxidation of lean methane. It can be seen that the methane conversions are independent on the inlet methane concentration under fuel-lean conditions [21]. This conclusion is also in agreement with that by Gosiewski et al. [11]. To facilitate the reactor design for thermal oxidation of lean methane fuel, homogeneous reaction kinetics models are developed and adapted in simulation work.

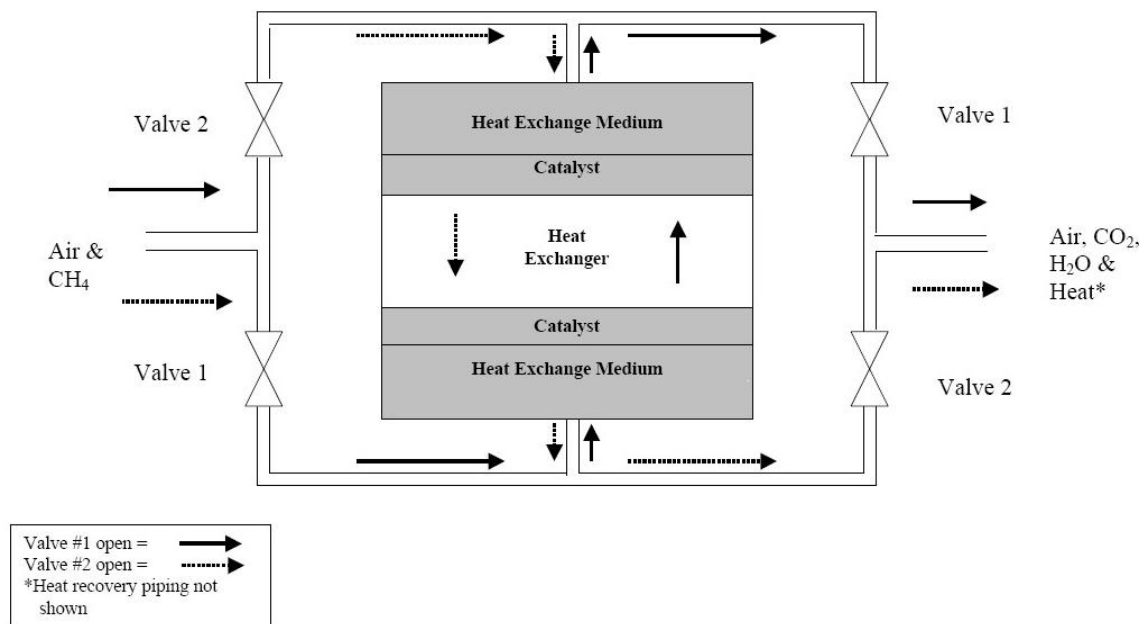


Figure 2.2: Schematic of the CFRR reactor.

To lower the start temperature, a catalytic flow reversal reactor (CFRR) was developed by CANMET. As a result of this new technology, the oxidation-initial temperature is decreased by several hundred degrees Celsius [19]. The CFRR has the same basic design and operation as the TFRR described above. A schematic of the process shows that the reactor has three sections (see Figure 2.2). The sections at the two ends of the bed are packed beds of inert materials. During “top-to-bottom” flow, the incoming ventilation air is

preheated by the heating element at the top section. Once it rises to the desired temperature around 773–1073 K, catalytic oxidation will commence in the centre section packed with particles of catalyst. The hot products continue to pass into the bottom section and the heat is transferred to the bed [19].

CFRR's operating principle is identical to that of its thermal counterpart except that the reaction mechanism is catalytic reaction and therefore takes place at much lower temperatures. CANMET asserts that catalytic oxidation allows the use of smaller units because with lower temperatures the wave front moves more slowly, thus travelling a shorter distance between flow reversals. Both the lower temperatures and smaller size tend to favour a lower capital cost [19]. Although the CFRR delivers some advantages over the TFRR, it comes up with some challenges on the design and operation. For instance, it needs to consume some expensive metals or metal oxides as catalyst like: Pd, Pt, Rh or PdO [12, 13, 22, 23]. In addition, its reactor design is more complicated in order to get enough contact surfaces. The performance of CFRR can be improved using the design of catalytic monolith reactor (CMR) developed by CSIRO, Australia [13]. This advanced technology is in common use due to its low-pressure drop at high mass flow rates and high geometric surface area. However, it can only treat VAM stream with a minimum methane concentration of 0.4 vol% [14].

Relevant studies on catalytic combustion of methane have been carried out for decades. Stasinska reviewed the catalyst in active oxide and metallic form for the utilisation of VAM. It was observed that noble metals or metal oxides showed the best activity for methane oxidation at low temperatures. Particularly supported Pd, Pt or PdO has been extensively employed as catalyst on methane combustion [22]. It was believed that the higher reactivity resulted from the larger surface area and therefore much more active sites. The effect of Pt loading on methane oxidation was investigated over the range 0.027–100 wt%. The rate increased with an increase in Pt loading and reached a maximum value at about 5 wt%. Above 10 wt%, the reaction rate decreased significantly [24]. Supports also play an important part in determining the activity of the catalysts. It was found that activity of catalysts decreased in the order: Pt/SiO₂-Al₂O₃>Pt/Al₂O₃>Pt/SiO₂ [25]. Yang believed that catalytic activity of Pd supported by Mg modified Al₂O₃ for methane combustion can be

enhanced by MgAl_2O_4 spinel [26]. Baldwin concluded that Pd catalysts supported on α -alumina are considerably more active than those supported on γ -alumina and become more active with time when heated in a methane/air atmosphere [27]. The support material played an important role in determining the period of activation. Silica-supported catalysts exhibited very quick, dramatic increases in activity while the activation with alumina-supported catalysts was over much longer periods but was equally dramatic as with silica-supported catalysts. It was proposed that a possible reason for the catalyst activation is the reconstruction of the palladium oxide crystallites [28]. Janbey disclosed that Pt is less active than Pd when deposited on the surface of the TiO_2 , but more active when deposited on γ - Al_2O_3 [29]. Gelin reviewed the noble metal catalyst for the abatement of natural gas vehicle methane emissions at low temperatures. From the open literature, some conclusions can be made: that supported Pd catalysts are the most active materials in the total oxidation of methane under lean-burn conditions. The sensitivity of Pd catalysts to H_2O and sulfur containing compounds represents a serious drawback to their use as an efficient catalyst while Pt catalysts have much less sensitivity to sulfur containing poisons than Pd catalysts under oxidising conditions [30]. Although PdO offers good activity with a relatively low light-off temperature, its main drawback is that it tends to lose activity at higher temperatures, owing to a transition of the active PdO to the less active Pd [31]. A Pt-Pd/alumina catalyst exhibited higher and longer-lasting hydrocarbon oxidation activity than Pt-Rh/alumina, Pt/alumina, and Pd/alumina catalysts. Increasing the palladium content in Pt-Pd/alumina catalyst led to the increase in the oxidation activity and durability [32].

However, they suffer from shortcomings such as poor availability and economics. To overcome the above challenges, some non-noble materials are adapted to replace the role of these noble metals, such as Fe_2O_3 , Co_3O_4 , CuO, MgO, Mn_3O_4 , and alumina industry waste or perovskite-type oxides [33-36]. Though they are not as active as noble metals, they possess better thermal stability and resistance to sintering. CuO deposited onto MgAl_2O_4 was found to be an efficient catalyst for the total oxidation of methane with a selectivity of 100% to carbon dioxide. The catalytic activity was preserved after a thermal treatment at 1273K in the presence of water and despite the partial formation of copper aluminate. But after 1473K, the Cu^{2+} was reduced to Cu species which was a totally inactive solid [34].

The study by Berg showed that magnesium oxide had a catalytic effect on the combustion kinetics of methane. The temperature needed for 10% conversion was decreased by 543K compared to an empty reactor [37]. The experimental results using Co_3O_4 as catalyst indicated that the active metal oxide loadings above 0.46 wt% were active starting at a temperature of 523K and complete conversion of methane to CO_2 was found below 823K [38]. Perovskite-based catalysts prepared via active phase dispersion on $\text{La}/\gamma\text{-Al}_2\text{O}_3$ porous washcoat showed good activity and stability in methane combustion up to at least 1273K. The inlet lean methane was completely converted to CO_2 and H_2O provided its inlet temperature was at about 773K. A weak deactivation of catalysts was observed in the initial operations, while after 120 h under reaction conditions, the activity appeared stable and still very high [39]. MgO supported LaMnO_3 perovskites samples, whose high activity was associated with remarkable thermal stability, was considered to be a more promising catalyst for VAM combustion than $\text{La}/\gamma\text{-Al}_2\text{O}_3$ supported samples [40]. The activity of some perovskite-type oxides, such as La-Fe, La-Mn, and La-Co oxide, and Sr-doped LaMnO_3 ($\text{La}_{0.6}\text{Sr}_{0.4}\text{MnO}_3$), was found to be compared with $\text{Pt}/\text{Al}_2\text{O}_3$ catalyst which was the most active one in the combustion of lean methane. Especially, Sr-doped LaMnO_3 , it was as active as Pt/alumina catalyst at a conversion level below 80% [36].

Iron oxide, as an industry abundant and cheap material, has the potential to be an alternative for complete oxidation of methane as it has been proven to be a good catalyst in a wide field of application like hydrogenation and hydroliquefaction. Barbosa [41] suggested that unsupported iron oxide presented remarkable initial activity but the stability was undermined at the operation temperatures. Fe_2O_3 supported by MgO or $\text{Ce}_{0.67}\text{Zr}_{0.33}\text{O}_2\text{-Al}_2\text{O}_3$ showed better performance in activity and the optimised loading content was found at 6%–8% [42, 43]. For Sol-gel Fe/TiO_2 catalysts, the optimised loading content was 5 wt% in the range of 1–10%. The temperature required to obtain 50% of CH_4 conversion was around 790K [44]. Three iron-based waste materials from the aluminium industry were used for catalytic combustion of methane [45]. It was shown that the activity increased with the increase in hematite content. Choudhary examined nano-gold catalysts, the $\text{Au}/\text{Fe}_2\text{O}_3$ (Au loading = 6.1%), which showed an excellent performance compared to Pd (1%)/ Al_2O_3 and Pt (1%)/ Al_2O_3 under identical conditions [46].

Based on the experiment results on a pilot scale CFRR, it could be concluded that it is possible to maintain the auto-thermal operation of the reactor at methane concentrations as low as 0.22 vol% with VAM flow feeding at ambient temperature. The overall performance of the system was dependent on methane concentration, cycle time and velocity [47]. The comparison of the performance of catalytic reverse flow reactors containing the catalyst, either as a packed bed or as monolith, showed that the particle bed performs better in terms of reactor stability, whereas the pressure drop was largely higher in the particle bed reactor. The results also indicated that monolithic reverse flow reactors perform with some favourable characteristics, such as the higher intra-particle effectiveness factor, and higher solid density [48]. Wang studied the combustion of VAM in CFRR with 0.15 wt% Pd/Al₂O₃ as catalyst, indicating that the reactor can run in stability with a methane concentration as low as 0.13 vol% with methane conversion around 90% [12].

Regarding the heat recovery from reverse flow reactors (RFRs), Aube predicted the theoretical heat recovery from a catalytic combustion reverse flow reactor for lean methane combustion and concluded that the configuration of hot gas removal from the central bed can recover much more heat than the heat exchange along the same location [49]. The comparison of the four different configurations for heat recovery from the combustion of lean methane mixtures in RFRs, indicated that withdrawing hot gas from the end of the catalytic bed affects the RFR stability to a lower extent than withdrawing the hot gas from the reactor centre. The configuration consisting of withdrawing part of the hot gas from the catalytic bed end, with no return of the cool gas, provided the most stable RFR operation, and allowed high-heat recovery efficiencies maintaining very high methane conversions [50]. Gosiewski's simulation work revealed an apparent contradiction between maximum temperature in the reactor and efficiency of the heat recovery. High efficiency of heat recovery can be obtained only at the expense of high catalyst temperature. However, too high a maximum temperature could cause sintering and deactivation to the catalyst [51].

There could be no doubt that the TFRR, CFRR and CMR technologies are technically feasible to mitigate ventilation air methane when the CH₄ concentration in air exceeds the minimum requirement and economic performance is not an issue. These technologies can cope with the variations of methane concentration and flow rate. However, for some mine

sites the continuous operation of these units may require additional fuel depending on the CH₄ concentration being not less than the minimum requirement and how long the operation can last at the minimum CH₄ concentration. In addition, to recover heat from these units for power generation additional fuel is needed to increase methane concentration to a constant level, perhaps, at least 0.9 vol% according to the current design practices [14].

2.1.2 Ancillary Use of VAM

In addition to the principle use of VAM noted above, ancillary use of VAM could be another noteworthy option applicable to many industrial settings. Generally, it involves using VAM to totally, or partly, replaces air in a combustion process. Some applications can be found in internal combustion engines and mine-mouth coal-fired power plants [19], where the heat requirement is provided by the combustion of main fuel. Due to the fact of containing dust in VAM, it has been a consent that VAM is more suitable for being used for coal fired projects which need a large amount of supply on air for combustion and is not influenced by the presence of dust. This approach is technically available and commercially proven by one of the latest demonstration projects built at Valse Point Power Station in Australia.

Another concern for this approach is the fluctuation of methane concentration which may bring about a unstable operation of the boiler. It was shown in You's laboratory experimental results that VAM oxidation does not obviously affect the boiler operation when the methane concentration is less than 0.6% [52]. However, when the methane concentrations changes rapidly over 1 vol%, it will lead to a rapid increase in the local combustion temperature which is detrimental to the boiler operation.

As a result of the combustion air substitution, not only the ventilation air methane is mitigated but also the fuel purchase cost is reduced. You estimated that around 4.3% of the total energy was provided by the intake of ventilation air methane. Similar results also showed by the project in Australia which employed VAM as feeding air into internal combustion engine. In this project, approximately 7% of the total energy arises from VAM.

2.2 Chemical Looping Processes

2.2.1 Chemical Looping Combustion

Chemical looping technology was initially developed to secure higher conversion efficiency due to its lower irreversibility loss during energy conversion. It was then found to own the ability of separating CO₂ from N₂ inherently, which causes large efficiency penalties in order to capture a concentrated stream of CO₂. Therefore, it was recommended for use in the field of fuel combustion for power generation due to the restraint in CO₂ emissions dictated by Kyoto protocol in 1997. The theoretical analysis revealed that the CLC system with gaseous fuels or solid fuels delivers a higher thermal efficiency than the conventional power plants either with or without CCS (carbon dioxide capture system). Ishida [53] evaluated the performance of a chemical looping combustion system with Fe-based oxygen carrier (Fe₂O₃-FeO) and the fuel of methane by graphic exergy analysis. Results showed the thermal efficiency was as high as 50.2% (LHV) compared with CCS of 45.9% and MPCS of 47% because it delivered less exergy loss during reactions. The performance of a similar system CLSA (chemical looping combustion with air saturation) with Ni-based oxygen carrier and methane as fuel was also investigated. The power efficiency was 55.1% which was 7% higher than that of a steam injected gas turbine cycle as the inefficiency in the low-, middle-, high-temperature regions became small when combining chemical looping combustion and air saturation technologies [54]. In 2000, a novel hydrogen fuelled chemical looping combustion system was proposed [55]. As expected 12 points higher efficiency (63.5% based on LHV) was obtained compared with a conventional hydrogen/pure oxygen combustion gas turbine cycle. Anheden [56] simulated three different chemical looping combustion processes with integrated coal gasification and compared with a conventional IGCC system. Three different oxygen carriers, i.e. NiO/Ni, Fe₂O₃/FeO, Mn₃O₄/MnO were used, while little difference was demonstrated in the plant configurations. The simulation results for power efficiency of four systems were identical but the CLC integrated coal gasification processes owned the inherent ability of CO₂ capture. In a later publication [57], a further detailed exergy analysis was performed for NiO/Ni with methane or syngas and Fe₂O₃/FeO with syngas. Rezvani [58] made a

comparison of coal-fired IGCC with various CO₂ capture technologies, i.e. physical absorption, membrane reactors and single or double stage CLC with NiO/Al₂O₃. Results revealed that the integration of CO₂ capture decreased 8~10% in net power efficiency. Double stage CLC offered the highest efficiency (36.6%) but the economic performance was outperformed by the others.

With the in-depth research in the application of chemical looping technology, in addition to the ability of improving the plant efficiency and inherent separation CO₂, it was found that the chemical looping technology could be adapted in more applications, such as pure hydrogen generation, air separation and CH₄ reforming.

2.2.2 Chemical Looping Hydrogen Generation

A number of literatures studied the performance of using chemical looping technique for coproduction of hydrogen and electricity. Xiang [59] investigated the thermodynamic performance of an integrated coal gasification CLC system for coproduction of hydrogen and electricity with inherent CO₂ capture. In the proposed system, the oxygen carrier (Fe₃O₄/FeO) was cycling between a fuel reactor and steam reactor. The overall efficiency was 57.85% with a steam reactor temperature of 815°C and steam conversion rate of 37%. With a higher conversion rate, i.e. 41%, the efficiency increased to 58.33%. A three reactors CLC system for hydrogen and electricity production was investigated in a later publication [60]. The total efficiency could reach a value of 61.66% and 59.98% with or without supplementary firing at the steam conversion rate of 37%. The higher efficiency was offset by a CO₂ emission of 238.9 kg/kWh. The efficiency went up to 62.68% while CO₂ emissions came down to 229.4 kg/kWh for the steam conversion rate of 50%. The flexibility of hydrogen and electricity could be adjusted by changing the oxygen carrier circulation ratio and adding inert support material.

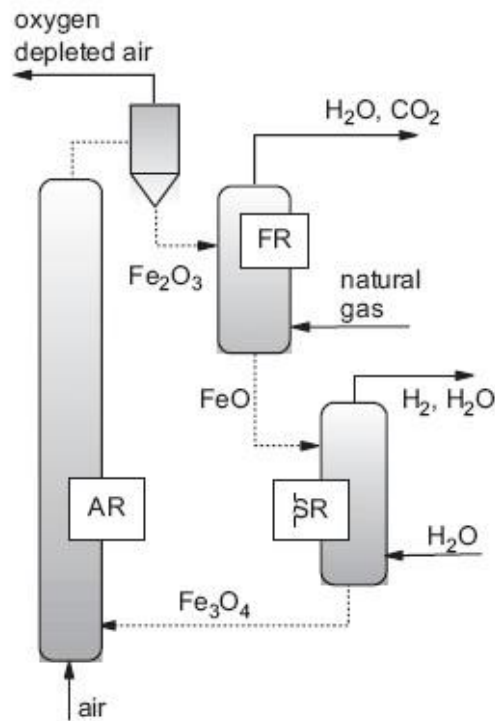


Figure 2.3: Schematic of three reactors CLHG process [61].

Chiesa [61] proposed a three reactor chemical looping process for producing hydrogen and electricity from natural gas as shown in Figure 2.3. Two plant configurations were presented: one was steam compression plant and another one was combustion turbine plant. The mass and energy balance method was used to analyse the system performance. Results uncovered that the steam compression plant delivered a higher global efficiency (78.09%) than that of the combustion turbine plant (76.6%) with a steam conversion rate of 50%. Compared with the proven steam reforming technology for hydrogen production, the efficiency is almost identical but with intrinsic CO₂ capture.

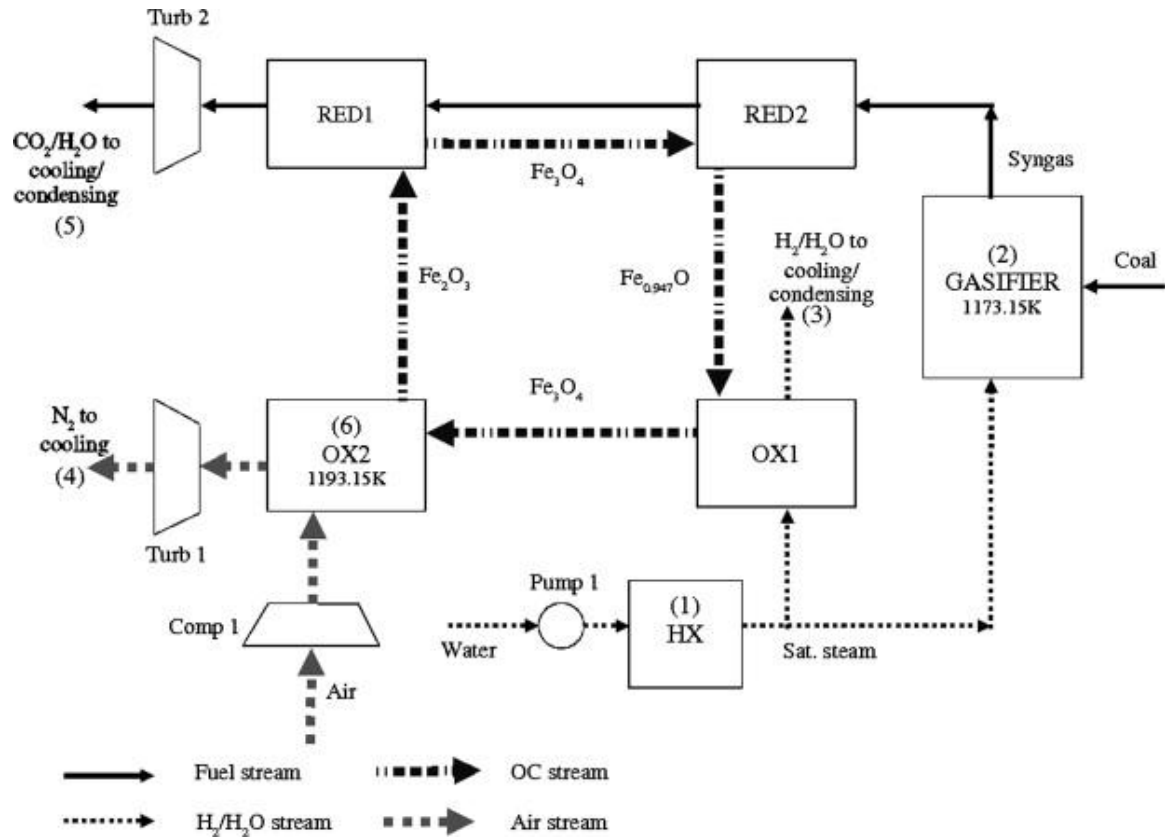


Figure 2.4: Flow sheet of four reactors CLHG process [62].

Cleaton [62] identified a suitable operation regime for a CLC system which is composed of four reactors for producing hydrogen associated with a steam coal gasification process in Figure 2.4. Through varying the oxygen carrier recycle rate and steam in flow rate, the system could be fully heat integrated. The peak exergetic efficiencies achieved for fully heat integrated systems were 48.4% and 58.3% at operating pressures of 1 atmosphere and 10 atmospheres respectively, and these were increased respectively to 53.7% and 59.7% when a bottoming steam turbine cycle was included to utilise waste heat. Gnanapragasam [63] assessed the operation and resource requirements for hydrogen production via SCL and CDCL process using coal as fuel. According to the comparison, the CDCL is superior to the SCL on either resource requirements or hydrogen production. Most important was that the CDCL had a higher H_2/CO_2 ratio, which requires less steam than the SCL process.

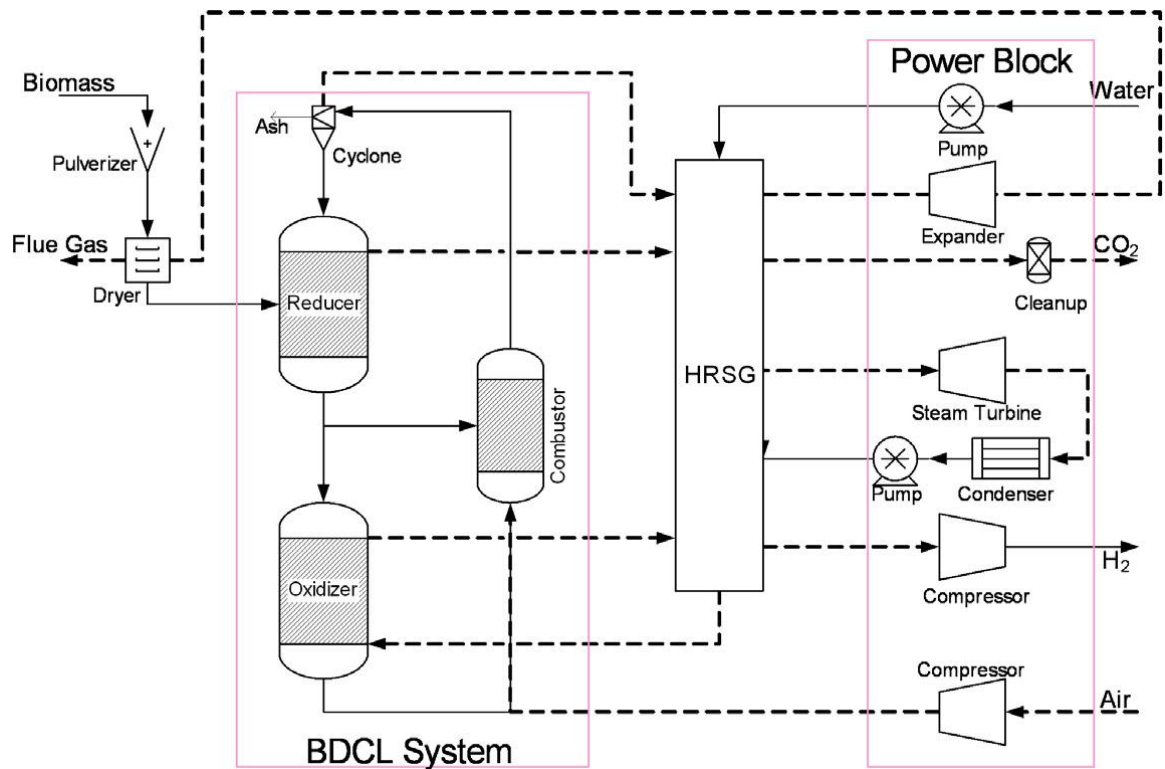


Figure 2.5: Diagram of the BDCL process for hydrogen production [64].

Li [64] proposed a biomass direct chemical looping process (BDCL) for hydrogen or electricity generation as shown in Figure 2.5. The investigation on the performance indicated that the steam conversion could be as high as 75% at 873K and 65% at 1073K. The system could reach a maximum hydrogen efficiency of 74.2% (HHV). Compared to conventional biomass combustion and gasification processes, the BDCL process was 10–25% more efficient. Cormos [65] evaluated an IGCC iron-based chemical looping process for hydrogen and electricity coproduction from technical aspects like: gasifier feeding system (slurry feed vs. transport gas); selection of gasification reactor; heat and power integration analysis; potential ways to increase the overall plant energy efficiency (e.g. integration of air separation unit with gas turbine compressor, steam integration of chemical looping unit into the combined cycle); hydrogen and electricity flexibility analysis; hydrogen and carbon dioxide quality specifications considering the use of hydrogen in transport sector (fuel cells); and carbon dioxide storage in geological formation or using for enhanced oil recovery (EOR). The author [66] also analysed the same process for hydrogen and electricity cogeneration from different fossil fuels, i.e. natural gas, syngas from coal and

lignite gasification. Results indicated that the process with natural gas fuel delivered the highest efficiency of 78.11% with a steam reactor temperature of 781°C and 92% steam conversion rate.

2.2.3 Other Chemical Looping Processes

One of the chemical looping processes should be mentioned is chemical looping air separation process (CLAS, see Figure 2.6). It is first developed by the group of Moghtaderi for the production of pure oxygen [67]. Based on the mass and energy balance calculations, it was found that the specific power was just one eighth of the advanced cryogenic systems. It is then proposed to replace the ASU and integrate with a typical oxy-fuel power plant which is called ICLAS (see Figure 2.7) [68]. The only difference between them is the oxygen decoupling in the presence of recycled flue gas other than steam. This change makes it possible to eliminate the need of steam generation and condensation and, as such, reduces the capital cost and operation cost as well as energy loss.

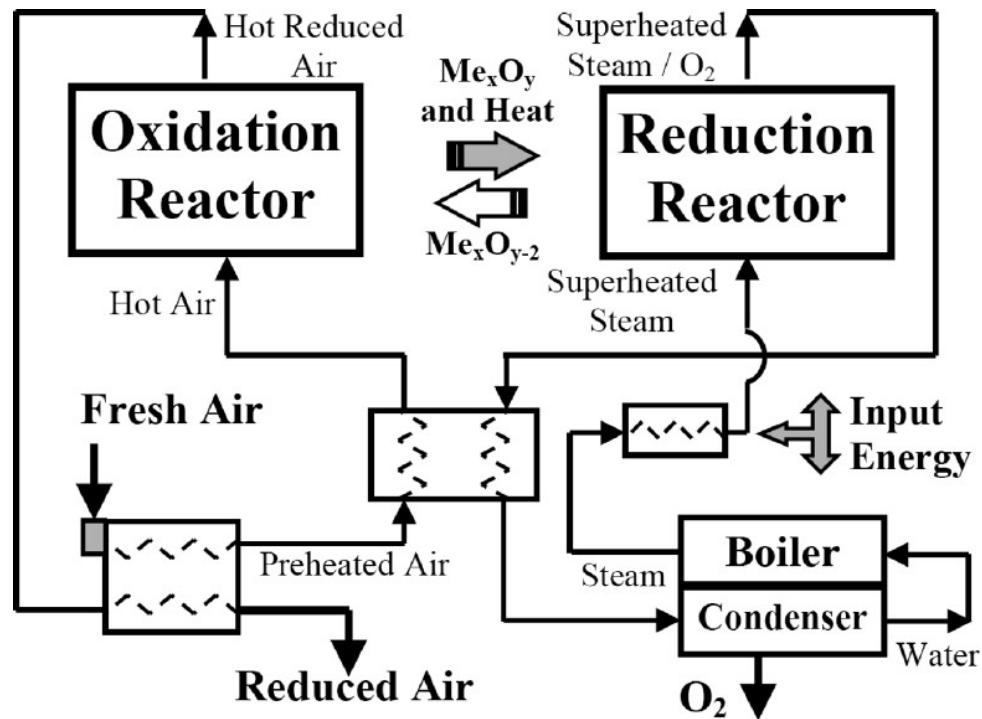


Figure 2.6: Schematic of CLAS [67].

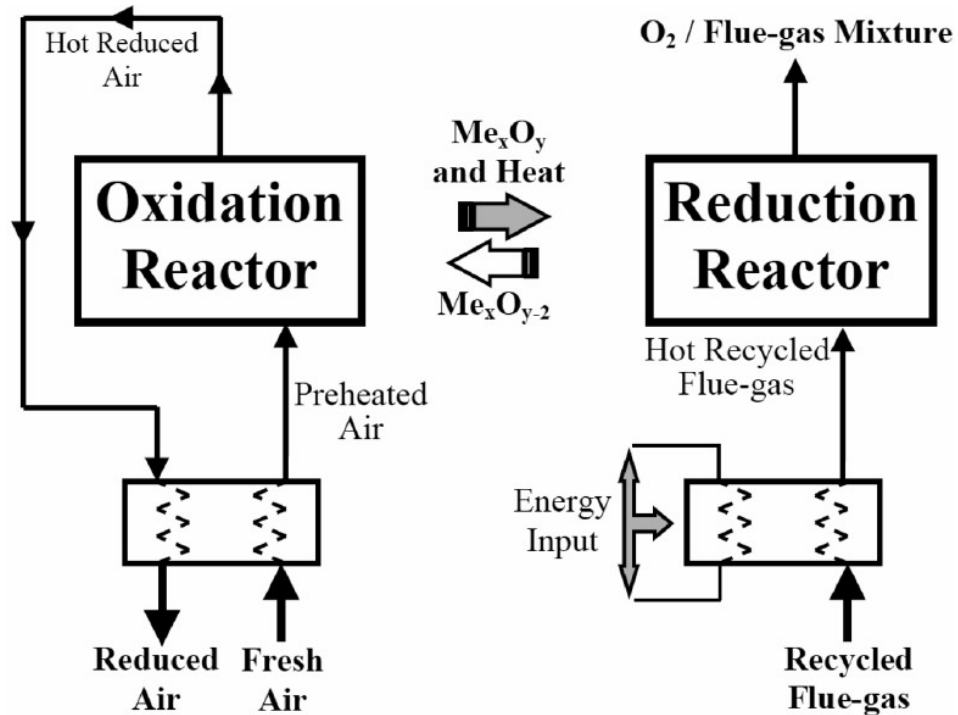


Figure 2.7: Schematic of ICLAS [68].

However, it should be noted that the successful execution of these processes is dependent upon the characteristics of oxygen carriers. The oxygen carriers must be capable of reacting reversely with oxygen at desired temperatures. From thermodynamics point of view, Cu-, Mn-, and Co-based metal oxides show better performance for decoupling oxygen in air. Hui compared comprehensively the reactivity of Al₂O₃ or SiO₂ supported Cu-, Mn, and Co-based oxygen carriers for air separation and suggested that CuO/SiO₂ showed the best performance regarding the performance on reactivity and cyclic stability [69]. He further suggested that the addition of MgO is able to promote the redox stability [70].

2.2.4 Oxygen Carriers in Chemical Looping Processes

Oxygen carriers are the most important elements of chemical looping processes as they shuttle the oxygen between various reactors (e.g. air and fuel reactors in the case of CLC) in a cyclic manner. Normally, there are several principles for selecting an appropriate oxygen carrier, such as the oxygen transfer capacity, reduction and oxidation reactivity, fuel conversion, physical strength, and melting temperature. A higher oxygen transfer

capacity results in the reduction of solid particle recirculation rate; lower reactivity increases the solid inventories; higher fuel conversion lowers the gas recirculation thus increasing the efficiency; to improve the resistant to attrition and fragmentation requires the increase in strength; higher melting temperature leads to reduction in tendency of agglomeration. In addition to the chemical and physical properties, environmental impacts and capital cost should be taken into account. Due to their excellent performance in chemical and mechanical stability, a number of metals and their corresponding oxides have been mentioned in the literature as possible candidates: Fe, Ni, Co, Cu, Mn and Ca. Iron oxide, as a nature abundant and cheap material, has the potential to fully convert gaseous fuel into a stream of CO₂ and H₂O. Moreover, from the perspectives of economics and environmental sustainability, it has advantages over the other alternatives. Obviously, nickel-, copper- and manganese-oxides are an economic issue for a large-scale industry operation while calcium oxide runs the risk of releasing sulfur dioxide in the exhaust gas stream from the reduction reactor. Therefore, iron oxide was believed to be a more promising oxygen carrier candidate and was widely used in the chemical looping combustion process.

Fe-based Oxygen Carriers for CLC

Fe-based metal oxides (Fe₂O₃/Fe₃O₄) are preferred as an oxygen mediator due to good reactivity with gaseous fuels, high gas conversion and high melting temperature, although the oxygen transfer capacity is not good (0.033). It is indicated that the transition state of Fe₂O₃ to Fe₃O₄ is able to fully convert CH₄ or syngas to CO₂ and H₂O at 1073K from thermodynamic aspects of view [71]. Ishida [72] investigated the performance of Fe₂O₃ supported by YSZ, Al₂O₃ or TiO₂ in the reduction of CO. Among these candidates, Fe₂O₃/YSZ exhibited the highest reactivity and oxygen transfer capacity. The reactivity was good during the phase of Fe₂O₃ to Fe₃O₄ with CO or H₂ even at 973K and quite dependent on the CO or H₂ concentration. However, the reaction rate became slow during the phase of Fe₃O₄ to FeO or FeO to Fe [73]. The continuous operation results showed that the gas conversion is very high (almost 100%) during the transition of Fe₂O₃ to Fe₃O₄ with 50 vol% H₂ and 50 vol% CO at temperatures ranging from 1073 to 1223K [74]. Leion [75] investigated the feasibility of using ilmenite as an oxygen carrier in the chemical looping

combustion of syngas (50 vol% H₂+50 vol% CO). The experimental results have shown that the gas conversion varied between 82% and 98% during 37 cycles at 1253K. More interesting, the final reduced form is FeTiO₃ other than metallic iron. Adanez [76] stated that the ilmenite is able to activate itself after redox cycles and the reactivity for H₂ and CO increases about five times.

In comparison with the CLC of iron oxides with syngas, the reactivity of iron oxides for CLC of CH₄ is low and the CH₄ conversion is not as good as expected. Mattisson [77] believed that the reduction rate of Fe₂O₃ (dX/dt) with methane was a function of the solid conversion range (ΔX) and gas yield (γ). For the gas yield range between 50–90%, the conversion range was from 2% to 13% with conversion rates limited between 2%–7%. To achieve a gas yield higher than 90%, the conversion range should be less than 5% with a lower conversion rate (less than 5%). To make an illustration, the conversion range is 11% and 33% for the reduction of Fe₂O₃ to Fe₃O₄ and Fe₂O₃ to FeO. Cho [78] investigated the reactivity of 60 wt% Fe₂O₃/Al₂O₃ with 50 vol% CH₄ balanced with H₂O at 1223K as well as the gas yield for the transition of Fe₂O₃-Fe₃O₄. The highest mass conversion rate was 5.2%/min and the initial gas yield was 70% during the transition interval, which corresponds to the solid inventory of 253 kg/MWth. Adanez [79] thought that Fe₂O₃ supported by Al₂O₃ or ZrO₂ showed high reactivity with CH₄ at 1223K for the transition phase of Fe₂O₃ to FeO. The solid conversion of 90% can be reached within less than 1min. Mattisson [80] developed 27 oxygen carriers composed of 40–80 wt% Fe₂O₃, together with Al₂O₃, ZrO₂, TiO₂ or MgAl₂O₄ by freeze granulation and sintered at temperatures of 1223–1673K. The study showed that Fe₂O₃ supported with MgAl₂O₄, ZrO₂ or Al₂O₃ sintered at temperatures of 1223K or 1373K exhibited good reactivity with CH₄ at 1223K which meant that less than 150 kg/MWth solid inventories were needed in the fuel reactor. Johansson [81] investigated the reduction reactivity of Fe₂O₃/MgAl₂O₄ to Fe₃O₄ with 50 vol% CH₄ at 1223K. It was shown that 60 wt% Fe₂O₃/MgAl₂O₄ sintered at 1373K was the best oxygen carrier considering both crushing strength and reactivity. The reaction rate and gas yield were strongly dependent on reaction temperature. To get a high gas yield (>80%) and high reactivity (solid inventory<500 kg/MWth), the lowest temperature was 1023K. Zafar [82] studied the reactivity of Fe₂O₃ supported by SiO₂ or MgAl₂O₄ with 10 vol% CH₄

at 1073–1273K. It seemed that $\text{Fe}_2\text{O}_3/\text{SiO}_2$ maybe not be a feasible oxygen carrier due to the formation of silicate at high temperature. The $\text{Fe}_2\text{O}_3/\text{MgAl}_2\text{O}_4$ showed high reactivity (solid inventory < 160 kg/MWth) during the phase of Fe_2O_3 to Fe_3O_4 but very slow for Fe_3O_4 to FeO . Corbella [83] tested the titania supported iron oxide as oxygen carrier in CLC of CH_4 at 1173K. The developed metal oxide showed acceptable reactivity and durability but low oxygen capacity due to the formation of irreversible FeTiO_3 after the first cycle. Ortiz [84] investigated the behaviour of an iron waste from an aluminium manufacturer as an oxygen carrier for combustion of the PSA tail gas from a steam methane reforming plant in a 500Wth CLC prototype. Syngas or methane was used as fuel for comparison. Either the reactivity or fuel gas conversion for methane was lower than for syngas.

In general, most of the work has proven that the suitable binders for Fe-based oxygen carriers are Al_2O_3 , MgAl_2O_4 , ZrO_2 and TiO_2 except SiO_2 . For the combustion of syngas or CH_4 , the phase of Fe_2O_3 to Fe_3O_4 is the best choice due to high reactivity and gas yield. However, in the CLC process for hydrogen production, the conclusion is still not clear enough especially using methane as fuel.

Fe-based Oxygen Carriers for CLHG

Two features are essential for a redox pair of metal oxide in the process of chemical looping hydrogen generation. One is the ability to convert fuel into CO_2 and H_2O with high selectivity during its reduction in the fuel reactor. The more important one is that it is able to produce hydrogen during the oxidation of reduced metal oxide by steam. Based on the thermodynamics analysis by Kang et al., when combining fuel and H_2 selectivity, the redox pairs of $\text{Fe}_2\text{O}_3/\text{FeO}$ and $\text{Fe}_2\text{O}_3/\text{Fe}$ are the most suitable candidates compared with the alternative metal oxide pairs, such as W-, Ce-, Cd-, Cu- and Mn-based metal oxides [85].

The metal oxide of Fe_2O_3 was proposed for use to convert fuels to pure hydrogen through the so-called steam iron principle, which was developed in the early 1900s for commercial hydrogen production and later abandoned due to the deactivation of iron oxides in cycles. Recently, interest in steam iron technology has been revived and integrated with the

concept of chemical looping combustion for hydrogen production with inherent CO₂ capture; i.e. three reactors CLC for cogeneration of hydrogen and electricity. The previous study on steam iron process were mainly concentrated on the application at low temperatures (<1023K) or of adding some metals or metal oxides to improve the durability and kinetics. Yamaguchi [86] added CeO₂ and/or ZrO₂ into Fe₂O₃ to increase the kinetics and stability at temperatures ranging from 873–1023K. Urasaki [87] investigated the effect of small amounts of additives (palladium and/or zirconia) over Fe₃O₄ in the steam iron process for hydrogen production at 723K. Lorente [88] concluded that the additives of Al, Cr, and Ce to the iron oxide increased the stability within cycles while the iron oxides modified with Al or Cr displayed poorer reduction kinetics by hydrogen below 1073K. Takenaka [89] suggested that Ni-Cr/FeO_x, Cu-Cr/FeO_x and Rh-Cr/FeO_x were promising mediators for hydrogen production repeatedly in a synthesis gas fuelled steam iron process. For using methane as fuel, Ni-Cr/FeO_x exhibited better redox ability within cycles. The effect of adding Rh and/or Mo to iron oxides was also studied at a low temperature (<873K) [90]. He stated that the addition of Cu to iron oxides containing Cr cation resulted in the increase in both reduction with methane and oxidation with water steam within redox cycles at temperatures below 1023K [91].

At present the three reactors chemical looping technology for coproduction of hydrogen and power is still in concept design or system analysis as mentioned earlier [59-62, 65, 66]. Only a few experimental works have been carried out with accessible literature. Chen [92] investigated the three reactor iron-based (90% Fe₂O₃/Al₂O₃) chemical looping process for hydrogen production using CO as fuel in a batch fluidised bed regarding the effect of reduction time (20~40min), operation temperature (1073–1223K), particle size and CO₂ partial pressure in the reducing gas (10 vol%, 40 vol%). As a result, long reducing time, high operation temperature, small particle size, and low CO₂ partial pressure favoured the hydrogen production. Considering the fuel conversion rate, it decreased with long reduction times to some extent due to the reduction of Fe₂O₃ to Fe_{0.947}O or to Fe. The iron oxide (Fe₂O₃) supported by Al₂O₃ or TiO₂ were prepared by a mechanical mixing method and their behaviour were presented in the reduction atmosphere of CO during the multi-cycle chemical looping hydrogen generation process [93]. According to TGA experiments, 60 wt%

$\text{Fe}_2\text{O}_3/\text{Al}_2\text{O}_3$ had a better reactivity than 90 wt% $\text{Fe}_2\text{O}_3/\text{Al}_2\text{O}_3$ or 60 wt% $\text{Fe}_2\text{O}_3/\text{TiO}_2$ at 1173K. The results were also verified by the experiments in a batch fluidised bed. It uncovered that 60 wt% $\text{Fe}_2\text{O}_3/\text{Al}_2\text{O}_3$ delivered a higher hydrogen yield because more metallic iron was generated in the reducing period, especially at a higher reduction temperature (1173K). A less hydrogen yield for 60 wt% $\text{Fe}_2\text{O}_3/\text{TiO}_2$ was due to the formation of FeTiO_3 and no metallic iron presented. The higher reduction temperature was also beneficial to obtain higher purity hydrogen in the steam reactor because of the mitigation of carbon deposition. The authors finally proposed a compact fluidised bed as fuel reactor to improve the fuel conversion considering the reversible transition of Fe_3O_4 to FeO or Fe with CO . Gupta [94] proposed a syngas redox (SGR) process to produce hydrogen from coal derived gas based on iron-based in three reactors chemical looping system where the fuel reactor and steam reactor were counter-current moving bed reactor. In this process, the oxygen transfer capacity of Fe_2O_3 could be maximised with 100% fuel conversion and no carbon formation. It is also demonstrated that sol-gel derived Fe_2O_3 is stable in 10 consecutive cycles. Bohn [95] suggested the process of reduction of Fe_3O_4 to $\text{Fe}_{0.947}\text{O}$ rather than Fe with syngas in a chemical looping system for hydrogen production because the reduction to metallic iron decreased the oxygen carriers' reactivity, hydrogen yield with repeated cycles and enhanced the carbon deposition dramatically thus decreasing the hydrogen purity. Muller [96] demonstrated the three-step chemical looping process for hydrogen production by coal gasification derived gas in a packed bed at 1073K. As a result, high purity hydrogen ($\text{CO} < 50\text{ppm}$) could be produced repeatedly within cycles but the fuel conversion was restricted at a low level during the transition phase of $\text{Fe}_3\text{O}_4\text{-Fe}_{0.947}\text{O-Fe}$. Kierzkowska [97] developed composite particles of Fe_2O_3 and Al_2O_3 using sol-gel technology and examined their redox performance for hydrogen production with CO in a packed bed at 1123K. It was stated that the durability was highly dependent on the final phase of FeO or Fe . The 60 wt% $\text{Fe}_2\text{O}_3/\text{Al}_2\text{O}_3$, oxygen carrier produced using sol-gel gave conversions competitive with those in other studies within 40 cycles. Hacker [98] explored the operation conditions of the steam iron process using alkaline or acidic iron oxides with methane or syngas at 773–1273K. The modification had a small influence on the reduction but the oxidation of alkaline iron oxide by steam was 2 times faster than the acidic one. The reduction rate with methane was acceptable above 1073K but the problem of carbon

formation was aggravated with an increase in temperature. When using syngas as fuel, the carbon deposition could be mitigated through adding CO₂ or increasing temperature.

Reduction Kinetics of Iron Oxides

Kinetics parameters are of significance in the reactor design and predicting the gas product and energy consumption. Unfortunately, very few studies are found in the literature that deals with the reduction kinetics of iron oxides and no universal kinetics model has been established in the literature for these oxides. However, such reaction kinetics for iron oxides are paramount in this study given that the three chemical looping processes described here are all iron oxide base processes.

Essentially, within a certain range of reaction conditions, a set of independent equations can be secured and used to interpret the reduction process. Generally speaking, the consecutive reduction of iron oxides by means of gaseous agents is an example of a complex heterogeneous gas–solid reaction whose rate is significantly affected by both chemical reaction kinetics on one hand and by mass transfer resistance on the other. Although a general agreement was reached on the rate-controlling mechanism for the reduction reactions, there has been considerable disagreement and diversity in the reaction rate constant and activation energy values that were reported in the literature. The activation energy for the complex reduction process is in the range of 9.54–271 kJ/mol depending on the temperature ranges, gas compositions, nature of raw materials and reduction step [99, 100]. Monazam [101] studied the reduction of hematite to wustite with different concentrations of methane (15%, 20% and 35%) at temperatures ranging from 973 to 1098K. He suggested a kinetic model based on two parallel reactions to describe the reduction data. Abad [73] tried using the shrinking core model (SCM) to predict the reduction of Fe₂O₃/Al₂O₃ with syngas. Go [102] indicated the reduction of iron oxide with CH₄ is in diffusion control for the temperature range between 1073K and 1173K. Piotrowski [103, 104] concluded that the activation energy values for the reduction of hematite to wustite are located in the order of 25–125 kJ/mol and the reaction mechanism could be interpreted by the two dimensional nucleation growth and first order models. Pineau [99] examined the reduction of Fe₂O₃ by H₂ in the temperature range of 493–1003K.

He confirmed that the reduction of Fe_2O_3 to Fe_3O_4 is featured with an apparent activation energy of 76 kJ/mol while 39 kJ/mol in the case of Fe_3O_4 to Fe at temperatures higher than 693K. He also claimed that the reaction rate for higher temperatures is controlled by phase boundary reaction.

Chapter 3: METHODS AND TECHNIQUES

This chapter introduces the methods and techniques that were used to study theoretically and experimentally chemical looping process. The theoretical calculation was conducted to evaluate the thermodynamics feasibility and performance of the processes for VAM treatment while the experimental work was conducted to determine the kinetics feasibility and performance.

3.1 Theoretical

Thermodynamics analysis is carried out using the commercially available process simulation software: ASPEN PLUS. Before the calculations started the appropriate reactors and property methods have to be selected which will determine the accuracy of the results.

3.1.1 Selection of Reactors

The theoretical calculations for the involved reactions are conducted in RGIBBS reactor, in which both the phase equilibrium and chemical equilibrium are considered. One of the key calculations performed in process simulations is phase equilibrium calculations. Phase equilibrium is regarded to be achieved when the fugacity of the component is equal in all phases.

Several alternatives can be found to numerically cope with chemical equilibrium problems. In general, the method to solve chemical equilibrium problems is to minimise the Gibbs free enthalpy of the system. In these methods, under the rule of element conservation, the species mole numbers n_i are adjusted to minimise the Gibbs function. However, it is difficult to ensure that the predicted mole fractions of very minor species are indeed non-negative.

In Gibbs function minimisation methods, the method of Lagrangian multipliers is generally used to enforce the satisfaction of the constraint of element conservation. A particular variant

of such methods is the element-potential method made popular by Reynolds [105]. Gibbs function is expressed as:

$$G = \sum_{i=1}^I n_i \left[g_i^{\circ}(T) + \bar{R}T \ln X_i + \bar{R}T \ln \left(\frac{P}{P^0} \right) \right] \quad (3.1)$$

The constraint of element conservation can be expressed as:

$$\sum_{i=1}^I a_{ji} n_i = n_j \quad (j = 1, \dots, J) \quad (3.2)$$

here J denotes the total number of elements present in the system, n_j is the elemental mole number of element j in the system, and a_{ji} is the number of atoms of element j in species i .

To minimise G for given T and p , equation 3.1 is differentiated after manipulations,

$$d \left(\frac{G}{\bar{R}T} \right) = \sum_{i=1}^I \left[\frac{g_i^{\circ}(T)}{\bar{R}T} + \ln X_i + \ln \left(\frac{P}{P^0} \right) \right] dn_i \quad (3.3)$$

Subtracting for each j a yet unknown multiple λ_j from (3.3) results in:

$$d \left(\frac{G}{\bar{R}T} \right) = \sum_{i=1}^I \left[\frac{g_i^{\circ}(T)}{\bar{R}T} + \ln X_i + \ln \left(\frac{P}{P^0} \right) - \sum_{j=1}^J \lambda_j a_{ji} \right] dn_i \quad (3.4)$$

The λ_j are the so-called Lagrangian multipliers. Their numerical values need to be determined. To attain a minimum Gibbs function, standard differential calculus requires the coefficients of the remaining $I-J$ dn_i in (3.4) to vanish, i.e.:

$$\sum_{j=1}^J \lambda_j a_{ji} = \frac{g_i^{\circ}(T)}{\bar{R}T} + \ln X_i + \ln \left(\frac{P}{P^0} \right) \quad i = 1, \dots, I \quad (3.5)$$

3.1.2 Selection of Property Method

When building a new simulation session, it is important to ensure the properties of pure components and mixtures being estimated appropriately. In fact, the simulation result will be influenced if the property method is not selected carefully. Therefore, it is important to consider carefully our choice of methods to estimate the different properties.

In ASPEN PLUS, a “property method” section is stored in for different properties. A property method is a collection of estimation methods to calculate thermodynamic (fugacity, enthalpy, entropy, Gibbs free energy, and volume) and transport (viscosity, thermal conductivity, diffusion coefficient, and surface tension). In addition, to estimate mixtures properties, a large database of interaction parameters are used with mixing rules.

When selecting a property method, a number of estimation equations are determined for the different properties. For example, when the Peng-Robinson equation is selected, it can be seen that the equation of state (EOS) selection is set to ESPR (equation of state Peng-Robinson) which is given by:

$$P = \frac{RT}{c + V_m - b} - \frac{a}{(V_m + c)(V_m + c + b) + b(V_m + c - b)} \quad (3.6)$$

Where a, b, and c are component specific parameters. The values of these parameters are stored in an ASPEN PLUS database for pure components or calculated using mixing rules for mixtures.

3.2 Experimental

3.2.1 Thermogravimetric Analysis

The reduction reactivity was examined in a thermogravimetric analyser (TA Q50, refer to Figure 3.1) under isothermal conditions. The samples (10–15mg) were placed in a platinum crucible (100 μ L) and heated in a furnace from the ambient temperature to the desired

reaction temperatures (873–1073K) at a constant heating rate of 20K min^{-1} under the inert gas flow of N_2 . During the reduction reaction, the reducing gas (i.e. CH_4 balanced by N_2) was introduced into the furnace and passed over the sample after the desired temperature was reached. Typically, each test consisted of five redox (reduction/oxidation) cycles to stabilise the reduction. The data set corresponding to the fifth redox cycle was then used for determination of reaction data since the redox properties reached a repeatable level at or on about the fifth cycle. The experimental procedure involved the following steps:

- (1) a sample of metal oxide (10–15mg) was loaded into the sample crucible which, in turn, was inserted into the TGA reactor;
- (2) the sample was reduced with the reducing gas in 10 min;
- (3) a purge gas flow of N_2 was introduced for about 5 min between the reducing gas and oxidising gas environment;
- (4) a diluted stream of air by N_2 was then introduced to start the oxidation step;
- (5) a stream of purge gas was introduced again for 5 min after the 5 min regeneration period; and
- (6) steps 1 to 5 were repeated at least four times, and the weight loss recorded by the computer were saved for future use.

All experiments were conducted under the following conditions: (1) gas flow rate of 200 mL min^{-1} ; (2) sample weight of around 10–15mg; and (3) sample particle size of 75–150 μm . Based upon the set conditions the external and/or internal diffusion effects were minimised and hence the reactions were promoted by chemical control kinetics.

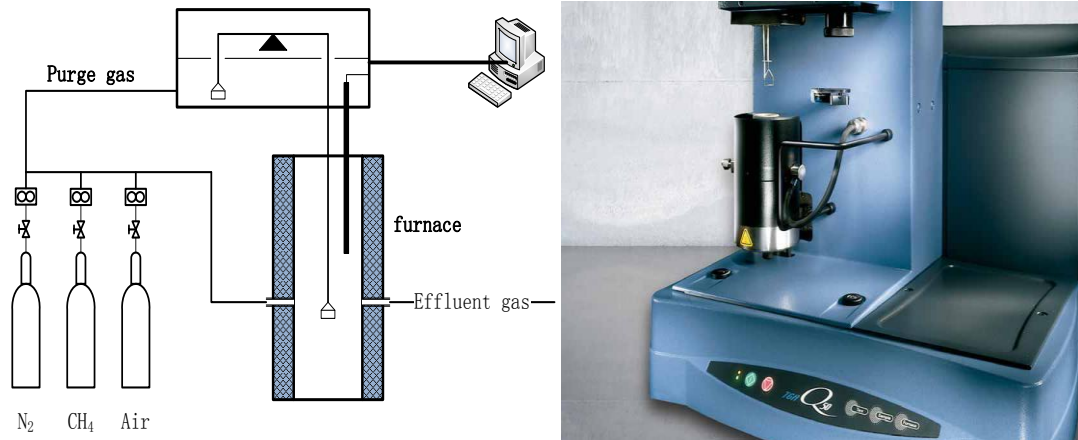


Figure 3.1: Scheme of TGA experiments.

The reduction and oxidation reactivity was evaluated using the TGA data and represented by the fractional conversion of oxygen carriers, X_{red} and X_{od} . The fractional conversion was defined as:

$$X_{red} = \frac{M_{ox} - M}{M_{ox} - M_{red}} \quad (3.7)$$

$$X_{od} = 1 - \frac{M_{ox} - M}{M_{ox} - M_{red}} \quad (3.8)$$

where M_{ox} is the weight of metal oxide in its oxidation state; M_{red} the sample weight in reduction state and M the instantaneous weight of the sample. The fractional conversion data as a function of time was fitted to obtain the polynomial regression equation. The reaction rates (dX/dt) at different fractional conversions (X) were calculated by differentiating a fifth-order polynomial equation.

3.2.2 Fixed Bed Reactor Rig

The CLC process was simulated in a fixed bed reactor rig (as shown in Figure 3.2). It comprises a gas control unit, reactor and furnace, condenser, and gas analyser. The reactor is a cylindrical fused-silica tube with the length of 800mm and diameter of 7mm. The oxygen carrier (i.e. $\text{Fe}_2\text{O}_3/\text{Al}_2\text{O}_3$) was placed in the middle area (400mm length) while both

sides were loaded with quartz wool to reduce the residence time of gases in the reactor as well as to prevent the solid materials from moving in the reactor. The reaction temperature was controlled and stabilised by the furnace and measured using an enclosed Pt/Rh thermocouple. The high purity reactant gases, CH₄, air and N₂, were led from the gas cylinder through mass flow controllers to two four-way valves, which was able to direct a stream of gas to the reactor while the others to the atmosphere. In this way, it was possible to control the amount of time exposed to reducing, inert and oxidising agent. The metal oxides were initially exposed to air until the desired reaction temperature was reached. After then it was exposed to the reducing and oxidising environment alternatively, between them the inert gas N₂ was introduced to avoid the mixture of these two gases. After the steam content was condensed in the condenser and desiccators the gas product was led to a gas analyser (i.e. Angilent Micro-GC 4900) where the concentrations of CH₄, CO₂, CO, H₂ and O₂ were measured in real time. The exhaust was eventually ventilated to the atmosphere. Every set of experiments were repeated in five cycles to guarantee the data was reproducible and the data for the fifth cycle was analysed for determining the results.

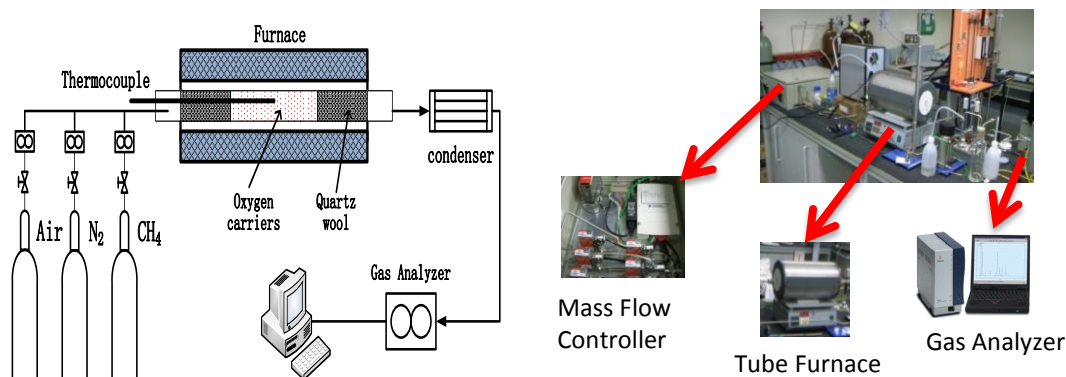


Figure 3.2: Schematic of the fixed bed reactor rig.

Gas Feeding Unit

The gas is led into the reactor tube through the gas feeding unit consisting of gas cylinders, regulators, mass flow controllers (MFCs), four-way valves and connection lines. The gas flow rate is controlled by MFCs that are calibrated before the test starts. The calibration is carried out with a standard bubbler flow meter. Given a signal the actual flow rate value can be obtained. To calibrate with a high accuracy it is repeated five times for every test

signal. The calibration results are illustrated in Figure 3.3–Figure 3.6. As can be seen, the fitting curves are linear with the values of R^2 being unity.

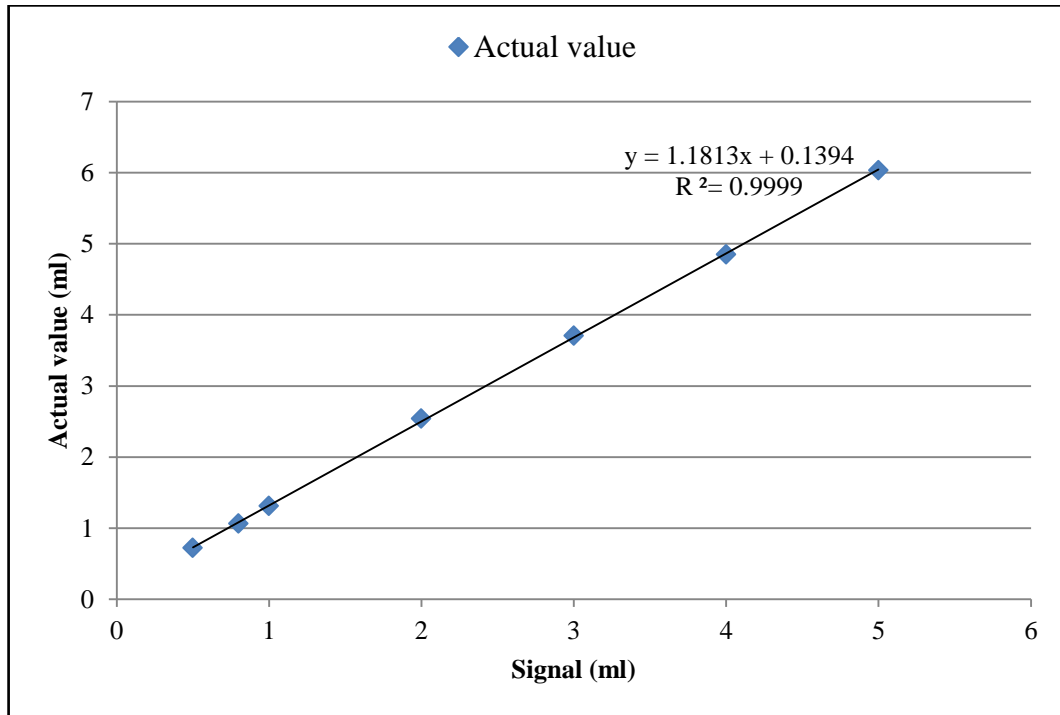


Figure 3.3: Calibration of MFC-CO₂-5 using CH₄.

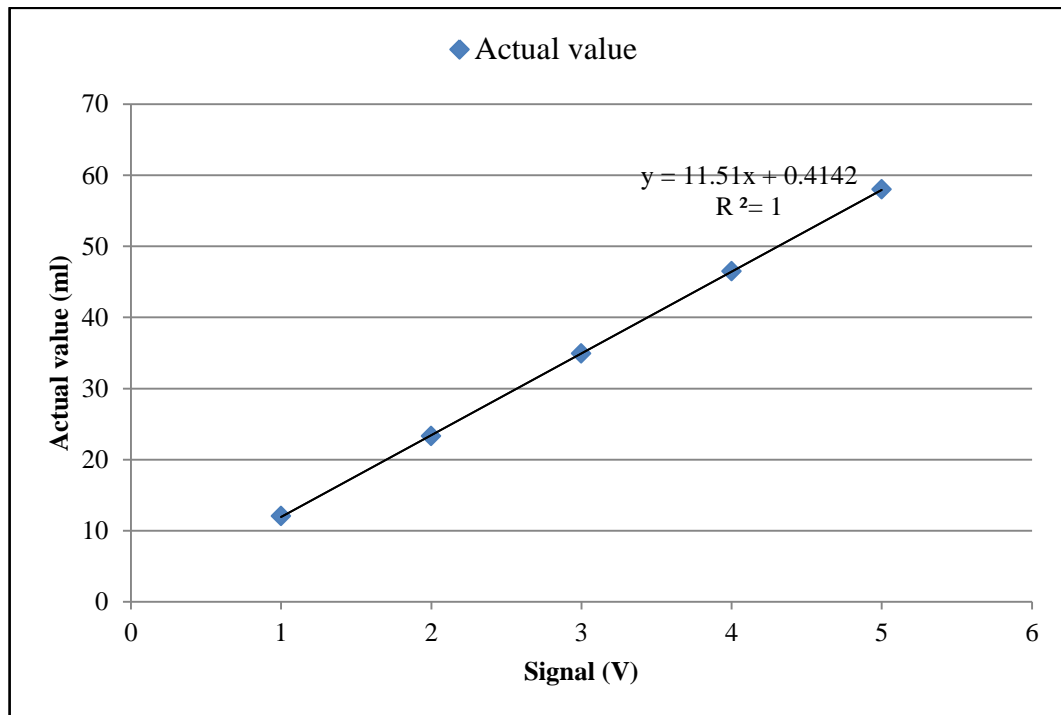


Figure 3.4: Calibration of MFC-CO-50 using instrument air.

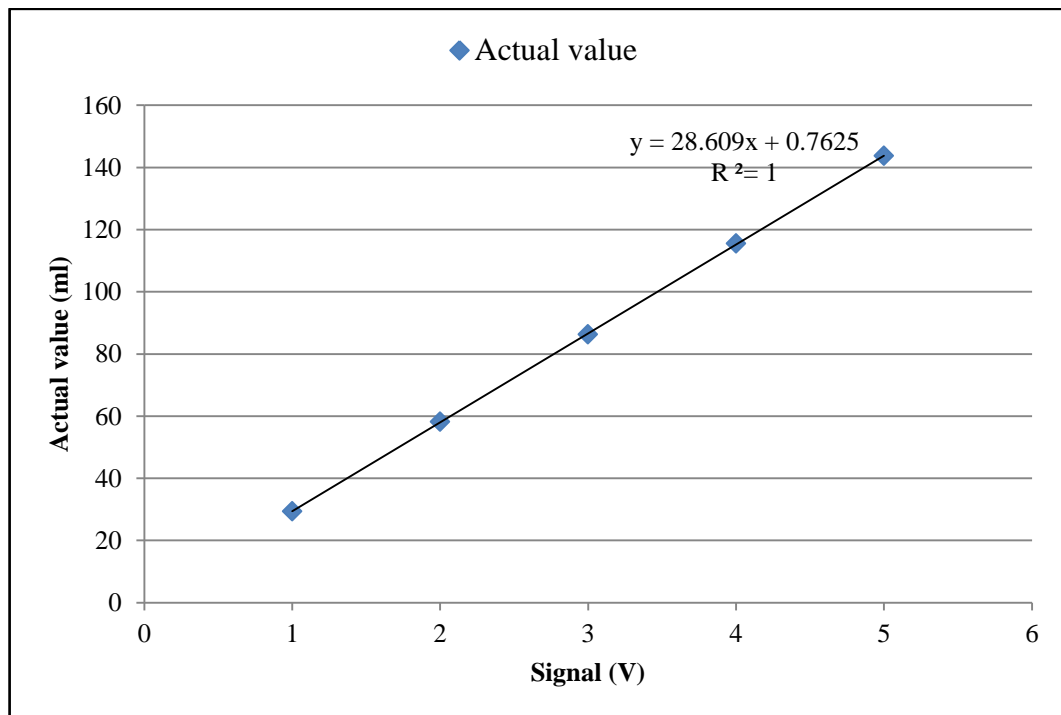


Figure 3.5: Calibration of MFC-CH₄-100 using N₂.

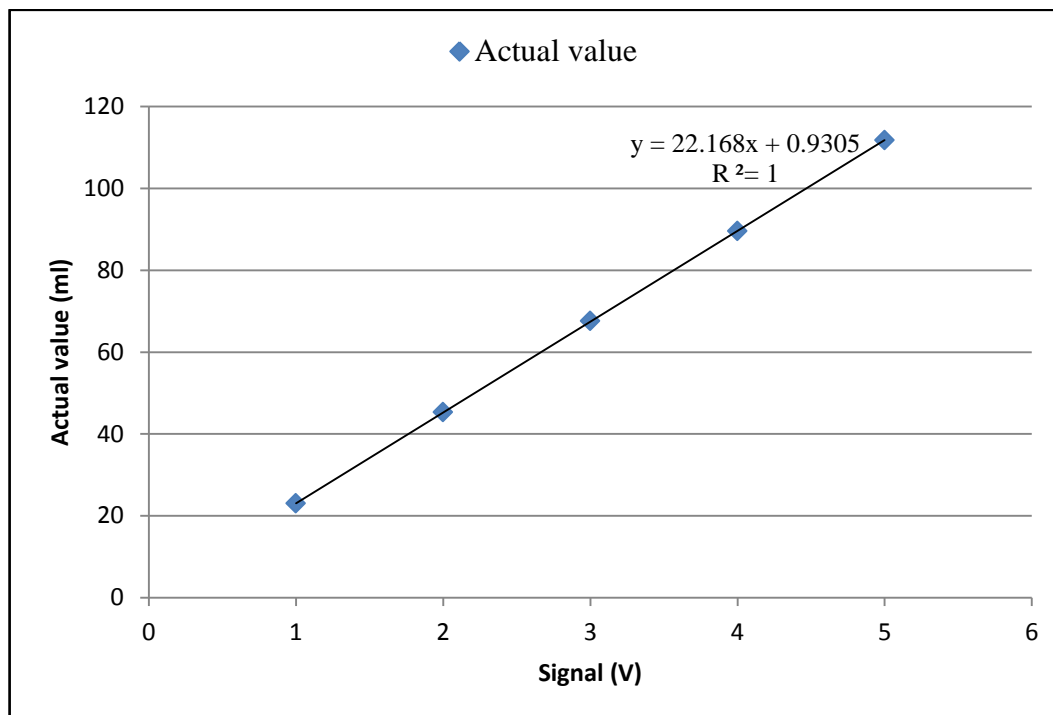


Figure 3.6: Calibration of MFC-N₂-100 using N₂.

Furnace and Temperature Control Unit

The reaction temperatures are programmed by the temperature control unit embedded into the furnace. The temperature is ramped up with a fixed heating rate of 30K/s until the desired temperature is reached. An enclosed Pt/Rh thermocouple is used to measure the actual temperature. The temperature calibration results are shown in Figure 3.7–Figure 3.9. As can be seen the difference between the setting temperature value and the actual one is almost invisible for temperatures lower than 1073K, especially for the temperature in the middle zone (100mm–300mm). The results suggested that the reaction must be taken place in this temperature stabilization area in order to run the test at desired conditions.

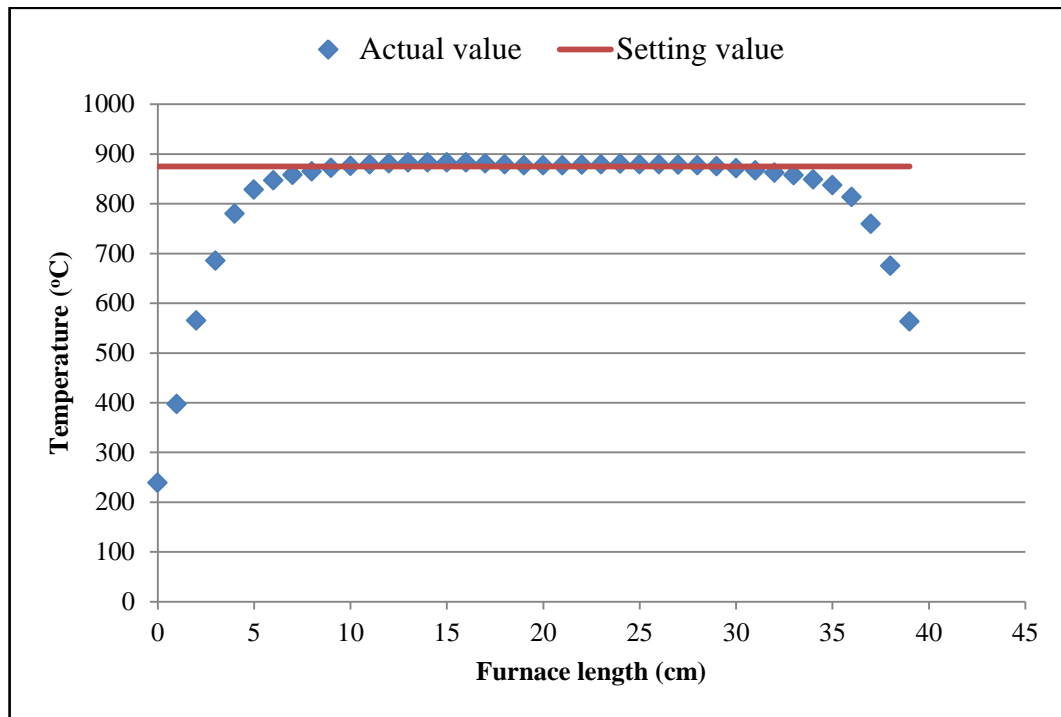


Figure 3.7: Calibration for temperature at 875°C.

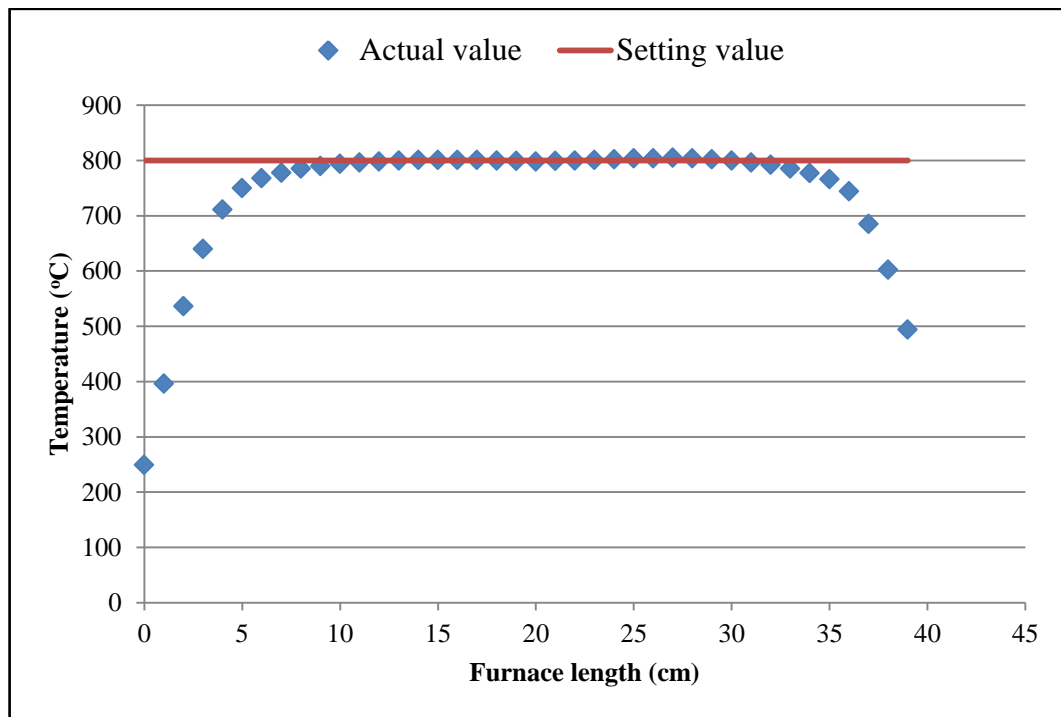


Figure 3.8: Calibration for temperature at 800°C.

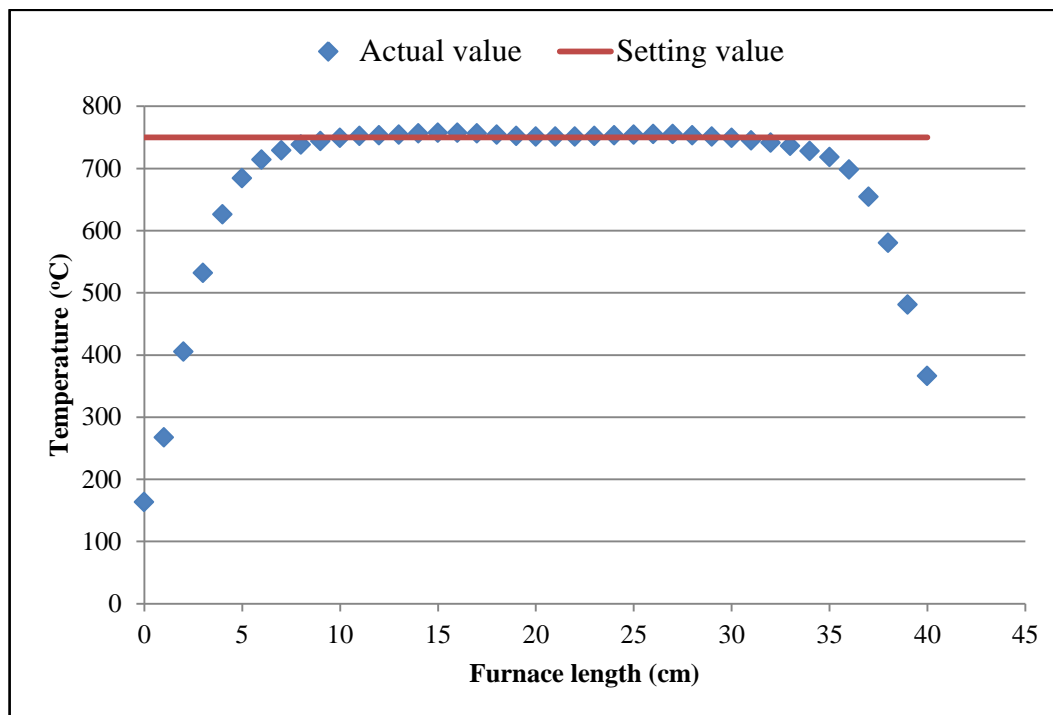


Figure 3.9: Calibration for temperature at 750°C.

Gas Analysis Unit

The gas analysis for the product gas is carried out in a Micro-GC apparatus, in which the Molsieve 5Å column is used to separate: hydrogen, carbon monoxide, methane, nitrogen, oxygen, and some noble gases while the PPQ column is used to separate carbon dioxide, air, and methane. Before experiments start, both columns are calibrated using GRAVE multi-component gas mixtures that have the determined gas concentration. Each gas content involved, including H₂, CO, CH₄, and CO₂, is calibrated using four different gas concentrations as shown in Figure 3.10–Figure 3.13. As can be seen, the fitting curves are linear with the values of R² being unity. The gas concentration can then be determined quantitatively by the peak area provided by the Micro-GC.

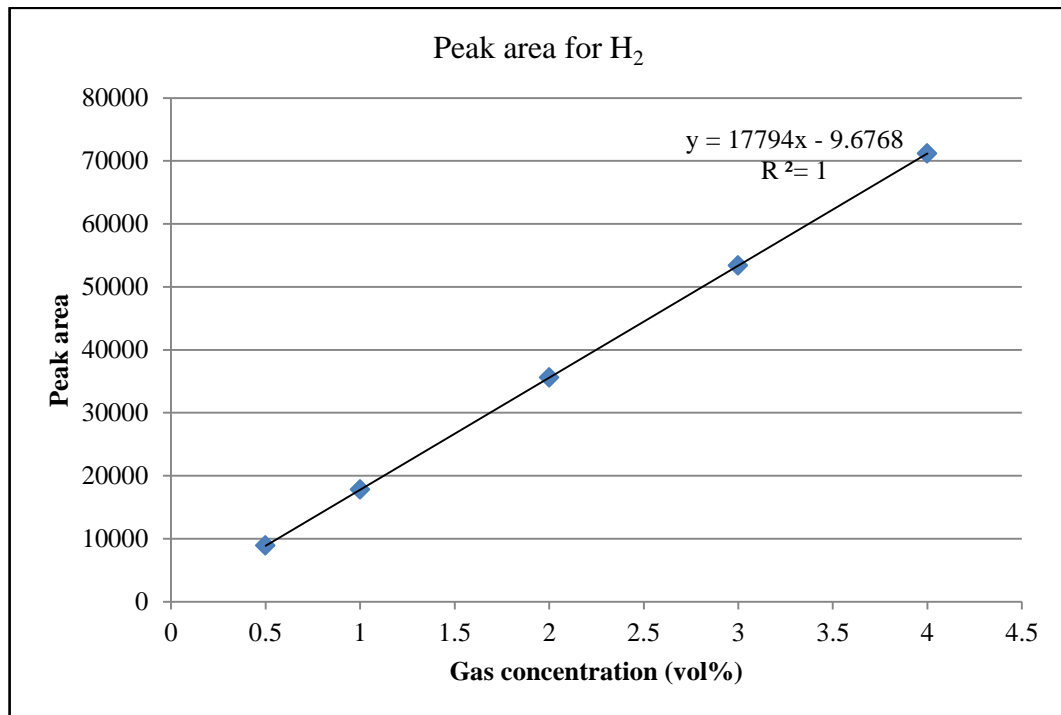


Figure 3.10: Plots of peak area vs. H₂ concentration.

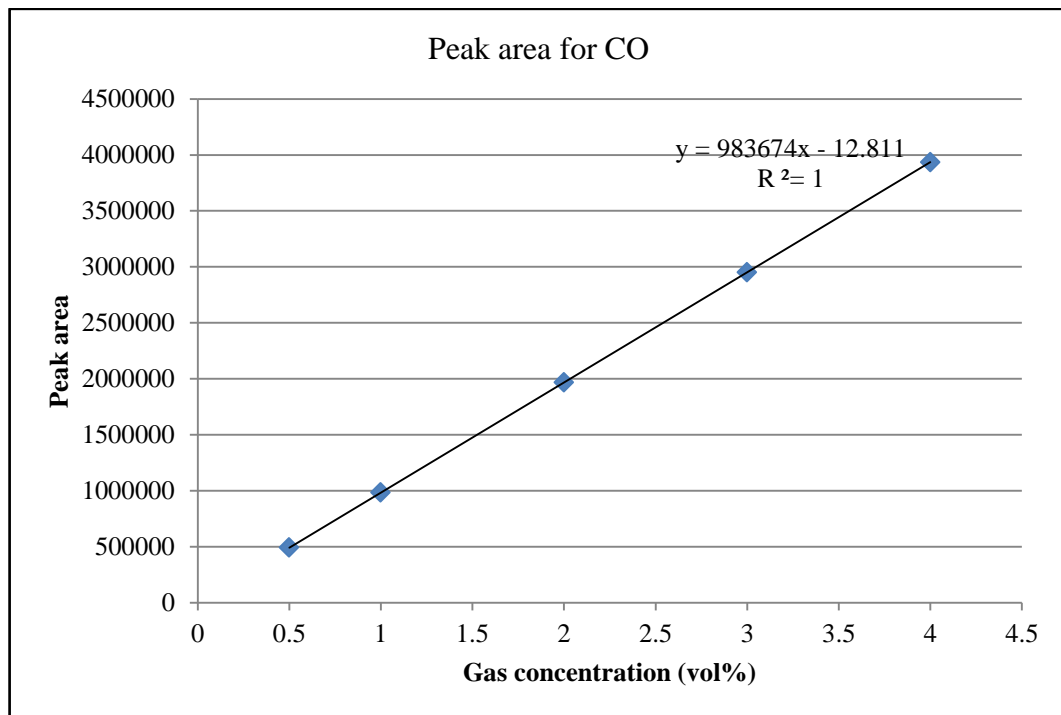


Figure 3.11: Plots of peak area vs. CO concentration.

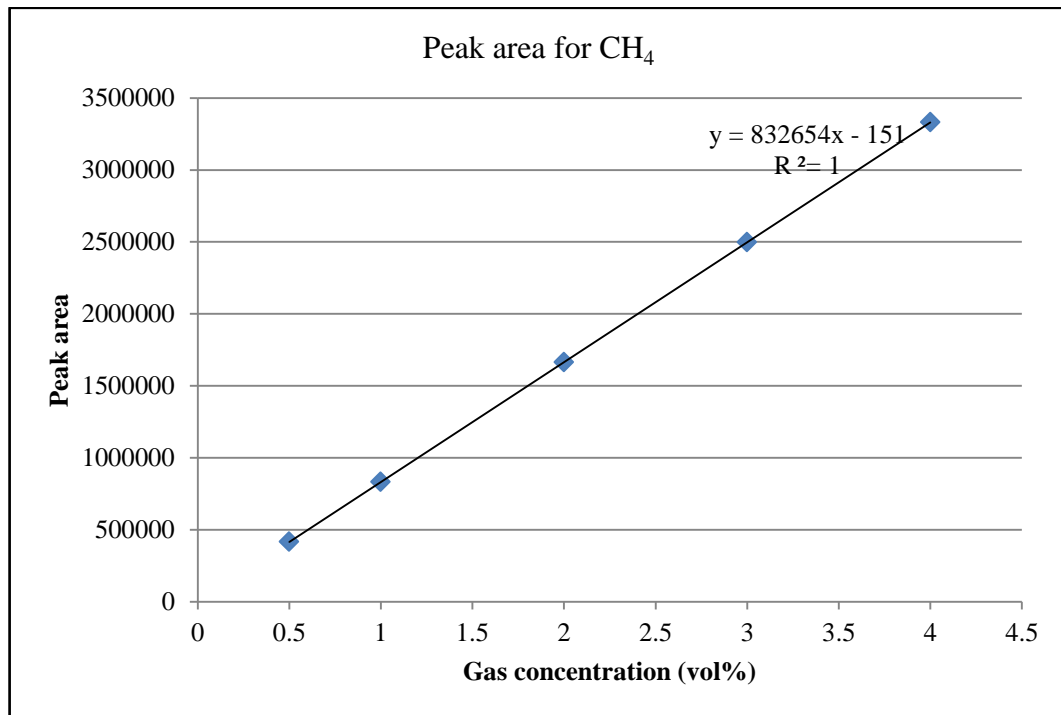


Figure 3.12: Plots of peak area vs. CH₄ concentration.

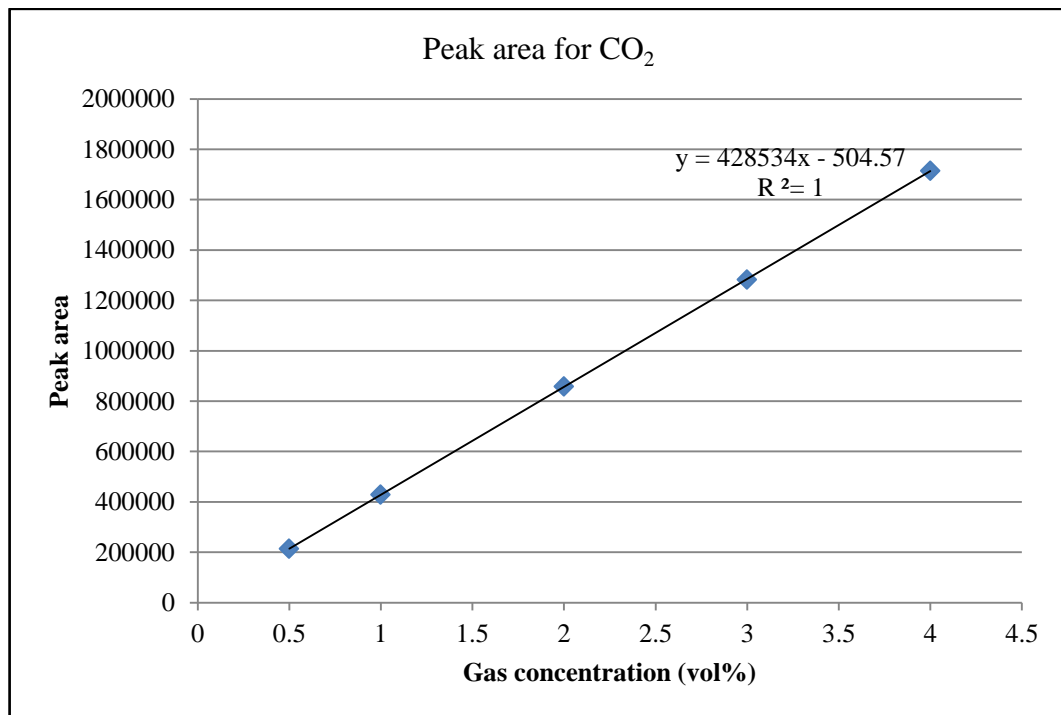


Figure 3.13: Plots of peak area vs. CO₂ concentration.

3.2.3 Samples Preparation

The pure iron oxide sample was produced by the direct thermal decomposition of the ferric nitrate, which was first heated at 873K for 3h and further heated at 1073K for 6h. The particle samples, $\text{Fe}_2\text{O}_3/\text{Al}_2\text{O}_3$, were prepared using dry impregnation method details of which can be found elsewhere [106]. The metal oxide samples were prepared by addition of a volume of iron ($\text{Fe}(\text{NO}_3)_3 \cdot 9\text{H}_2\text{O}$) nitrate solution corresponding to the total pore volume of the support particles. The aqueous solution was slowly added to the alumina particles, with thorough stirring at room temperature. No filtration or drying steps were required with this method. Metal oxides with three different $\text{Fe}_2\text{O}_3/\text{Al}_2\text{O}_3$ weight ratios (10/90, 25/75, and 45/55) were prepared by two or three successive impregnations, respectively. The samples were calcined in air atmosphere for 3h at 600 °C in a muffle oven to decompose the impregnated iron into insoluble iron oxide. Finally, the oxygen carriers were calcined in air atmosphere for 6 h at the desired temperature of 850 °C). The calcined samples were sieved to a particle size range of 75–150 μm (mesh 170 < particle size < mesh 140 (ASTM-E11 standard)).

3.2.4 Scanning Electron Microscope (SEM)

Morphology and microstructure inside the fresh and reacted oxygen carrier particle were determined by means of a Philips XL30 scanning electron microscope.

Chapter 4: REDUCTION OF Fe₂O₃ BY ULTRA-LOW CH₄

4.1 Introduction

The reduction of Fe₂O₃ to FeO with ultra-low CH₄ is studied here as it constitutes a key step in producing pure hydrogen through the three reactors chemical looping process to be discussed in Chapter 6. The aim is to investigate the reduction reactivity of Fe₂O₃/Al₂O₃ with ultra-low concentration CH₄ over a range of temperatures between 873K and 1073K. Furthermore, to identify the most suitable alumina-supported iron-based oxygen carrier for chemical looping hydrogen production by ultra-low concentration methane, a range of Fe₂O₃ loading content (10–45 wt%) is applied and their reactivity and cyclic stability are compared in a thermogravimetric analyser. The further investigation on the gas conversion is carried out in a fixed bed rig. Moreover, the effect of operation parameters—i.e. reaction temperatures (873K–1073K), methane concentrations (0.1–1.5 vol%), CO₂ compositions (10–50 vol%)—on the reactivity of Fe₂O₃ with CH₄ is discussed.

4.2 Experimental Studies

The experimental studies were carried out in a TGA setup and a fixed bed setup as shown in Chapter 3, in which the experimental procedure was described in detail. The specific experiments matrix is shown in Tables 4.1-4.2.

Table 4.1: Fixed bed reactor experiments matrix.

	873 K	923 K	973 K	1023 K	1073 K
Pure Fe ₂ O ₃					
Fe10Al				※	
Fe25Al				※	
Fe45Al	※	※	※	※	※

Table 4.2: TGA experiments matrix.

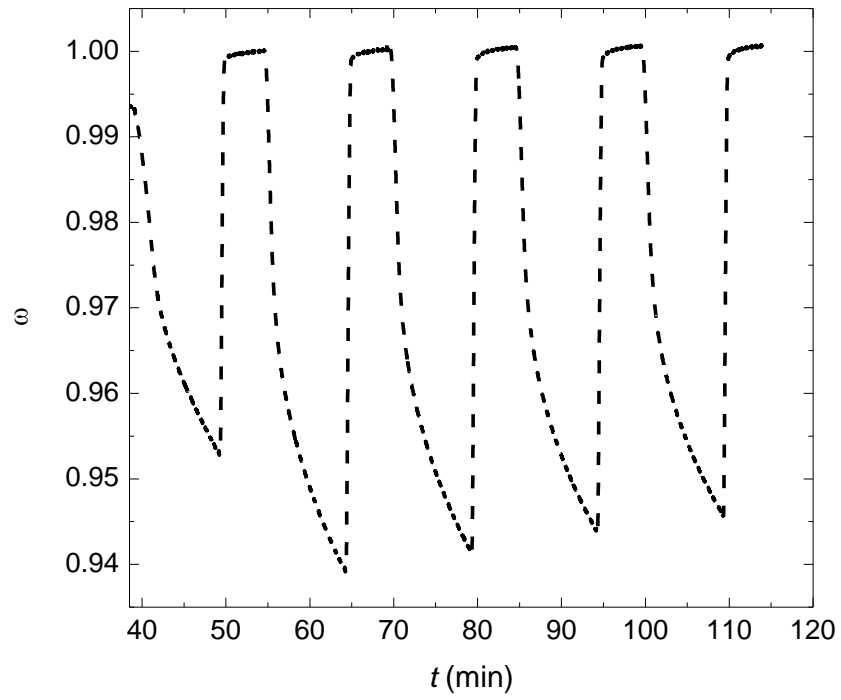
	873 K	923 K	973 K	1023 K	1073 K
Pure Fe ₂ O ₃			※	※	※
Fe10Al				※	
Fe25Al				※	
Fe45Al	※	※	※	※, 0.1-1.5 vol% CH ₄ , 0-50% CO ₂	※

4.3 Results and Discussions

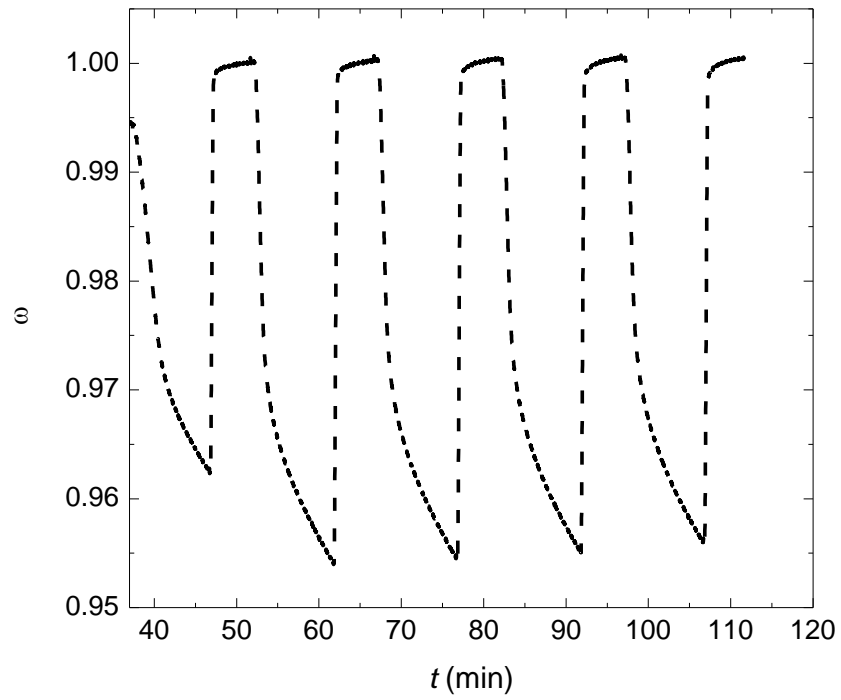
4.3.1 Reduction of Pure Fe₂O₃ with CH₄

Pure metal oxides have been proved to be incompetent as oxygen carriers due to instable redox reactivity by a large number of researches. The purpose for the test conducted in this section is to show a baseline result, in comparison with the results demonstrated in the next section. Five-cycle test for pure Fe₂O₃ was conducted in TGA at different reaction temperatures (isothermal at 973, 1023 and 1073 K) and each cycle was in a 10 min time scale as shown in Figure 4.1 (note that the inert time is not shown). As can be seen, the reactivity of pure Fe₂O₃ is extremely unstable even at a low temperature of 973 K, which

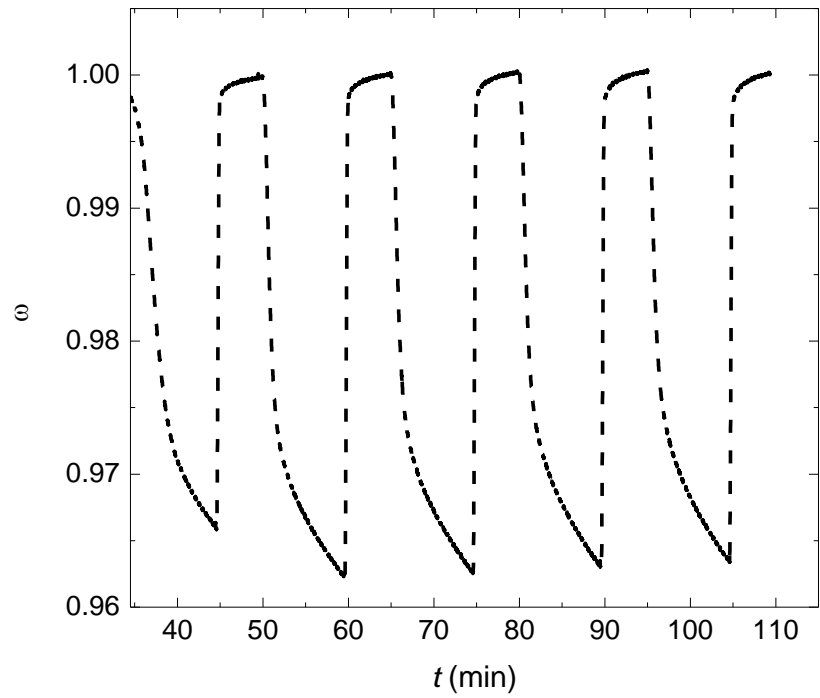
decreases gradually except for the first two cycles. It is also observed that an increase in temperature leads to a higher reaction rate but also a worse reactivity stability. To obtain an in-depth vision a 30-cycles test is further carried out at 1023 K. Not surprisingly, the reactivity is decreased with cycles except the first two cycles. To analyse the reason for the decline of reactivity with cycles at different temperatures, SEM images of the regenerated samples after cyclic test at these temperatures are shown in Figure 4.2. From comparison of Figure 4.2(a) to 4.2(c) it can be deduced that the size of agglomerates is increasing with the increase in reduction temperatures (range of 973–1073 K). Besides, the bigger agglomerates can be found for the sample at thirtieth cycle (Figure 4.2(d)) compared with that at fifth cycle (Figure 4.2(b)). The surface morphology results are in agreement with the above-mentioned reactivity results, which in turn can be explained by the fact that, with the agglomeration of the particles, the pore size on the surface is decreased gradually and as such, the mass transfer resistance increases.



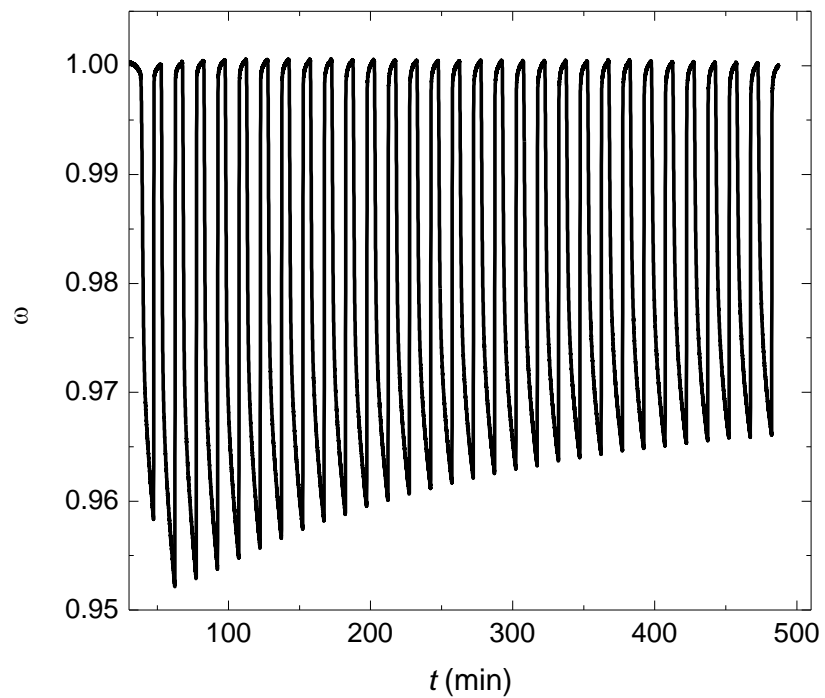
(a)



(b)



(c)



(d)

Figure 4.1: Reduction of pure Fe_2O_3 with 1 vol% CH_4 at: (a) 1073 K, (b) 1023 K, and (c) 973 K in 5 cycles and (d) 1023 K in 30 cycles.

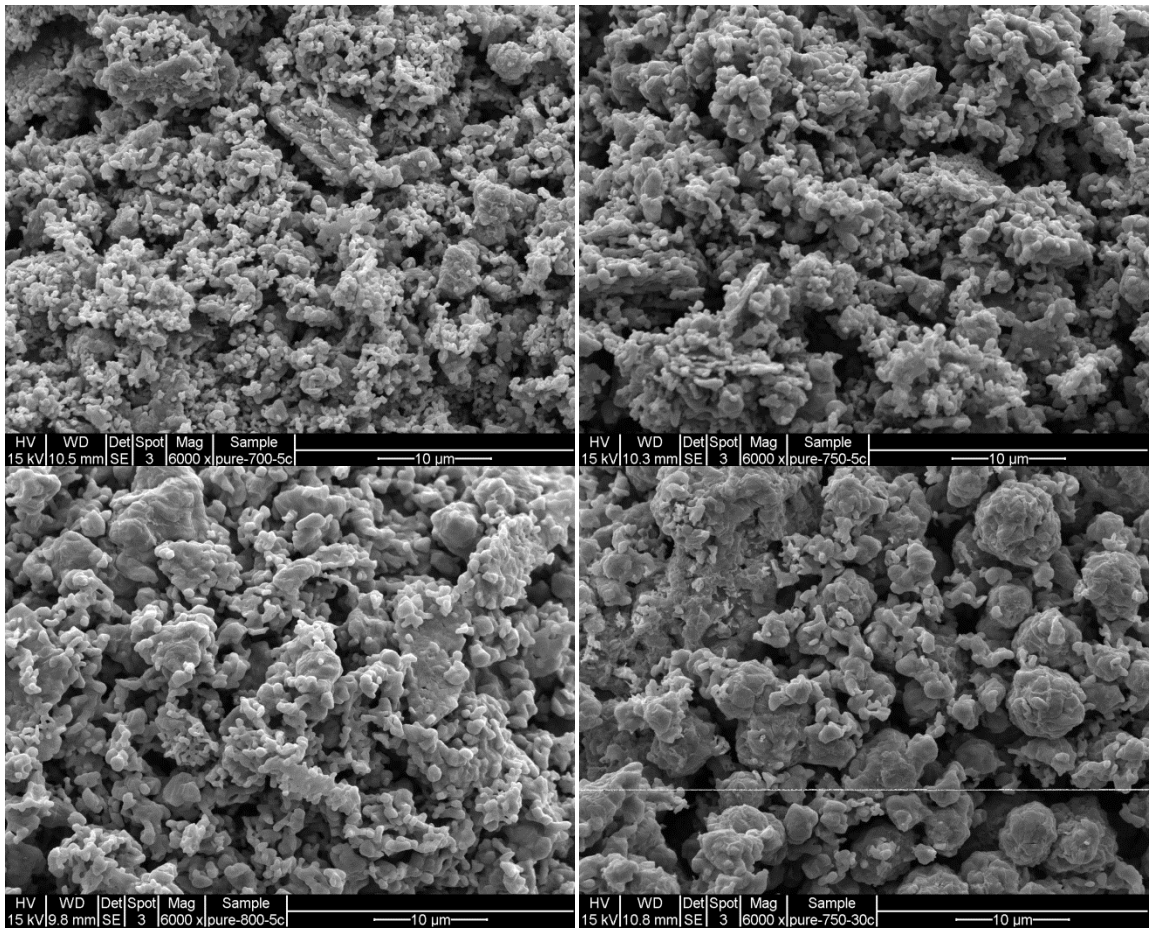


Figure 4.2: SEM images at 6000 \times magnification for unsupported iron oxide, after 5 cycles at: (a) 973 K, (b) 1023 K, and (c) 1073 K; (d) after 30 cycles at 1023 K.

4.3.2 Reduction of Alumina-supported Fe_2O_3 with CH_4

Three alumina-supported iron-based oxygen carriers were prepared and used to achieve a higher reactivity and better stability. Based on the knowledge, the optimum metal oxide content for chemical looping combustion using iron-oxide oxygen carriers should be between 40-60 wt%. In the case of the chemical looping combustion of ultra-low concentration methane, however, a suitable oxygen carrier should be selected more carefully. Normally speaking, in a chemical looping combustion process, the reactions in the air reactor are exothermic while the reactions in the fuel reactor are endothermic. As a result, the temperature gap between the air reactor and fuel reactor becomes larger and larger and the temperature in the fuel reactor decreases gradually. It brings a difficult to run the system steadily over a number of cycles. This problem can be solved if the fuel reactor

is able to utilize the released heat from the air reactor. Under such circumstances, it requires an intermediate, i.e. oxygen carrier, which plays the role of transferring the heat energy from the air reactor to fuel reactor. To maintain the temperature in fuel reactor at a higher level, more energy is needed to be transferred. This can be partially solved by adjusting the weight content of the support material. It is confirmed by the thermodynamics calculation in ASPEN PLUS software. The used oxygen carrier couple is $\text{Fe}_2\text{O}_3/\text{Fe}_3\text{O}_4$ and the methane concentration is set to be 1 vol%. The temperature in the air reactor is set to be the typical values, i.e. 1173 K and 1273 K and the fuel reactor is in auto-thermal condition. The variations of fuel reactor temperature with the content of alumina are plotted in Figure 4.3. As shown by the curve the temperature increases with the decrease in the content of Fe_2O_3 (5–100 wt%). It is also found that the curve is steeper at the higher Al_2O_3 content. In reality, the temperature increases by 230 K and 270 K when the Al_2O_3 loading varies from 50 wt% to 90 wt%. This is almost twice as that observed when alumina loading varies from 0 to 50 wt%. The results indicate that the oxygen carriers with Fe_2O_3 content lower than 50% are more suitable for chemical looping combustion of ultra-low concentration methane. Similar results are also reported for the reduction of Fe_2O_3 to FeO by ultra-low concentration methane in Section 6.5.2.

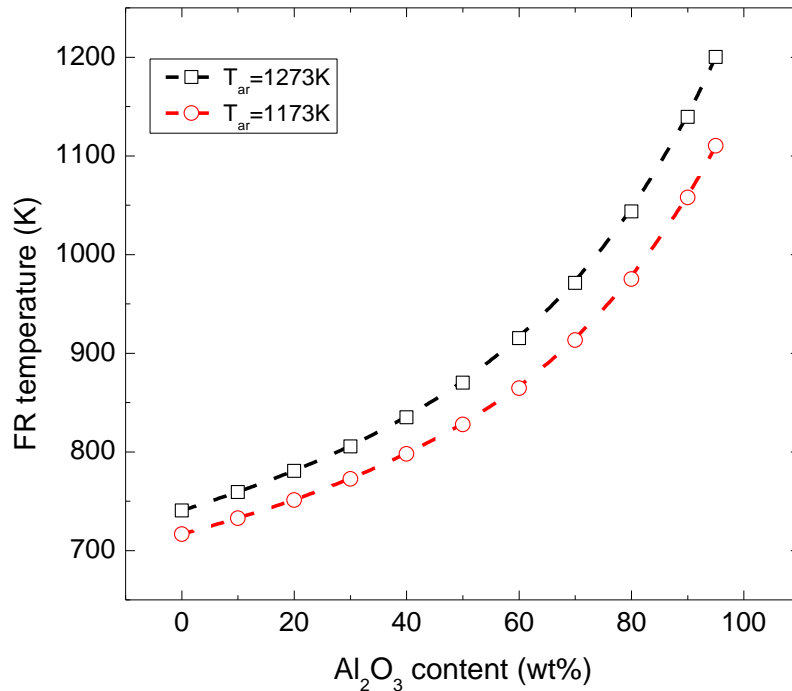


Figure 4.3: The variations of the temperature in fuel reactor with Al_2O_3 content.

The corresponding reactivity for the three using alumina-supported iron oxides is investigated in 30 cycles for the purpose of comparison with the pure iron oxide. As shown in Figure 4.4, the stability of the reduction reactivity is improved by the additive of alumina on Fe_2O_3 . Specifically, the deviation on mass loss, defined as $\omega = m/m_{ox}$, is 1.88%, 7.79% and 2.51% for Fe10Al, Fe25Al and Fe45Al respectively, whereas it is 28.82% for unsupported iron oxide. It also can be found in Figure 4.4, that the more additive on the metal oxide leads to a higher ω , i.e. the lower oxygen transfer capacity (OTC) defined as $OTC = (m_{ox}-m)/m_{ox}$, which is 0.048, 0.027, 0.0185 and 0.012 for the additive in 0, 55, 75 and 90 wt%. One possible reason is that the addition of support material provides a site for the distribution of active component, resulting in the increase in the specific surface area. It is no doubt that the mass transfer rate on the surface benefits from a larger specific surface area. Another likely reason is that the porous support material has a strong adsorption capability to the gas phase and hence the contact surface between the gas phase and solid phase increases. This also causes the increase in the mass transfer rate. With the increase of mass transfer rate the reactivity increases naturally.

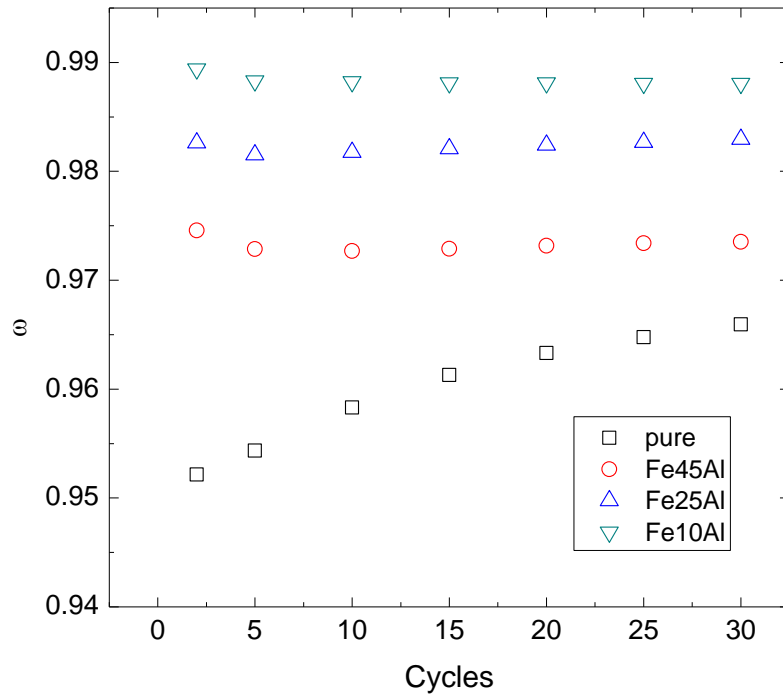


Figure 4.4: Mass loss at 1023 K in 30 cycles for pure Fe₂O₃, Fe45Al, Fe25Al and Fe10Al.

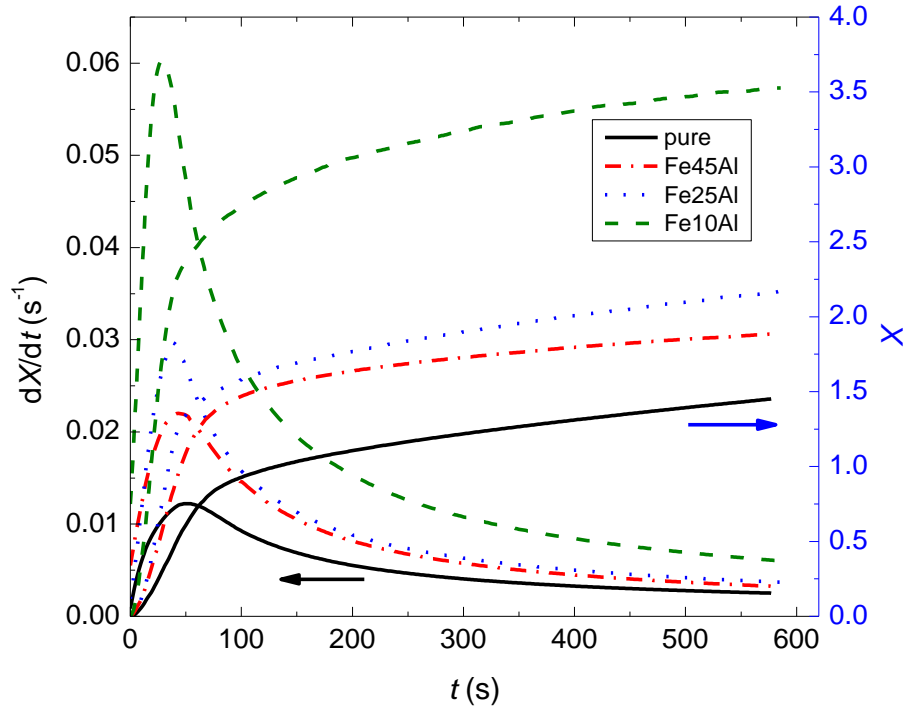
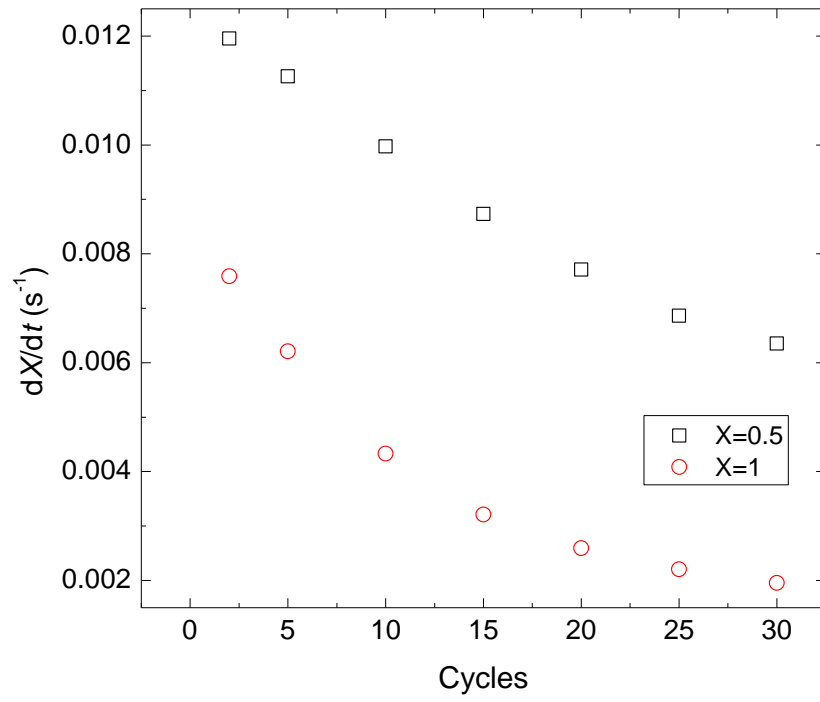
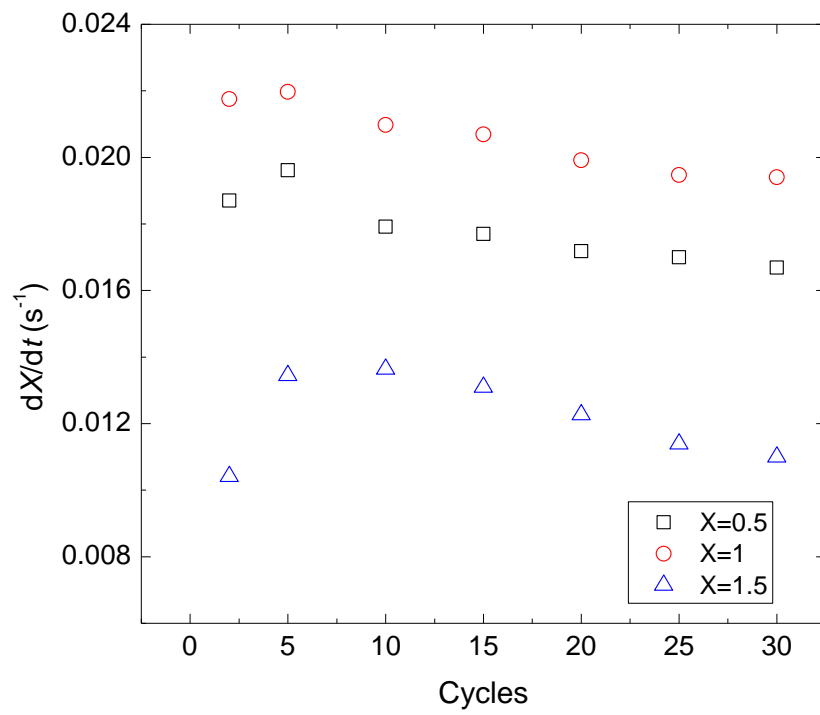


Figure 4.5: Reduction conversion and reaction rate for the 5th cycle at 1023 K for pure (2nd cycle), Fe45Al, Fe25Al and Fe10Al.

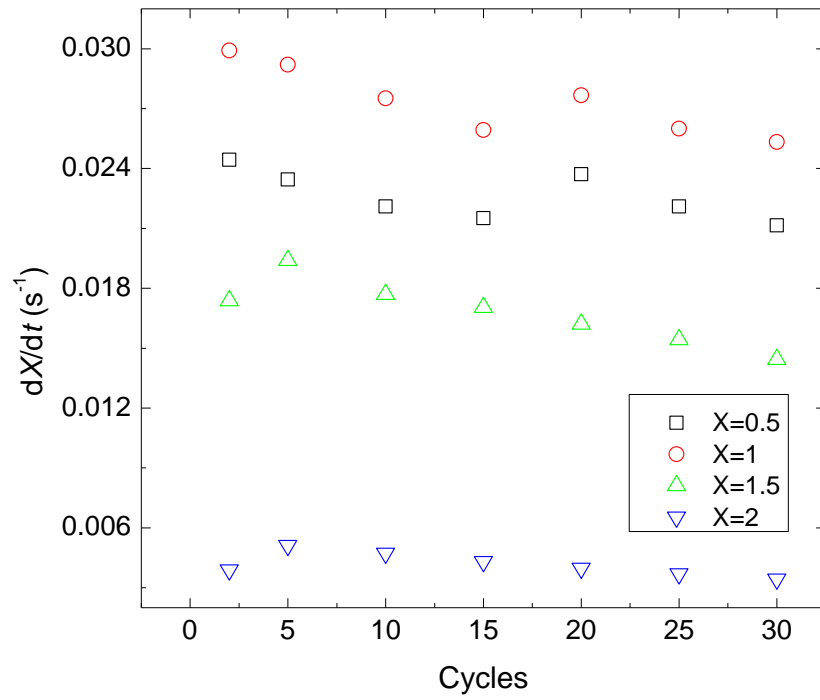
Moreover, the conversion and reaction rates during 10 min reduction at 1023 K are illustrated in Figure 4.5. The results corresponded to the data from the fifth cycle in a 30-cycle test for Fe45Al, Fe25Al and Fe10Al while the second cycle for pure iron oxide. It should be noted that the conversion equal to unity represented the full conversion of Fe₂O₃ to Fe₃O₄, 3 for Fe₂O₃ to FeAl₂O₄ as indicated by the ratio of Fe/Al. During reductions of 10 min, the reduction for all test materials proceeds in two steps. The conversion is increasing at a fast rate during the first step. Later, a slower reduction step is observed which explained why a longer time is needed to reach a complete conversion to Fe. As can be observed, the fast step ends at around $t=60$ sec corresponding to the conversion of 0.8–2.5 depending on the weight content of Fe₂O₃. It is then followed by a plateau (i.e. slow step) which represented the conversion curve of Fe₃O₄ to FeAl₂O₄ and/or Fe. This is also demonstrated in the figure of dX/dt vs. t where the reduction rate climbs to its peak value in a short time frame of around 60 sec followed by a steep decrease. The sharp points on the reaction rate curves are clearly visible as shown in Figure 4.5. Besides, the weight content of Fe₂O₃ put a significant impact on the reduction rate and as such, the conversion. The higher metal oxide content leads to a lower reaction rate, i.e. lower conversion. It should be noted that, however, the conversion difference between Fe25Al and Fe45Al is less distinct than that between Fe45Al and unsupported iron oxide or Fe10Al and Fe25Al.



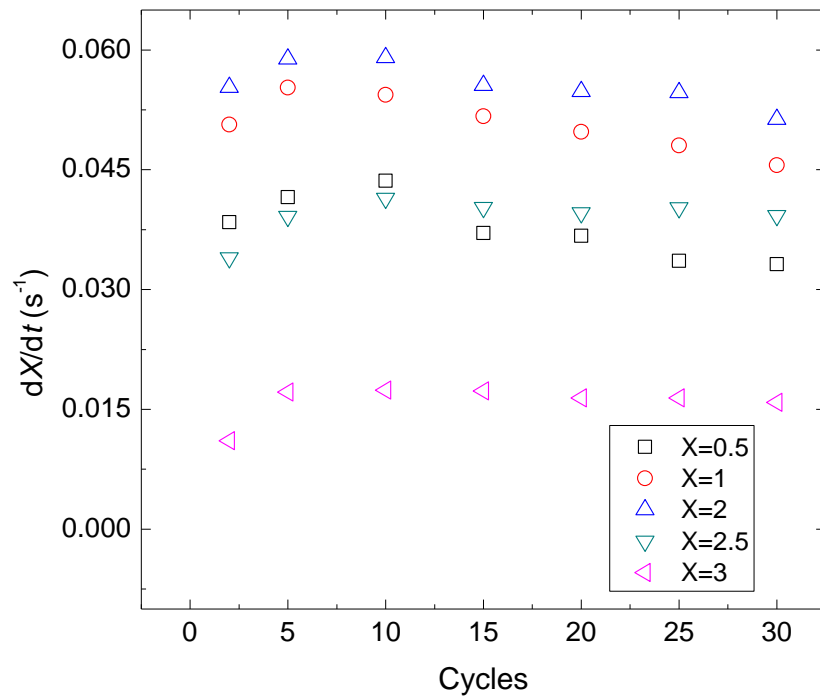
(a)



(b)



(c)



(d)

Figure 4.6: Reactivity variations with cycles at different conversions for: (a) pure Fe_2O_3 , (b) Fe_{45}Al , (c) Fe_{25}Al , and (d) Fe_{10}Al .

Table 4.3: Detailed deviations on reaction rates for different conversion values.

	X=0.5	X=1	X=1.5	X=2	X=2.5	X=3
pure	46.87	74.24	/	/	/	/
Fe45Al	12.90	11.68	19.33	/	/	/
Fe25Al	13.44	15.33	25.56	32.93	/	/
Fe10Al	23.94	17.53	/	13.06	5.20	8.89

A detailed comparison in reduction rates at different conversions during 30 cycles is presented in Figure 4.6. As shown, the reaction rates at X=0.5 and 1 are presented in all figures though for different materials the selected conversion values differs. It is again revealed that pure iron oxide delivers the least reactivity stability compared with the three alumina-supported ones. It is also revealed that the reaction rate stability is rather dependent on the conversion value. For Fe10Al the reaction rate is more stabilised with the increase in conversion and the reverse is true for the other three. The detailed deviations on reaction rates are summarised in Table 4.3 for different conversion values. As can be seen, at low conversion X=0.5 and 1 (i.e. conversion of Fe₂O₃ to Fe₃O₄) Fe45Al has the best reactivity stability during 30 cycles followed by Fe25Al, Fe10Al and pure one in sequence. The figures show that the reaction rate dX/dt is varied with the conversion range. The comparative high reaction rate level is found within the conversion range less than 1 for all tested materials as observed.

For the reduction of iron-based oxygen carriers with CH₄, the conversion of Fe₂O₃ to Fe₃O₄ and/or FeAl₂O₄ is of more interest due to the capacity of converting CH₄ fully to CO₂ from a thermodynamics point of view. With regards to the reactivity, it depends on the conversion range and loading content of metal oxide. The comparison of reactivity at conversion X=0.5, 1 and 1.5 is shown in Figure 4.7 for three supported iron oxides. As can be seen it decreases with the increase in the weight content of Fe₂O₃. However, it requires taking into account the oxygen transport capacity (ROC) together in order to evaluate the

performance of oxygen carrier candidates [106]. The so-called rate of oxygen transport is therefore applied and defined by:

$$ROT = ROC \times \frac{dX}{dt} \quad (4.1)$$

where dX/dt is the reaction rate.

The reaction rates corresponding to $X=0.5$, 1 and 1.5 are used in conjunction with ROC to determine the ROT values for all metal oxide cases as summarised in Figure 4.7. Interestingly, the case of Fe10Al does show the highest reduction reactivity for the highlighted conversion range. With respect to the value of ROT , along the conversion of Fe₂O₃ to Fe₃O₄, Fe10Al has a much lower ROT than the cases of Fe25Al and Fe45Al, which in turn shows the highest ROT . During the reduction of Fe₃O₄ to FeAl₂O₄, Fe10Al shows a similar value of ROT with Fe45Al and Fe25Al owning the lowest value. The above analysis clearly highlights the shortcomings of just relying on reactivity and conversely the benefits of using ROT , which combines both ROC and reactivity.

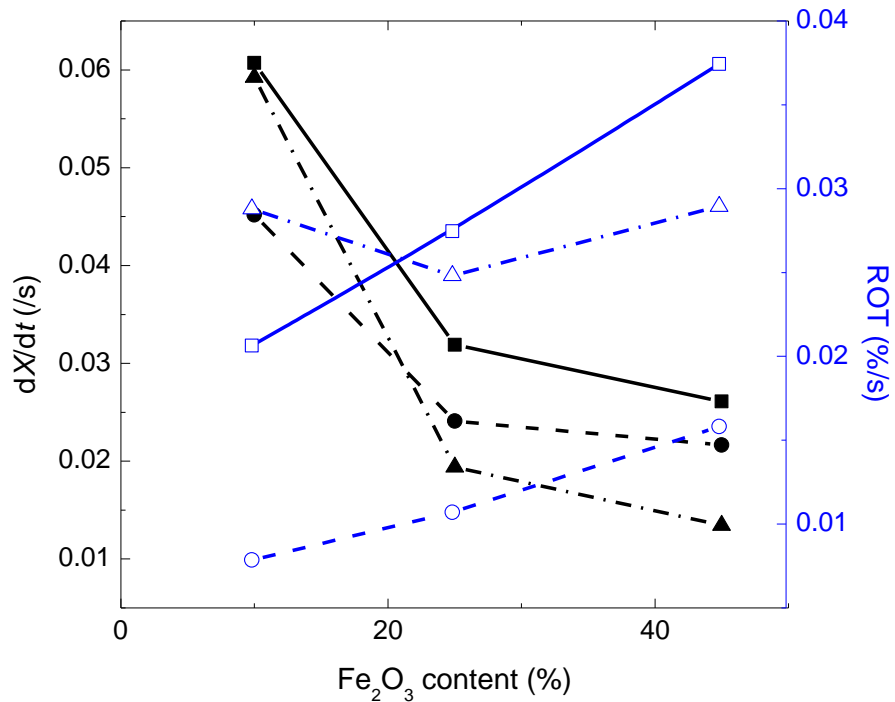


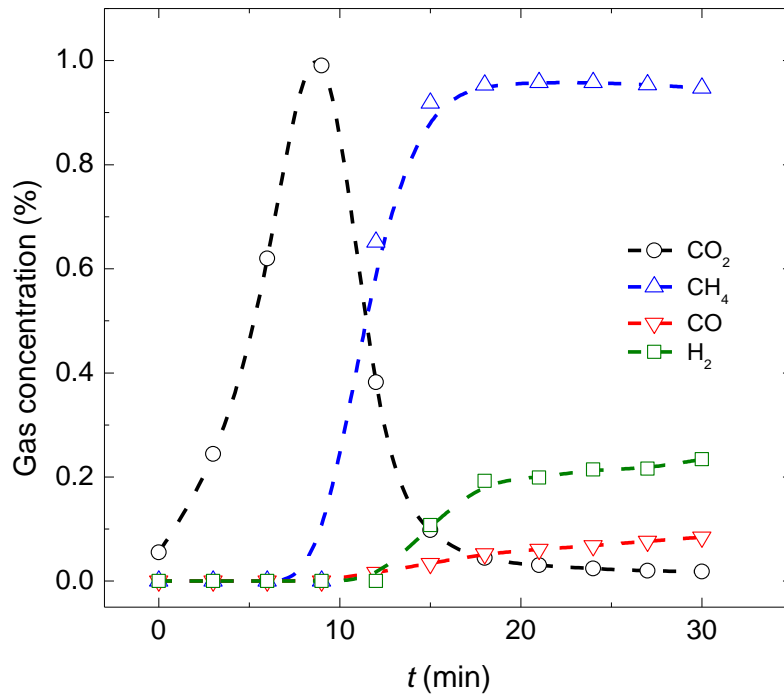
Figure 4.7: The effect of loading content on reaction rate (solid) and ROT (open): $X=0.5$ (\circ); $X=1$ (\square); $X=1.5$ (Δ).

4.3.3 Gas Analysis for the Reduction of Alumina-supported Fe_2O_3 with CH_4

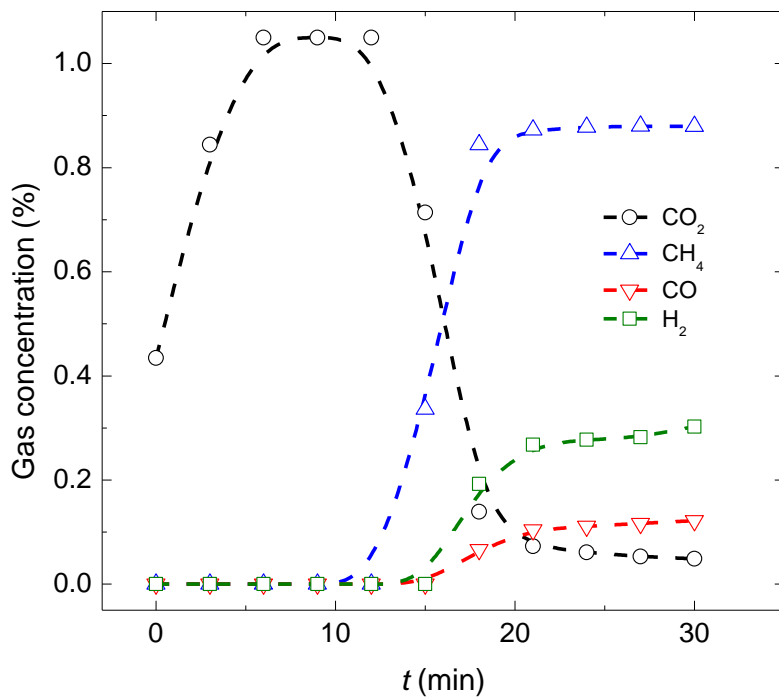
The comparison in outlet product gas concentration with time for Fe10Al, Fe25Al and Fe45Al is shown in Figure 4.8(a–c). All experiments are conducted in five redox cycles and the data from the fifth reduction period is applied. The reaction temperature is at 1023 K in order to compare in an accurate manner, because with higher temperatures (like 1073 K) carbon deposition is found in 30 min reduction periods except for Fe45Al. For Fe10Al, the concentration of CO_2 decreases after an initial increase with time and the concentration of CH_4 increases. At the same time, some CO and H_2 content is observed because the oxygen in Fe10Al is insufficient and CH_4 is partially reduced to CO and H_2 rather than CO_2 and H_2O as shown in Figure 4.8(a). Regarding the reduction of Fe25Al in Figure 4.8(b), the product gas has a similar profile with that of Fe10Al, and the only difference is that the concentration of CO_2 is maintained at very high levels between the dramatic increase and decrease. During the 30 min reduction of Fe45Al, the only detected component is CO_2 which indicated that CH_4 is completely oxidised to CO_2 and H_2O as shown in Figure 4.8(c).

To avoid carbon deposition during the reduction of Fe₂O₃ with CH₄, the best way is to achieve a high conversion of CH₄ to CO₂ and H₂O [107]. Figure 4.8(d) shows the conversion of methane during 30 min reduction of Fe10Al, Fe25Al and Fe45Al. It is found that Fe10Al has the lowest conversion and never reaches the full conversion to CO₂. The peak value is around 94% during the reduction. CH₄ can be completely oxidised to CO₂ by both Fe₂₅Al and Fe₄₅Al but a longer duration time on the full conversion is provided by the later one.

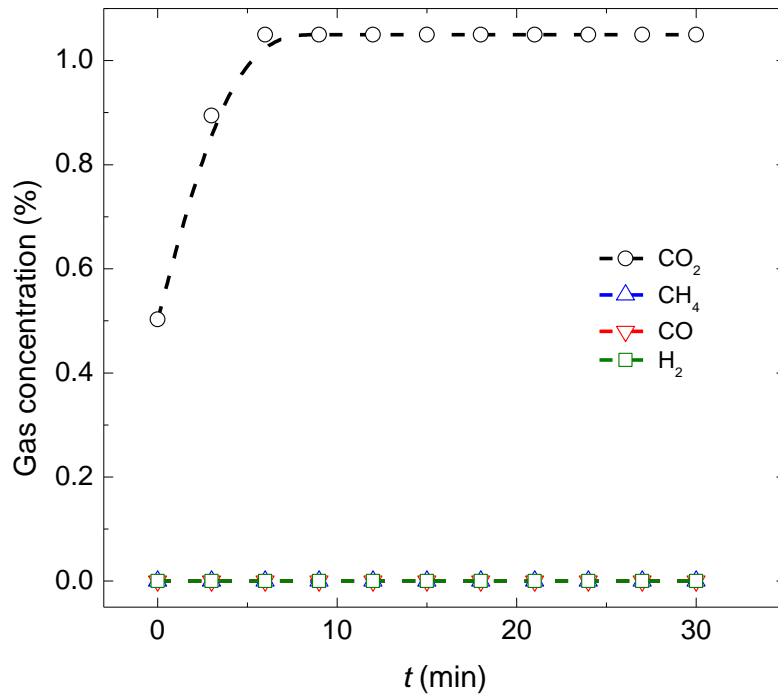
Based on these results, it can be summarised that all test alumina-supported Fe₂O₃ delivers better reactivity stability than unsupported materials during cyclic redox experiments. In terms of the reaction rate, it is decreasing with the increase in Fe₂O₃ weight content and therefore the reduction of Fe10Al is with the highest reaction rate. Regarding the conversion range, to achieve a full conversion of CH₄ the solid conversion of Fe₂O₃ to FeAl₂O₄ is in favour for the reduction of CH₄ on the basis of thermodynamics and experimental assessment. In this conversion range, Fe45Al shows the most stabilised reactivity as well as the highest rate of oxygen transport (*ROT*) which evaluates an oxygen carrier coupling the reactivity with oxygen transport capacity (*OTC*). Besides, the gas analysis results revealed that Fe45Al exhibits the best performance on methane conversion as well as duration on the high-level conversion. It can therefore be concluded that Fe45Al could be the most suitable oxygen carriers for chemical looping hydrogen generation process with ultra-low methane conversion as far as the reactivity associated with gas analysis results are concerned.



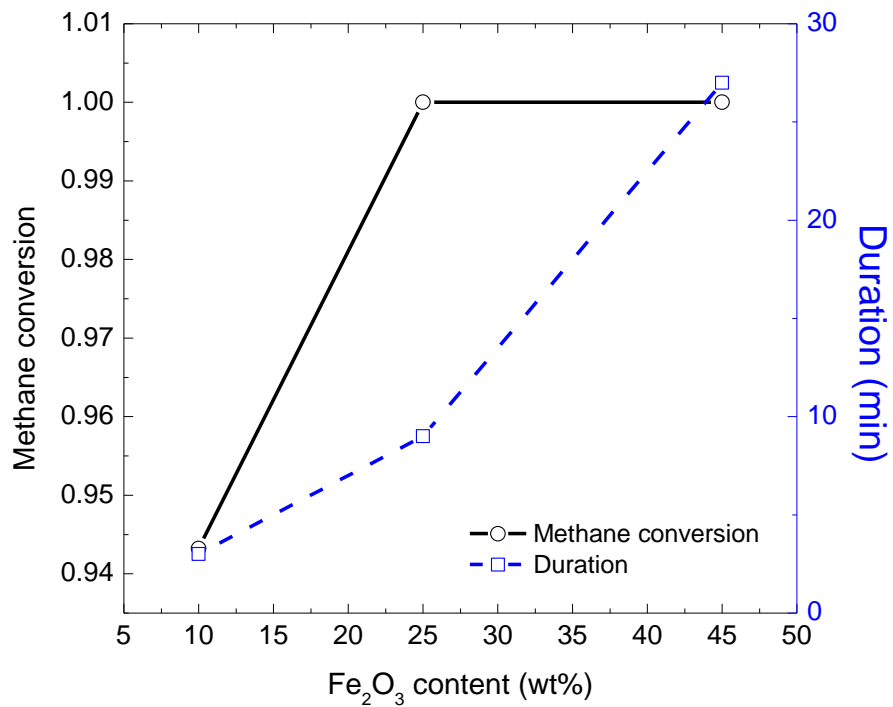
(a)



(b)



(c)



(d)

Figure 4.8: Gas concentration profile for: (a) Fe10Al, (b) Fe25Al (c) Fe45Al with 1 vol% CH_4 at 1023 K, and (d) CH_4 conversion as well as the duration on high conversion.

4.3.4 The Influential Factors on Reduction Reactivity of Fe_2O_3 to FeO

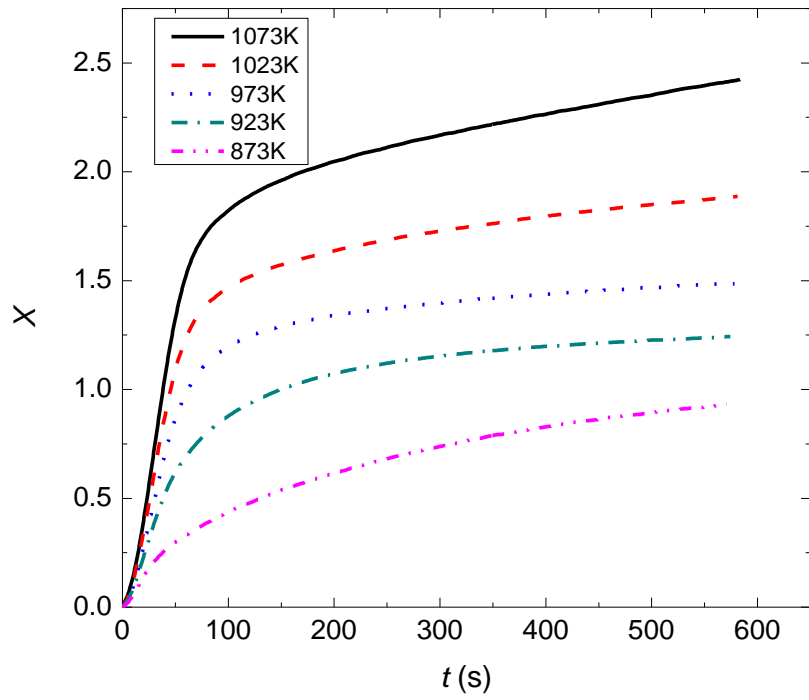
In a real system for the combustion of low concentration methane, the role of some operational parameters is significant and may put some critical effect on the reduction reactivity. In the present study, the effect of reaction temperature, methane concentration and CO_2 composition in reducing gas is investigated and discussed. The reactivity on conversion of $X=0.5$ and 1.5 is used and compared, which represents the reactivity for the transformation pairs of $\text{Fe}_2\text{O}_3/\text{Fe}_3\text{O}_4$ and $\text{Fe}_3\text{O}_4/\text{FeAl}_2\text{O}_4$. The reaction rates at lower fractional conversion ($<20\%$) were not analysed because the concentrations of reaction gases cannot be accurately determined due to the dilution of the reaction gas by the purge gas (N_2) at the beginning of each reduction cycle.

The Effect of Reaction Temperature

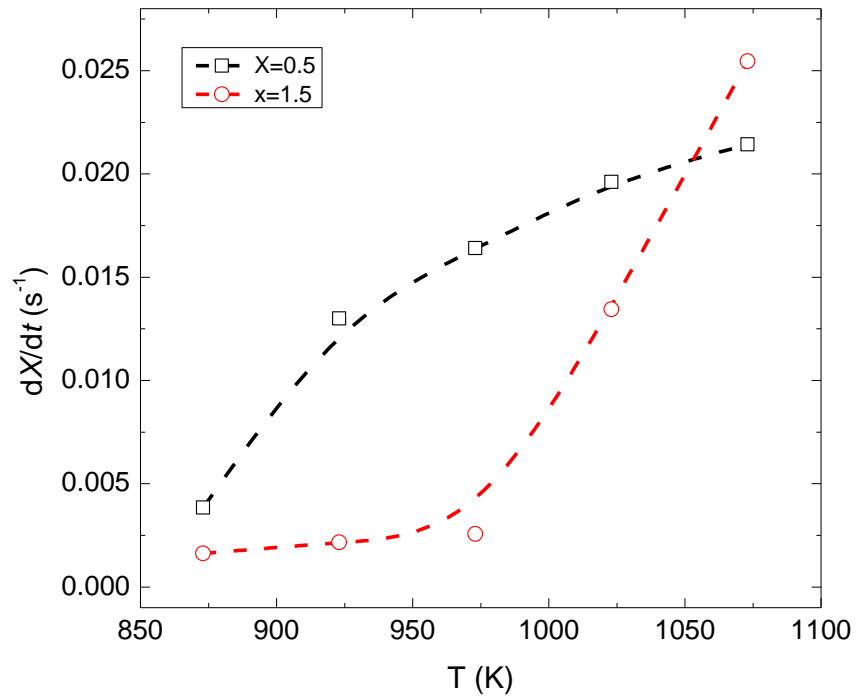
Figure 4.9 shows the effect of reaction temperature on the reduction conversion and reactivity. As shown the reduction conversion is increasing with the temperature as stated by other studies. It should be noted that temperatures higher than 973 K are more preferred as with lower temperatures it takes a much longer time to reach the conversion aim of $X=1$ (i.e. conversion of Fe_2O_3 to Fe_3O_4). Specifically, the time to achieve $X=1$ is around $38\text{--}62$ seconds within the temperature range of $973\text{--}1073\text{ K}$ while it increases dramatically to 150 seconds for temperature at 923 K which is two times longer at a temperature of 973 K . With respect to the reactivity for $X=0.5$, it increases initially with a fast rate at lower temperatures and later with a lower rate for temperatures higher than 973 K . It is also observed that the reduction rate increases with the decrease in conversion at lower temperatures while the adverse trend is found for the higher temperature. Also it reveals that the reactivity at high conversion ($X=1.5$) is more sensitive to the variation on temperature, particularly for that higher than 973 K . The overall increases for $X=0.5$ and 1.5 are 0.017 and 0.024 within the temperature range of $873\text{--}1073\text{ K}$.

Figure 4.10 presents the effect of temperature on the gas composition in product gas stream, methane conversion and duration on high-level conversion. The reduction is conducted in 60 min with Fe45Al over the temperature of $873\text{--}1073\text{ K}$. During the reduction, only CH_4 and CO_2 are detected as illustrated in Figure 4.10(a). Most importantly, the concentration of

CO₂ and CH₄ is quite dependent on the reaction temperature and reduction time. At the same time the concentration of CO₂ is increased with the temperature whereas that of CH₄ decreases. The exception is found at the temperature of 1073 K, for which only CO₂ is detected and no CH₄ is observed, even when the concentration of CO₂ is decreased to a low level, which implies carbon deposition occurred. The fact is proved by the observation of CO₂ during the oxidation step but for the other temperatures no CO₂ is observed in the oxidation. As per the methane conversion, it increases with the increase in temperature and reached the full conversion to CO₂ at 973 K and maintains this level at the higher temperatures. Nevertheless, it exhibits a better ability to avoid carbon deposition at 1023 K due to the longer duration on the high conversion level in Figure 4.10(b).

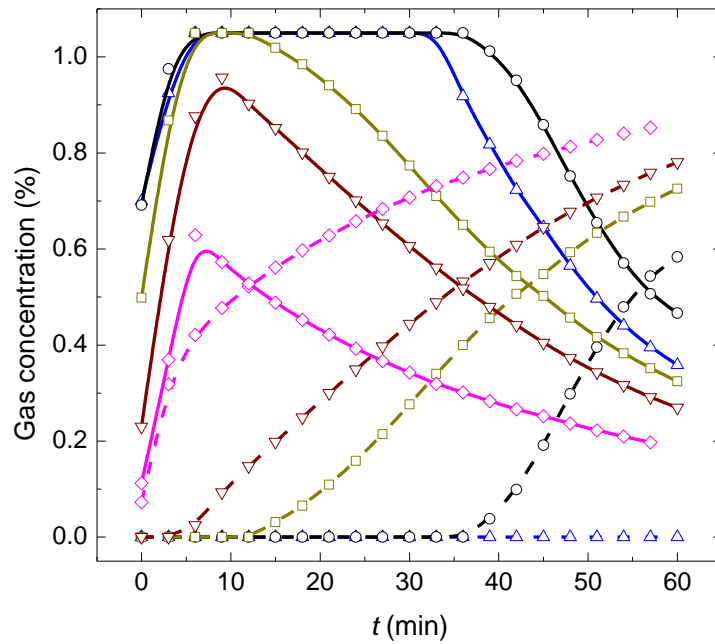


(a)

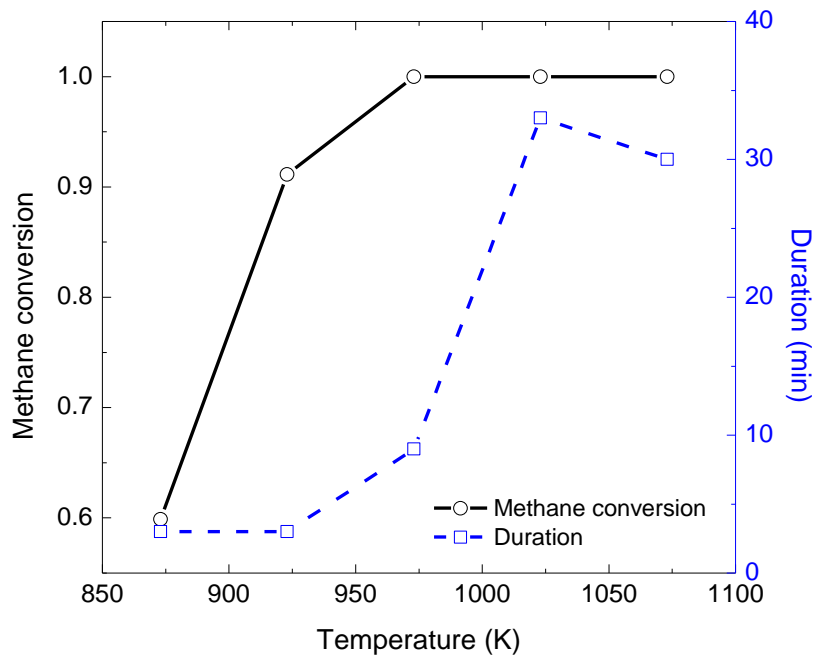


(b)

Figure 4.9: The effect of temperature on: (a) the conversion and (b) reactivity.



(a)



(b)

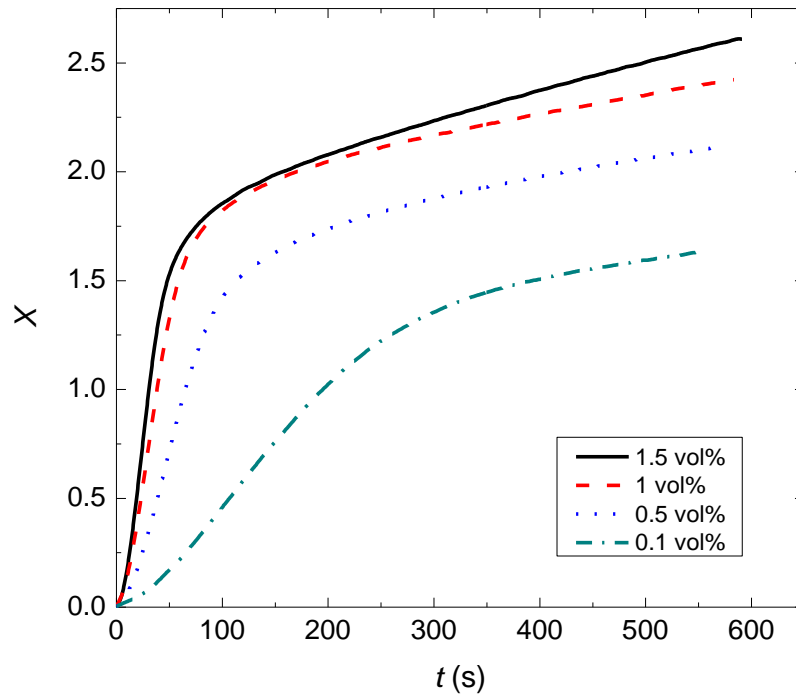
Figure 4.10: The effect of temperatures (◇ 873 K, ▽ 923 K, □ 973 K, ○ 1023 K and △ 1073 K) on the product gas concentration, (a) CO₂ (solid line) and CH₄ (dash line); and (b) methane conversion and duration on high level conversion.

The Effect of Methane Concentration

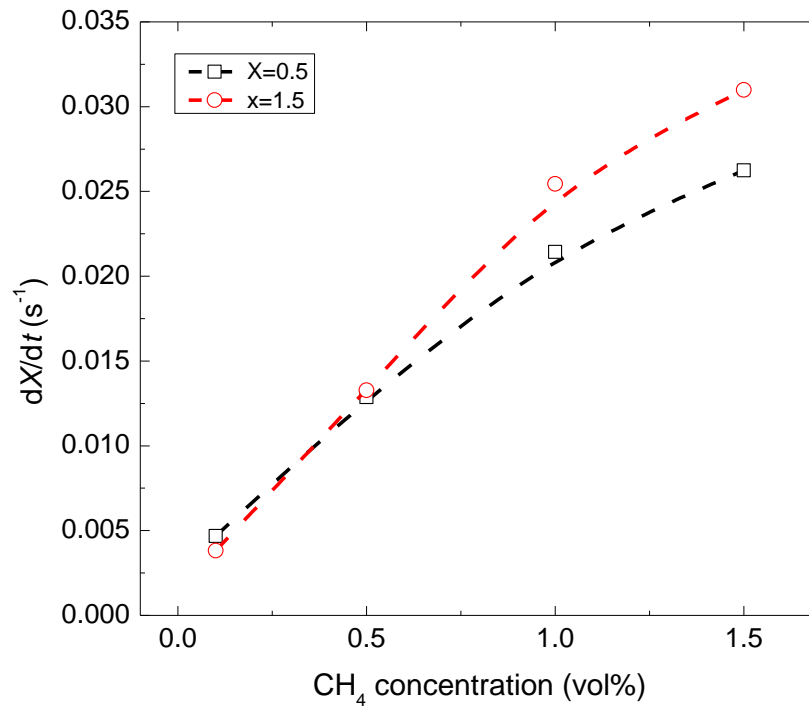
Figure 4.11 presents the effect of methane concentration (varying in the range of 0.1–1.5 vol%) on the reduction conversion and reactivity. The results reveal clearly that the higher methane concentration leads to higher reduction conversion. But for the methane concentration higher than 1 vol% the increase in the conversion become smaller. If only taking into account the phase of Fe₂O₃/Fe₃O₄, the time to achieve full conversion is 31, 38, 65 and 195 seconds for the different cases. It implies that the lower methane concentration causes a larger decrease on the reactivity as shown in Figure 4.11(b). For instance, the reactivity at $X=0.5$ is 0.026, 0.021, 0.013 and 0.005 s⁻¹ with 1.5, 1, 0.5 and 0.1 vol% CH₄, corresponding the decline of 18%, 40% and 64%. Besides, the conversion of Fe₃O₄ to FeAl₂O₄ has a stronger sensitivity on the methane concentration than the pair of Fe₂O₃/Fe₃O₄.

The Effect of CO₂ Composition in the Reducing Agent

In a gas stream with ultra-low concentration methane, a large amount of CO₂ may also be contained and somehow put a significant influence on the reduction reactivity. Figure 4.12 shows the effect of CO₂ composition in the gas stream on the reduction conversion and reactivity. As can be seen, for the CO₂ composition higher than 10% the effect on the conversion and reactivity is almost invisible. Compared with the reduction of the gas stream without CO₂, however, the reduction conversion is lower and nearly constant after the conversion reaches the level of $X=1.90$ with the reducing gas containing CO₂. It can be deduced from the fact, that the reduction reactivity of Fe₂O₃ with CH₄ is inhibited by CO₂ gas. The reactivity detailed in Figure 4.12(b) indicates that the reactivity decreases around 42% due to the reducing gas containing CO₂.

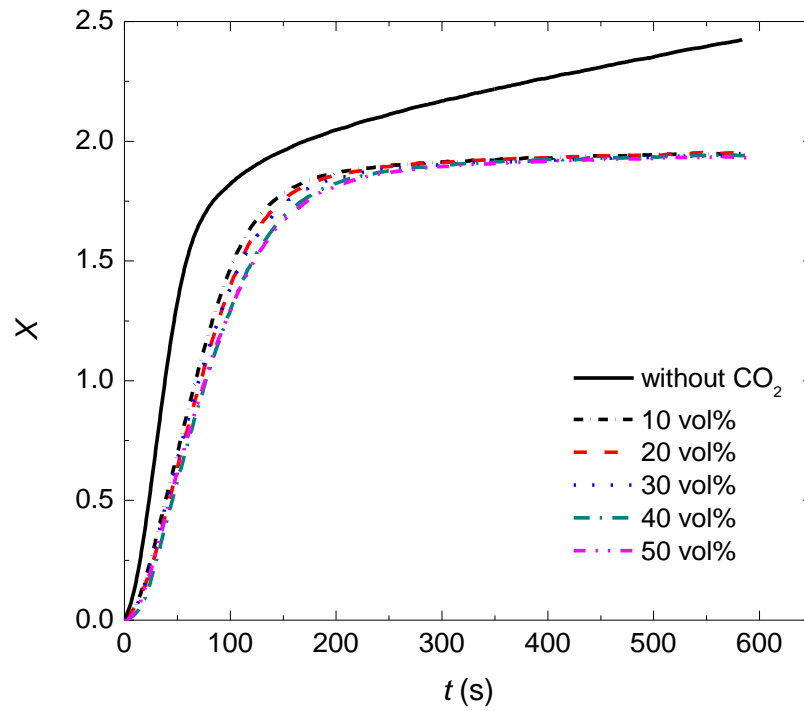


(a)

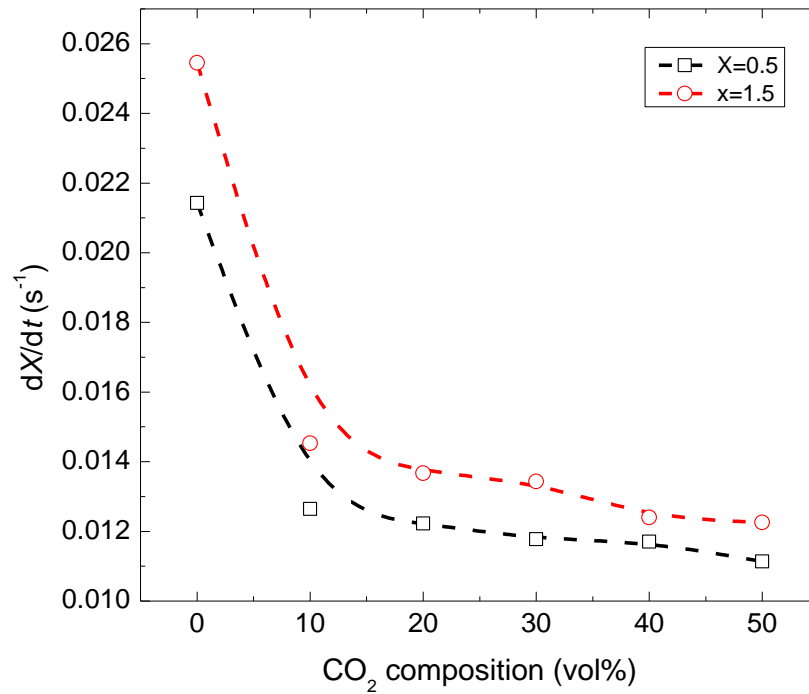


(b)

Figure 4.11: The effect of gas concentrations on: (a) the conversion and (b) reactivity.



(a)



(b)

Figure 4.12: The effect of CO_2 composition in the reducing gas on: (a) the conversion and (b) reactivity.

4.4 Conclusions

A comprehensive study was carried out to identify suitable alumina-supported iron-based oxygen carriers for the chemical looping combustion of ultra-low concentration methane. The thermodynamics results indicated that iron oxides with support content higher than 50 wt% were more suitable for this case; three alumina-supported iron oxides were prepared using the impregnation method with different metal oxide content, i.e. Fe10Al, Fe25Al and Fe45Al. To determine their performance on reactivity and gas conversion, a set of experiments was carried out in TGA apparatus and fixed bed reactor. The major findings from the experimental study were listed as following:

- (1) Both the reactivity and cyclic stability were improved significantly due to the additive of Al_2O_3 . But the values of OTC were declined with the decrease in the content of Fe_2O_3 .
- (2) The reduction reactivity was varying with the reduction conversion range. In most cases, the conversion of Fe_2O_3 to Fe_3O_4 showed the highest reactivity.
- (3) It also increased with the decrease in the content of parent material, i.e. Fe10Al had the highest reactivity. But it showed least stability in the desired conversion range.
- (4) In terms of the rate of oxygen transport (ROT), which took into account oxygen transfer capacity and reactivity together, the highest value was for Fe45Al.
- (5) The gas analysis results uncovered that Fe45Al were the most suitable oxygen carrier candidates due to the contribution of complete conversion of CH_4 to CO_2 as well as longest duration on high-level conversion.
- (6) The role of operation parameters, such as reaction temperature, methane concentration and CO_2 composition in the reducing gas, was investigated and discussed in the final section. It should be highlighted in the results that the most suitable reduction temperature was 1023 K and the reactivity was inhibited by the containing of CO_2 .

Chapter 5: REDUCTION KINETICS OF Fe_2O_3 BY ULTRA-LOW CH_4

5.1 Introduction

Kinetics parameters are of significant importance in the reactor design and predicting the gas product and energy consumption. However, very few works were found to study the reduction kinetics of iron oxides and no universal kinetics model was established in the literature. Essentially, within a certain range of reaction conditions, a set of independent equations can be secured and used to interpret the reduction process. The aim of the current study is to investigate the reduction kinetics of $\text{Fe}_2\text{O}_3/\text{Al}_2\text{O}_3$ with ultra-low concentration CH_4 in the temperature range 973K–1073K. This is in support of the study presented in Chapter 6 on hydrogen production using a dual-loop system.

5.2 Experimental Studies

The experimental setup and procedure were described with detailed information in Chapter 3 (refer to Section 3.2.1) and Chapter 4.

5.3 Kinetic Model

Three groups of kinetic model are normally used to interpret the reaction mechanism for solid-gas reactions so-called: (a) diffusion controlled model, (b) phase boundary controlled model, and (c) nucleation and growth model. Some algebraic equations are derived to illustrate these models in a mathematical manner with some reasonable assumptions. Nine typical equations used for the mathematical modelling of the kinetic data of the reactions are presented in Table 5.1. To determine which model is the best fit to the experimental data and as such used for calculating the kinetic data, Hancock and Sharp [108] developed a

convenient method to compare the kinetics of isothermal gas solid reactions based on an equation describing nucleation and growth process:

$$\ln[-\ln(1-X)] = \ln \beta + m \ln t \quad (5.1)$$

where X is the fractional conversion at time t , β is a constant, which partially depends on nucleation frequency and rate of grain growth, and m is a constant that varies with the geometry of the system. Hancock and Sharp pointed out that kinetic data which follow any one of a number of kinetic equations, including the equations for nucleation and growth process, give rise to approximately linear plots of $\ln-\ln(1-X)$ vs $\ln t$ if the range of X is limited to values 0.15–0.50. The slopes of such plots are diagnostic of the reaction mechanism. It can be seen that for values for m below unity ($m < 1$), the reactions tend to be diffusion controlled, phase boundary controlled for m ranging from 5.1 to 5.2, and Avrami-Erofe'ev equations for m equal to 5.2 and 5.3.

Kinetic parameters can be obtained from isothermal kinetic data using the rate law equation,

$$\frac{dX}{dt} = k \cdot f(X) \quad (5.2)$$

$$k = A \cdot e^{-E/RT} \quad (5.3)$$

Integration (5.2),

$$\int_0^X \frac{dX}{f(X)} = g(X) = kt \quad (5.4)$$

Where X is the fractional conversion, t is time, k is reaction rate constant, A is pre-exponential factor, E is activation energy, R is gas constant, T is absolute temperature, and $f(X)$, $g(X)$ are the differential form and integral form expressions for the reaction mechanism.

The rate constant k can be determined by applying the equation (5.4). The values of $g(X)$ are first plotted with time t and then it is fitted by a linear line with the intercept equal to

zero. The slope represents the rate constant for a certain temperature. The relation of the k values obtained with the reaction temperature is established by the Arrhenius plots. It results in a straight line with the slope $-E/R$ and an intercept, which is the logarithm of pre-exponential factor A . Note that by taking the logarithm of equation (5.3), we have:

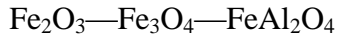
$$\ln k = \ln A + \left(-\frac{E}{R}\right) \cdot \frac{1}{T} \quad (5.5)$$

Table 5.1: Kinetic equations for different reaction mechanisms.

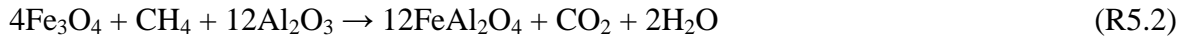
Reaction mechanism	Integral form $g(X)=kt$	Values of m
1-D diffusion D1	X^2	0.62
2-D diffusion D2	$X + (1 - X) \ln(1 - X)$	0.57
3-D diffusion-Jander D3	$\left[1 - (1 - X)^{1/3}\right]^2$	0.54
3-D diffusion-Ginstling-Brounshtein D4	$1 - \frac{2}{3}X - (1 - X)^{2/3}$	0.57
Phase boundary controlled (contracting cylinder) R2	$1 - (1 - X)^{1/2}$	1.11
Phase boundary controlled (contracting sphere) R3	$1 - (1 - X)^{1/3}$	1.07
Phase boundary controlled (infinite slabs) R1	X	1.24
2-D growth of nuclei A2	$[-\ln(1 - X)]^{1/2}$	2
3-D growth of nuclei A3	$[-\ln(1 - X)]^{1/3}$	3

The reduction kinetics of Fe₂O₃/Al₂O₃ was determined by monitoring the weight changes during the course of its reduction under isothermal conditions. However, there was no agreement on the transformations product of Fe₂O₃ during its reduction. Some researchers

thought the reduction to FeO occurred after Fe₂O₃ was completely transformed to Fe₃O₄ while others suggested that the reduction of Fe₂O₃ to Fe₃O₄ and FeO were proceeding simultaneously. According to Abad et al. [73], considering the reduction sequence for particles composed by Fe₂O₃ and Al₂O₃:



For both Fe45Al and Fe25Al particles, the molar ratios of FeO to Al₂O₃ are 1.043 and 0.425 respectively, which means the final state of Fe is in the form of FeAl₂O₄. The theoretical weight changes in accordance to reaction stoichiometry for CH₄ gas reduction of Fe₂O₃ were calculated according to the reactions listed below:



It was thus determined that the theoretical weight decrease corresponding to the transformation of Fe₂O₃ into Fe₃O₄ is 3.3 wt% and to FeAl₂O₄ is 10 wt%. The reduction reactivity was evaluated using the TGA data and represented by the fractional conversion of oxygen carriers (see details in Section 3.2.1).

The root mean square deviation (*RMSD*) values were employed to compare the calculation results (*X_{cal}*) with the experimental data (*X_{exp}*). The following equation was applied,

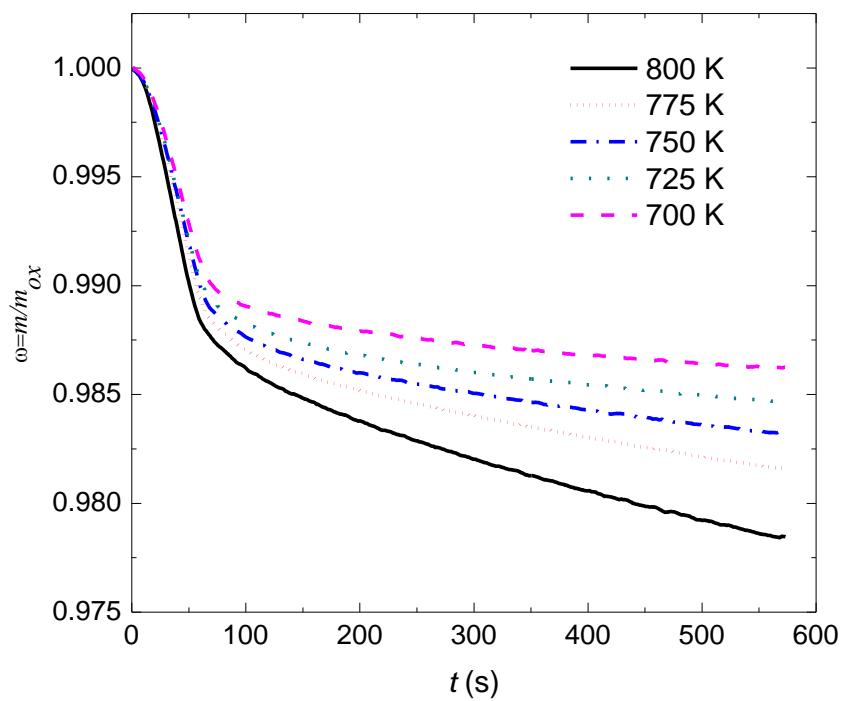
$$RMSD = \sqrt{\frac{\sum (X_{cal} - X_{exp})^2}{n-1}} \quad (5.6)$$

where *n* is the number of data points.

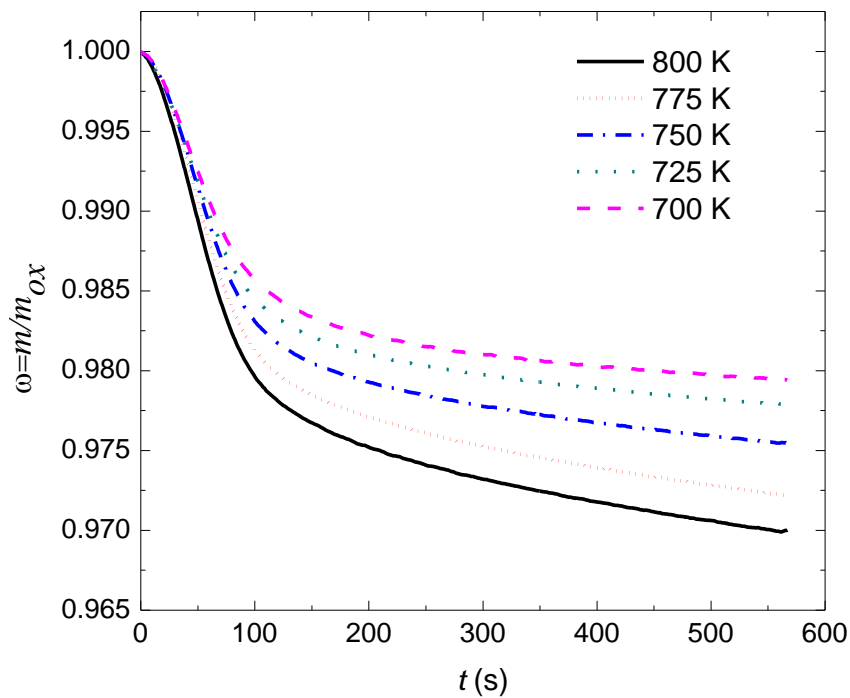
5.4 Results

5.4.1 Reduction of Fe₂O₃/Al₂O₃ by CH₄

Reduction for both oxygen carriers was carried out in the temperature range 973 K–1073 K and the mass loss, defined as $\omega = m/m_{ox}$, obtained with 0.5 vol% CH₄ is shown in Figure 5.1. During reductions of 10 min, the conversion of Fe₂O₃ proceeds in two steps. The sample mass was decreasing at a fast rate during the first step. Later, a slower reduction step is observed corresponding to the reduction from Fe₃O₄ to FeAl₂O₄, resulting in a longer time needed to reach full conversion to Fe. With an increase in reduction temperature, a larger mass loss can be found within the same reduction time. But it should be noted that the difference on mass loss during the first step reduction (i.e. Fe₂O₃ to Fe₃O₄) is not as distinct as that observed in the reduction of Fe₃O₄ to FeAl₂O₄. This means that the conversion of Fe₃O₄ into FeAl₂O₄ is a more temperature dependent process than from hematite to magnetite.



(a)



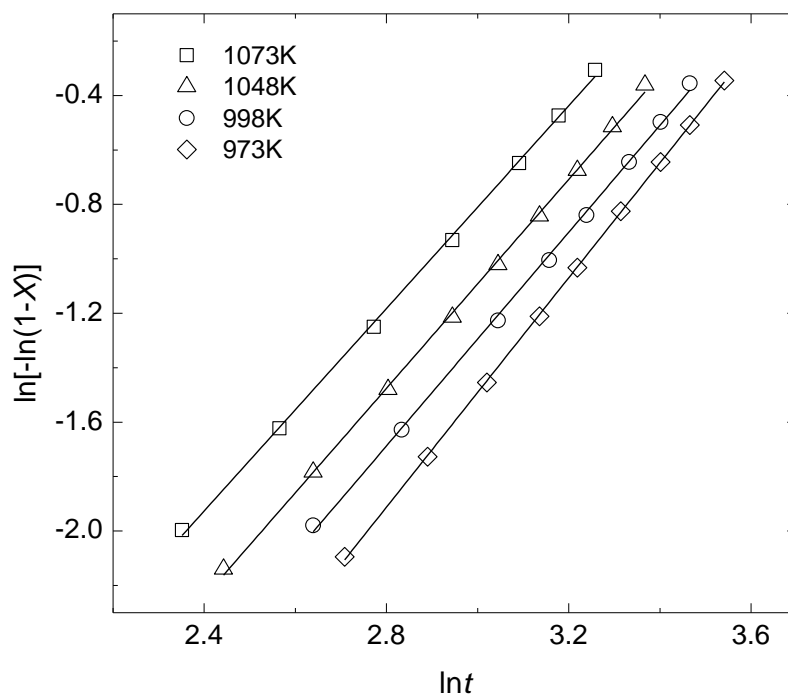
(b)

Figure 5.1: Reduction of: (a) Fe₂₅Al and (b) Fe₄₅Al with CH₄ at different temperatures.

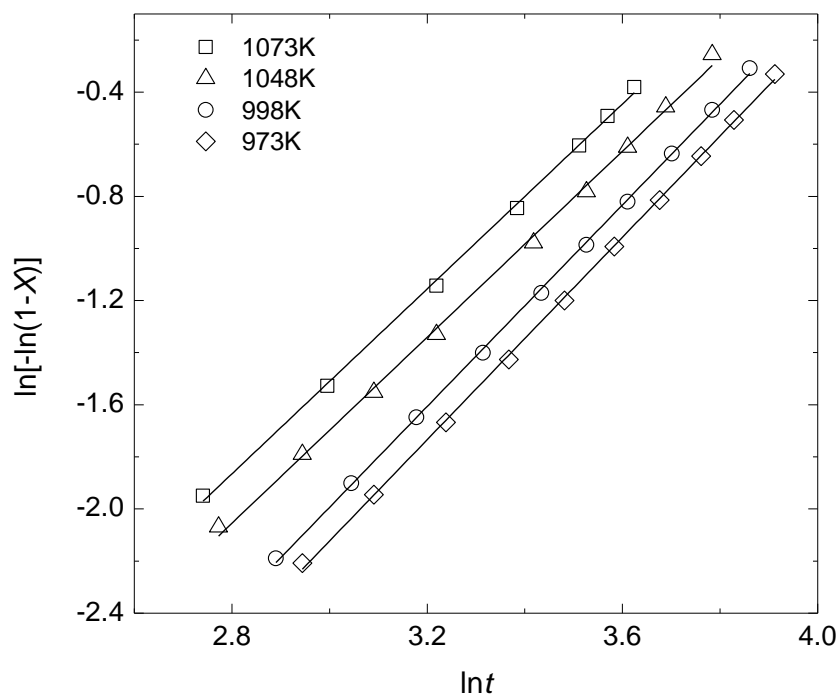
5.4.2 Reduction Kinetics of Fe₂O₃ to Fe₃O₄

To determine m values for different temperatures, plots of $\ln(-\ln(1-X))$ vs $\ln t$ for the transformation of Fe₂O₃ into Fe₃O₄ are illustrated in Figure 5.2 (note that the plot for temperature 1023 K is not presented because the curves between 998 K and 1023 K are too close). The slopes for Fe25Al and Fe45Al are 1.98 ± 0.12 and 1.86 ± 0.08 (see Table 5.2), indicating that the reaction within the temperature range (973–1073K) is isokinetic, i.e. the mechanism is the same. These m values indicate that the reaction mechanism could be described by 2-D nuclei growth model A2 (i.e. Avrami-Erofe'ev equation). However, it seems that since the m value is an intermediate between 1 and 2, both phase boundary controlled models R1, R2 and R3 ($m=1.07, 1.11$ and 1.24) and 2-D growth of nuclei model A2 ($m=2$) are selected to fit the experimental data. The fitting coefficient r suggests that A2 is the most suitable model to describe the reduction of Fe₂O₃ to Fe₃O₄ for both samples. The best fitting model sequence is A2>R1> R2>R3 and the comparison of r is shown in Table 5.3. The curves of $g(X)$ vs t are found to be linear as the least square coefficient r is higher than 0.99. The slopes of these linear lines are represented k listed in Table 5.4, which is used to plot $\ln k$ vs $1000/T$. From the data in this table, it can be found that the reactivity of Fe25Al was higher than that of Fe45Al during this reduction stage.

The comparison of the experimental data with calculation results from the A2 model is shown in Figure 5.3. As can be seen, the 2-D nuclei growth model predicts the experimental data very well. It can be explained by the fact that by reducing Fe₂O₃ to Fe₃O₄, the lattice transforms from rhombohedra to cubic, so that the phase change occurs which confirms phase change mechanism is applicable [103]. However, the difference between the experimental data and calculation results is significant for the higher conversions ($X>0.8$), especially for Fe25Al over the whole range of temperatures and Fe45Al at high temperatures. The underlying reason for this phenomenon will be discussed in the discussion session.

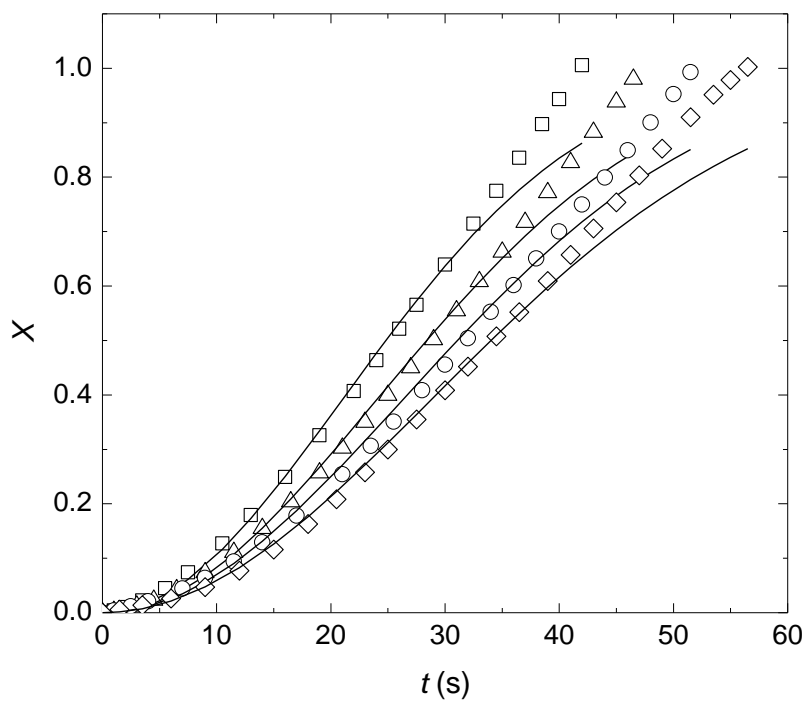


(a)

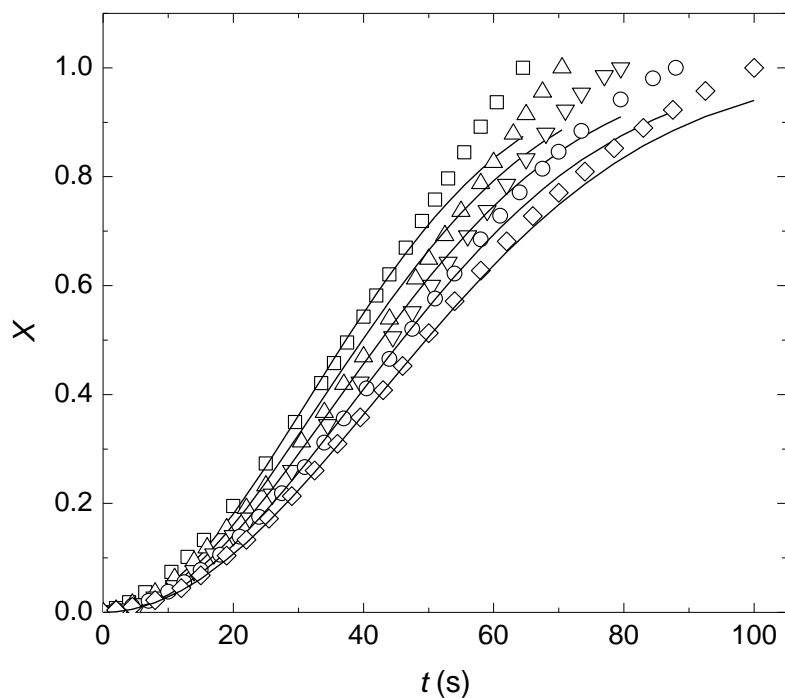


(b)

Figure 5.2: Plots of $\ln(-\ln(1-X))$ vs $\ln t$ for the reduction of Fe_2O_3 to Fe_3O_4 for samples: (a) Fe25Al and (b) Fe45Al.



(a)



(b)

Figure 5.3: Comparison of experimental data (symbol) with calculation results (line) for the reduction of Fe_2O_3 to Fe_3O_4 with samples: (a) Fe25Al and (b) Fe45Al, (\square):1073 K, (\triangle):1048 K, (\circ):998 K, (\diamond):973 K).

Table 5.2: *m* value for Fe₂O₃-Fe₃O₄.

T(K)	Fe25Al		Fe45Al	
	<i>m</i>	<i>r</i>	<i>m</i>	<i>r</i>
973	2.1075	0.9999	1.9432	0.9990
998	1.9633	0.9990	1.9343	0.9996
1048	1.9188	0.9993	1.7851	0.9983
1073	1.8603	0.9993	1.7748	0.9991

Table 5.3: Fitting correlation coefficient *r* for different diffusion model (Fe₂O₃-Fe₃O₄).

T(K)	Fe25Al				Fe45Al			
	<i>R1</i>	<i>R2</i>	<i>R3</i>	<i>A2</i>	<i>R1</i>	<i>R2</i>	<i>R3</i>	<i>A2</i>
973	0.9314	0.8876	0.8694	0.9946	0.9538	0.9124	0.8938	0.9990
998	0.9466	0.9071	0.8905	0.9951	0.9447	0.9034	0.8859	0.9980
1048	0.9429	0.9046	0.8888	0.9975	0.9525	0.9148	0.8991	0.9966
1073	0.9563	0.9239	0.9101	0.9966	0.9647	0.9292	0.9135	0.9946

Table 5.4: Kinetic parameters using 2-D nuclei growth model A2.

T(K)	Fe25Al		Fe45Al	
	<i>K</i> (1/s)	<i>RMSD</i>	<i>K</i> (1/s)	<i>RMSD</i>
973	0.0248	0.0582	0.0172	0.0207
998	0.0267	0.0488	0.0184	0.0297
1048	0.0293	0.0441	0.0205	0.0384
1073	0.0336	0.0467	0.0226	0.0411

Upon comparing *RMSD* values (refer to Table 5.4), it is observed that the experimental results for Fe45Al can be better predicted by using the A2 model. The average *RMSD* value is 0.0494 for Fe25Al and 0.0324 for Fe45Al, noting that the *RMSD* value for Fe45Al is increasing with the increase in temperatures while decreasing for Fe25Al.

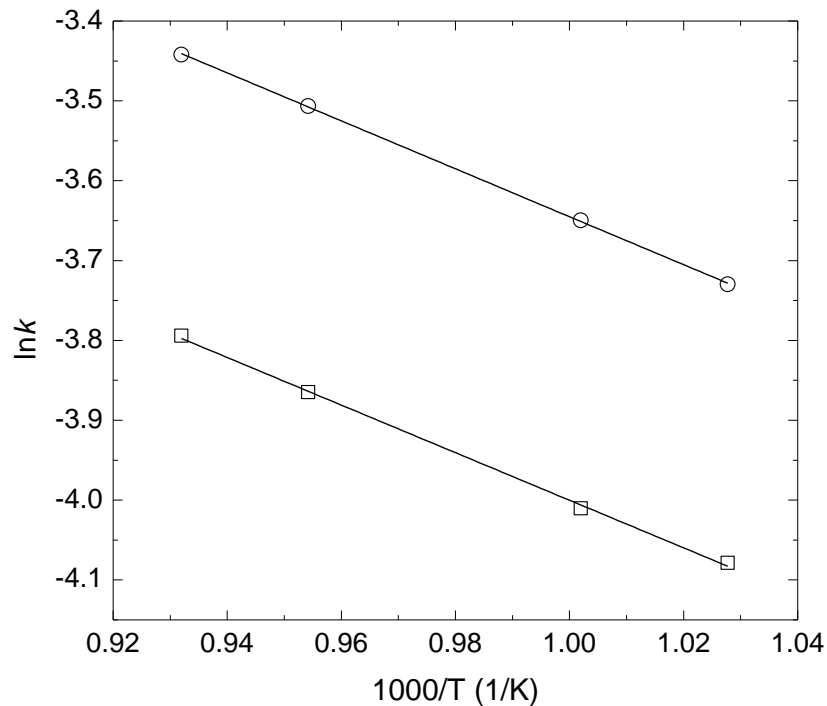


Figure 5.4: Plots of $\ln K$ vs $1000/T$ for the reduction of Fe_2O_3 to Fe_3O_4 with samples (\circ :Fe25Al and \square :Fe45Al).

The rate constant in Table 5.4 is applied to obtain the activation energy from the Arrhenius equation (Equation 5.5). The plots of $\ln k$ vs. $1000/T$ are presented in Figure 5.4. As expected they are straight lines with negative slopes which are then used to estimate activation energy values. For both samples, Fe25Al and Fe45Al, the difference in slopes—thus, in activation energy values is almost invisible. The activation energies for Fe25Al and Fe45Al are estimated to be 24.96 and 24.77 kJ/mol.

5.4.3 Reduction Kinetics of Fe_3O_4 to FeAl_2O_4

Once the reduction of Fe_2O_3 to Fe_3O_4 was accomplished, it continues to transform into the form of FeAl_2O_4 as mentioned earlier. Apparently, the later transformation occurs with a slow rate (refer to Figure 5.1). This is because, with the formation of a thin reduced layer on the surface, the reducing agent CH_4 would have to diffuse to reach the reaction interface. Under such circumstances, the diffusion-controlled reaction takes place and the diffusion-controlled mechanism is applicable during this time period. Based on Hancock and Sharp's method, the variation of $\ln(-\ln(1-X))$ with $\ln t$ is plotted in Figure 5.5. Using the regression

method, m values, i.e. the slopes, are obtained and shown in Table 5.5. The average m values of Fe25Al and Fe45Al are 0.41 ± 0.06 and 0.45 ± 0.03 , confirming the reduction is of the same kinetic mechanism and a diffusion-controlled process. To distinguish the model, which is able to best predict the reduction conversion, four diffusion-controlled models (D1, D2, D3 and D4) are applied to fit the experimental data and the comparison of the least square coefficient r is presented in Table 5.6. For Fe45Al, the D3 model shows the best prediction in the temperature range with a least square coefficient about 0.9877, sequentially D4, D2 and D1. In the case of Fe25Al, the most suitable one is the D3 model except for the temperature of 973 K. They are followed by D4, D2 and D1 as the last resort. This is also confirmed by the comparison in *RMSD* values as shown in Figure 5.6. Based on these conclusions, the D3 model is the best-fit model for the reduction of Fe₃O₄ to FeAl₂O₄, and thus the Jander equation is used to calculate the rate constant k for different temperatures as summarised in

Table 5.7. It is shown that Fe25Al delivers bigger rate constant values indicating that the reactivity of Fe25Al is higher for the later reduction stage.

Table 5.5: m value for Fe₃O₄-FeAl₂O₄.

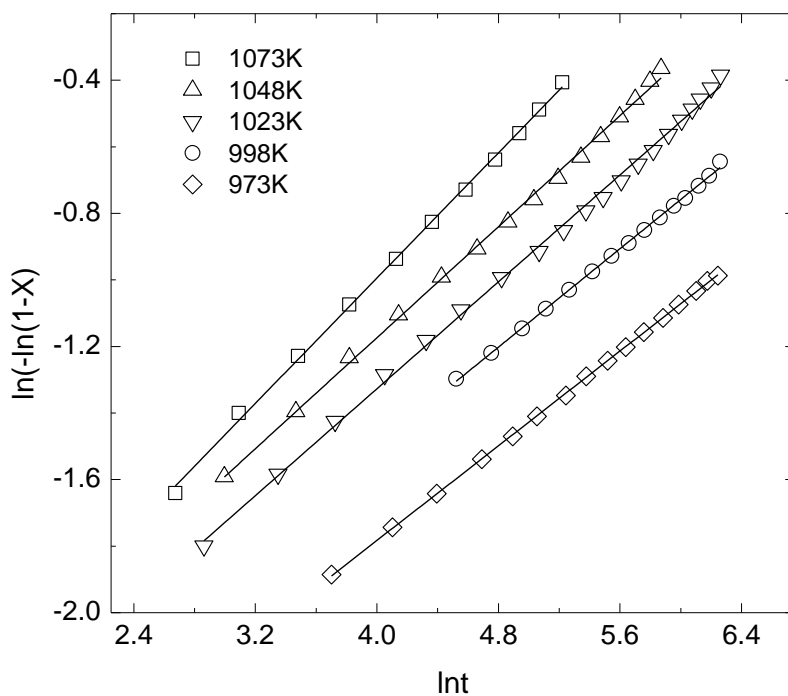
T(K)	Fe25Al		Fe45Al	
	m	r	m	r
973	0.35	0.9998	0.42	0.9990
998	0.37	0.9991	0.43	0.9987
1023	0.40	0.9982	0.44	0.9979
1048	0.42	0.9985	0.44	0.9991
1073	0.47	0.9990	0.48	0.9921

Table 5.6: Fitting correlation coefficient r for different diffusion controlled models.

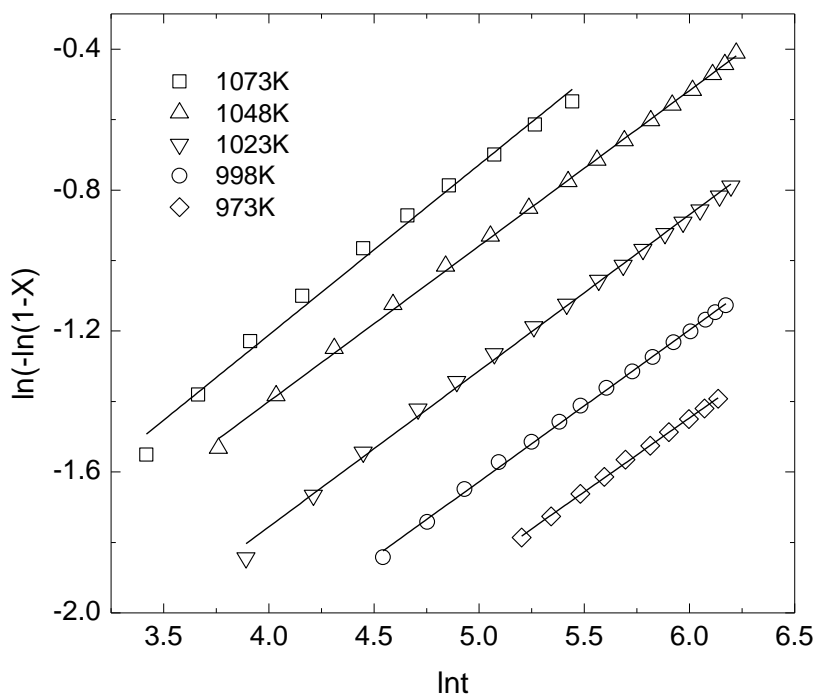
T(K)	Fe25Al				Fe45Al			
	$D1$	$D2$	$D3$	$D4$	$D1$	$D2$	$D3$	$D4$
973	0.9907	0.9965	0.9778	0.993	0.9838	0.9875	0.9907	0.9887
998	0.9626	0.9829	0.9943	0.988	0.9762	0.9826	0.9881	0.9846
1023	0.9421	0.9636	0.9803	0.9700	0.968	0.9782	0.9866	0.9813
1048	0.9094	0.9331	0.9537	0.9405	0.9577	0.9745	0.9873	0.9794
1073	0.9211	0.9365	0.9505	0.9414	0.9425	0.9674	0.9858	0.9746

Table 5.7: Kinetic parameters for diffusion controlled model $D3$.

T(K)	Fe25Al		Fe45Al	
	k (1/s)	$RMSD$	k (1/s)	$RMSD$
973	0.0000299	0.02157	0.00001565	0.00734
998	0.0000504	0.02096	0.0000266	0.00873
1023	0.0000817	0.02119	0.000052	0.01268
1048	0.000126	0.02219	0.000105	0.01785
1073	0.000223	0.02512	0.00016	0.02237



(a)



(b)

Figure 5.5: Plots of $\ln(-\ln(1-X))$ vs $\ln t$ for the reduction of Fe_3O_4 to FeAl_2O_4 for samples: (a) Fe25Al, and (b) Fe45Al.

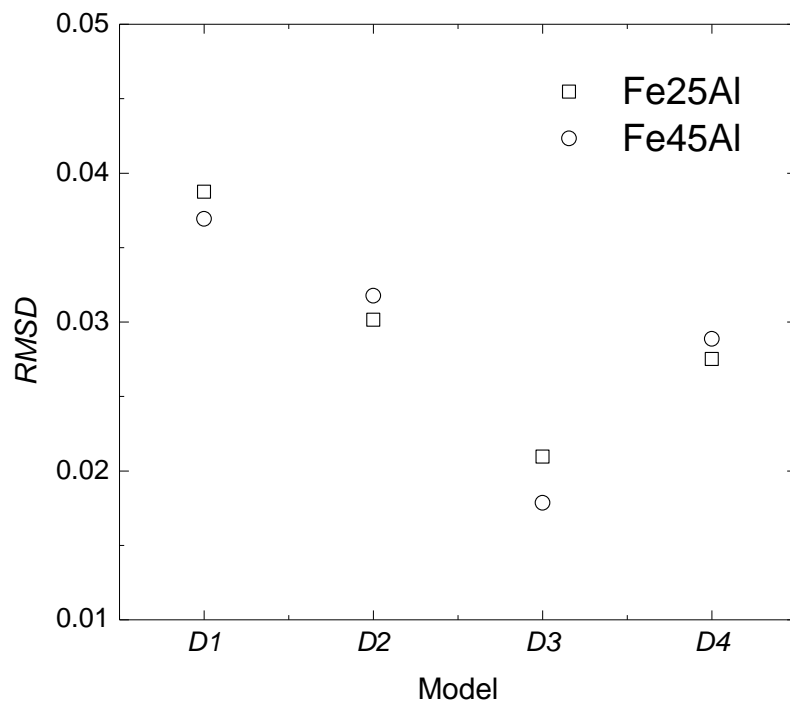
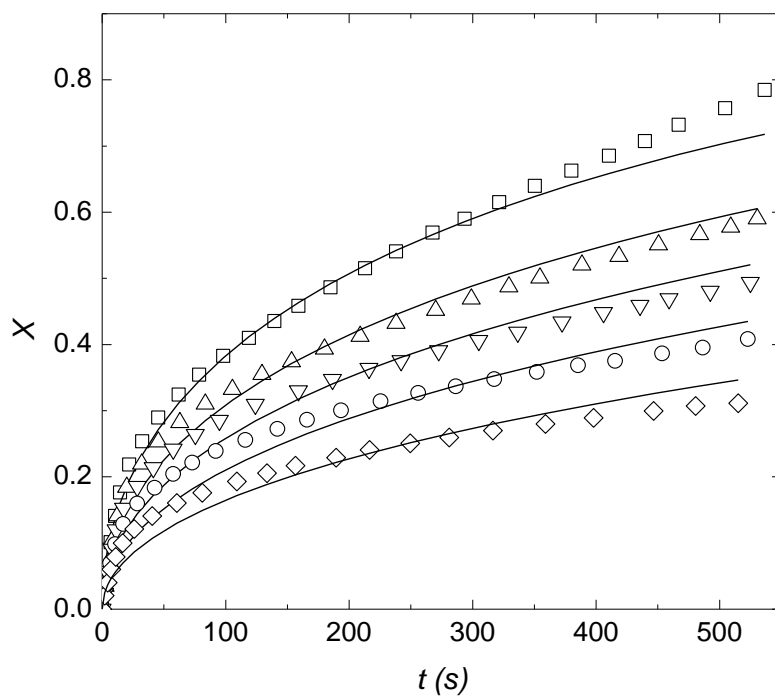
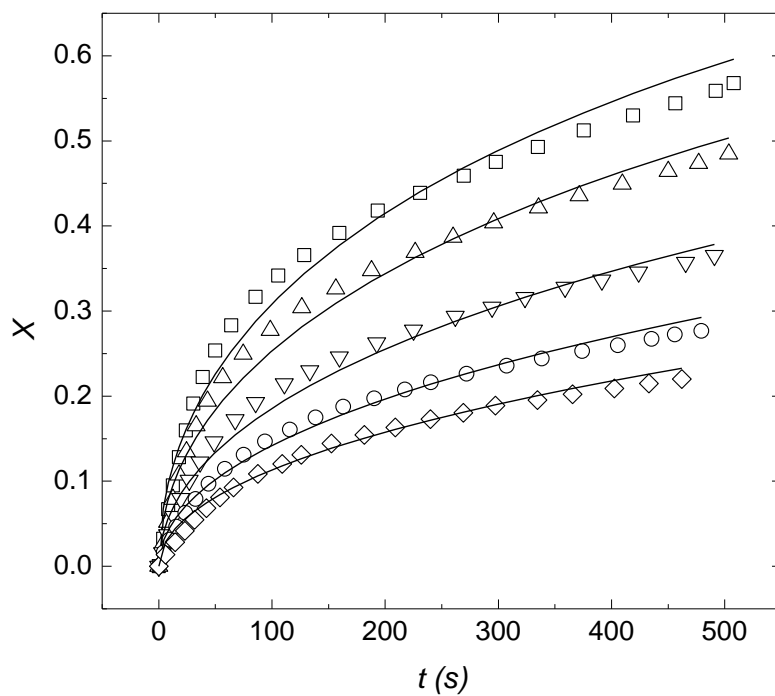


Figure 5.6: *RMSD* values for different reaction models.



(a)



(b)

Figure 5.7: Comparison of experimental data (symbol) with calculation results (line) for the reduction of Fe_3O_4 to FeAl_2O_4 with samples: (a) Fe25Al and (b) Fe45Al, (\square :1073 K, \triangle :1048 K, ∇ :1023 K, \circ :998 K, \diamond :973 K)

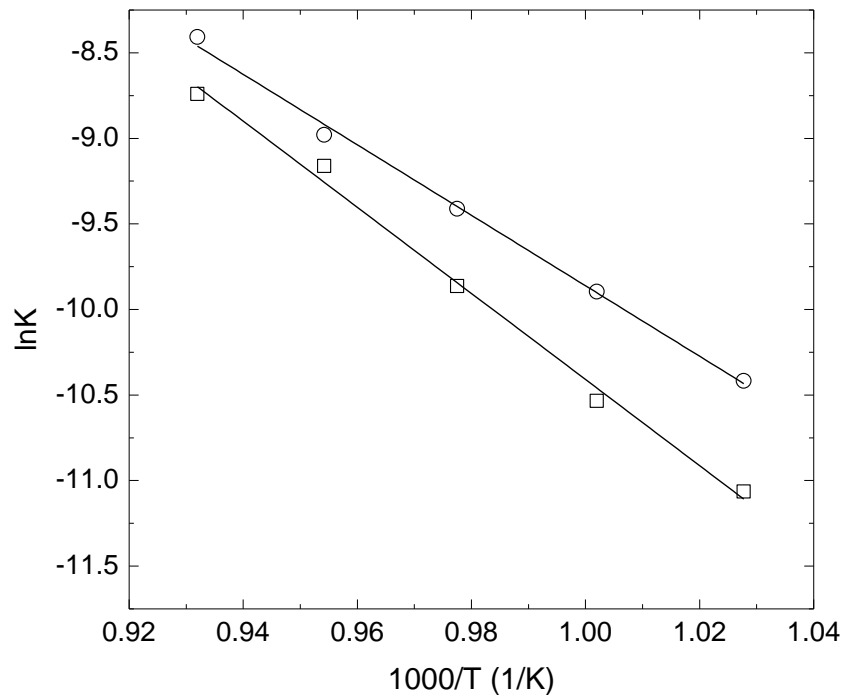


Figure 5.8: Plots of $\ln k$ vs $1000/T$ for the reduction of Fe_3O_4 to FeAl_2O_4 with samples (○:Fe25Al and □:Fe45Al).

The theoretical conversion values from the D3 model are plotted with time and compared with the experimental data in Figure 5.7. The calculation results are in good agreement with the obtained experimental data as shown in this figure. Therefore, it can be concluded that the reaction is in diffusion controlled mechanism for the reduction of Fe_3O_4 to FeAl_2O_4 . However, it is noted that the conversion is located in the range of 0.2–0.8 depending on the temperatures due to the experiment time limitation. With an increase in the reaction time, a thicker product layer is formed on the initial surface which gradually develops more stable conditions for a diffusion process [104]. From this point of view, the reaction model for the conversion within the range of 0.2–0.8 can be more or less used to represent the model for the whole reduction conversion.

The activation energy for the reduction of Fe_3O_4 to FeAl_2O_4 is estimated from the plot of $\ln k$ vs. $1000/T$ as illustrated in Figure 5.8. As expected, the $\ln k$ with $1000/T$ is a straight line and has a negative slope using the regression method. According to Equation 5.5 the activation energies are 171.24 kJ/mol for Fe25Al and 209.16 kJ/mol for Fe45Al. The difference between them could be explained by the fact that Fe45Al has more Fe_2O_3

content, and thus forms a thicker product layer on the surface resulting in a higher diffusion resistance. As a result, Fe45Al delivers a higher activation energy value and a lower reduction rate.

5.5 Discussion

The reduction of Fe₂O₃/Al₂O₃ with low concentration methane was conducted over the temperature range of 973–1073K in TGA. The reduction conversion with time was quite dependent on the reaction temperatures. With temperatures increasing, the time for the conversion of Fe₂O₃ to FeAl₂O₄ shortens. Considering the transformation of Fe₂O₃ into FeAl₂O₄ as a two-stage process, the initial stage was the reduction of Fe₂O₃ to Fe₃O₄ with a high reaction rate while in the later stage Fe₃O₄ continued reducing to FeAl₂O₄ with a slow reaction rate. Also, the initial stage was less temperature sensitive than the followed one.

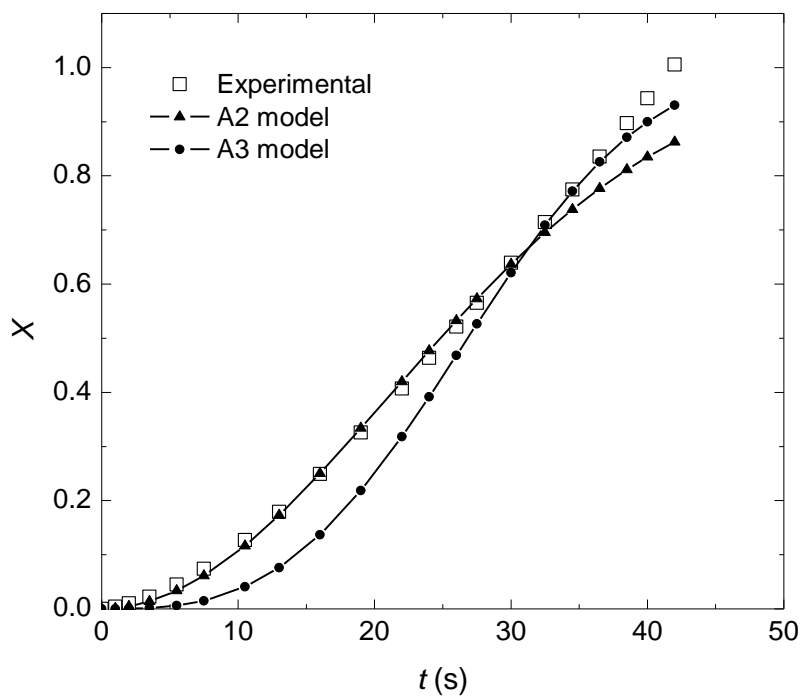
The reduction mechanism was analysed to facilitate the reactor design and energy consumption estimation. Hancock and Sharp's method was then used to determine the rate controlled mechanism for the reduction. Based on the m values from the regression calculation, the reduction rate was first controlled by phase change mechanism at the initial stage followed by the diffusion mechanism. The 2-D nuclei growth model was successfully applied to describe the heterogeneous reaction, which was closely coupled with the phase change from rhombohedra Fe₂O₃ to cubic Fe₃O₄. In fact, at low conversion the calculation results agreed with the experimental data very well. However, with the conversion, increasing the difference between the model and experimental results was more significant and the experimental values were higher than those predicted ones. The underlying reason for this is that the obtained m values are calculated with X values within the range of 0.15–0.50. To solve this issue, a topochemical approach was introduced and applied according to Piotrowski's study [104]. With this approach, Hancock and Sharp's method was applied to determine the m values for the conversion within the range of 0.6–0.9 as summarised in Table 5.8. As can be found, the m values were increasing to 2.89 ± 0.10 for Fe25Al and 2.81 ± 0.13 for Fe45Al at the higher conversion, because these m values were close to $m=3$ for the A3 model, which was used to fit the experimental data instead of the A2 model. The

comparison of experimental data with results from A2 and A3 models is presented in Figure 5.9. As expected, the A3 model predicts the experimental data better at high conversion while A2 is a better model for the low conversion. It means that the reaction mechanism has a shift from 2-D nuclei growth to 3-D nuclei growth. It can be explained by the fact that the nuclei is small and unstable at the initial stage which leads to a low growth rate, with the time increasing the nuclei grows and has a larger radius so that a higher growth rate is obtained.

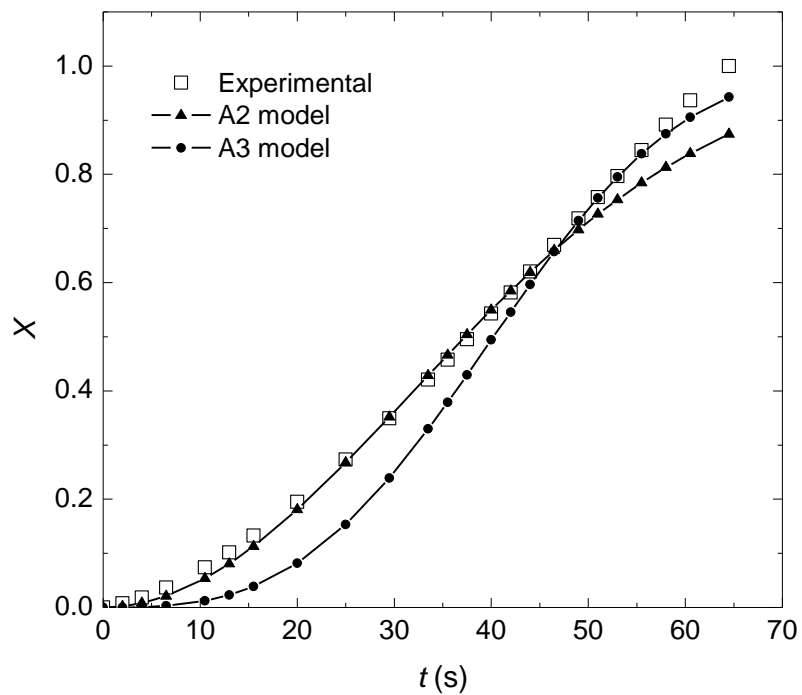
Table 5.8: *m* value for Fe₂O₃-Fe₃O₄ within the conversion range of 0.6-0.9.

T(K)	Fe25Al		Fe45Al	
	<i>m</i>	<i>r</i>	<i>m</i>	<i>r</i>
973	2.981	0.984	2.577	0.989
998	2.982	0.987	2.813	0.993
1048	2.794	0.989	2.897	0.985
1073	2.932	0.987	2.937	0.982

Two different oxygen carriers were used in the current study to conduct the reduction kinetic mechanism analysis. The only difference between them was on weight content of Fe₂O₃ on Al₂O₃, 25 wt% (Fe25Al) and 45 wt% (Fe45Al) respectively. It can be concluded that the reaction was controlled by the same kinetic mechanism for the weight content range 25–45%. For these samples, the reduction of Fe₂O₃ to Fe₃O₄ can be described by nucleation and growth model while Fe₃O₄ into FeAl₂O₄ by diffusion model. It also can be found that the weight content made a dramatic impact on the rate constant value (refer to Table 5.3 and Table 5.6) and as such the reactivity, i.e. the lower the weight content, the higher the reduction rate. With respect to the activation energy, the effect of weight content is insignificant. The obtained activation energies in this study are summarised in Table 5.9 and compared with the findings of other investigations reported in the literature. It should be noted that the values of the activation energy observed here are comparable with those published data in the open literatures.



(a)



(b)

Figure 5.9: Comparison of experimental data with A2 model and A3 model results for the reduction of Fe_2O_3 to Fe_3O_4 with samples: (a) Fe25Al and (b) Fe45Al at temperature 1073 K.

Chapter 5: REDUCTION KINETICS OF Fe₂O₃ BY ULTRA-LOW CH₄

Table 5.9: Summary of activation energy in this study and literature.

Gas	Solid	Reduction step	Temperature range (K)	Activation energy (kJ/mol)	Reduction mechanism	Ref.
CH ₄	25 wt% Fe ₂ O ₃ /Al ₂ O ₃	Fe ₂ O ₃ -	973–1073	24.96	Nuclei growth	Current study
		Fe ₃ O ₄		171.24	Diffusion control	
CH ₄	45 wt% Fe ₂ O ₃ /Al ₂ O ₃	Fe ₂ O ₃ -	973–1073	24.77	Nuclei growth	
		Fe ₃ O ₄		209.16	Diffusion control	
CH ₄	Fe ₂ O ₃	Fe ₂ O ₃ -	1073–1173	271	Diffusion control	Go et al. [102]
		FeO				
CH ₄	45 wt% Fe ₂ O ₃ /Al ₂ O ₃	Fe ₂ O ₃ -	873–1223	49	Phase boundary control	Abad et al. [73]
		Fe ₃ O ₄				
CH ₄	Hematite	Fe ₂ O ₃ -	973–1098	39.3	Nuclei growth	Monazam et al. [101]
		Fe ₃ O ₄ -		34.4	Topochemical	
CO	Hematite	FeO	1023–1173	122.52	Phase boundary control	
		Fe ₂ O ₃ -				
H ₂	Hematite	Fe ₂ O ₃ -		28.08		
		FeO				
CO	Iron ore	Fe ₂ O ₃ -Fe	973–1373	14.98-28.92	Diffusion control	Nasr et.al [109]
H ₂	Fe ₂ O ₃	Fe ₂ O ₃ -	573–1173	89.1	First order reaction	Lin et al. [110]
		Fe ₃ O ₄		70.4	Nuclei growth	

5.6 Conclusions

The reaction kinetics of Fe₂O₃/Al₂O₃ reduced by low concentration methane was evaluated with a series of isothermal TGA experiments in the temperature range of 973–1073K. Two oxygen carriers with different weight contents of Fe₂O₃ on Al₂O₃, Fe25Al and Fe45Al, were prepared and used in these reduction experiments. Topochemical approach coupled with Hancock and Sharp's method was applied to determine the rate controlled mechanism for the reduction process. The findings from this study can be summarised as follows:

- (1) The reduction of Fe₂O₃/Al₂O₃ was proved to be a two-step process, i.e. Fe₂O₃ to Fe₃O₄ with a fast reaction rate followed by a slower conversion from Fe₃O₄ to FeAl₂O₄. The later step was found to be more temperature dependent than the initial step.
- (2) The reduction mechanism for the transformation of Fe₂O₃ into Fe₃O₄ can be described by the Avrami-Erofe'ev phase change model, A2 model for low conversion and A3 model for high conversion. The activation energies are found to be 24.96 kJ/mol for Fe25Al and 24.77 kJ/mol for Fe45Al.
- (3) With the continuity of the reduction to FeAl₂O₄, a thin layer is formed on the surface, the reaction mechanism shifts to diffusion control. Higher activation energies were obtained, 171.24 kJ/mol for Fe25Al and 209.16 kJ/mol for Fe45Al.
- (4) The reaction mechanism was the same for the Fe₂O₃ weight content in the range of 25–45%. However, the weight content significantly influences the rate constant (i.e. reduction reactivity).
- (5) The obtained activation energies were comparable with the observation by other investigators.

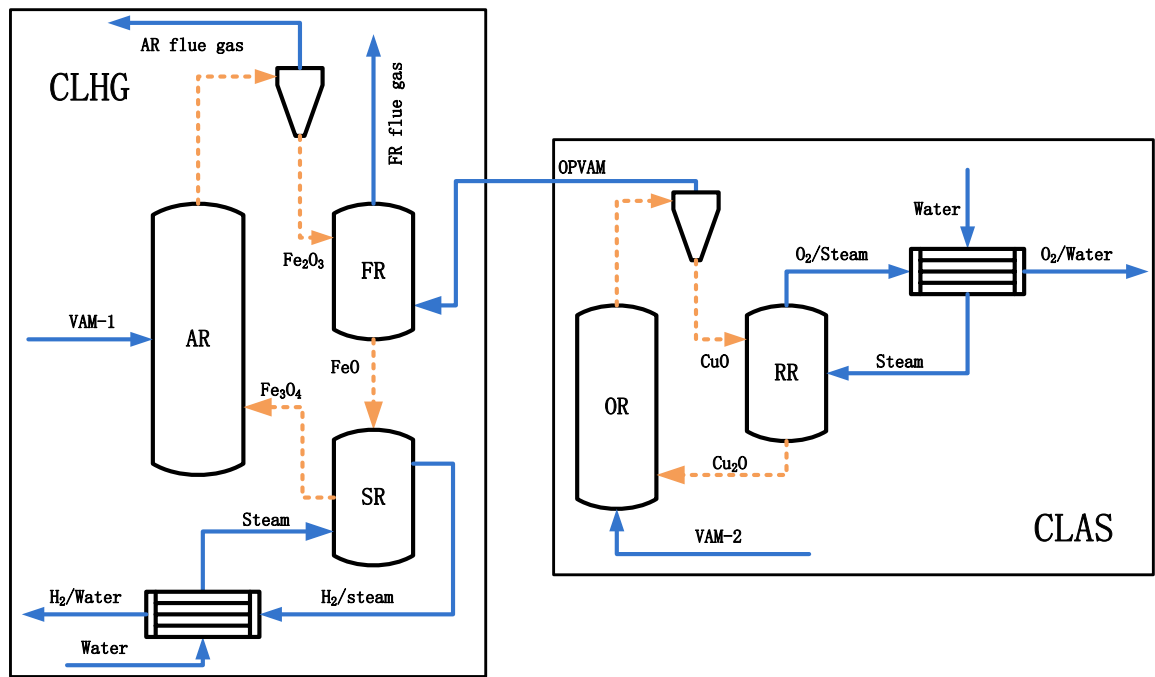
Chapter 6: CONVERSION OF VAM INTO HYDROGEN IN A DUAL-LOOP SYSTEM

6.1 Introduction

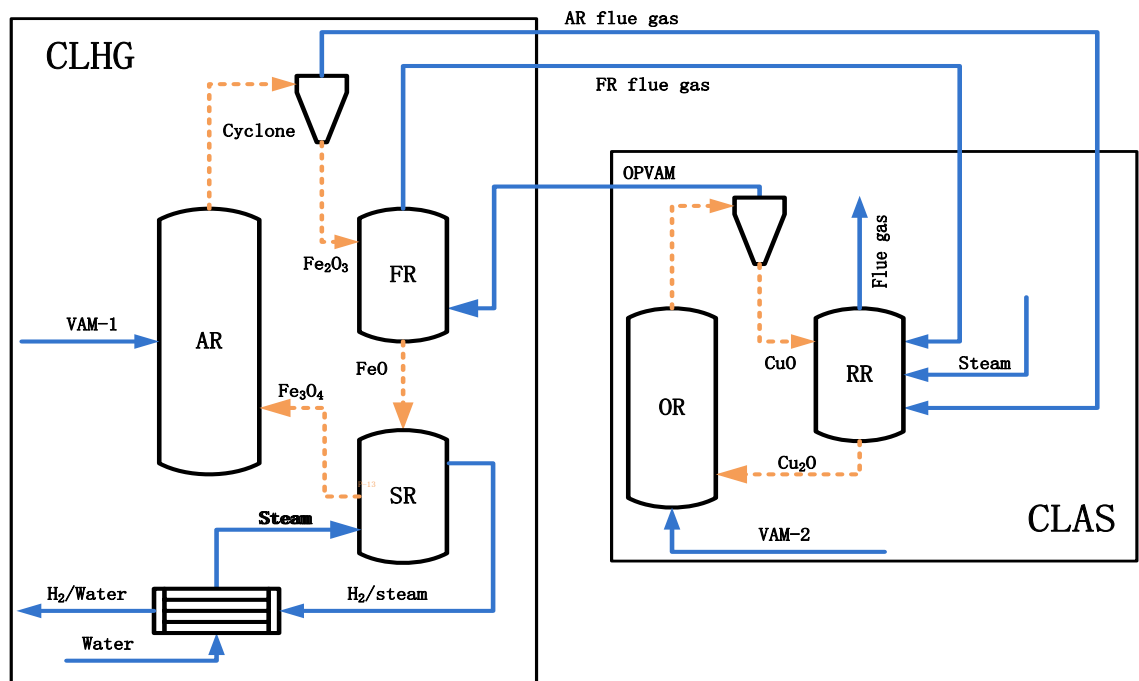
This chapter discusses the novel chemical looping based system that was developed as part of this thesis to produce hydrogen from by ventilation air methane. The feasibility of this novel system was analysed and its performance was studied thermodynamically using the commercial process modelling software: ASPEN PLUS. The materials already presented in Chapters 4 and 5 about reduction of iron oxides are of significant importance in this context.

6.2 Description of the Dual-Loop Chemical Looping Process

The proposed process consists of two reaction loops, one is for oxygen removal from VAM and the other one is to produce hydrogen with the oxygen depleted VAM (OPVAM) stream. A Cu-based chemical looping air separation (CLAS) unit is used to remove oxygen in the VAM stream and a Fe-based three-step chemical looping hydrogen production system is incorporated to reduce the methane content in OPVAM as well as producing high purity hydrogen. The detailed three-step chemical looping system for hydrogen production can be found in Chapter 7:. As illustrated in Figure 6.1, the CLAS unit is mainly comprised of two reactors, a reduction reactor (RR) and an oxidation reactor (OR). In the reduction reactor, the fully oxidised copper oxide (CuO) is decomposed into Cu_2O and O_2 with the aid of steam or oxygen depleted flue gas. The lower price copper oxide is then transported to the oxidation reactor where Cu_2O particles are oxidised to form CuO particles and the oxygen in VAM is consumed.



(a)



(b)

Figure 6.1: Flow sheet of a dual loops CLC system for reforming VAM into H_2 .

Chapter 6: CONVERSION OF VAM INTO HYDROGEN IN A DUAL-LOOP SYSTEM

The main reaction taking place in RR is a strong endothermic heterogeneous reaction (see Reaction R6.1) and occurs at around 1073 K with an extremely low oxygen partial pressure which indeed increases with the increase in temperature as shown in Table 6.1. It also can be seen that CuO is unable to release oxygen in air unless the temperature is above 1301 K, which may put a negative effect on the cyclic reactivity. According to Moghtaderi's recommendations [70], the most suitable temperature in the RR is around 1223 K at which the optimised reactivity and stability can be achieved. In this case, steam or oxygen depleted flue gas should be used as the gas agent instead of air. In our simulation the temperature in RR is 1223K and the gas agent is preheated steam or the mixture of preheated steam and flue gas depending on whether pure oxygen is one of the final products or not. The oxygen partial pressure in the product stream is 0.043, which is close to the theoretical value (i.e. 0.045).



Table 6.1: Oxygen partial pressure at various temperatures.

T (K)	923	973	1023	1073	1123	1173	1223	1273	1323	1373
O ₂ partial pressure	0	0	0	0.001	0.005	0.015	0.045	0.124	0.313	0.736

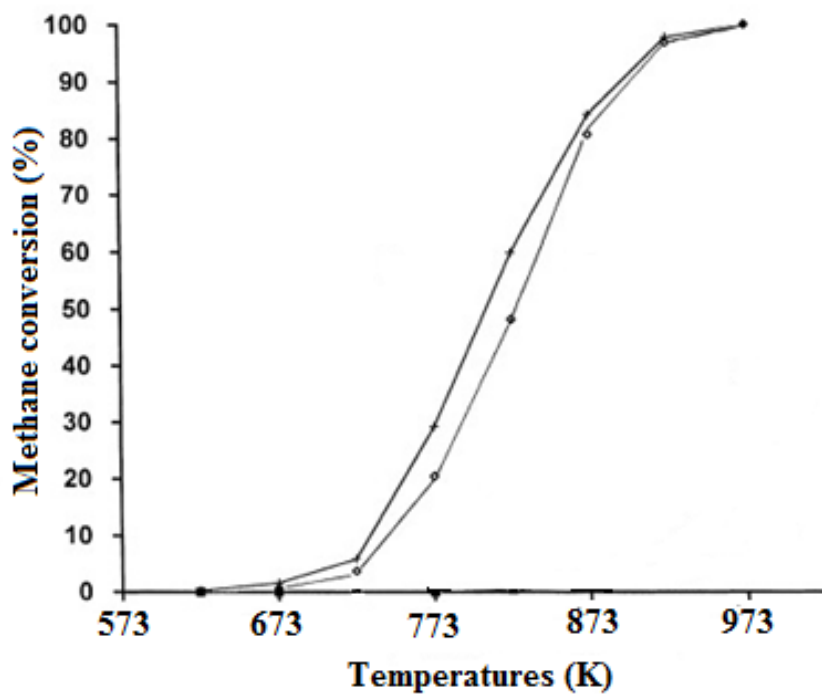


Figure 6.2: Combustion of 1 vol% methane in O₂ over CuO/MgAl₂O₄ (refer to Artizzu et al. [34]).

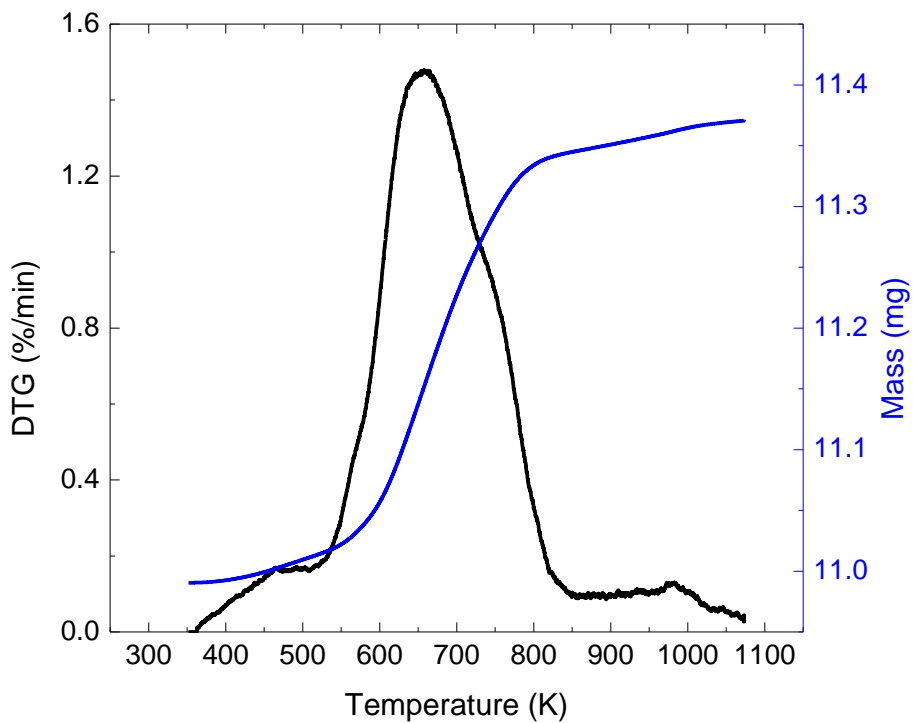


Figure 6.3: Non-isothermal oxidation of Cu₂O in air.

The reaction occurring in OR is the oxidation of Cu_2O transported from the RR unit by O_2 content in VAM stream through the backward reaction of R6.1. Given that the backward reaction of R6.1 is strongly exothermic the temperature in OR can be as high as 1073 K. However, an appropriate temperature should be selected to prevent the occurrence of reaction between methane content with oxygen on one hand, which is normally lower than 673 K due to the catalytic effect of copper oxide. The light-off curve of 1 vol% over $\text{CuO/MgAl}_2\text{O}_4$ is illustrated in Figure 6.2. It can be observed that the catalytic activity is inactive for temperatures below 673 K. Even with a temperature of 723 K, the methane conversion is below 10%. For temperatures higher than 723K, the methane conversion starts increasing dramatically with the increase in temperature and reaches 50% at 823 K and 100% at 973 K.

On the other hand, with the temperature the oxidation of Cu_2O by oxygen in VAM is able to proceed at a moderate kinetics rate. Based on our experimental result, the oxidation of Cu_2O by oxygen in air starts at the temperature around 473 K, which is in agreement with the research in the literature [111-114]. The oxidation of Cu_2O in air within a TGA setup is shown in Figure 6.3. The results show that the oxidation of Cu_2O in air is initiated at temperatures as low as 473 K. But the oxidation kinetics rate is quite low for the temperature range of 473–573 K. The faster oxidation kinetics is found within the temperature range of 573–773 K.

In light of the above analysis, the temperature in OR is given a value of 653 K. With this temperature the catalytic effect of copper oxides on the combustion of methane can be minimised while the oxidation of Cu_2O in air is able to conduct without a temperature barrier.

6.3 Process Simulation and Model

All reactors are modelled using the "RGIBBS" reactor model, which employs a Gibbs Free Energy Minimisation method to perform the relevant chemical equilibrium calculations for any given set of operational conditions. The temperature in the air reactor is 1223 K, which

is a typical temperature in AR. Most of the heat requirements can be met by the exothermic oxidation reaction and partly by the oxidation of methane in VAM which is used to substitute air as an oxidation agent. The fuel reactor (FR unit) is a two stage counter-current moving reactor (a top reactor and a bottom reactor) operated in auto-thermal condition. In the top reactor, the main reaction is the reduction of Fe_2O_3 to Fe_3O_4 , which makes it possible to achieve a complete fuel conversion. The other manner to improve fuel conversion rate to CO_2 and H_2O is to adapt excess hematite (more than the stoichiometric requirements) [61, 115]. An auto-thermal RGIBBS reactor model is used to simulate the operation of the hydrogen generator reactor (HR unit) where iron oxides can mix perfectly with steam and reach the desired equilibrium, which is around 40%. An excess air feed rate is also used to make sure the full oxidation of VAM to CO_2 and magnetite to hematite.

To evaluate the system performance, some indicators are defined as follows,

$$\eta_{\text{H}_2} = \frac{m_{\text{H}_2} \text{LHV}_{\text{H}_2}}{Q + m_{\text{CH}_4} \text{LHV}_{\text{CH}_4}} \quad (6.1)$$

$$Q_t = \frac{Q + m_{\text{CH}_4} \text{LHV}_{\text{CH}_4} - m_{\text{H}_2} \text{LHV}_{\text{H}_2}}{M_{\text{O}_2} \times 3600} \quad (6.2)$$

$$Q_d = \frac{Q}{M_{\text{O}_2} \times 3600} \quad (6.3)$$

where η_{H_2} , Q_t and Q_d are the hydrogen efficiency in %, total energy needed per cubic meter O_2 in kWh/m^3 , extra energy demand per cubic meter O_2 in kWh/m^3 ; LHV_{H_2} and LHV_{CH_4} are the lower heating value hydrogen and methane; m_{H_2} and m_{CH_4} are the mass flow of hydrogen product and input methane in kg/s . Q is the extra energy demand in MW. M_{O_2} is the mole flow of O_2 product.

6.4 Case Study

A case study was carried out to examine the system performance based on the following assumptions listed in Table 6.2.

Table 6.2: Assumptions and operation parameters.

O₂ removal unit	
Reduction reactor (RR)	Temperature~1223K, P _{O₂} ~0.043bar
Oxidation reactor (OR)	Temperature~653K, Cu ₂ O/CuO=1:4
VAM flow rate	1000 m ³ /s
CH ₄ concentration	0.5 vol%
H₂ generation unit	
Air reactor (AR)	Temperature~1223K, air excess ratio~1.4
Fuel reactor (FR)	Autothermic, OCs excess ratio~2
Hydrogen generator (HR)	Autothermic, steam conversion~40%
Oxygen carriers	Fe ₂ O ₃ -Fe ₃ O ₄ -Fe _{0.947} O supported by 80 wt% Al ₂ O ₃
Gas cooling temperature	323K

Table 6.3: Case study results.

	With O₂ product	Without O₂ product
Fuel reactor-top	Temperature~1188K, Fe ₂ O ₃ /Fe ₃ O ₄ =2.5:1, fuel conversion~100%	
Fuel reactor-bottom	Temperature~1078K, Fe ₃ O ₄ /Fe _{0.947} O=1.3:1, fuel conversion~63.5%	
Hydrogen generator	Temperature~1079K, H ₂ /H ₂ O=2:3	
Cu ₂ O flow rate	3645 kg/s	
Fe ₂ O ₃ flow rate	1463 kg/s	
VAM-1	50.8 m ³ /s	
VAM-2	1000 m ³ /s	
H ₂ O-1	9.1 kg/s	
H ₂ O-2	3365.4 kg/s	2970 kg/s
H ₂ production	0.2 kmol/s	0.2 kmol/s
O ₂ production	8.5 kmol/s	0
Extra energy needed	0.254 MW/m ³ VAM	/
Energy output	/	0.031 MW/m ³ VAM
H ₂ efficiency	11.1%	35.1%
Q _t (kWh/m ³ O ₂)	0.57	/
Q _d (kWh/m ³ O ₂)	0.39	/

The results of a case study for methane concentration~0.5 vol% are summarised in

Table 6.3. The results demonstrates that at a VAM flow rate of $1000 \text{ m}^3/\text{s}$, the circulation rate of Cu_2O is 3645 kg/s and Fe_2O_3 is 1463 kg/s , VAM flow rate to AR $50.8 \text{ m}^3/\text{s}$, water steam feed rate to HR 9.1 kg/s , while H_2 production is 0.4 kg/s , and the water steam feed rate to RR is quite dependent on the system configuration. In this case, the auto-thermal temperatures in top and bottom fuel reactors are 1188 K and 1078 K respectively. In bottom reactors, part of iron oxide is reduced to $\text{Fe}_{0.947}\text{O}$ with the fuel conversion of 63.5% . The remaining fuel is then oxidised in the top reactor completely to CO_2 and H_2O . In HR, $\text{Fe}_{0.947}\text{O}$ is oxidised back to Fe_3O_4 at 1079 K with a steam conversion rate of 40% to H_2 . When O_2 is a favourable product, the amount of energy needed to input is around 267.2 MW . The specific energy demand for producing O_2 is about 0.39 kWh/m^3 . It can be compared with the specific power of conventional cryogenic systems [67, 116], which typically require 0.4 kWh per cubic meters of O_2 produced. However, it should be noted that there is some energy produced in the form of H_2 and the H_2 efficiency is 11.1% . For the system configuration without O_2 product, the H_2 efficiency boosts to 35.1% with energy output of 32.6 MW .

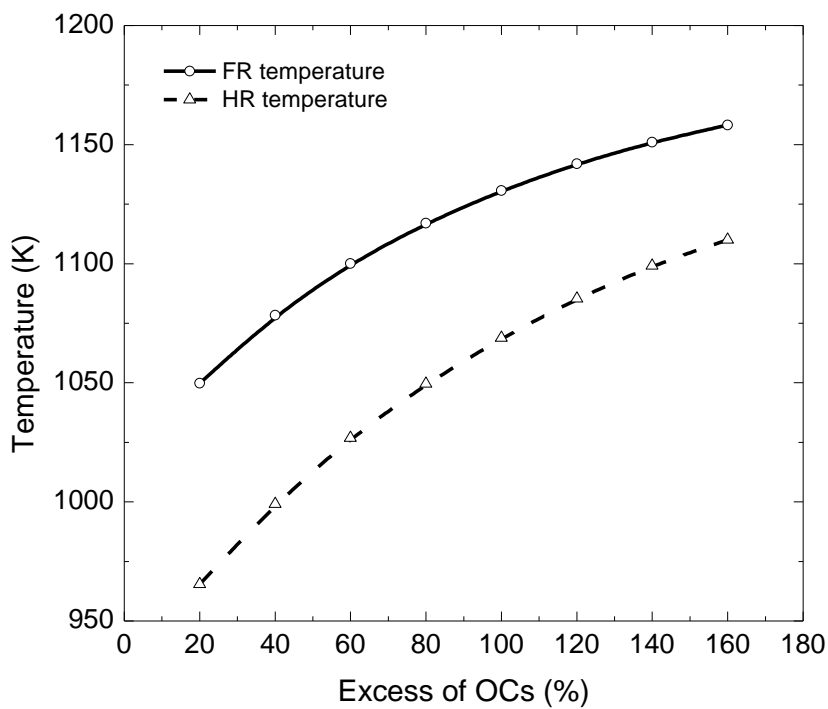
6.5 Parametric Study

6.5.1 Impact of Excess Rate of Oxygen Carrier Circulation

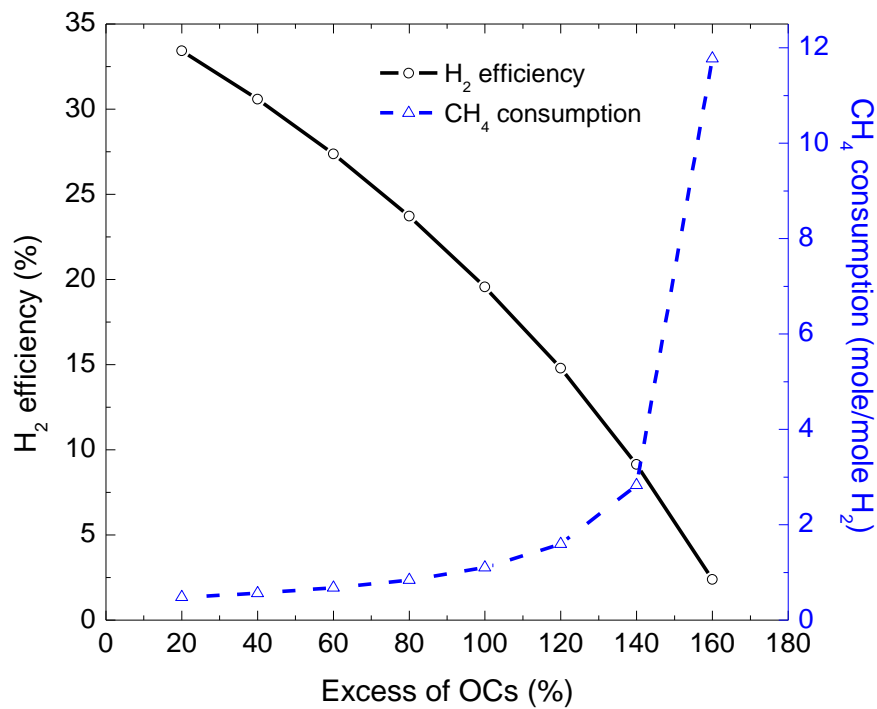
The application of excess oxygen carrier circulation rate within reactors is to maintain a high fuel conversion and neutralise the temperature in different reactors of the loop. Figure 6.4(a-c) shows the impact of the oxygen carrier circulation rate on the temperature in FR and HR, H_2 efficiency, CH_4 consumption per mole H_2 and energy requirement to produce molar unit O_2 . The temperature in FR and HR increases when increasing the oxygen carrier circulation rate. This is because more energy is brought into FR and HR from AR with a higher metal oxide circulation rate. Note that the temperature increase becomes slighter at the higher circulation rate. The more noticeable impact by the circulation rate is the variation in H_2 efficiency and energy requirements to produce unity of O_2 as shown in Figure 6.4(b-c). The increase in Fe_2O_3 circulation rate leads to a decrease in H_2 efficiency as more Fe_2O_3 shuttled within reactors results in less $\text{Fe}_{0.947}\text{O}$ produced in FR and as such

less H_2 generated in HR. This result is also indicated by the figure of CH_4 consumption for generating unity molar H_2 , which shows that the consumption of CH_4 increases dramatically for oxygen carrier circulation rate higher than 100%. For instance, the increase in CH_4 consumption is 0.62 mole for excess of OCs increasing from 20% to 100% while it is 1.72 mole from 100% to 140%. It also should be noted that no hydrogen can be generated if the excess rate of oxygen carrier circulation is more than 160%. With the cost of H_2 efficiency, the energy requirement to produce unity O_2 decreases. Although both the total energy requirement and demanding energy are decreasing when increasing the oxygen carrier circulation rate, the decrease in demanding energy is more significant being around $0.4 \text{ kWh/m}^3 O_2$ which is almost 6 times of the value in total energy requirement. The reason for the decrease in demanding energy is explicit, i.e. the energy in the form of H_2 is decreasing on one hand while more energy input in AR from the combustion air (i.e. VAM) on the other hand. The reason for the decrease in total energy requirement is most probably due to less energy loss in HR during the production of H_2 .

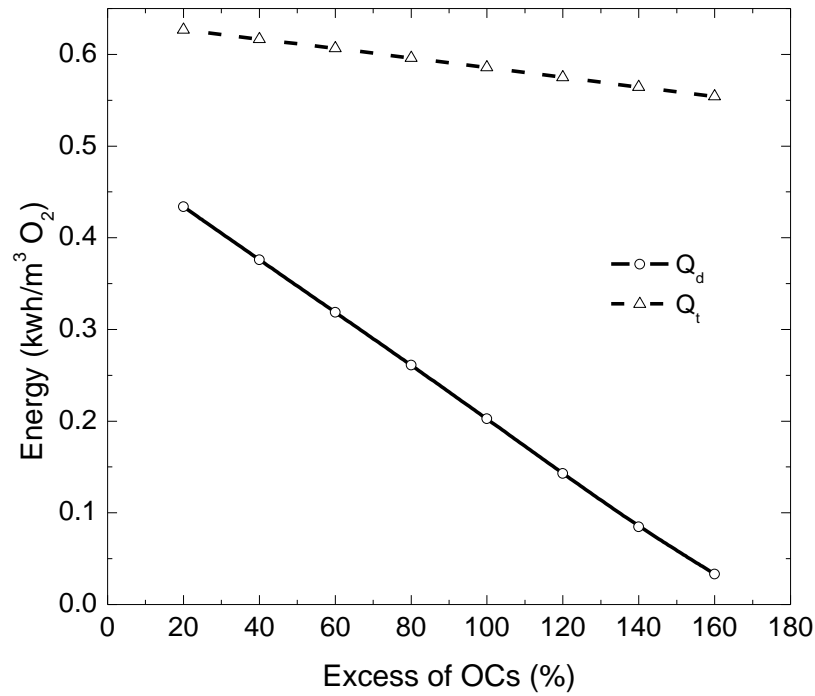
It can be concluded that increasing oxygen carrier circulation rate is a very efficient way to improve the temperature level in FR and HR as well as the energy consumption on unity O_2 . However, if H_2 efficiency is desired, it should be kept at a low level. Considering both sides 100% excess rate must be the most suitable value.



(a)



(b)



(c)

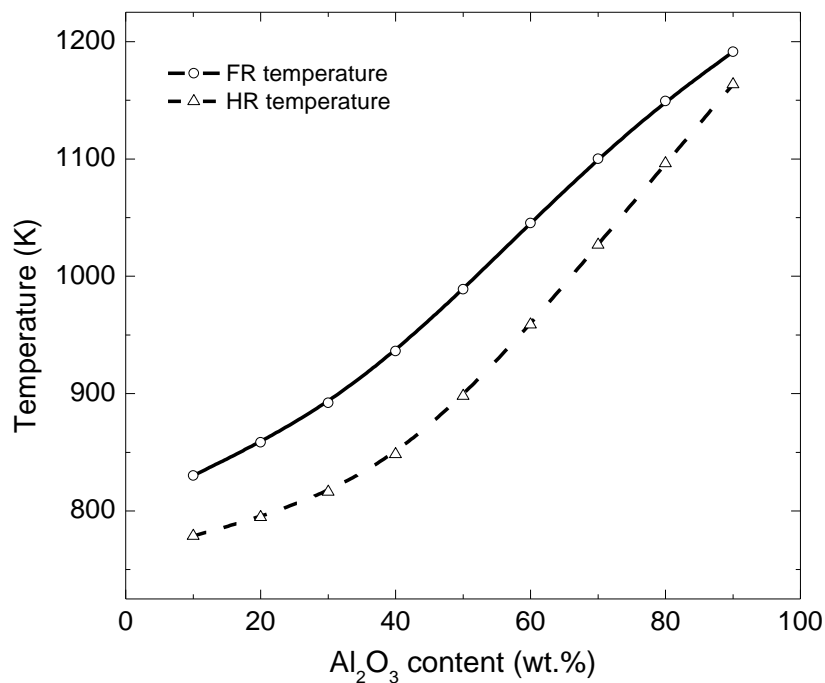
Figure 6.4: The impact of oxygen carrier circulation rate.

6.5.2 Impact of Al₂O₃ Content

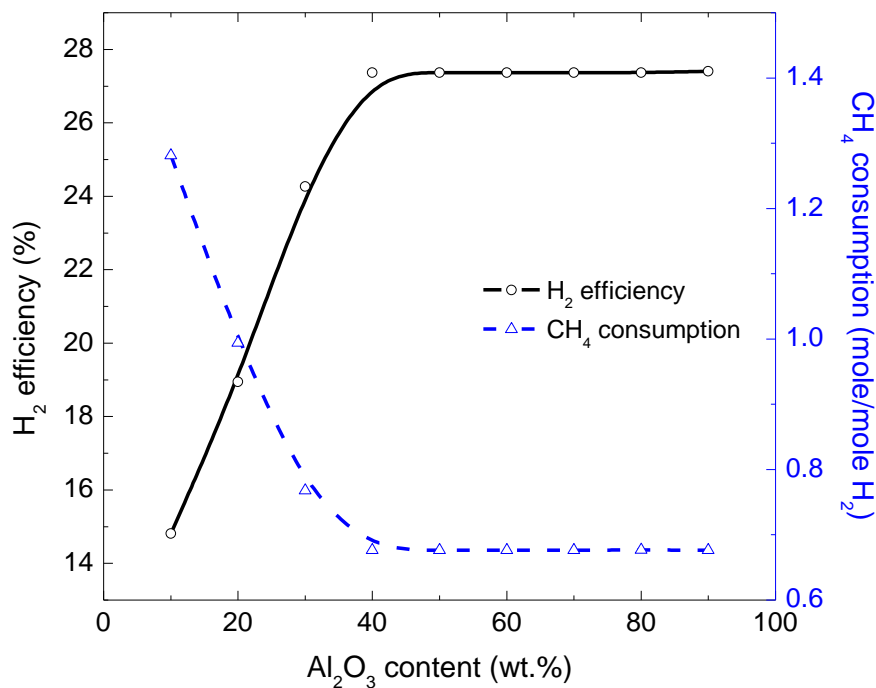
In a chemical looping system, inert support material plays an equally important role as the active metal oxides. It normally functions to improve the mechanical strength and chemical stability and the chemical activity in most cases. In fact, with the circulation of oxygen carriers between reactors the inert material also acts as the role of heat exchange medium which transfers the energy from the reactors with high-level temperatures to these with lower temperatures. In the case of this study, the energy is transferred from AR to FR and HR by both active and inert metal oxide, which is Al₂O₃. Figure 6.5(a) shows the impact of Al₂O₃ content on the temperature in FR and HR units. Obviously, the temperature in FR and HR increases when increasing Al₂O₃ weight content, especially for the Al₂O₃ content higher than 40 wt%. The results also show that the temperature difference between reactors is narrowed with higher content in inert materials. To maintain appropriate temperature levels in both reactors, which are around 1023 K for FR and 973 K for HR, the weight content of Al₂O₃ should be higher than 60 wt%. With such a high Al₂O₃ content, the H₂

Chapter 6: CONVERSION OF VAM INTO HYDROGEN IN A DUAL-LOOP SYSTEM

efficiency as well as CH_4 consumption is almost kept constant as shown in Figure 6.5(b). The increase of H_2 efficiency at Al_2O_3 content lower than 40 wt% is because the methane conversion in FR increases and reaches the full conversion at 40 wt%.



(a)



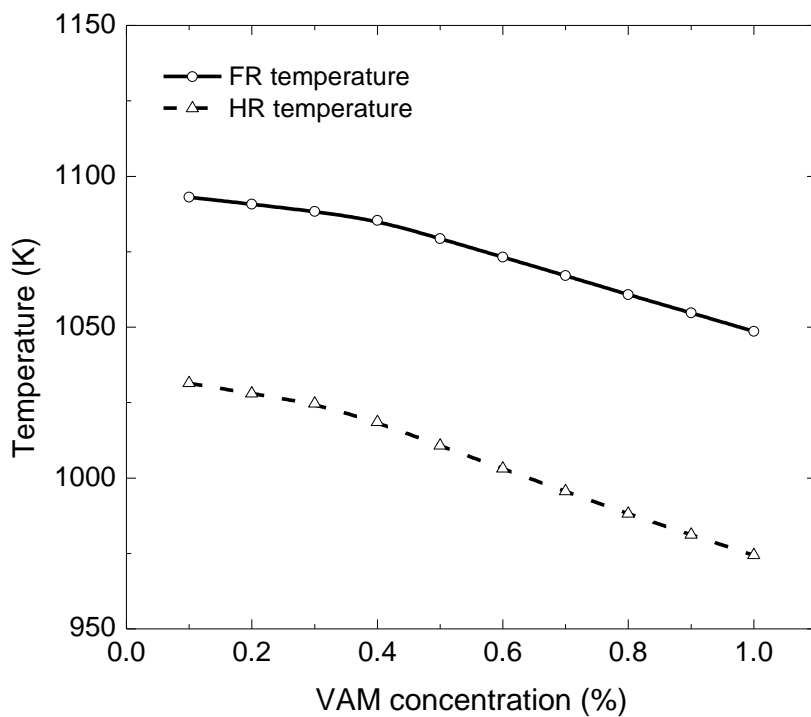
(b)

Figure 6.5: The impact of Al₂O₃ content on: (a) temperature and (b) H₂ efficiency.

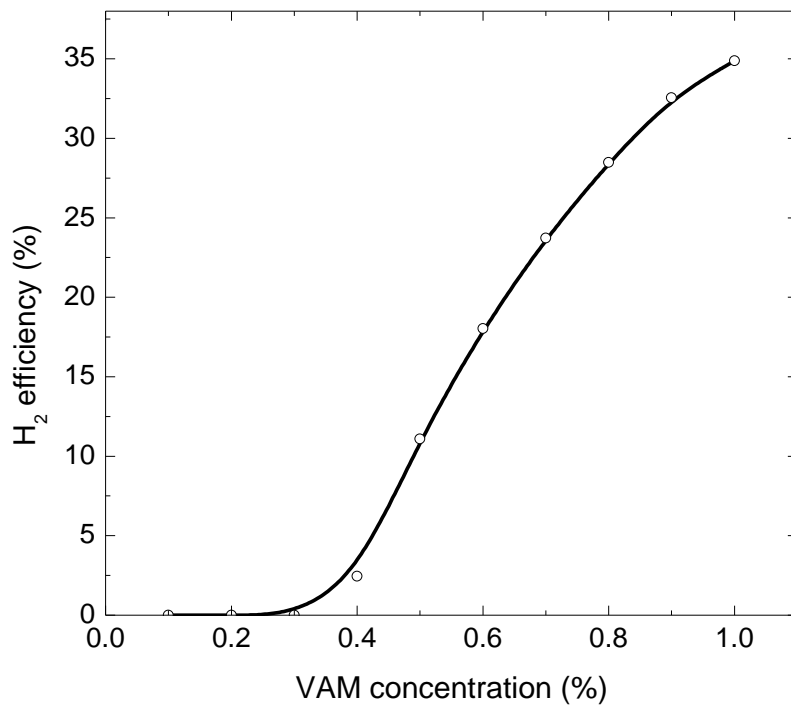
6.5.3 Impact of VAM Concentration

As stated in Chapter 2, the methane concentration in a stream of VAM is varied with time between 0.1–1 vol%. The effect of methane concentration in VAM on the temperature in FR and HR, H₂ efficiency, energy consumption and demand is shown in Figure 6.6(a–c). The thermodynamics calculations are conducted with a fixed oxygen carrier circulation rate, which is 100% excess of the stoichiometric requirement for methane concentration of 0.5 vol%. The weight content of Al₂O₃ is 70 wt%. As can be seen, the temperature in FR and HR decreases with the increase in methane concentration. This is probably because the reduction reactions of iron oxides by methane are endothermic. With the methane concentration lower than 0.4 vol% only the reduction of Fe₂O₃ to Fe₃O₄ occurs and no H₂ is generated in HR as shown in Figure 6.4(b). With the increase of methane concentration, the iron oxides are further transformed to Fe_{0.947}O and thereby H₂ is produced. This is the reason why the decrease rate in temperature is more significant at the methane concentration higher than 0.4 vol%. The H₂ efficiency is increasing exponentially with the increase of methane concentration in VAM. This can be explained by the fact that, the fuel conversion in FR decreases due to the decrease in FR temperature. In terms of the energy requirement in producing unity O₂ as shown in Figure 6.6(c), it has a strong relation with H₂ efficiency. When there is no H₂ produced, the total energy consumption keeps constant while the energy demand decreases due to more energy input from VAM. When H₂ production increases both the total energy consumption and demand increase as most of the energy is generated in the form of H₂.

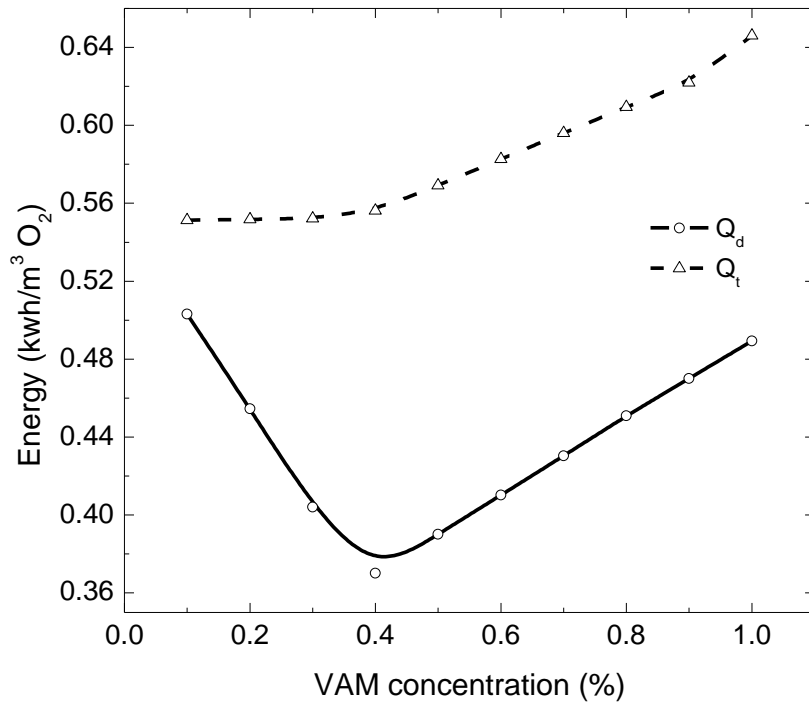
It can be concluded that the methane concentration significantly effected system performance. The higher methane concentration gives a higher H₂ efficiency but also a lower FR and HR temperature, which should improve to appropriate levels through some measurements, such as increasing the temperature in AR and Al₂O₃ content. If the temperature is improved H₂ can be produced with a methane concentration as low as 0.4 vol%. Although the temperature can also be improved by increasing the oxygen carrier circulation rate the hydrogen production will decrease correspondingly.



(a)



(b)

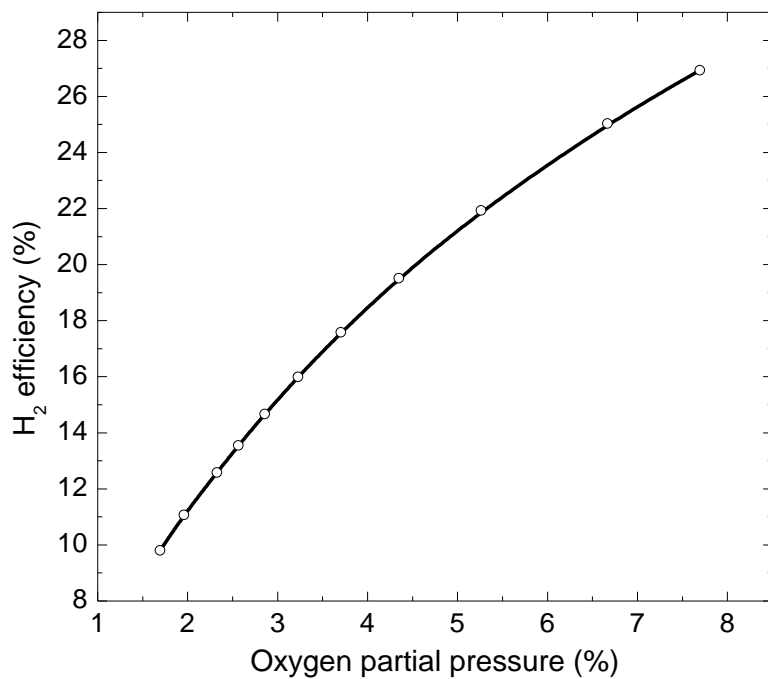


(c)

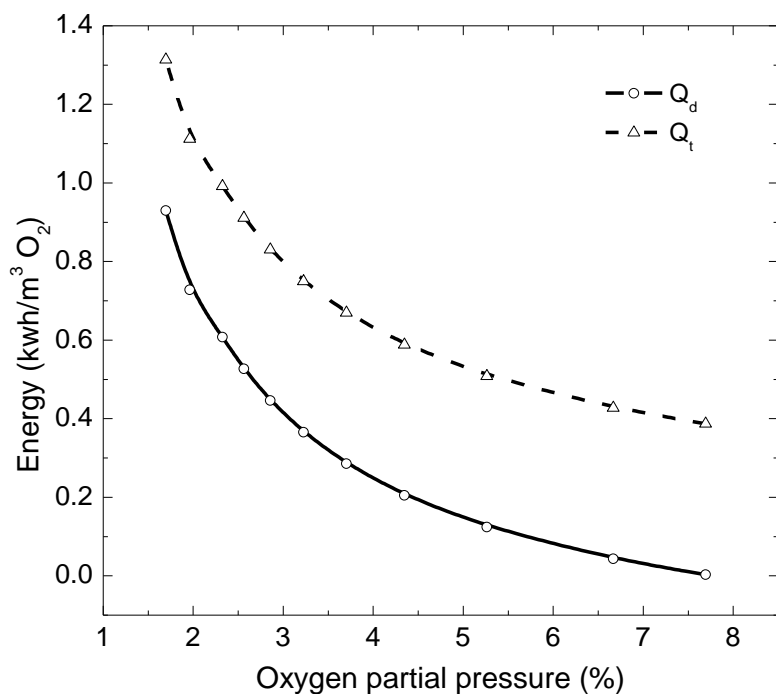
Figure 6.6: The impact of methane concentration in VAM stream.

6.5.4 Impact of Oxygen Partial Pressure in Reduction Reactor

The outlet oxygen partial pressure in the gas stream from reduction reactor (RR) varies with the reactor temperature. Within the temperature of 1173–1273 K, the oxygen partial pressure is located in the range of 1.5–12.4% (see Table 6.1). Figure 6.7 shows the effect of oxygen partial pressure on H₂ efficiency and energy consumption for unity O₂. As expected, the H₂ efficiency is increasing when increasing the oxygen partial pressure. This is because a high oxygen partial pressure indicates that less steam is needed to inject into the reduction reactor to obtain the full decomposition of CuO to Cu₂O. As a result, the energy loss in RR is reduced and the H₂ efficiency is improved. This is also why the total energy consumption and energy demand are decreasing with the increase in oxygen partial pressure. The most important finding is that there is almost no requirement for extra energy when the oxygen partial pressure is around 0.077 bar.



(a)



(b)

Figure 6.7: The effect of oxygen partial pressure on: (a) H₂ efficiency and (b) energy consumption.

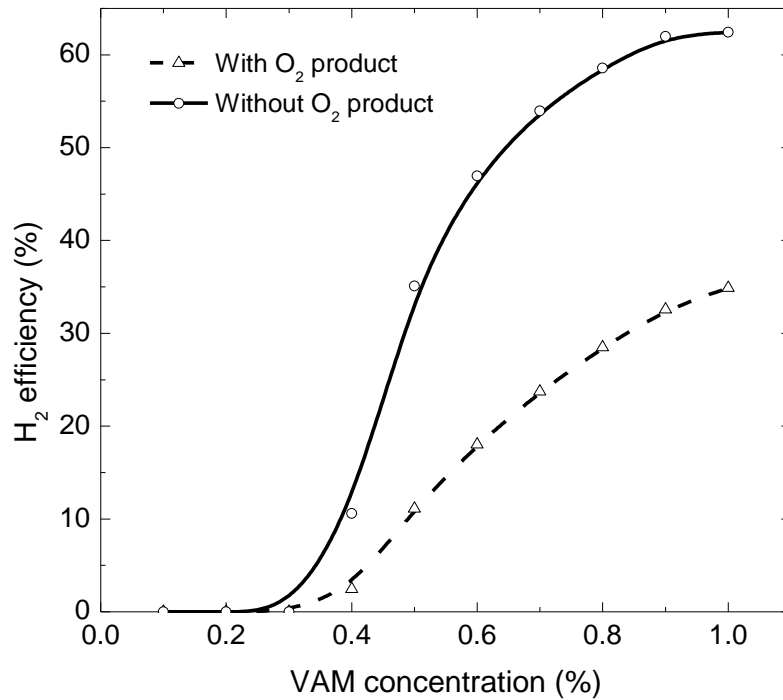


Figure 6.8: The difference in H₂ efficiency between the configurations with and without O₂ product.

6.5.5 Impact of System Configurations

If pure oxygen is not a desired product, the oxygen depleted flue gas can be used and injected to the reduction reactor other than the preheated steam. In this case, the energy loss from the water steam heating and cooling process is able to be avoided. As a result the energy efficiency can be improved and it is possible that no extra energy input is needed to match the energy requirement. Figure 6.8 shows the difference in H₂ efficiency for the system configurations with and without O₂ product at various methane concentrations. The comparison result indicates that the system without O₂ product delivers much higher H₂ efficiency and the difference becomes more significant at high methane concentration levels. For example, the difference at the methane concentration of 0.4 vol% is about 8 percentage points which is only one third of that at 1 vol% around 28 percentage points.

6.6 Conclusions

A novel integrated two loops system is proposed to mitigate ventilation air methane emission and reform the methane to pure hydrogen. In the first loop, the oxygen content in the stream of VAM is removed by a similar loop with a chemical looping air separation system (CLAS) consisting of oxidation reactor (OR) and reduction reactor (RR). The oxygen depleted VAM gas stream is then fed to a three reactors chemical looping system for hydrogen production. The feasibility of the proposed system is analysed thermodynamically and experimentally. It is found that the oxygen is able to be completely removed in the oxygen removal looping with Cu_2O as the intermediate. However, the temperature of OR should be located in the range of 573–673 K. With this condition, the reaction between Cu_2O and oxygen is conducted without kinetics barrier while the catalytic combustion of methane in air is inactive and the reduction of copper oxides by methane is inhibited as well. A case study with 0.5 vol% methane concentration in VAM is carried out to determine the system performance based on some proper assumptions. It is found that, with pure O_2 as a final product, 0.254 MW per cubic meter VAM is needed to input from external sources. The specific power demand is $0.39 \text{ kWh/m}^3 \text{ O}_2$ which can be compared with the specific power of conventional cryogenic systems. If the H_2 efficiency is considered, the specific power demand decreases by 18% to $0.32 \text{ kWh/m}^3 \text{ O}_2$. If there is no O_2 product, 0.031 MW of energy can be produced from per cubic meter VAM with a hydrogen efficiency of 35.1%. The parametric study shows that, even though the system performance is influenced by some factors, such as: oxygen carrier circulation rate, Al_2O_3 weight content, methane concentration and system configurations, etc., hydrogen can be produced with a methane concentration as low as 0.4 vol%.

Chapter 7: THERMAL OXIDATION OF HYDROGEN ENRICHED VAM

7.1 Introduction

A novel Fe-based chemical looping system was developed to mitigate the emission of ventilation air methane and utilised the produced energy. It mainly consists of two parts: a novel IGCLC process in which pure hydrogen is produced and the hydrogen product is used as the additional fuel to assist the oxidation of VAM in a gas burner, which is a so-called VAM combustor. The flow sheet diagram for the whole system is illustrated in Figure 7.1.

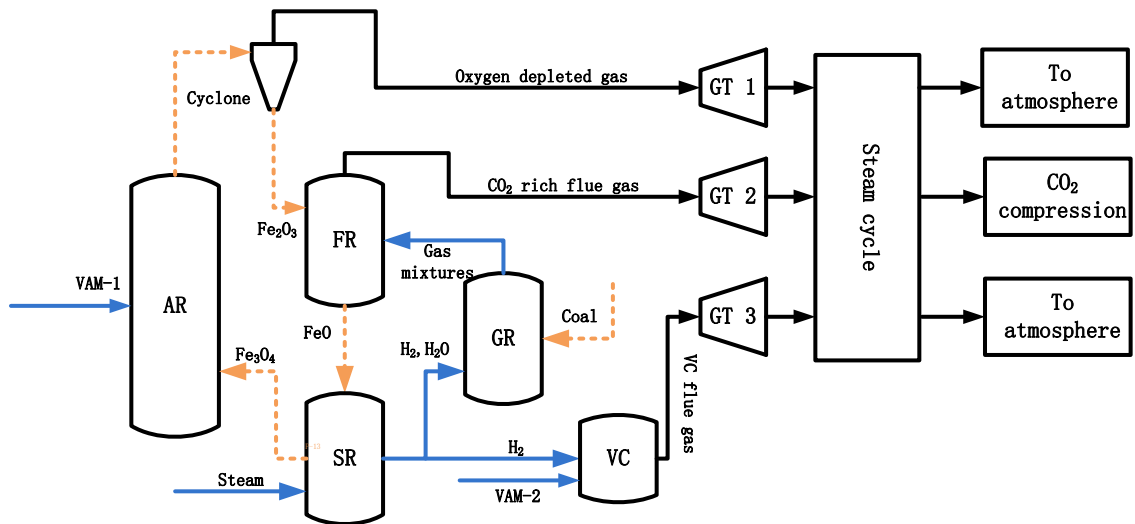


Figure 7.1: Diagram of a novel IGCLC-VC system.

7.2 A Novel IGCLC System for Producing Hydrogen

7.2.1 The Working Principle

The basic steps in the IGCLC process are:

- Generation of H₂ from steam using suitable oxygen carriers
- Fuel gasification in the presence of a H₂ / steam mixture
- Combustion of the fuel off-gas from the gasification process in the presence of oxygen carriers
- Regeneration of oxygen carriers.

The IGCLC process incorporates a three-step chemical loop to fully integrate the above steps into a unified platform. Because of the need for high purity hydrogen, the IGCLC process can work best with metals with multiple oxidation states, particularly Fe which is reasonably reactive, cheap and environmentally benign and has good mechanical and chemical stability.

As illustrated in Figure 7.1, in a Fe-based IGCLC process an equi-molar steam-hydrogen mixture is first generated in a steam reforming reactor (SR) through chemical reactions between steam and particles of wustite (FeO). The steam-hydrogen mixture is then fed into a gasifier unit (GR) where the particles of the solid fuel are gasified. The gaseous fuel mixture resulting from the gasification process then flows to a gaseous fuel reactor (FR) where fuel off-gas mixture from the gasification process (e.g. H₂, CH₄ and CO) is oxidised into CO₂ and steam by hematite (Fe₂O₃) particles. During this process, hematite is reduced to wustite, which is fed back to the SR reactor. The oxidation of wustite particles in the SR reactor result in the formation of magnetite (Fe₃O₄) as well as the steam-hydrogen mixture. The solid product from the SR reactor (i.e. magnetite) is then transported to an air reactor (AR) where magnetite particles are oxidised to form the hematite particles needed in the FR.

The IGCLC process as outlined above has several key advantages over the ex-situ, in-situ and CLOU approaches described earlier. Firstly, coal is able to transform to gaseous fuel in

a thermo-neutral manner (see Section 7.2.2 for details). As such, the gasification process does not require extra oxygen or air to generate heat by combusting a portion of coal. An ASU unit is also no longer necessary. Secondly, the direct contact between OC particles and coal is avoided in the IGCLC process and, thus, unlike the CLOU or in-situ methods the deactivation of oxygen carrier particles by carbon deposits and ash is eliminated in the IGCLC process. This would minimise the likelihood of carbon combustion and hence unwanted CO₂ formation in the AR unit, in turn, maximising the overall CO₂ capture efficiency of the system (note: that ideally the exhaust gas stream from the AR unit should only contain N₂ while that of the FR unit should be rich in CO₂).

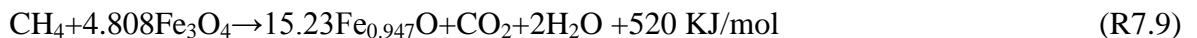
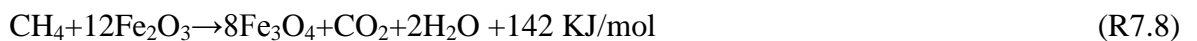
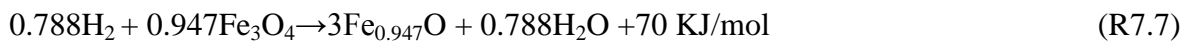
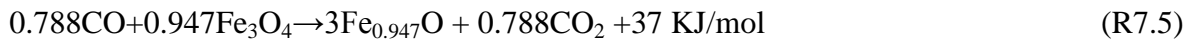
7.2.2 Key Reactions

The main gasification reactions associated with IGCLC of coal are heterogeneous exothermic methanation reaction (R7.1), heterogeneous endothermic hydrogasification reaction (R7.2), and homogeneous exothermic water-gas shift reaction (R7.3). The latter two reactions are restricted to a small extent due to the thermodynamic constraints. The dominant role of reaction R7.1 enables the gasification process to run on an auto-thermal basis, thereby eliminating the need for the addition of oxygen or external heat supply. While in general the reaction of solid carbon with carbon dioxide also takes place during coal gasification, this reaction has been ignored in the present study because the fraction of CO₂ and the reaction temperatures examined here are such that they limit the extent of the C+CO₂→CO reaction. As a result, the contribution of this reaction in the overall reaction scheme becomes very modest and, hence, this reaction can be ignored to simplify the relevant thermodynamic equilibrium calculations.



Similarly, there are six key heterogeneous reactions taking place in the FR unit between various components of the incoming gas mixture from the GR unit and particles of hematite (see Reaction R7.1 to R7.9). With the exception of reactions R7.4 and R7.6, reactions

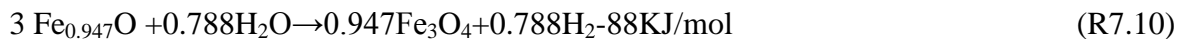
taking place in the FR unit are endothermic, requiring heat to proceed at favourable temperatures. The heat is partly provided by the circulation of oxygen carrier particles, hematite in this case, and partly by the high temperature gas mixture from the GR unit. As a result of reactions R7.4 to R7.9 in the FR unit, hematite (Fe_2O_3) is reduced to wustite ($\text{Fe}_{0.947}\text{O}$) and small quantities of magnetite (Fe_3O_4). It should be noted that FeO is a non-stoichiometric species in which the Fe to O ratio varies between 0.83~0.95. For this reason wustite (FeO) in thermodynamic equilibrium calculations is commonly represented by $\text{Fe}_{0.947}\text{O}$ [117]. Furthermore, as Bohn [95] suggested, in a chemical looping system for hydrogen production it is preferred that Fe_3O_4 reduces to $\text{Fe}_{0.947}\text{O}$ rather than Fe because: (i) the reduction to metallic iron decreases the reactivity of oxygen carriers through repeated cycles and dramatically enhances the carbon deposition, and (ii) the reduction to metallic iron needs a higher CO/CO_2 , $\text{H}_2/\text{H}_2\text{O}$ ratio than to $\text{Fe}_{0.947}\text{O}$ and, hence, takes a longer time for reduction. This, in turn, increases the reactor size and its physical dimensions. It is therefore assumed in this study that the CO/CO_2 and $\text{H}_2/\text{H}_2\text{O}$ ratios as well as the reactor size are such that the reduction of Fe_3O_4 to $\text{Fe}_{0.947}\text{O}$ is favoured.



The main reaction taking place in the SR unit is the steam reforming reaction between the wustite/magnetite particles that originated from the FR unit and steam (see Reaction R7.10). As a result of this reaction, wustite is oxidised to magnetite and steam is reduced to hydrogen. Reaction R7.10 is exothermic and thermodynamically favourable at a low temperature. A higher temperature will lead to a low steam conversion rate, i.e. a low equilibrium hydrogen concentration. For example, the equilibrium concentration of hydrogen at 1200K is 25%, which is half of that at 1000K. To keep R4.10 proceeding at an

adequate rate and obtain the desired equi-molar mixture of steam and hydrogen, the temperature of the SR unit is hereby maintained around 1000K at which the conversion rate of steam could reach 50%.

Thermodynamic calculations suggest that the steam conversion rate can reach values as high as 50% for reaction R7.10 at temperatures about 1000K although 50% is almost the upper limit according to experiment results [60]. However, given that our paper is a thermodynamic assessment of the IGCLC process, we were interested to find the performance characteristics of the process at its thermodynamic limits. To this end the results were obtained assuming a 50% steam conversion rate.



The main reaction in the AR unit is the oxidation of magnetite particles transported from the SR unit by air through reaction R7.11. Given that R7.11 is strongly exothermic the temperature of the products can be as high as 1300K. The product gas from the AR unit can be directly sent to a gas turbine (GT) or first used to preheat the mixture of steam and hydrogen recycled to the GR unit (to minimise the heat demand of the GR unit) and then directed to the GT.



7.2.3 Process Simulation and Model

Chemical equilibrium calculations for IGCLC process were carried out using the commercially available process simulation software: ASPEN PLUS. Figure 7.1 demonstrates the flow sheet diagram of the process, which mainly comprises four reactor blocks, namely: GR, FR, SR, and AR. All reactors were modelled using the "RGIBBS" reactor model, which employs a Gibbs Free Energy Minimisation method to perform the relevant chemical equilibrium calculations for any given set of operational conditions.

A well-known gasification model [118, 119] was adapted to describe the key gasification reactions. Calculations were performed for a common black coal for which the proximate

and ultimate analyses have been summarised in Table 7.1. It was assumed that unconverted carbon in the coal accounted for 5% of the total input carbon. The remaining carbon was fed with the gasifying agent into a RGIBBS type reactor where chemical equilibrium calculations for the gasification process were being undertaken (i.e. GR unit). The final product composition was evaluated by considering H₂, H₂O, CO, CO₂, CH₄, and C(s) as the main products of the gasification process. Due to importance of steam/hydrogen and carbon concentrations on the final product, composition a steam/hydrogen to carbon ratio (SHTCR) was defined and used as a parameter in the analysis. The SHTCR is expressed by:

$$SHTCR = \frac{n_{H_2O} + n_{H_2}}{n_C} \quad (7.1)$$

where n_{H_2O} and n_{H_2} are the flow of steam and hydrogen recycled to the gasifier unit (i.e. GR unit), and n_C is the carbon species input.

Table 7.1: Coal analysis

Proximate analysis		Ultimate analysis (%W/W dry basis)	
Volatiles (%w/w dry)	34.1	C	74.1
Fixed carbon (%w/w dry)	58.5	H	4.47
Moisture(%w/w)	5.4	O	9.43
Heating values		N	1.19
HHV (KJ/kg dry)	29 806	S	3.41
LHV (KJ/kg wet)	27 000	Ash	7.4

The fuel reactor (FR unit) was simulated by a two stage counter-current moving reactor model where gas fuel can almost be fully converted [60]. To achieve a complete oxidation of fuel gases to CO₂ and H₂O, excess hematite (more than the stoichiometric requirements) was applied [61]. It was found that the full conversion of gaseous fuel could be reached at 1100K or above for 1% excess hematite. Given that the excess hematite (Fe₂O₃) could not be reduced to Fe_{0.947}O, the solid product stream from the FR unit was determined to be a mixture of 95% Fe_{0.947}O and 5% Fe₃O₄ (mole percentage) based on the equilibrium calculations.

A RGIBBS reactor model was also used to simulate the operation of the hydrogen generator reactor (SR unit) where iron oxides can mix perfectly with steam and reach equilibrium at desired operating temperatures. A reaction temperature of 1000K was selected for the operation of SR as noted in Section 7.2.2. As shown in Figure 7.1 a fraction of steam/hydrogen mixture is fed into the GR unit while the excess can be used to produce pure hydrogen after condensing water. The net hydrogen product is expressed by:

$$n_{H_2} = n_{total} - n_{rcy} \quad (7.2)$$

where n_{H_2} is the molar amount of hydrogen produced as the final product, n_{total} is the total molar amount of hydrogen produced in the SR unit and n_{rcy} is the moles of hydrogen transported into the GR unit.

7.2.4 Gasification Reactor (GR) Unit

The viability of the gasification process in the GR unit is largely underpinned by its heat demand (i.e. overall endothermicity or exothermicity), carbon conversion and product gas composition. Generally, gasification of coal is endothermic. However, adding hydrogen into the feed steam promotes the exothermic methanation reaction (R7.1) enabling the gasification process to become auto-thermal. Figure 7.2 illustrates the variations of thermo-neutral temperatures of the GR unit with SHTCR (1~3) and feeding gasification agent temperature T_{Feed} (1000~1100 K). It is observed that the gasification temperature is increased due to an increase in the SHTCR and the temperature of the steam/hydrogen feed. The lowest gasification temperature is just above 1030K at SHTCR~1 and a steam/hydrogen feed temperature of 1000K, while the highest gasification temperature is above 1080K corresponding to a SHTCR~3 and a steam/hydrogen feed temperature of 1100K. The auto-thermal gasification process can operate at temperature in excess of 1023K at a fixed pressure of 70 bar when SHTCR is between 1 and 3 and the steam/hydrogen feed temperature is about 1000K.

With regards to carbon conversion which is generally influenced by the reaction rate, residence time and the gasifying agent (e.g. SHTCR in the IGCLC process), it is shown

here that reasonably high conversions can be achieved in the GR unit. The carbon conversion for the IGCLC process can be expressed by the following equation:

$$\varphi_c = 1 - \frac{n_{ubc}}{n_c} \quad (4.3)$$

where n_{ubc} and n_c are the molar amounts of the unburnt carbon in the GR unit and the carbon in the GR's feed stream.

Since the simulation here is based on the chemical equilibrium approach, the residence time is long enough for the reaction to reach the equilibrium status. Also, it is assumed that when the reaction temperature is above 1023K the reaction rate is fast enough to enable the gasification process to reach its thermodynamic equilibrium even at short residence times. That is why the gasification temperature appears to have a negligible impact on the conversion of carbon (Figure 7.2). As shown in Figure 7.2, the carbon conversion linearly rises to about 0.95 when SHTCR is increased from 1 to 2. At SHTCR values greater than 2, the carbon conversion levels off at 0.95 which is consistent with experimental data [120] (98%) obtained from gasifiers with similar features to the GR unit. The key conclusion here is that the SHTCR has to be at least ~2 to achieve a high carbon conversion (~95%). While at these temperatures (~1023K) the reaction rate might be slow, according to US patent US3847567 [120], coal hydrogasification with a mixture of steam and hydrogen can be carried out over alkali metal catalysts (such as potassium carbonate) at temperatures ranging from 930~1088K and pressure from 35~70 bar without sacrificing high reaction rates. As noted also by Wen [121] the key here is that the reaction rate in hydrogasification of coal is not only a function of temperature but also hydrogen pressure. Therefore, combining high temperatures with high H₂ pressures similar to what has been considered in this study would inevitably improve the reaction rate and hence carbon conversion to reasonably high levels.

As noted earlier, the composition of the product gas from the GR unit is also of significance in the successful operation of an IGCLC type system. The product gas from the GR unit is a mixture of gaseous species such as H₂, H₂O, CO, CO₂ and CH₄, which flows to the FR unit where reduction of hematite takes place. This reduction process can significantly

benefit from high selectivity towards the formation of H₂ and CO (i.e. synthesis gas formation). This can be best expressed in terms of molar ratios such as [CO+H₂]/CH₄, H₂/H₂O or CO/CO₂. A high synthesis gas selectivity (i.e. high ratio of [CO+H₂]/CH₄) lowers the endothermicity as the reduction of hematite by CO or H₂ (R4.4 and R4.6) can be exothermic (depending on reaction temperatures) whereas the hematite reduction by CH₄ (R4.8 and R4.9) is strongly endothermic. Also, the transition of hematite to wustite favours the high hydrogen to steam selectivity (i.e. high H₂/H₂O molar ratio) or high carbon monoxide to carbon dioxide selectivity (i.e. high CO/CO₂ molar ratio). According to our thermodynamic analyses and those of Piotrowski et al., [103] the reduction of Fe₃O₄ to Fe_{0.947}O occurs only for CO/CO₂ >0.627 or H₂/H₂O >0.612 at 1100 K. Moreover, as noted by Piotrowski et al. [103] from a series of experimental studies a higher CO/CO₂ or H₂/H₂O ratio enhances both reactivity and conversion of the reduction to Fe_{0.947}O. Figure 7.3 shows plots of synthesis gas to methane selectivity (i.e. [CO+H₂]/CH₄), hydrogen to steam selectivity (i.e. H₂/H₂O) and carbon monoxide to carbon dioxide selectivity (i.e. CO/CO₂) against SHTCR at three different GR feed temperatures (i.e. the temperature of hydrogen/steam feed to the GR unit). The plots corresponding to the [CO+H₂]/CH₄ selectivity show a modest rise at SHTCR smaller than 2 but at SHTCR greater than 2 a dramatic rise is observed at all GR feed temperatures; with the plots corresponding to higher GR feed temperatures showing steeper slopes. This is partly due to the impact of SHTCR (i.e. higher hydrogen to carbon) and partly because R7.2 favours high temperatures while R7.1 low temperatures. The plots corresponding to the H₂/H₂O selectivity show peaks at or about a SHTCR of 2. Similarly, plots associated with the CO/CO₂ selectivity show peaks but they plateau at SHTCR values greater than 2 despite showing a relatively rapid rise over the range of SHTCR values between 1 and 2. Although the variations in product selectivity due to SHTCR are diverse, for any given selectivity ratio the GR feed temperature appears to have a similar impact; that is the highest selectivity is always achieved at the highest GR feed temperature.

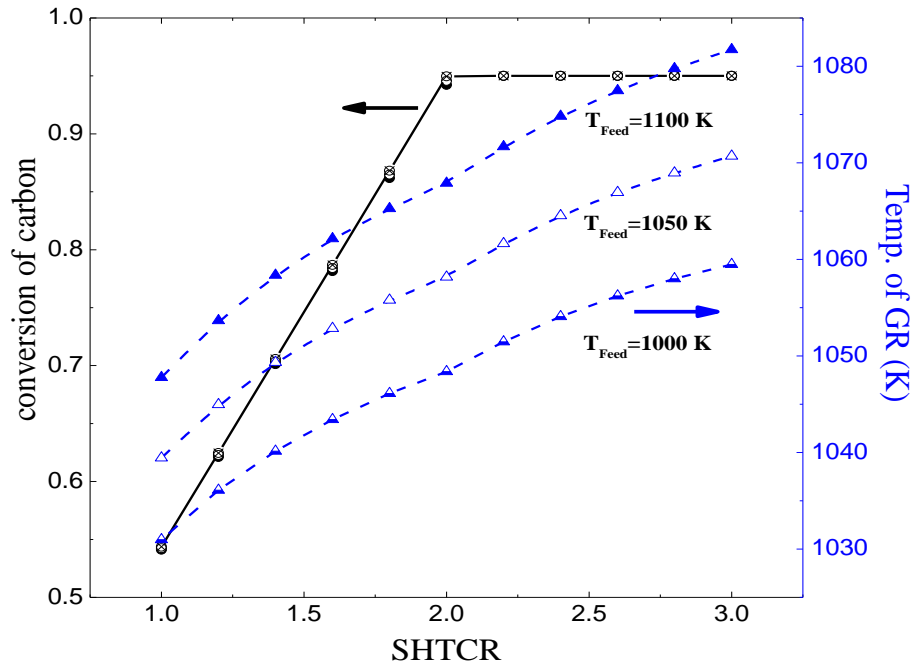


Figure 7.2: Gasification temperature and carbon conversion in the GR unit.

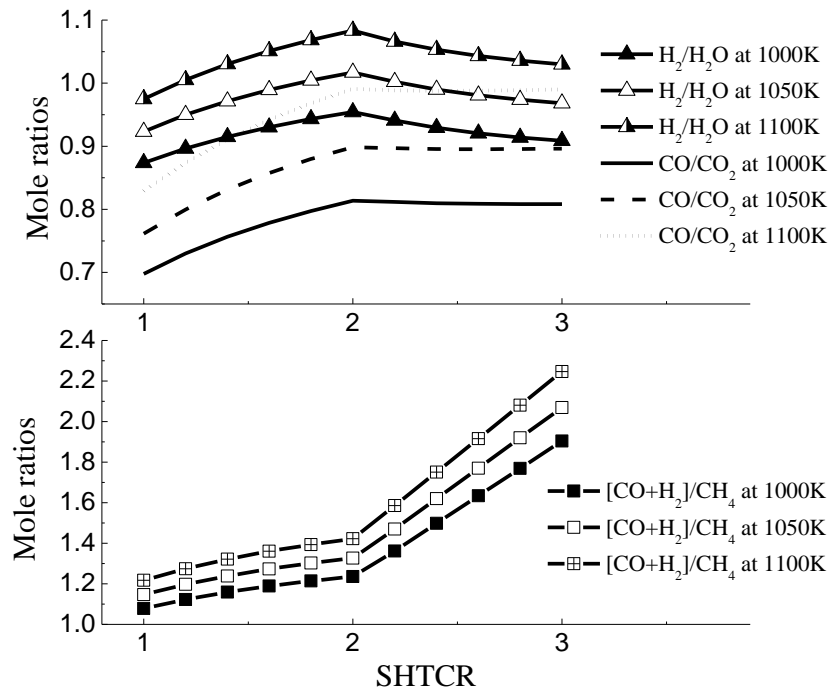


Figure 7.3: Plots of product selectivity as a function of SHTCR and T_{Feed} .

7.2.5 Fuel Reactor (FR) Unit

The temperature of the FR unit is critical to the reduction of hematite. A high FR temperature not only enhances the reduction reactivity but also promotes the conversion of hematite to wustite. However, excessively high FR temperatures (>1300 K) may lead to sintering of metal oxide oxygen carrier particles; detrimentally impacting on their redox properties [122]. Figure 7.4 shows the variations of the FR and AR temperatures as a function of SHTCR and the GR feed temperature. Ideally, the temperature of the FR unit should increase with an increase in the GR feed temperature. However, the rapid growth in the quantity of CH_4 formed in the GR unit over SHTCR values between 1 and 2, plus the strong endothermic reaction between methane and hematite create some level of endothermicity in the FR unit; lowering its temperature. As can be seen from Figure 7.4 the impact of methane formed in the GR unit on the FR temperature diminishes at SHTCR values greater than 2 because the amount of CH_4 formed in the GR unit levels off whilst more synthesis gas is formed at $\text{SHTCR} > 2$ (see also $[\text{CO}+\text{H}_2]/\text{CH}_4$ plots in Figure 7.3). With respect to the amount of CH_4 , although a high reaction temperature prompts the reaction R7.1 backward, the added hydrogen enhances the forward reaction. This can partly explain why the amount of CH_4 levels off at $\text{SHTCR} > 2$ where the input carbon has been fully converted.

The AR temperature also shows a slight declining trend over the range of SHTCR between 1 and 2 (see Figure 7.4). The reason for this slight decrease is that the wustite content of the solid mixture fed into the AR unit decreases gradually as the level of steam used to oxidise the iron sulphide diminishes. It is possible to operate FR with a temperature between 1100 K and 1200 K under a self-sustainable thermal condition. The feasibility of using the AR flue gas to preheat gasification agent stream to 1100 K can be also accomplished because the flue gas temperature is always above 1270 K (assuming the temperature gap between cold side and hot side is 100 K).

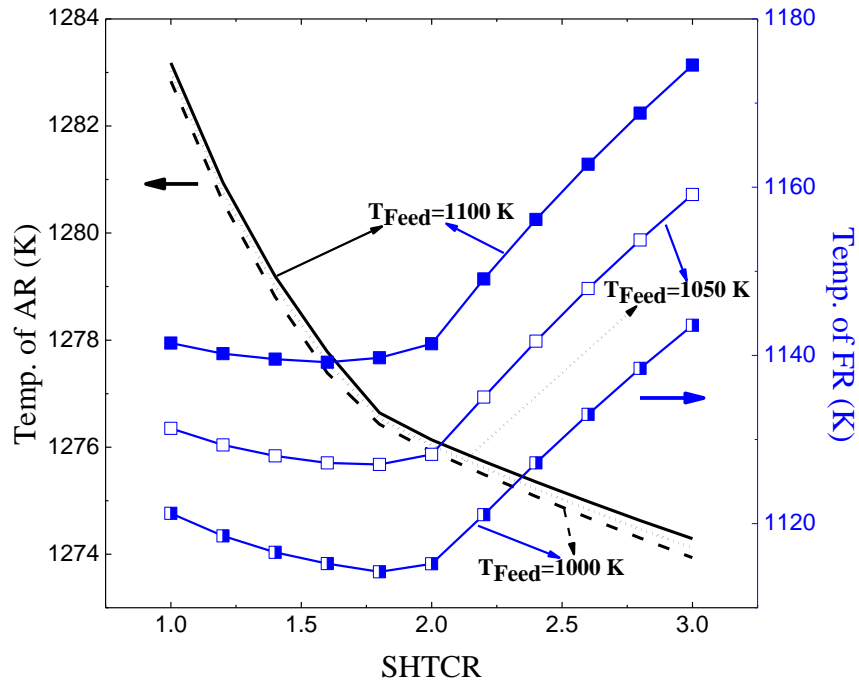


Figure 7.4: Variations of the FR and AR temperatures with the SHTCR and T_{Feed} .

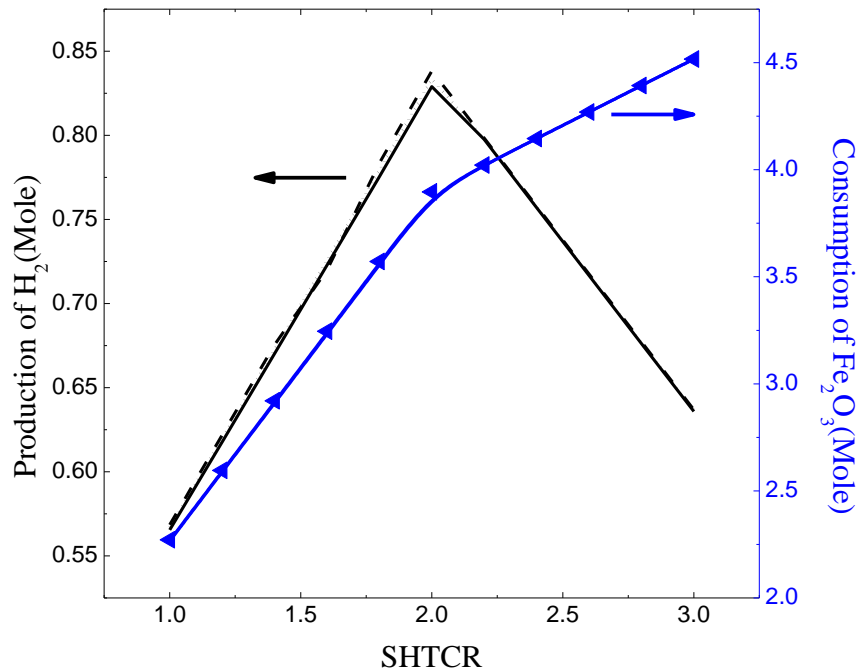


Figure 7.5: Production of H_2 and consumption of hematite as a function of SHTCR and T_{Feed} .

7.2.6 Hydrogen Generator (SR) Unit

As noted earlier, the product gas stream from the SR unit is divided into two smaller streams. One stream is fed to the GR unit and used as the gasifying agent in the gasification of the solid fuel after compressing to 70 bar while the other stream is taken out as the final product stream (i.e. H₂ after condensing the steam). The productivity of H₂ is heavily influenced by the SHTCR as can be seen from Figure 7.5. It increases rapidly to a peak value of 0.83 moles per mole of carbon at a SHTCR of about 2. The hydrogen production curve then sharply plunges to values as low as 0.63 moles per mole carbon input at SHTCR~3. The reason for the observed increase in hydrogen production over $1 < \text{SHTCR} < 2$ is that the rate of gas fuel production in the GR unit is greater than the rate of hydrogen consumed. But as SHTCR reaches values around 2 and beyond, the production of gas fuel in the GR unit rises only slightly given that the conversion of carbon levels off at $\text{SHTCR} > 2$. In contrast, the rate of hydrogen used as a gasifying agent remains the same as before. This can also be explained in terms of the increase in the rate of hematite consumption as shown in Figure 7.5. As can be seen, the curve corresponding to hematite consumption generally exhibits a rising trend although the slope seems to be steeper for SHTCR between 1 and 2. Compared with a conventional CLC system in which coal is gasified with steam and oxygen at H₂O/C mole ratio~0.12 and O₂/C mole ratio~0.45 and gasification temperature at 1700 K, simulation results presented here show that the productivity of hydrogen is 0.77 mole per mole carbon. The comparison is presented in Table 7.2. As can be seen from the table, the proposed novel IGCLC has several advantages over the conventional CLC. Firstly, the need for high purity oxygen is eliminated as hydrogen is used in the IGCLC process for power generation. Secondly, the cold gas efficiency is around 95%, which is 18 percentage points higher than the conventional counterpart. Finally, the net hydrogen production is 7.8% higher although the carbon conversion is three percentage points lower.

Table 7.2: The comparison of IGCLC with conventional coal gasification CLC

Items	IGCLC system	Conventional coal CLC system
H ₂ O/C mole ratio	1	0.12
H ₂ (or O ₂)/C mole ratio	1	0.45
Gasifier temperature (K)	1068	1700
Gasifier pressure (bar)	70	30
Carbon conversion	95%	98%
Net hydrogen production (mole/mole carbon)	0.83	0.77

7.3 Performance Characteristics of the System Integrated with VAM Combustor

In the above section, the feasibility of using a novel IGCLC system to produce high purity hydrogen from coal was examined through the thermodynamics analysis method. The inspiring preliminary results revealed that the novel system was of some advantage and with high hydrogen productivity. In this section, the system was integrated with a VAM combustor where ventilation air methane was burnt with the aid of produced hydrogen. Besides, to increase the mitigating capacity the combustion air to AR was substituted by VAM. The performance of the integrated system was thereby characterised by a thermodynamics approach within the software of ASPEN PLUS.

The goal of this section was to determine the effect of SHTCR, steam conversion, excess of oxygen carriers (OCs) circulation rate, excess of VAM feed to AR, mole ratio of VAM to H₂ in VAM combustor and VAM concentration on the overall system performance, such as the overall efficiency and CO₂ capture rate. To perform the simulation the following assumptions are made:

- Input: 1MW coal.

- The pressure of the gasification unit is fixed at 70 bar and the feeding hydrogen/steam mixture is at 1000K.
- Unconverted carbon in the coal accounts for 5% of the overall input carbon.
- 10% excess stoichiometric oxygen carrier circulation rate at the base case.
- 110% excess stoichiometric air feed rate to the AR unit for keeping a high velocity.
- Gas turbine discharge pressure in 1 bar; turbine polytropic efficiency in 0.9; mechanical/generator efficiency in 0.98/0.98.
- Steam cycle is of 40% efficiency.
- CO₂ compression to 90 and 60 bar for storage.

To be clear, some indicators, such as fuel conversion in FR, the overall efficiency and CO₂ capture rate, are defined as:

$$\varphi = \frac{\alpha_{CO_2}}{\alpha_{CO_2} + \alpha_{CO} + \alpha_{CH_4}} \quad (4.4)$$

$$\eta_E = \frac{W_{net}}{m_{coal} LHV_{coal}} \quad (4.5)$$

$$E_{CO_2} = \frac{m_{cap}}{m_{cap} + m_{uncap}} \times 100\% \quad (4.6)$$

where φ is the fuel conversion in fuel reactor; α_{CO_2} , α_{CO} and α_{CH_4} are the mole fractions of CO₂, CO, CH₄ in the gas product of fuel reactor; η_E is the electric power efficiency based on LHV in %; W_{net} is the net power of the system in KW; LHV_{coal} and LHV_{CH_4} are the LHV of coal and CH₄ in kJ/kg; m_{coal} and m_{CH_4} are the mass flow of coal input and CH₄ in VAM; E_{CO_2} is the CO₂ capture rate in %; m_{cap} and m_{uncap} are the mass of captured and released CO₂.

7.3.1 Effect of SHTCR

SHTCR significantly affects the performance of the developed IGCLC system as shown in the last section. It should therefore be necessary to examine the effect of SHTCR on the whole system's performance which is shown in Figure 7.6Figure 7.7. As can be seen in Figure 7.6, the fuel conversion in the FR unit varies with the variation of SHTCR. It is increased with SHTCR for SHTCR less than 2 while decreasing for higher values of SHTCR. The peak value is around 97.1% at SHTCR~2. The variations of overall efficiency and CO₂ capture rate with SHTCR are divided into two stages as shown in Figure 7.7. For the plot of overall efficiency vs. SHTCR, in the initial stage, within SHTCR ranging from 1 to 2, the overall efficiency increases linearly to the maximum value around 49.3% from 35.1%, equivalent to about a 40% increase. It is then followed by a plateau at the second stage, during which there is an extremely slight decrease of around 1.05% for the overall efficiency. The linear increase in the initial stage is mainly attributed to the increase in the carbon conversion (see Figure 7.2) on one hand. On the other hand, the increase in the ratio of H₂ to H₂O and CO to CO₂ (Figure 7.3) indicates that the gasification efficiency in GR is increased within the initial range of SHTCR which might contribute to the increase in the overall efficiency. The slight decrease in the overall efficiency can also be explained by the fact of the decrease in the syngas ratio. As per the variation of CO₂ capture rate with SHTCR which is shown in Figure 7.7, it initiates with a slight increase from 78.1% to 79.9% at SHTCR~2 followed by a dramatic increase to 83% at SHTCR~3. Both the carbon conversion and hydrogen production (note: that more hydrogen production causes higher VAM flow rate in VAM combustor) are the contribution to the change in CO₂ capture rate. As noted, the produced CO₂ in FR can be captured completely while the CO₂ from VAM cannot be captured. With SHTCR in the range of 1–2, both carbon conversion and hydrogen production are increasing, as a result both the amounts of captured CO₂ and uncaptured CO₂ increased. For SHTCR within the range of 2–3, the carbon conversion is in constant value while hydrogen production is drop down. In this case, the CO₂ capture rate is derived from a levelled-off captured CO₂ and a decreased released CO₂ causing it to increase at a higher rate.

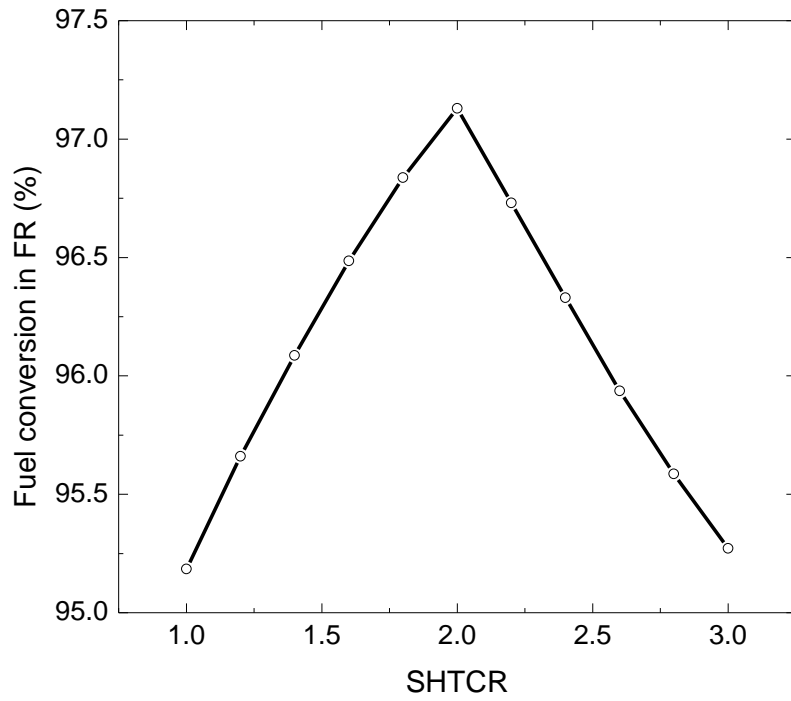


Figure 7.6: The effect of SHTCR on the fuel conversion in the fuel reactor.

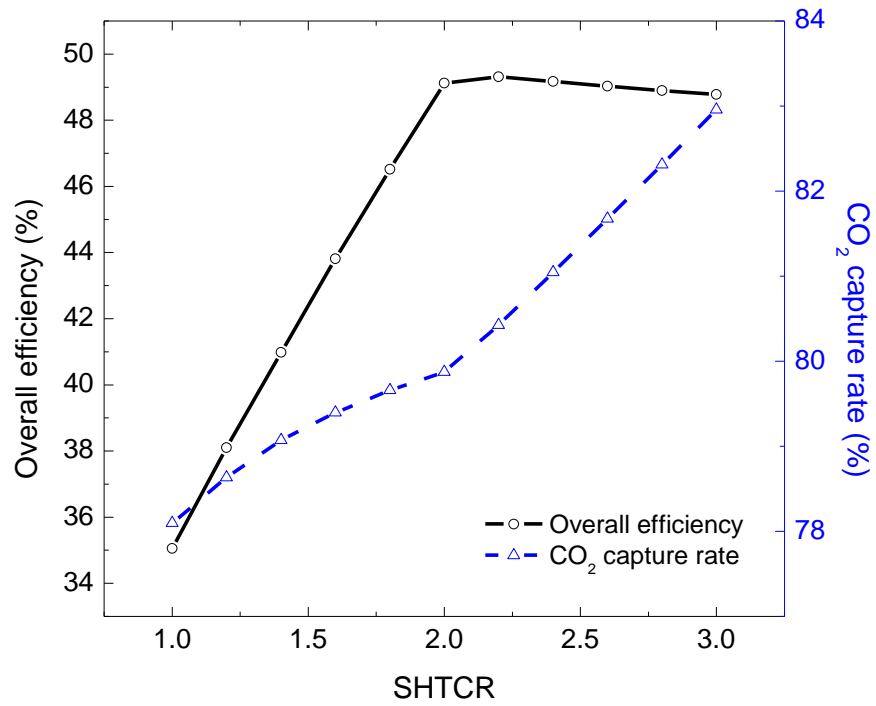


Figure 7.7: The effect of SHTCR on system performance.

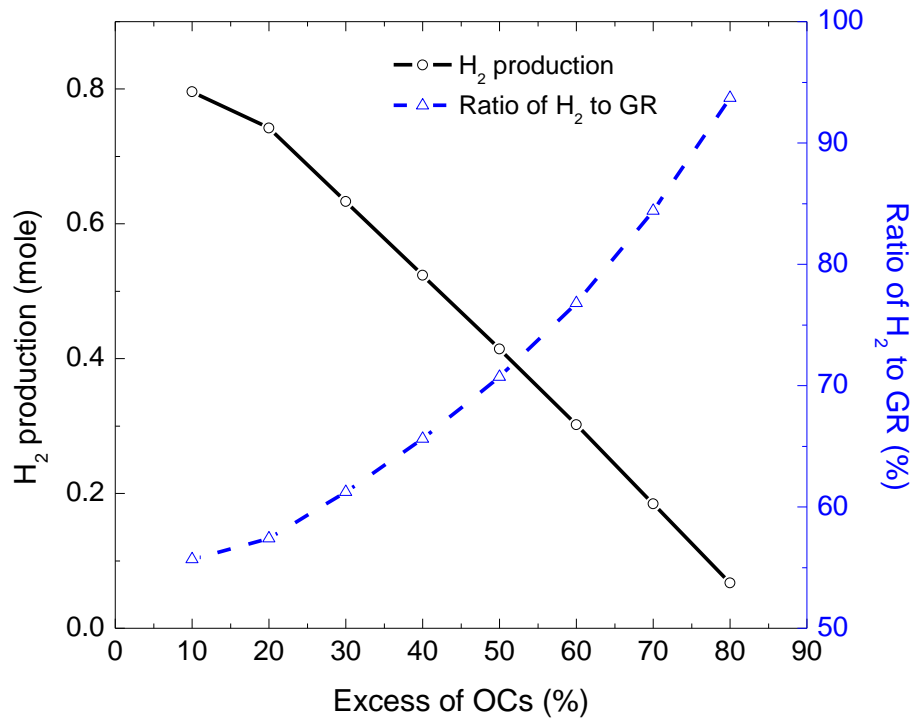


Figure 7.8: The effect of oxygen carrier circulation rate on H₂ production.

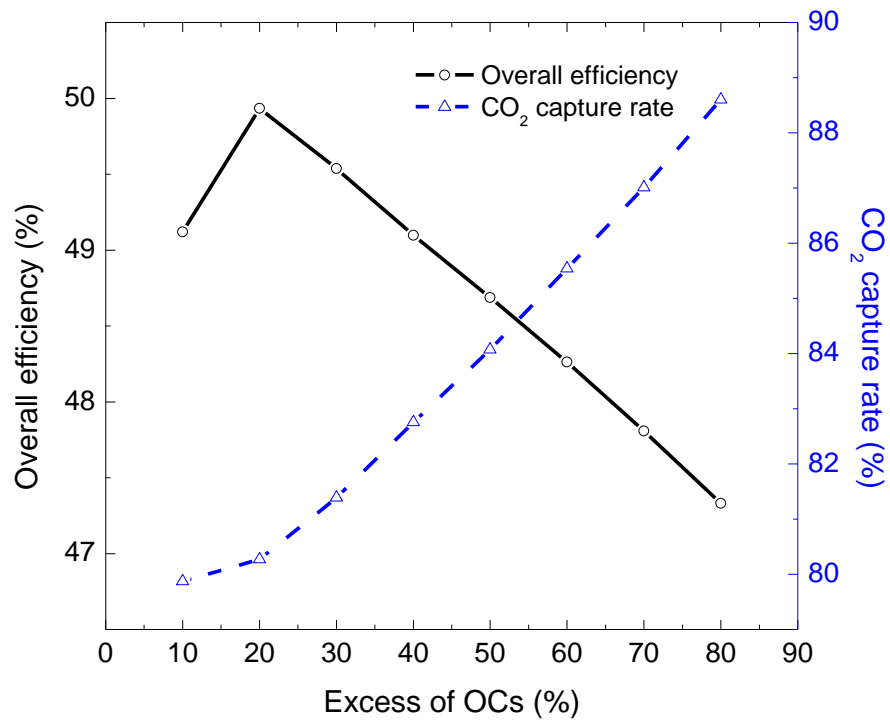


Figure 7.9: The effect of oxygen carrier circulation rate on system performance.

7.3.2 Effect of Oxygen Carrier Circulation Rate

In order to obtain high conversion of fuel to carbon dioxide and steam, an excess of oxygen carrier circulation rate is applied in the FR. However, it should be noted that the higher oxygen carrier circulation rate, the lower wustite content in the reduced solid stream; and as a result a lower hydrogen production is obtained. The effect of oxygen carrier circulation rate on the hydrogen production, which is defined as mole H_2 per mole input carbon, is shown in Figure 7.8. In general, the hydrogen production is decreasing linearly with the increase in oxygen carrier circulation rate and it drops to 0 with the excess stoichiometric oxygen carrier circulation rate around 80%. The exception for 10% excess of OCs is due to the partial fuel conversion to CO_2 in the fuel reactor, whereas the complete fuel conversion can be achieved with the excess of OCs higher than 20%. The decrease in the hydrogen production is also indicated by the ratio of H_2 to GR in Figure 7.8, which increases from 55% to 95%. Besides, the oxygen carrier circulation rate significantly influenced the system performance indicated by the variation in overall efficiency and CO_2 capture rate in Figure 7.9. With the excess of OCs lower than 20%, a slight increase is found from 49.12% to 49.93%, which is the result of the increase in fuel conversion. For a high oxygen carrier circulation rate, the more the excess rate of OCs the lower in the overall efficiency, decreasing from 49.93% at excess rate of 20% to 47.33% at excess rate of 80%. The underlying reason for this phenomenon could be the decrease in hydrogen production and as such the decrease in high-level energy from the VAM combustor (note that VAM combustion has the highest temperature level in the system). It also causes the increase in CO_2 capture rate from 79.9% to 88.6%, as smaller amounts of VAM is needed for lower hydrogen production indicating that the mass of released CO_2 is decreased.

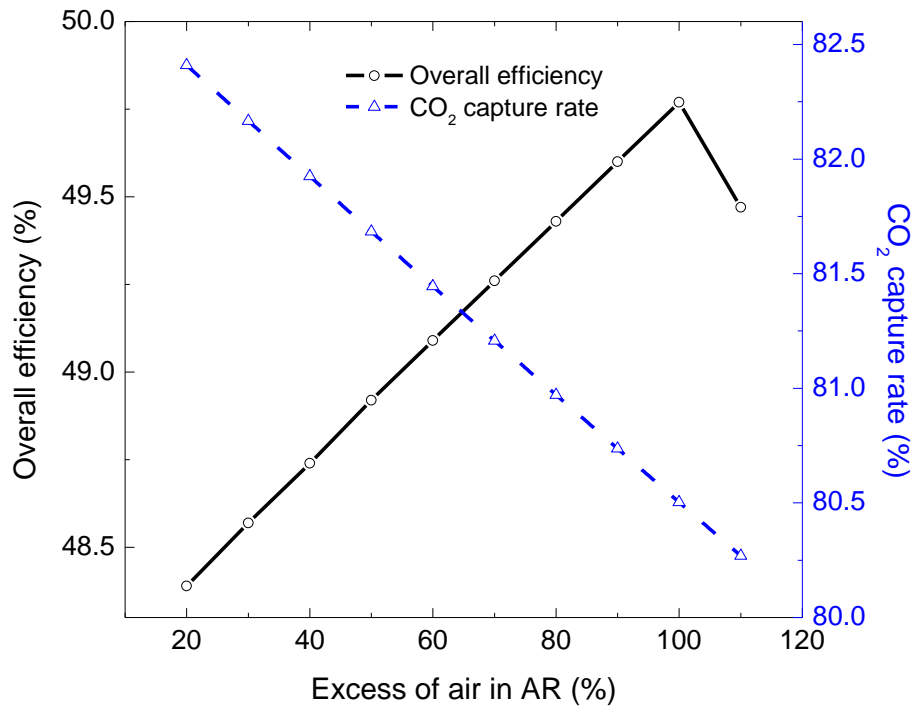


Figure 7.10: The effect of airflow rate in AR.

7.3.3 Effect of Air Flow Rate

An excess of airflow rate feeding to AR is to obtain a full oxidation of the circulated oxygen carriers and maintain high velocity in the rising reactor (AR) on one hand. The higher airflow rate also functions to maintain the temperature in AR at the desired level on the other hand. The effect of airflow rate in AR on the overall efficiency and CO₂ capture rate is plotted in Figure 7.10. As shown, the overall efficiency is increasing with the increase in the airflow rate until it reaches the maximum value of 49.77% at 100% excess rate of air. As AR has the second highest temperature level, more feeding air makes it possible to produce more relative high-level energy and as such higher overall efficiency. However, if the energy produced in AR becomes more than that produced in a VAM combustor (the highest temperature level) it may cause a drop in the efficiency. The effect of excess of feeding air in AR on CO₂ capture rate is negative because more methane is brought into and the produced CO₂ cannot be captured. It indicates that the airflow rate should be quantified with the balance between the overall efficiency and CO₂ capture rate.

The higher CO₂ capture rate leads to the lower overall efficiency and vice versa for excess of air in the range of 20–100%.

7.3.4 Effect of Steam Conversion

The steam conversion in SR is normally located in the range of 25–50% according to the thermodynamics and experimental research. Although it favours lower temperatures (i.e. the lower the temperature the higher hydrogen equilibrium partial pressure), the reaction kinetics is limited at temperatures lower than 973K. Generally speaking, the SR temperatures preference is in the range between 973K and 1123K. Correspondingly, the steam conversion rate is varied between 25% and 50%. As can be imagined, the higher steam conversion rate indicates that lower steam flow rate is required to achieve a complete conversion of wustite to magnetite and vice versa. It in turn generates lower reversibility and obtains higher energy efficiency, which is shown in Figure 7.11. It can be observed that the overall efficiency is increasing with the increase in the steam conversion as expected. The overall efficiency is 49.26% with steam conversion of 25% and increases to 50.19% with 50% of steam conversion to hydrogen. It is equivalent to 1.9% increase over the steam conversion range, which is not as significant as that caused by the above-stated factors. Compared with the variation plot with other factors, the curve of overall efficiency with steam conversion is a parabolic rather than linear one. This could be the reason why it is not varied as significantly as the others.

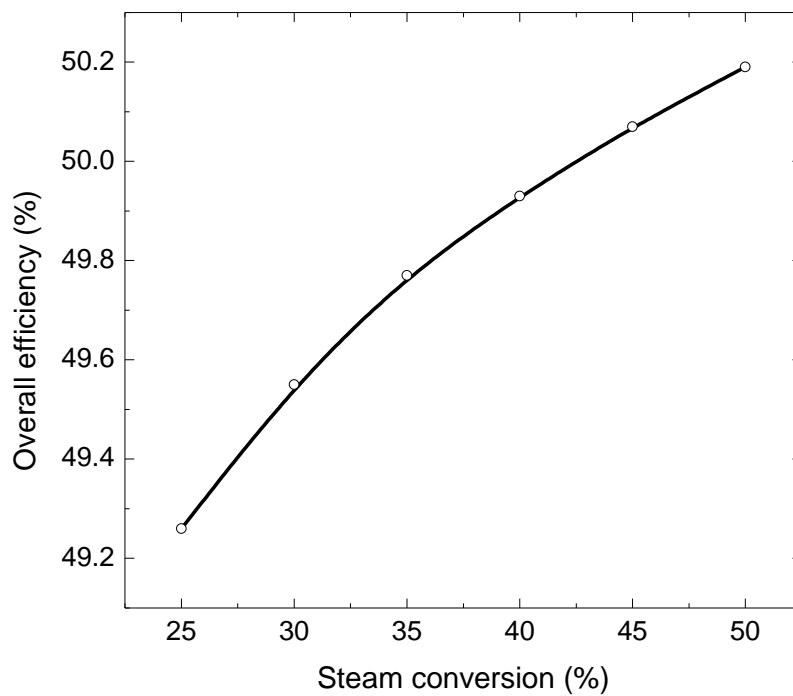
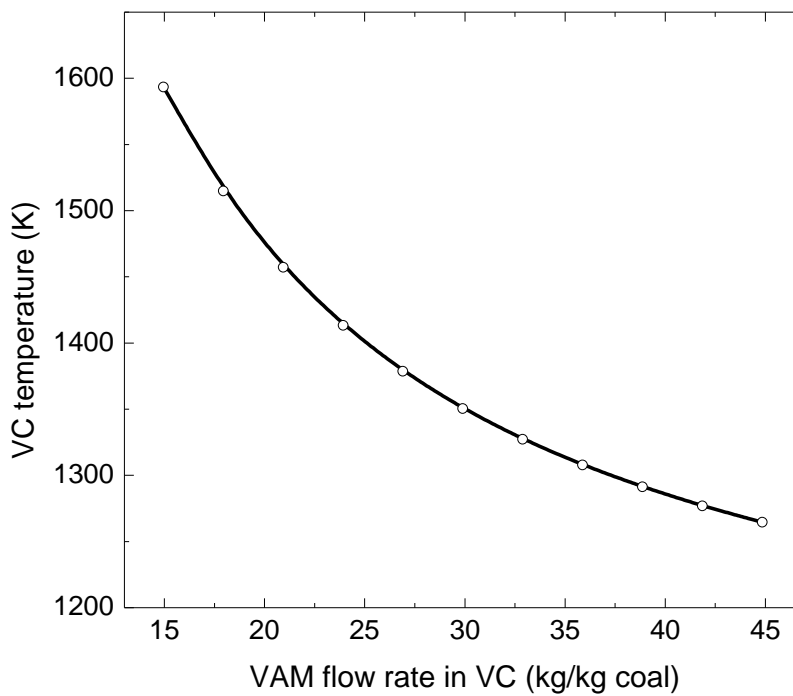
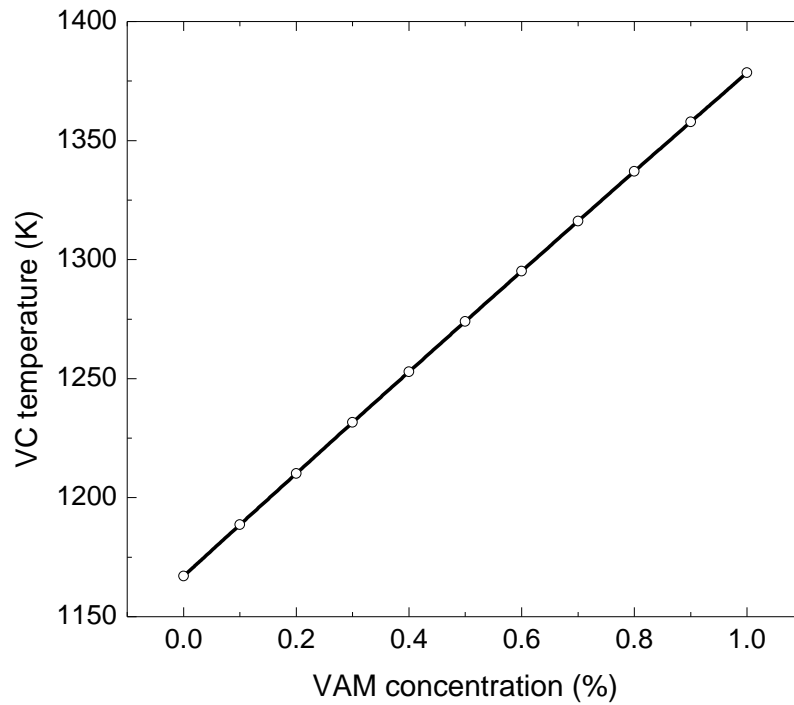


Figure 7.11: The effect of steam conversion in SR.



(a)



(b)

Figure 7.12: The effect of: (a) VAM flow rate and (b) VAM concentration on VC temperature.

7.3.5 Effect of VAM Flow Rate and VAM Concentration

In a real coalmine the VAM flow rate and methane concentration are varied with time and unable to predict. The VAM flow rate is quite dependent on the coalmine scale and the methane concentration is normally varied in the range of 0.1–1 vol%. The influence of VAM flow rate and methane concentration on VAM combustor temperature is plotted in Figure 7.12. It can be found that the plot of VAM flow rate with VC temperature is an exponential curve while a linear line is found for the relation between methane concentration and VC temperature. The VC temperature is indeed decreasing with the increase in VAM flow rate and decrease in methane concentration.

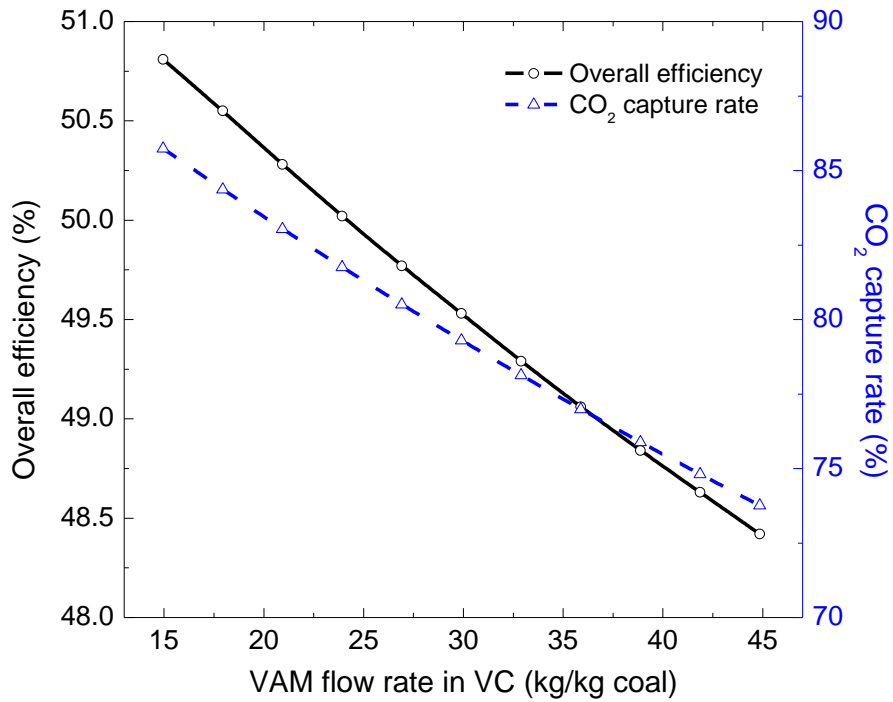


Figure 7.13: The effect of VAM flow rate on system performance.

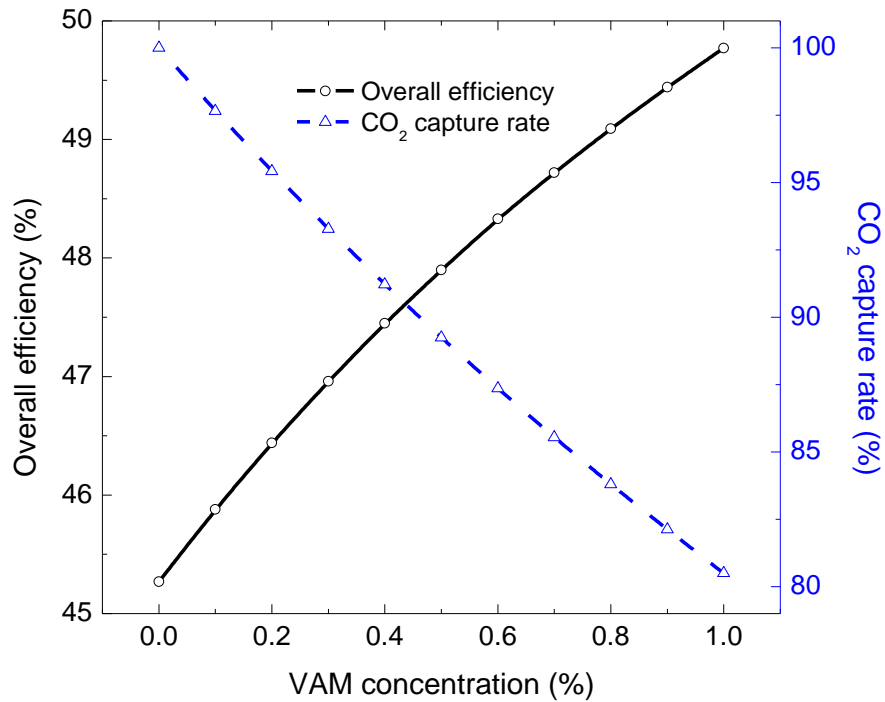


Figure 7.14: The effect of VAM concentration on system performance.

The variations in the VAM properties also placed a critical impact on the system performance shown in Figure 7.13 and Figure 7.14. It is expected that both the increase in VAM flow rate and methane concentration can lead to a decrease in the CO₂ capture rate as more uncaptured CO₂ is produced. For the overall efficiency, it increases with the decrease in VAM flow rate and increase in methane concentration. This is inconsistent with the variations in the VC temperatures, which put the most important influence on the overall efficiency.

7.4 Conclusions

This study is to determine the feasibility and performance of an integrated IGCLC-VC system using the thermodynamics method. Besides the effect of some factors on the system, performance is investigated, including SHTCR, excess of OCs circulation rate, excess of airflow rate, steam conversion rate, VAM flow rate, and methane concentration. The following are the major findings:

- The IGCLC process is feasible and there are no thermodynamic barriers to its operation.
- The use of the product gas (i.e. steam-hydrogen mixture) from the SR unit for gasification of coal is a viable option and the gasification process can be made auto-thermal (i.e. no need of external heat) if the reaction temperature is greater than 1023 K and the pressure is fixed at 70 bar.
- The gasification temperature and hence the performance of the gasifier can be significantly improved by either increasing SHTCR or preheating the steam/hydrogen mixture using the hot flue gas from the AR unit before the mixture is fed into the GR unit.
- The optimised SHTCR value is 2 at which the system shows the highest hydrogen production, fuel conversion, overall efficiency and middle level CO₂ capture rate.

- The most suitable excess of oxygen carrier circulation rate and airflow rate are found to be 20% and 100% regarding the overall efficiency. In this case, the CO₂ capture rate is around 80%.
- The steam conversion only put a slight effect on the overall efficiency compared with other factors.
- Both the VAM flow rate and methane concentration influenced the system performance. The influence on the overall efficiency is due to the variation in VC temperature with VAM flow rate and methane concentration.

Chapter 8: USE OF VAM AS AN OXIDISING AGENT IN CHEMICAL LOOPING COMBUSTION OF SYNTHESIS GAS

8.1 Introduction

In this chapter, a novel method was proposed for ancillary use of ventilation air methane. The process provides an advanced technology platform for treatment of VAM and can be employed as part of any use and/or destruction mitigation strategies [68]. The motivation behind this research is that the process possesses clear advantages over both TFRR and CFRR systems. When the system is operating with temperatures higher than 1273K, the ventilation air methane will be reduced mainly by the reaction mechanism of thermal oxidation. For the operating temperatures under 1073K, the catalytic combustion will activate and take the initiative due to the presence of metal oxide (i.e. oxygen carriers). Under such circumstances, the ventilation air methane is able to be oxidized completely with a flexible operation regime. It is also no doubt that the produced heat can be recovered without any compromise.

The aim of this study is to examine the effect of the variations in VAM flow rate and methane concentration on the system performance. This was accomplished thermodynamically by simulating the process in commercially available simulation software-ASPEN PLUS. Moreover, sets of experiment were carried out in a fixed bed setup to determine the conversion of VAM in air reactor with $\text{Fe}_2\text{O}_3/\text{Al}_2\text{O}_3$ as oxygen carrier over temperatures lower than 800°C under which the thermal oxidation is not dominant. The experimental component of this study was carried out because the oxidation characteristics of VAM is an important factor in the overall performance of the proposed ancillary system. Although many of past studies have focused on the catalytic combustion of VAM in air, the prevailing used catalysts were supported noble metals or metal oxides like Pt, Pd or PdO due to their high reactivity, even with a very low loading content (less than 1 wt%). Very

few works were found on the use of Fe₂O₃ supported by Al₂O₃ as catalyst in the catalytic combustion of VAM [41, 44]. Five metal oxides with different Fe₂O₃ loading content are used to investigate the effect of Fe₂O₃ content on the methane conversion, which made it possible to find an optimised alumina-supported iron oxide for the proposed process.

8.2 Thermodynamics Analysis

The process is involved using VAM to substitute the combustion air in an IGCLC system as shown in Figure 8.1. It mainly consists of three reactors: gasification reactor (GR), fuel reactor (FR) and air reactor (AR). The gasification reactor is a pipe type pressurised coal gasifier which is immersed in the air reactor and takes in the heat released from AR [123]. In AR, the oxidative gas is VAM instead of air as mentioned earlier. Before coming into the AR, it is compressed to the desired pressure. All reactors are modelled using the "RGIBBS" reactor model, which employs a Gibbs Free Energy Minimisation method to perform the relevant chemical equilibrium calculations for any given set of operational conditions. To achieve a complete oxidation of fuel gases to CO₂ and H₂O, excess hematite (more than the stoichiometric requirements) is applied [61, 115]. An excess air feed rate is also used to ensure the full conversion of VAM and magnetite. Some assumptions are made and listed in Table 8.1.

To be clear, the overall efficiency and CO₂ capture rate are defined as

$$\eta_E = \frac{W_{net}}{m_{coal} LHV_{coal}} \times 100\% \quad (8.1)$$

$$E_{CO_2} = \frac{m_{cap}}{m_{cap} + m_{uncap}} \times 100\% \quad (8.2)$$

where η_E is the electric power efficiency based on LHV in %; W_{net} is the net power of the system in KW; LHV_{coal} is the coal LHV in KJ/kg; m_{coal} is the mass flow of coal input; E_{CO_2} is the CO₂ capture rate in %; m_{cap} and m_{uncap} are the mass of captured and released CO₂.

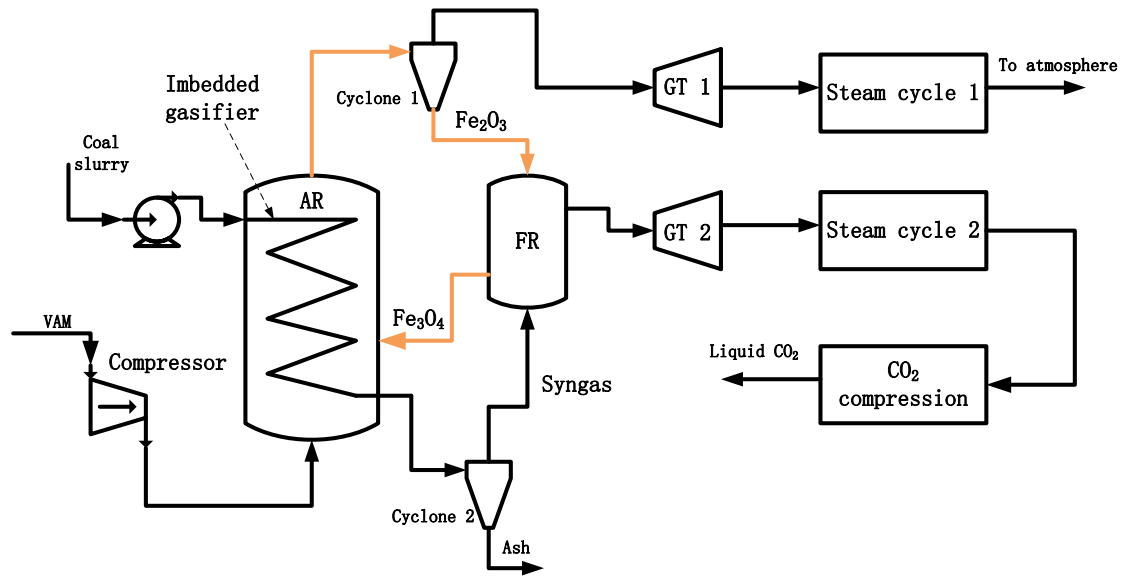


Figure 8.1: Flow sheet of the proposed combustion method of VAM.

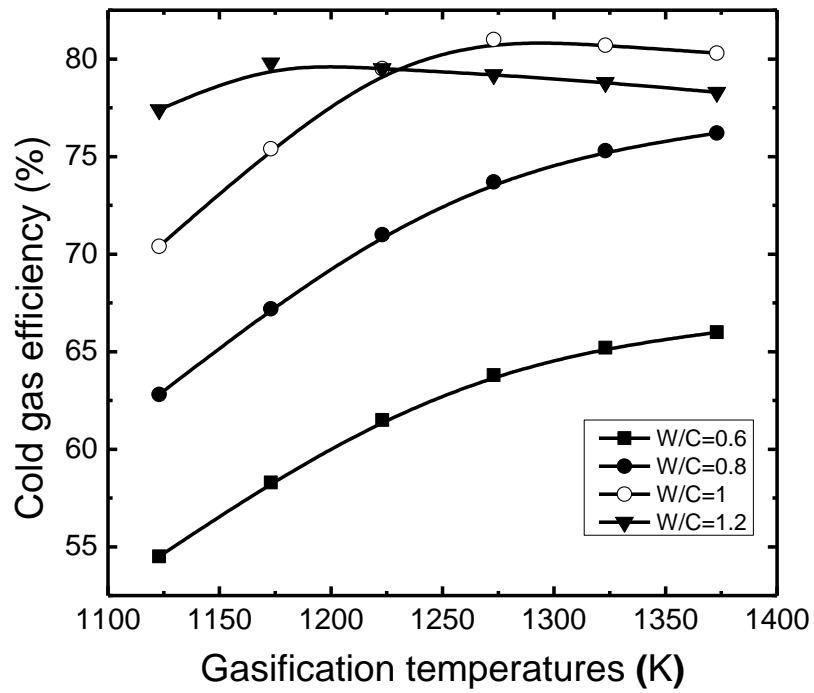
Table 8.1: Assumptions and operation parameters.

Gasification reactor	Temperature~1273 K, pressure~30bar, carbon conversion~98%, steam/coal ratio~1; pressure loss~5%; heat loss~0.5% of input LHV
Fuel reactor	Temperature~1373 K, oxygen carrier excess ratio~1.5
Air reactor	Temperature~1373 K, air excess ratio~1.5
Oxygen carriers	Fe ₂ O ₃ -Fe ₃ O ₄
Turbine	Discharge pressure~1 bar, turbine polytropic efficiency~0.9, mechanical/generator efficiency~0.98/0.98
Steam cycle	Approach point~15 K, pinch point~25 K, exhaust gas temperature~353 K
CO ₂ compression	Single stage compression ratio~3.5, isentropic efficiency~0.85, mechanical/electric efficiency~0.99/0.99, liquid CO ₂ to disposal~300 K and 120 bar
Air compressor	Isentropic efficiency~0.85, mechanical/electric efficiency~0.99/0.99

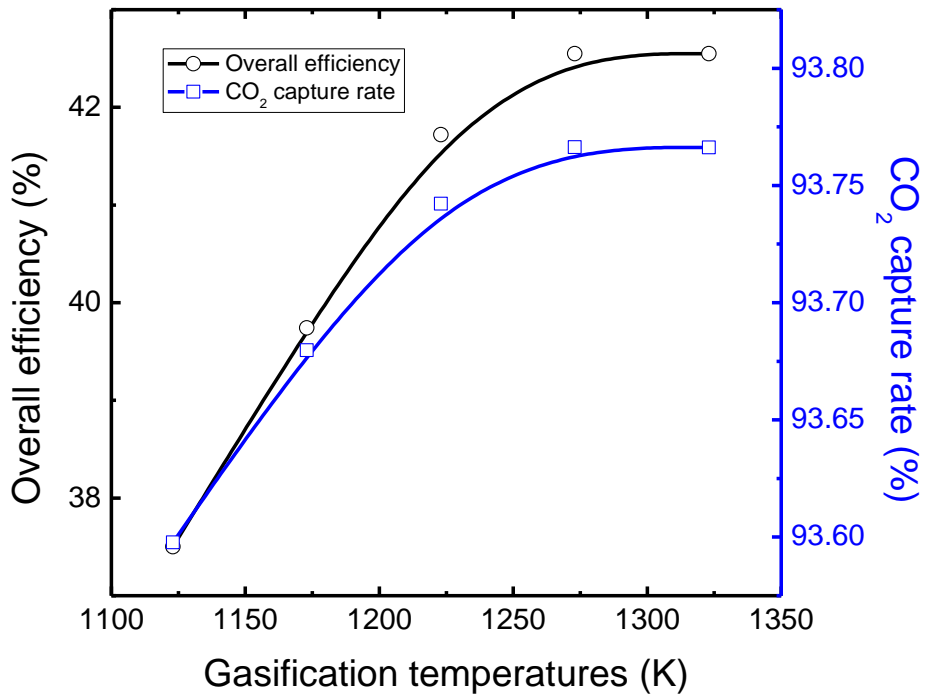
8.2.1 The Optimisation of the System Performance

In order to achieve an optimised system performance, it is necessary to determine the maximum value for cold gas efficiency (CGE), as defined as the ratio of the LHV for product gas to coal LHV. The variations of cold gas efficiency are evaluated with varying gasification temperatures (1123–1373 K) and water to carbon ratios (0.6–1.2) in Figure 8.2(a). As shown, the cold gas efficiency is rather dependent on the gasification temperature and water to carbon ratio. It is generally increasing with these two factors. For the water to carbon ratio less than equity, CGE values increases rapidly at temperatures lower than 1273 K, followed by a plateau. The optimised value is found to be 81% at 1273 K with the water to carbon ratio~1. It is also observed that the optimised overall efficiency and CO₂ capture rate can be obtained at the same conditions as illustrated in Figure 8.2(b). It is also found the phenomenon that the overall efficiency and CO₂ capture rate are increasing rapidly at temperatures lower than 1273 K, followed by a plateau for higher temperatures. The maximum values are 42.55% and 93.77%. It should be noted that the effect of gasification temperature was more significant on the overall efficiency than the CO₂ capture rate. As shown, the overall efficiency increased by about 5 percentage points

from 37.5% to 42.55% while the counterpart for CO₂ capture rate was just 0.16 percentage points. Based on these conclusions, we believe that the system performance is optimised under the conditions of: (a) the gasification temperature of 1273 K, and (b) water to carbon ratio~1, which will be applied in the following calculations.



(a)



(b)

Figure 8.2: The optimisation of: (a) CGE and (b) the overall efficiency and CO₂ capture rate.

8.2.2 Effect of VAM Flow Rate

As stated before, the flow rate of VAM is quite variable and dependent on the coalmine capacity. Therefore, it is necessary to understand the influence of VAM flow rate on the system performance. Figure 8.3 illustrates the effect of VAM flow rate on the air reactor temperature, CO₂ capture rate and overall efficiency. Not surprisingly, a higher VAM flow rate could result in a lower air reactor temperature. It is shown that the air reactor temperature is decreasing linearly with the increase in the VAM flow rate, and the overall temperature change is around 50 K over the VAM flow rate range from 165 kg/s to 350 kg/s with a methane concentration of 1%. In addition, the growth in VAM flow rate causes a drop of the CO₂ capture rate because more CO₂ is released into air and cannot be separated inherently. In fact, it declines from 94% to 87% with the VAM flow rate increasing from 165 kg/s to 350 kg/s. In contrast, it indicates that the overall efficiency has a reverse trend. It grows more than 10% from 43.1% to 48.3% over the whole range of VAM flow rate. The underlying reason for this is that more methane is intaken by a higher VAM flow rate and as such more high level energy is generated.

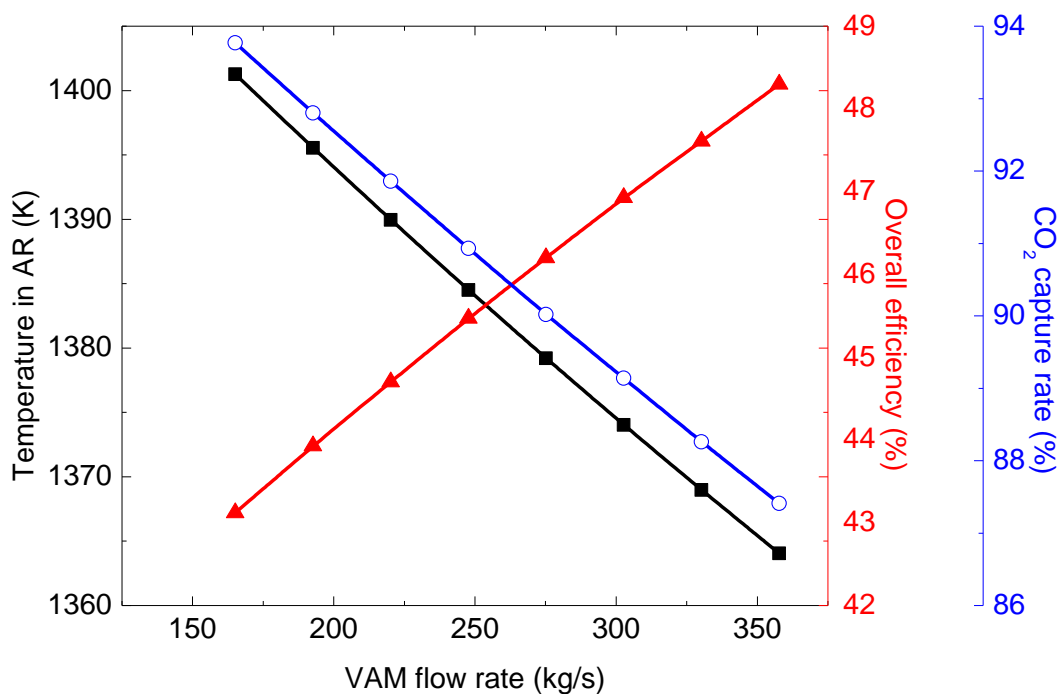
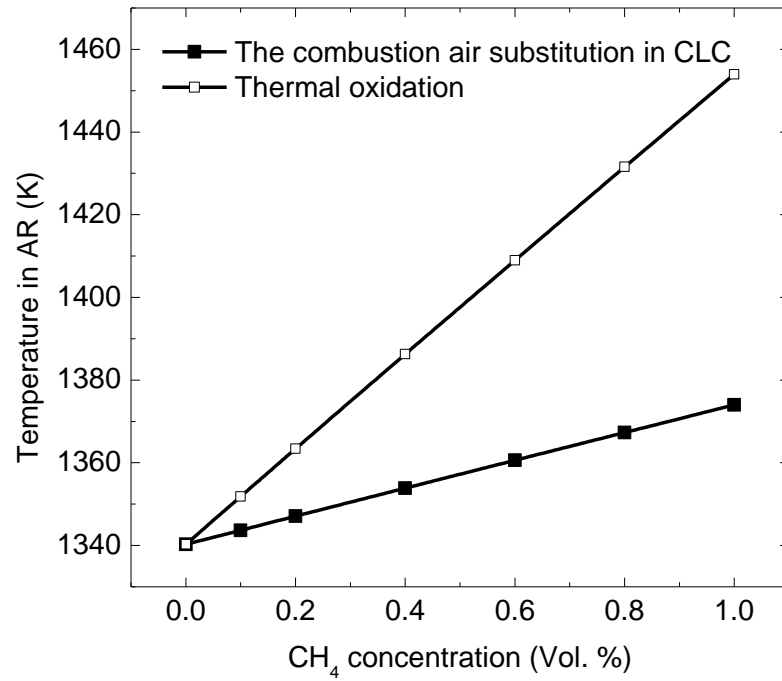


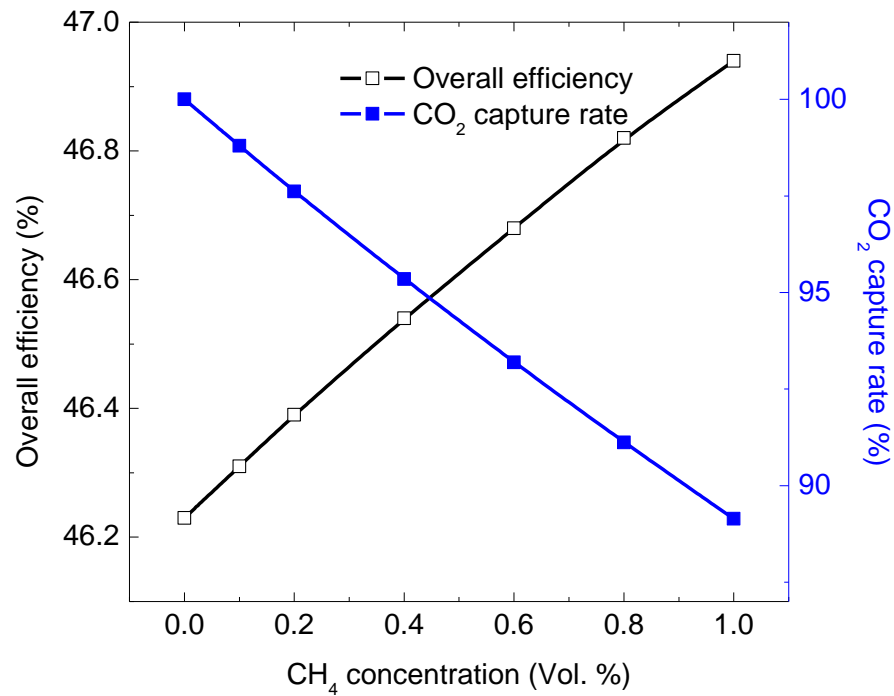
Figure 8.3: The effect of VAM flow rate on the air reactor temperature (■), CO₂ capture rate (○) and overall efficiency (▲).

8.2.3 Effect of Methane Concentration in VAM

Apart from the flow rate, the variation of methane concentration in VAM also has a great effect on the performance when the system involving the combustion air substitution with VAM. Apparently, it put some effects on the air reactor temperature, CO₂ capture rate and overall efficiency. As shown in Figure 8.4(a), with the methane concentration in VAM varying between 0 and 1%, the air reactor temperature had a variation of 34 K which is equivalent to 3% increase. If the VAM is oxidised in a thermal oxidation reactor, the variation in temperature is 114 K equivalent to 11% increase. It implies that the temperature variation can be minimised through the method of combustion air substitution with VAM in CLC due to the involvement of circulated oxygen carriers. As a result of the narrowed temperature variation, the technical barrier on the heat recovery or utilisation could be removed.



(a)



(b)

Figure 8.4: The effect of CH₄ concentration on system performance.

The effect of methane concentration (0~1 vol %) in VAM on CO₂ capture rate and overall efficiency is illustrated in Figure 8.4(b). It is unquestionable that the CO₂ capture rate decreases with the increase in the methane concentration as more CO₂ is released from the air reactor exhaust gas. It declines to 89% from 100% over the examined methane concentration range. As the same reason stated above, more introduced methane leads to more energy generation from air reactor which has the highest energy level in the whole system. That is why the overall efficiency is increasing when increasing the methane concentration. However, the increase is not as remarkable as that resulting from the increase in the VAM flow rate. It is only 0.7% ascending from 46.2% to 46.9%.

8.3 Experimental Study

The experimental study was conducted to simulate the oxidation of VAM in the air reactor in the presence of circulated oxygen carriers. To be compared, the oxidation of VAM in air without the presence of oxygen carrier was also examined. The experiments are carried out in a fixed bed reactor rig (as shown in Figure 3.2). It comprises a gas control unit, reactor and furnace, condenser and gas analyser. Methane and air are mixed in the gas control unit whereas the desired methane concentrations are reached. The reactor is a cylindrical fused-silica tube with a length of 800mm and diameter of 7mm. The oxygen carrier (i.e., Fe₂O₃/Al₂O₃) was placed in the middle area (200mm in length) while the both sides were loaded with quartz wool to reduce the residence time of gases in the reactor as well as prevent the solid materials from moving in the reactor. The reaction temperature is controlled and stabilised by the furnace and the temperature stable length is 400mm. The gas product is analysed in the gas analyser (i.e. Angilent Micro-GC 4900) after the steam content is condensed in the condenser and desiccator. The exhaust stream is eventually ventilated to the atmosphere. The particle samples, Fe₂O₃/Al₂O₃, were prepared using dry impregnation method details, which can be found elsewhere [106]. The loading content of Fe₂O₃ on Al₂O₃ is between 1wt% and 50 wt%.

All experiments were carried out within the temperature range of 573–1123 K. The simulated gas flow rate is around 150 mL/min (i.e. equivalent to the gas velocity of 0.065

m/s). The corresponding residence time is 6.15 seconds. The methane volume concentrations in air are 0.23, 0.51 and 0.95 vol%.

For the purpose of comparison, the methane conversion is defined as:

$$X_{\text{CH}_4} = \left(1 - \alpha_{\text{CH}_4,\text{out}} / \alpha_{\text{CH}_4,\text{in}}\right) \times 100\% \quad (8.3)$$

$$X_{\text{CO}_2} = \left(\alpha_{\text{CO}_2,\text{out}} / \alpha_{\text{CH}_4,\text{in}}\right) \times 100\% \quad (8.4)$$

where X_{CH_4} , X_{CO_2} are the methane conversion and the conversion of methane to carbon dioxide; $C_{\text{CH}_4,\text{out}}$ is the methane concentration in the outlet gas; $C_{\text{CH}_4,\text{in}}$ is the inlet methane concentration; $C_{\text{CO}_2,\text{out}}$ is the outlet CO₂ concentration.

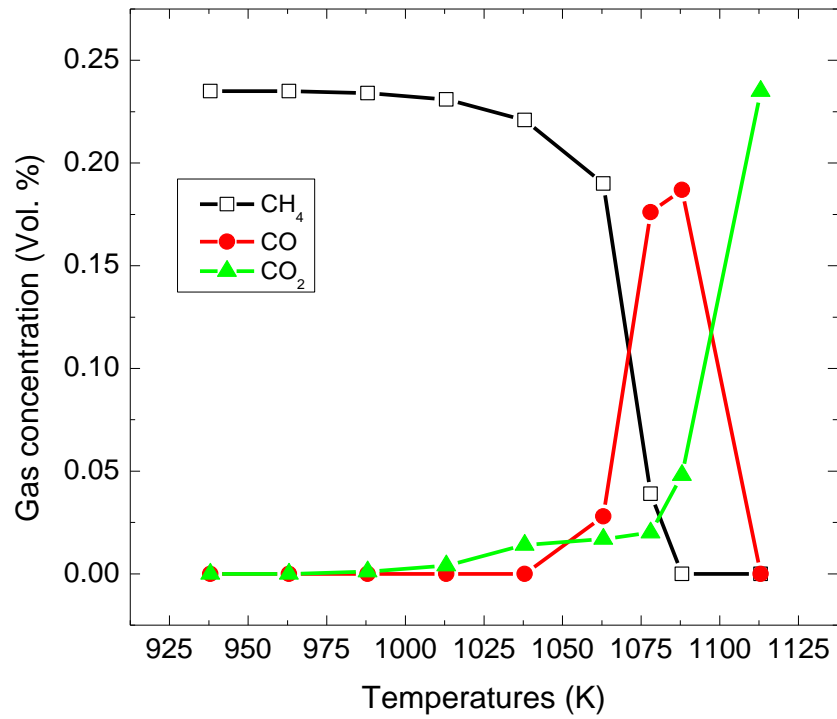
8.3.1 Oxidation of VAM in the Empty Reactor

The homogeneous oxidation of VAM in air was conducted in an empty reactor. The variations of gas concentration with the pre-set temperature at different methane concentrations (0.23, 0.51 and 0.95 vol %) are illustrated in Figure 8.5. Over the range of test conditions, the methane concentration starts with a slight decrease followed by a rapid drop to zero. At the beginning, only the conversion of CH₄ to CO₂ is observed, and no CO can be found in the gas product. After then, CO content increases rapidly and the maximum concentration of CO occurs. At the final stage, CO is oxidised to CO₂ completely as well as the methane concentration fully converted. This phenomenon indicates that both the conversion degrees of CO₂ and CO depend on the reaction temperature and it seems that the formation of CO is much more sensitive to the increase in temperature. This can be explained by the kinetic parameters illustrated in the study of Wang et.al [21], showing that the conversion of CH₄ to CO is with lower activation energy than that of CH₄ to CO₂. The results shown in Fig.6 also confirm that the oxidation of CO is inhibited by a large amount of methane (higher than 500 ppmv) through the reaction (CH₄ + 3CO₂ ↔ 4CO + 2H₂O). The observed results are quite consistent with previous studies [11, 21, 124]. However, the temperatures to observe these phenomena are varied with the inlet methane concentration,

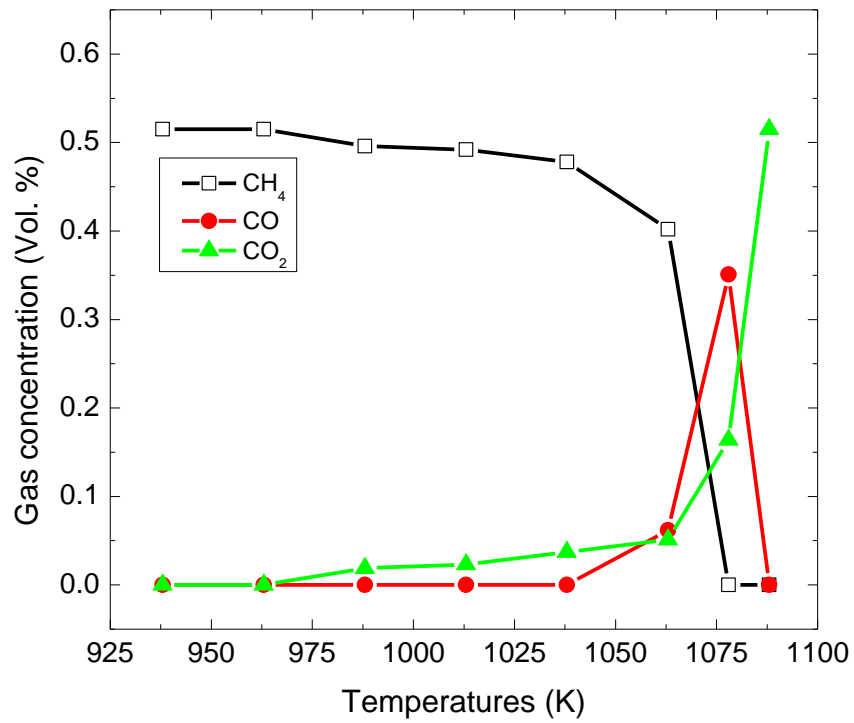
which is inconsistent with the observation in accessible literature [21]. As can be seen in Figure 8.5, the methane combustion is started at 938K with an inlet methane concentration of 0.95 vol%, increasing to 963 K and 988 K for that of 0.51 vol% and 0.23 vol%. Besides, the temperature to occur the maximum CO concentration increases with the decrease in the inlet methane concentration, from 1063 K to 1078 K and 1088 K. It is justified due to the fact that, the higher methane concentration should have the higher reaction rate constant for the methane oxidation reaction,



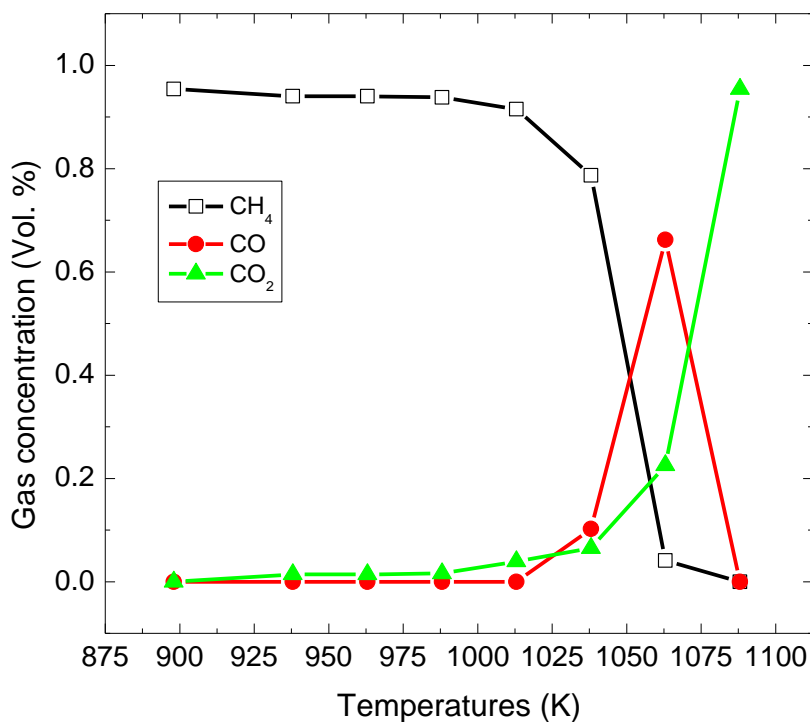
and as such the higher oxidation rate at the same temperature and in turn the observed peak temperature for CO lowered.



(a)



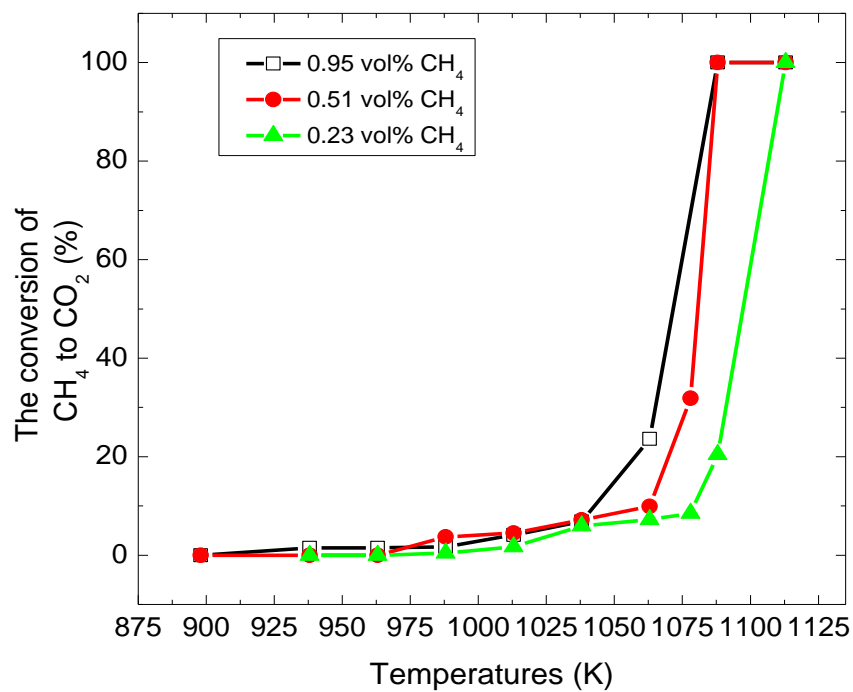
(b)



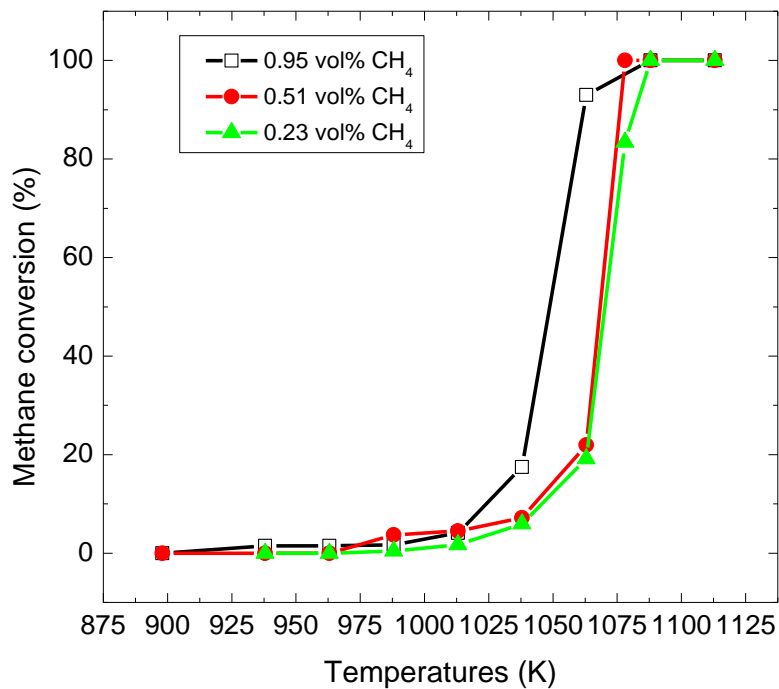
(c)

Figure 8.5: The profiles of outlet gas concentration with inlet methane concentrations in: (a) 0.23 vol%, (b) 0.51 vol%, and (c) 0.95 vol% in empty reactor.

The conversion of CH₄ versus the pre-set temperatures were also calculated and shown in Figure 8.6. The difference between the methane conversion and the conversion of CH₄ to CO₂ is the conversion of CH₄ to CO. It can be seen that the methane conversion is quite temperature dependant. It increases rapidly from 1013 K and reaches full conversion at 1078 K. It is also observed that the methane conversion is independent of the inlet methane concentration when it is below 0.51 vol%. For the conversion of CH₄ to CO₂, it lags behind the methane conversion. It is increasing sharply at 1038~1078 K and completes at 1088~1113 K (depends on the inlet methane concentrations). Generally speaking, the conversion degree of CO₂ is a function of the inlet methane concentration. As illustrated, it increases with the increase in the inlet methane concentration. This is also contributed by the higher reaction rate constant for the higher inlet methane concentration.



(a)

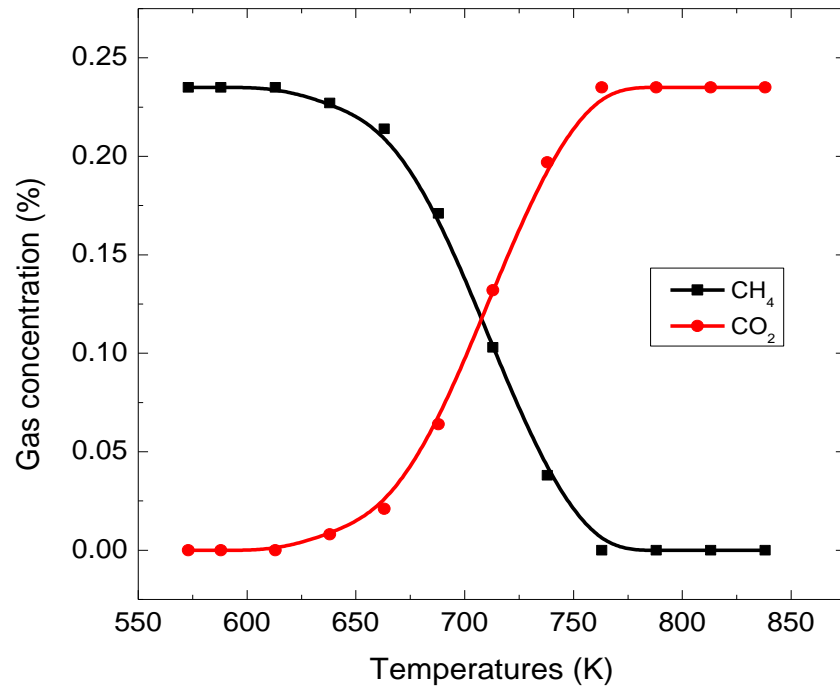


(b)

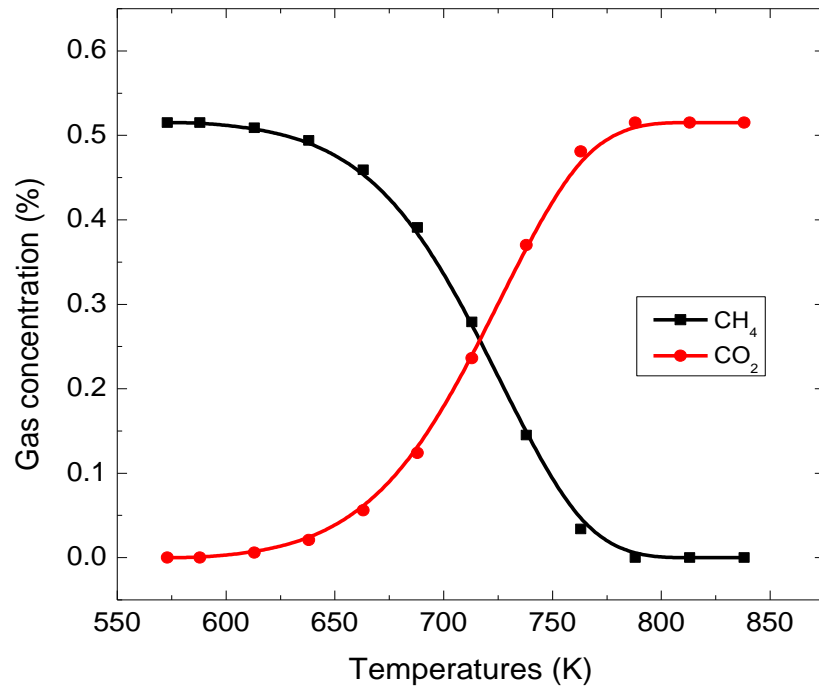
Figure 8.6: The variation of methane conversion with temperatures in empty reactor.

8.3.2 Oxidation of VAM with the Presence of Oxygen Carriers

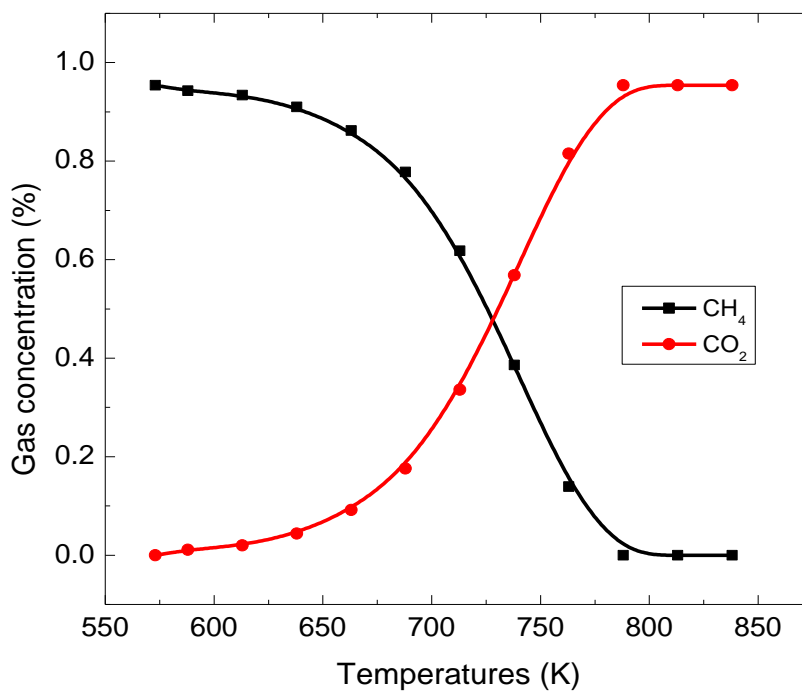
To simulate the oxidation of VAM in the air reactor of a CLC system, the particles of $\text{Fe}_2\text{O}_3/\text{Al}_2\text{O}_3$ sample were packed into the reactor center (i.e., the reaction zone). The profiles of gas concentration and methane conversion versus preset temperatures are demonstrated in Figure 8.7. It is indicated that the clear conversion of CH_4 can be found even at a temperature around 623 K, and no conversion of CH_4 to CO_2 is discovered over the temperatures. This is probably because the sample of $\text{Fe}_2\text{O}_3/\text{Al}_2\text{O}_3$ promotes the conversion from CO to CO_2 more significantly and the residence is long enough to complete the conversion of CH_4 to CO and further to CO_2 . The full conversion can be achieved around 773 K for the range of inlet methane concentrations. At lower temperatures (573~663 K), as shown in the methane conversion profile (Figure 8.7d), the methane conversion is independent of inlet methane concentrations, and it increases slightly onto about 10%. At temperatures between 663 K and 773 K, however, it grows quickly to 100%, and the inlet methane concentration exerts a great effect on the methane conversion during this stage. At the same pre-set temperature, a higher inlet methane concentration results in a lower methane conversion [35, 45]. For example, the methane conversions at 738 K are 60%, 72% and 84% for inlet methane concentrations of 0.95 vol%, 0.51 vol% and 0.23 vol% respectively. One of the possible reasons is that the higher $[\text{O}_2/\text{CH}_4]$ ratio for the lower inlet methane concentration leads to higher methane oxidation rate [23]. But it should notice that the total amount of CH_4 converted to CO_2 actually increases when increasing inlet methane concentration. Specifically the amount of converted methane for inlet methane concentration of 0.95 vol% is almost 3 times of that for 0.23 vol%.



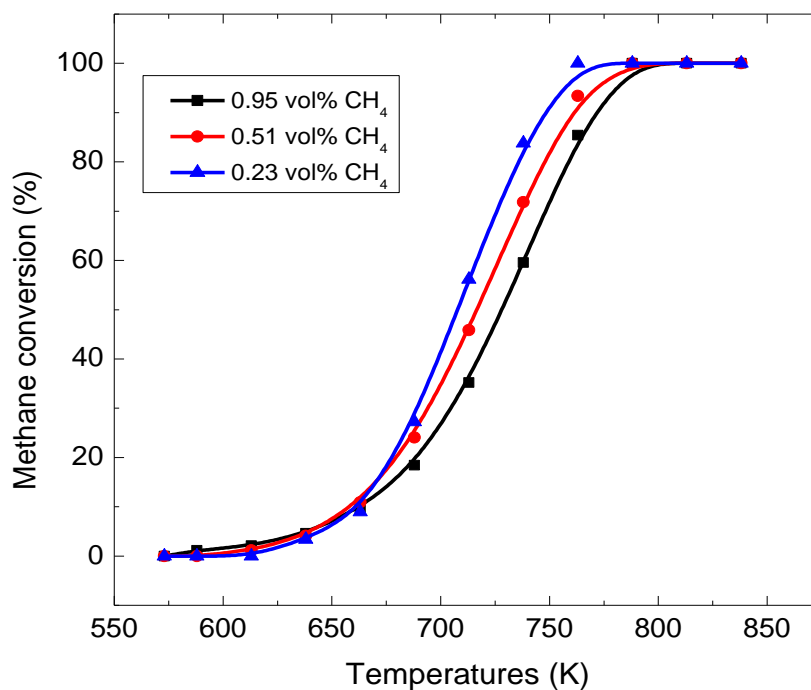
(a)



(b)



(c)

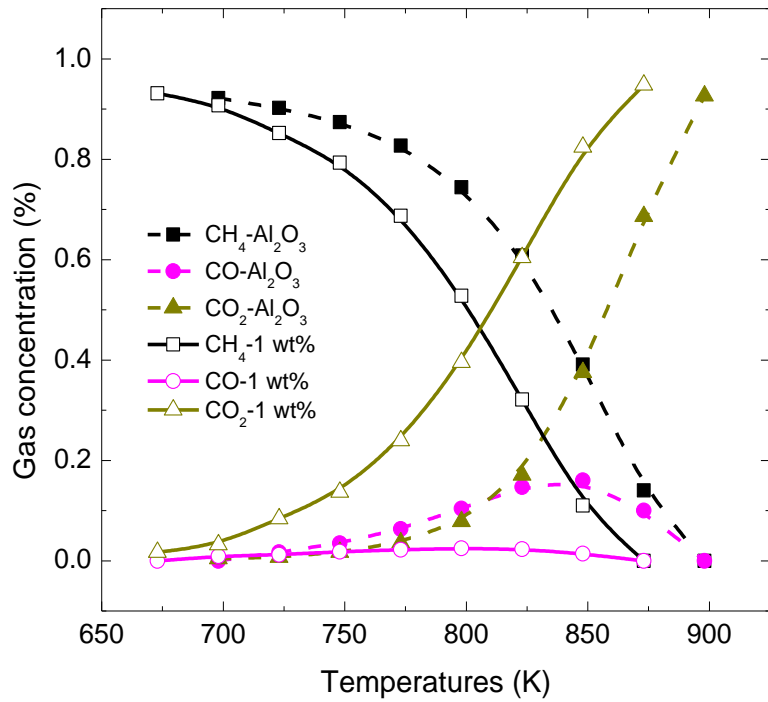


(d)

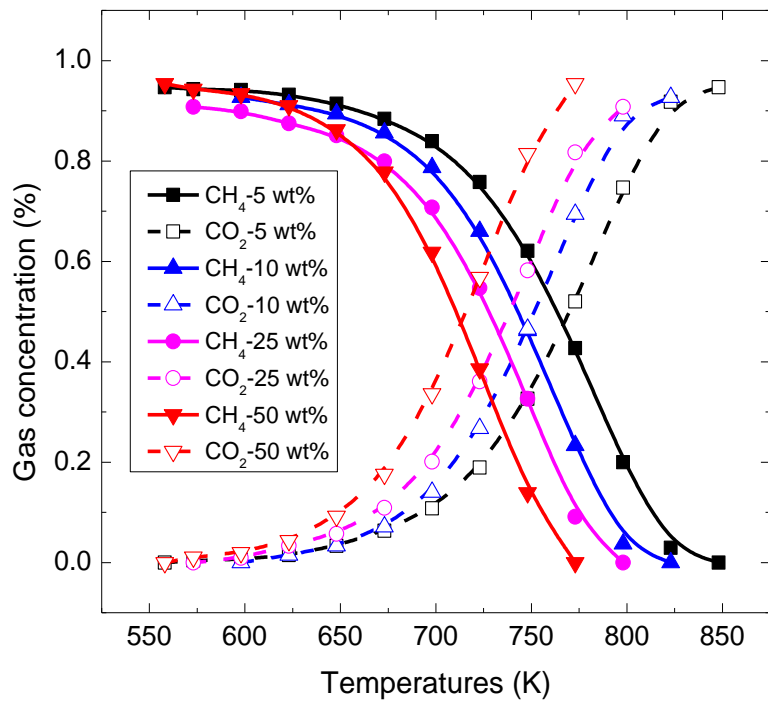
Figure 8.7: The profiles of outlet gas concentration with inlet methane concentrations in: (a) 0.23 vol%, (b) 0.51 vol%, (c) 0.95 vol% in a packed reactor with Fe₂O₃/Al₂O₃, and (d) methane conversion in packed reactor with Fe₂O₃/Al₂O₃.

8.3.3 Effect of Fe₂O₃ Loading Content on Al₂O₃

Five metal oxides with different Fe₂O₃ loading content (1, 5, 10, 25 and 50 wt%) were examined to determine the effect of Fe₂O₃ loading content on the catalytic oxidation of low concentration methane. The actual loaded quantities in the reaction zone were 6.02, 6.09, 6.15, 6.41 and 6.85 g, respectively. It provides the possibility to find the optimised Fe₂O₃ loading content which delivers the best catalytic effect. The outlet gas distribution is plotted with different temperatures in Figure 8.8 in which the oxidation of VAM on alumina is shown as a baseline. It indicates that some CO contents were found with low Fe₂O₃ content in the mixture (Fe₂O₃ content less than 1 wt%). However, the CO concentration is negligible (less than 1 vol%). Besides, the temperature for the formation of CO is decreased and in the range of 698 K to 848 K compared with the oxidation in an empty reactor. For the other Fe₂O₃ content mixtures, only CO₂ can be found in the product gas stream and the temperature for the full conversion is increasing with the decrease in Fe₂O₃ content. The variation of CH₄ conversion with temperatures is plotted in Figure 8.9. Experimental results show that the metal oxide with 50 wt% Fe₂O₃ owns the best catalytic activity which decreases sequentially with the decrease in the active iron oxide loading content. The oxidation initiation temperature is quite in dependence on Fe₂O₃ loading content especially when it is less than 5 wt%. It increases to 673 K for 1 wt% Fe₂O₃ from 573 K for 5 wt% Fe₂O₃. For Fe₂O₃ loading content higher than 5 wt%, it is almost the same: around 573 K. However, a big difference is observed on the light-off temperature which shows a great dependence on the iron oxide loading content which is in agreement with the results in the literature [43, 45]. It decreased from 873 K to 773 K with the increase in the weight percentage of Fe₂O₃.



(a)



(b)

Figure 8.8: The profiles of outlet gas concentration with 0.95% inlet methane concentrations in a packed reactor with different loading content $\text{Fe}_2\text{O}_3/\text{Al}_2\text{O}_3$, (a) 1% and (b) 5%-50%.

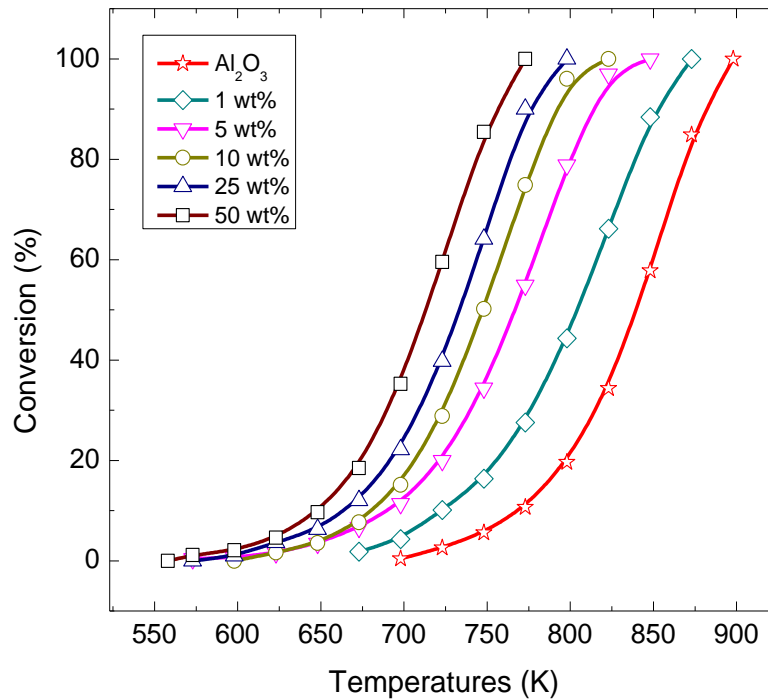


Figure 8.9: Methane conversion in packed reactor with different loading content $\text{Fe}_2\text{O}_3/\text{Al}_2\text{O}_3$.

8.4 Discussion

The coalmine ventilation air methane (0.1–1 vol%) can be reduced and/or used in an IGCLC system as the combustion air substitution in the air reactor. This is an iron-based chemical looping combustion of coal which is gasified in a pipe-type pressurized coal gasifier incorporated into air reactor. This special design makes it possible to transfer the heat released from AR to the gasifier which is dominated by an endothermic reaction (i.e., $\text{C} + \text{H}_2\text{O} \leftrightarrow \text{H}_2 + \text{CO}$). The optimized gasification efficiency was found to be 81% at 1273 K with the water to carbon ratio~1. At lower temperatures (1123-1173 K), the higher water to carbon ratio~1.2 was required in order to obtain better gasification efficiency around 77-80%. The thermodynamics analysis results indicated that the effect of methane concentration was able to be minimised in this manner. Particularly, the temperature change was decreasing to 3% from 11% in the thermal oxidation method. This was because of the involvement of oxygen carriers. In fact, part of the functions of oxygen carriers in an air reactor was like the heat exchange media in a thermal oxidation reactor. The difference was

that the temperature of the oxygen carriers had already been as high as 1073–1273 K before coming into the air reactor and such that the preheating process was avoided. But it should be noted that the effect of VAM flow rate was much more significant compared with that of methane concentration. A quite stable flow rate was necessary to achieve operation stability. This can be achieved through the installation of mass flow controller or other similar functional devices. In addition, even though the sacrifice in CO₂ capture rate had to be made, which dropped down to under 90% from 100%, the process was characterized with high overall efficiency and high CO₂ capture rate, higher than 45% and 90% respectively in most cases.

As shown in the experimental results in Section 8.3.2-8.3.3, in addition to being the heat exchange media, the used oxygen carriers (i.e. Fe₂O₃/Al₂O₃) also acted as the catalyst during the oxidation of VAM. The oxidation-initiation temperature was decreasing to around 573K due to the catalytic effect. The selective behaviour was also found in this work. No intermediate CO is detected in the product while the maximum conversion of CH₄ to CO could reach around 80% in the oxidation without the presence of Fe₂O₃/Al₂O₃. It indicated that the catalyst sample promoted the conversion of CO to CO₂ even at very low temperature level, rather than changing the chemical equilibrium. The oxidation of VAM can be explained by the two justified reaction mechanisms. One is consecutive-parallel reaction mechanism for the homogeneous reaction [11]:



The reaction mechanism for the catalytic reaction is quite complicated and may involve hundreds of reactions. However, it was found that under fuel-lean conditions, the predominant reaction was as follows [125],



which is so-called single-step reaction mechanism and can be used to predict the experimental result in good agreement.

For the two-step mechanism, CH₄ is firstly converted to CO then CO₂ even it is in the oxygen rich condition, which can be confirmed by the experimental results. For the single-step one, both CH₄ and O₂ are absorbed to the surface of metal oxides, and the formed gas product of CO₂ is coming out from the surface.

In a real CLC system, the active content may be varied depending on the reactor design. For this reason, five samples of Fe₂O₃/Al₂O₃ with active content ranging of 1-50 wt% were used to examine its effect on the oxidation of VAM. It can be concluded that the oxidation conversion increased when increasing the active metal oxide content and it can be completed at temperature below 600°C even with the active content as low as 1 wt%.

The experimental results indicated that VAM can be completely oxidized when used as the oxidation agent for CLC process even at operating temperatures as low as 600°C. This result is quite meaningful especially for these CLC processes with the special requirement of low operational temperature in the air reactor.

8.5 Conclusions

A novel ancillary method for mitigating VAM was proposed in this study. In this method, VAM was reduced and/or utilised in an IGCLC process as the combustion air substitution. Due to the fact of variations in the flow rate and methane concentration of VAM, their effects on the system performance were examined thermodynamically. Both significantly influenced the air reactor temperature. However, it was abated and smaller than that in the thermal oxidation reactor. Although the increase in the flow rate and methane concentration led to the growth in the overall efficiency, the drop in CO₂ capture rate occurred correspondingly. Besides, the oxidation of VAM in the air reactor was investigated experimentally in a packed bed reactor. The packed sample was the particle of Fe₂O₃ supported with Al₂O₃, which was prepared using the dry impregnation method. The experimental results showed that the presence of oxygen carriers (i.e. Fe₂O₃/Al₂O₃) led to

the change in reaction mechanism, from thermal oxidation to catalytic oxidation. As a result, the combustion temperature was declined between 573K and 873K. It was confirmed that the full methane conversion could be achieved in the air reactor and no methane residual was detected in the product even at a temperature lower than 1073K.

Chapter 9: CONCLUSIONS AND RECOMMENDATIONS

Given the current dependence on and large reserves of fossil fuel, especially coal and natural gas, the methane emissions resulting from the extraction of coal and natural gas are increasingly concerning. Ventilation air methane as a major part of the methane emissions is found to be difficult to mitigate primarily because: (1) the methane concentration in the mixture is dilute and (2) the concentration and flow rate of methane is variable. The processes under development in this thesis for the use of VAM with chemical looping technologies provides an advanced technology platform for treatment of VAM and can be employed as part of any use and/or destruction mitigation strategies. These processes require thermodynamics and experimental investigations, which have been presented.

9.1 Conclusions

9.1.1 The Use of VAM to Produce Pure Hydrogen

A dual loops chemical looping process was proposed to reform ventilation air methane into pure hydrogen. It mainly consists of two loops, an oxygen removal loop and a hydrogen production loop. The oxygen removal looping is a Cu-based chemical looping air separation process, in which the oxygen is separated through the oxidation of Cu_2O and the oxygen depleted stream is fed into the hydrogen production loop. The ultra-low concentration methane is then reduced in a Fe-based three reactors chemical looping system for hydrogen production. In light of the thermodynamics and experimental results, the oxygen removal temperature should locate in the range of 573–673K in order to commence the oxidation of Cu_2O at a proper kinetics rate while inhabiting the catalytic combustion of VAM and reduction of copper oxides with methane.

The thermodynamic performance was evaluated by a case study with methane concentration of 0.5 vol% and compared between two configurations. It was found that,

with pure O₂ as a final product, 0.254 MW per cubic meter VAM was needed from external sources. The specific power demand was 0.39 kWh/m³ O₂, which can be compared with the specific power of conventional cryogenic systems. If the H₂ efficiency was considered, the specific power demand decreased by 18% to 0.32 kWh/m³ O₂. If there was no O₂ product, 0.031 MW of energy can be produced from per cubic meter VAM with a hydrogen efficiency of 35.1%.

The parametric study was also conducted and the results indicated that:

- (1) the excess of oxygen carrier circulation rate should locate between 40% and 100% when combining the concerns in FR and HR temperature, hydrogen production and hydrogen efficiency;
- (2) when using oxygen carrier circulation rate of 100% excess of the stoichiometric requirement for methane concentration of 0.5 vol%, the temperature changes in both FR and HG were less than 50K and pure hydrogen can be produced with methane concentration as low as 0.4 vol%; and
- (3) in order to sustain the temperature in FR and HR, the inert content should be higher than 60 wt% when using Al₂O₃ as the inert material.

The feasibility of reforming ultra-low concentration methane (i.e. oxygen depleted VAM) to hydrogen in Fe-based three reactors chemical looping process was investigated experimentally in both TGA and fixed bed setup. In order to produce pure hydrogen, it is necessary to reduce Fe₂O₃ into FeO or Fe which can be oxidised by steam and produce hydrogen. The reduction of Fe₂O₃ to FeO by ultra-low concentration methane was investigated with four different iron-based metal oxides, i.e. pure Fe₂O₃, Fe45Al (45 wt% Fe₂O₃/Al₂O₃), Fe25Al (25 wt% Fe₂O₃/Al₂O₃) and Fe10Al (10 wt% Fe₂O₃/Al₂O₃). The findings were as follows:

- (1) the reduction reactivity and cyclic stability can be improved by employing Al₂O₃ as support material but the oxygen transfer capacity was declined when increasing the weight content of Al₂O₃;

- (2) all of the supported iron oxides can be reduced to FeO, however, the reactivity increased with the decrease in Fe₂O₃ weight content, especially during the reduction of Fe₃O₄ to FeO;
- (3) in terms of the rate of oxygen transport (ROT), which took into account oxygen transfer capacity and reactivity together, Fe45Al was the most suitable oxygen carrier candidate for the transformation of Fe₂O₃ to Fe₃O₄ while Fe10Al for the pair of Fe₂O₃/FeO;
- (4) the gas analysis results uncovered that Fe45Al was the best choice for the oxidation of ultra-low concentration methane due to the contribution of complete conversion of CH₄ to CO₂ as well as longest duration on high level conversion; and
- (5) parametric studies indicated that the best reduction temperature was 1023K; Fe45Al can be reduced to the form of FeO even with the methane concentration as low as 0.1 vol%; the suppressing effect of CO₂ on the reduction of Fe₂O₃ was observed, especially on the pair of Fe₃O₄/FeO.

Kinetics parameters are of significance in the reactor design and predicting the gas product and energy consumption. The reduction kinetics of Fe₂O₃/Al₂O₃ with ultra-low concentration methane was evaluated and the rate controlled mechanism parameters were determined using a topochemical approach coupled with Hancock and Sharp's method. It was found that:

- (1) Avrami-Erofe'ev phase change model described the reduction mechanism for the transformation of Fe₂O₃ into Fe₃O₄, A2 model for low conversion and A3 model for high conversion. The activation energies were found to be 24.96 kJ/mol for Fe25Al and 24.77 kJ/mol for Fe45Al;
- (2) the reaction mechanism for reduction of Fe₃O₄ to FeO shifts to diffusion control model. The activation energies were equal to 171.24 kJ/mol for Fe25Al and 209.16 kJ/mol for Fe45Al; and
- (3) when Fe₂O₃ contents in the oxygen carriers were in the range of 25–45 wt%, the reaction mechanism was the same but a significant difference was observed on the rate constant (i.e. reduction reactivity).

9.1.2 Thermal Oxidation of Hydrogen Enriched VAM

A novel process was proposed to mitigate VAM emission in the use of thermal oxidation approach. The combustion temperature of VAM was improved and stabilised by the addition of hydrogen, which was produced in an integrated gasification chemical looping process using coal as fuel. Its advantages over conventional thermal oxidation process are: (1) no special reactor design is required and the combustion temperature is higher than 1273K independent of the methane concentration; (2) the system is of high CO₂ capture rate although it is fuelled with coal. The thermodynamics analysis showed that the IGCLC process was able to produce pure hydrogen with an auto-thermal coal gasifier and there were no thermodynamic barriers to its operation provided that the gasification temperature is greater than 1023K and the pressure is fixed at 70 bar.

For this IGCLC process, the most important outcome is hydrogen production, which is a key role to sustain the temperature in VC at a high level. Given an equi-molar steam-hydrogen mixture fed into the gasifier unit, the best system performance can be found with the value of SHTCR~2 with respect to the carbon conversion, hydrogen production, fuel conversion in fuel reactor and overall efficiency. The oxygen carrier circulation rate also put a significant impact on the hydrogen production. The lower the circulation rate the higher the hydrogen production. However, the fact is that the system requires more oxygen carrier to achieve higher fuel conversion in the fuel reactor. The results indicated that the excess of oxygen carrier circulation rates higher than 80% were not acceptable because the produced hydrogen cannot even satisfy the gasification of coal in GR. When taking into account the overall system efficiency, the excess rate of 20% was the most suitable value as the optimised overall efficiency was obtained around 50%.

Regarding the overall efficiency, in addition to SHTCR and oxygen carrier circulation rate, it was influenced by the airflow rate and steam conversion. The peak value of overall efficiency was found with the excess of airflow rate of 100%. It increased when increasing the steam conversion. The overall efficiency was around 50% for a normal steam conversion rate of 40%. In most cases, the overall efficiency for the whole system was higher than 45% and CO₂ capture rate was higher than 80%. A typical pulverised fuel coal-

fired power plant with no CCS has a net thermal efficiency of 35–38%. When such plants are fitted with CCS their efficiency may drop by as much as 25%, down to 26–29% net. A comparison between an IGCLC type plant and a conventional power station with no CCS measure reveals that the IGCLC approach on average delivers about 30% higher efficiency for the same input. This figure rises to about 80% if the conventional plant is retrofitted with CCS measures.

Although the process features high overall efficiency and CO₂ capture rate, the variation of VC temperature is quite significant with VAM flow rate and methane concentration. Especially, the temperature increases linearly with the increase in methane concentration, which increases by 200K from 1188K at 0.1 vol% to 1380K at 1 vol%. Similar issues were also observed with variable VAM flow rate. If no measurement can be taken to solve this issue, the process is not be a suitable approach to utilise the VAM as a source of energy. However, there is no doubt on the function of VAM mitigation in this process.

9.1.3 The use of VAM as oxidation agent in a CLC process

A chemical looping based process is proposed for ancillary use of VAM, in which VAM is used as the oxidation agent instead of air. It is an iron-based chemical looping combustion of coal, which is gasified in a pipe type pressurised coal gasifier incorporated into the air reactor. This special design makes it possible to transfer the heat released from AR to the gasifier which is dominated by an endothermic reaction (i.e. $C+H_2O=H_2+CO$). The optimised gasification efficiency was found to be 81% at 1273K with the water to carbon ratio~1. When with a lower temperature around 1123–1173K, the higher water to carbon ratio~1.2 was required in order to obtain better gasification efficiency around 77–80%.

This process has the potential to minimise the influence of VAM flow rate and methane concentration on the system operation due to the involvement of circulated oxygen carriers. Specifically, the temperature change was around 34K with the methane concentration varying from 0.1 vol% to 1 vol%, which is about one sixth of the change in the process described in Section 10.1.1. Moreover, the process was characterised with high overall efficiency and high CO₂ capture rate, higher than 45% and 90% respectively in most cases.

The oxidation of VAM in AR was simulated in a packed bed reactor, in which the particles of $\text{Fe}_2\text{O}_3/\text{Al}_2\text{O}_3$ were located in the centre of the reactor. As shown in the experimental results, the oxidation of VAM to CO_2 and H_2O can be observed at the temperature as low as 350°C even with the methane concentration of 0.23 vol%. During the oxidation, only CO_2 was observed and no CO was detected. The complete conversion of CH_4 to CO_2 occurred around 500°C . Although the methane concentration significantly affected the oxidation conversion, the start and complete temperatures for the oxidation were quite similar over the range of methane concentrations.

In a real CLC system, the active content may vary with the reactor design requirement. Five samples of $\text{Fe}_2\text{O}_3/\text{Al}_2\text{O}_3$ with active content ranging between 1–50 wt% were used to examine its effect on the oxidation of VAM. It can be concluded that the oxidation conversion increased when increasing the active metal oxide content and it can be completed at temperatures below 600°C even with the active content as low as 1 wt%.

The experimental results indicated that VAM can be used as the oxidation agent for the CLC process even though it operates with a temperature in AR as low as 600°C . This result is quite meaningful, especially for these CLC processes with metal oxides of low melting temperature as oxygen carriers, like copper oxides.

9.2 Recommendations for Future Work

The conclusions given in the previous section clearly indicate that chemical looping technology can prove to be a ground breaking technology for highly efficient mitigation and utilisation of ventilation air methane. However, there also exist a number of technological barriers that must be overcome before a pilot scale plant can be built. The recommendations given in this section will help the CLC-community in identifying challenges associated with applications in mitigation and utilisation of VAM.

The proposed process can be employed to mitigate the emission of ventilation air methane through oxidation of methane into carbon dioxide in various manners. However, the gas

product is the mixture of CO_2 and N_2 in a large fraction and cannot be separated inherently. This will result in a decrease in CO_2 capture rate and the issue of greenhouse gas emissions (even the GHG index is lower than the emission of CH_4). To avoid the decrease in CO_2 capture rate and/or efficiency penalty some other chemical looping based process should be developed in which CO_2 can be captured inherently without extra steps and equipment. For example, a Ca-based chemical looping process can be employed to oxidise the ventilation air methane and capture CO_2 simultaneously. This system should be analysed in both thermodynamic and experimental aspects.

The process of reforming of VAM into pure hydrogen has been presented in this work. The experimental results have proved that the oxygen can be removed from the stream of VAM and the iron oxide can be reduced to the form of FeO by ultra-low concentration methane. However, the chemical and mechanical stability of copper oxides requires further investigation during the reduction and oxidation cycles for removing oxygen in VAM. The performance of copper oxides can be stabilised by preparation with various methods and incorporating support metal oxides, such as Al_2O_3 , ZrO_2 , TiO_2 and MgAl_2O_4 . Once the most suitable prepared method and support metal oxide are determined, the oxidation kinetics of Cu_2O in air as well as the reduction kinetics in reduction reactor should be determined to carry out the scale of the oxidation reactor for removing oxygen completely.

In the future, inert supports not used in the present investigation, ZrO_2 and MgAl_2O_4 , will also be investigated as candidates for stabilising the repeated reduction to FeO. Especially MgAl_2O_4 , it is an interesting support candidate since it does not form any intermediates with the iron species. With these supported iron oxides, the operational parameters should be optimised for producing hydrogen with highest purity and productivity. With the experimental data, the pilot scale system can be designed and built for further research study.

Nomenclature

G	gibbs free enthalpy	kJ/mol
n_i	species i mole numbers	
R	gas constant	J/mol · K
T	temperature	K
X_i	mole fraction of species i	
P	partial pressure	Pa
P^0	standard state pressure	Pa
a_{ji}	number of atoms of element j in species i	
n_j	mole number of element j	
λ_j	Lagrangian multipliers	
X	fractional conversion	
M	sample weight	mg
ω	deviation on mass loss	
t	time	s or min
k	reaction rate constant	1/s
A	pre-exponential factor	1/s
E	activation energy	kJ/mol

References

- [1] IPCC, *Climate change 2007: The physical science basis* 2007: Cambridge, United Kingdom.
- [2] IPCC, *Climate Change 2007: Synthesis Report.* , a.A.R. R.K. Pachauri, Editor 2007, Cambridge University Press. p. 104.
- [3] IPCC, *Climate change 2013: The physical science basis*, 2013, Cambridge University Press: Cambridge, United Kingdom:.
- [4] <http://www.esrl.noaa.gov/gmd/aggi/>.
- [5] <http://cait.wri.org>.
- [6] Council, N.R., *Advancing the Science of Climate Change* 2010: Washington, DC, USA.
- [7] Council, N.R., *Climate Stabilization Targets: Emissions, Concentrations, and Impacts over Decades to Millennia*, 2011: Washington, DC, USA.
- [8] EPA, *Global Mitigation of Non-CO₂ Greenhouse Gases 1990-2020*, 2006.
- [9] IEA, *Energy sector methane recovery and use*, 2009: France.
- [10] IEA, *Energy Technology Perspectives*, IEA/OECD, Editor 2008: Paris, France.
- [11] Gosiewski, K., et al., Homogeneous vs. catalytic combustion of lean methane-air mixtures in reverse-flow reactors. *Chemical Engineering Science* 2008; **63**(20): 5010-5019.
- [12] Wang, Y., C. Man, and D. Che, Catalytic Combustion of Ventilation Air Methane in a Reverse-Flow Reactor. *Energy & Fuels* 2010; **24**(9): 4841-4848.
- [13] Su, S. and J. Agnew, Catalytic combustion of coal mine ventilation air methane. *Fuel* 2006; **85**(9): 1201-1210.
- [14] Su, S., et al., An assessment of mine methane mitigation and utilisation technologies. *Progress in Energy and Combustion Science* 2005; **31**(2): 123-170.
- [15] Horst, J.R. and F.K. Karl, Reversibility of Combustion Processes, in *Efficiency and Costing*. 1983, AMERICAN CHEMICAL SOCIETY. p. 71-85.
- [16] EPA, *Options for reducing methane emissions internationally*, O.o.A.a.R. U.S. Environmental Protection Agency, Editor 1993: Washington, D.C.
- [17] IPCC, *Climate Change 1995, Impacts, Adaptations, and Mitigation of Climate Change: Scientific-Technical Analysis*, 1996: Cambridge University Press, Cambridge, UK.

- [18] IPCC, *IPCC Special Report on Carbon Dioxide Capture and Storage*, B. Metz, et al., Editors. 2005, Cambridge University Press, Cambridge, United Kingdom and New York, NY, USA,. p. 440.
- [19] Carothers, P. and M. Deo, *Technical and economic assessment: mitigation of methane emissions from coal mine ventilation air*, 2000, Coalbed Methane Outreach Program, Climate Protection Division, US Environmental Protection Agency
p. EPA-430-R-001.
- [20] Liu, R., Y. Liu, and Z. Gao. Methane Emission Control by Thermal Oxidation in a Reverse Flow Reactor. in *Bioinformatics and Biomedical Engineering*, 2008. ICBBE 2008. The 2nd International Conference on. 2008.
- [21] Wang, Y., et al., Homogeneous Combustion of Fuel Ultra-Lean Methane-air Mixtures: Experimental Study and Simplified Reaction Mechanism. *Energy & Fuels* 2011; **25**(8): 3437-3445.
- [22] Stasińska, B. and A. Machocki, Catalysts for the utilization of methane from the coal mine ventilation air. *Polish Journal of Chemical Technology* 2007; **9**(3): 29-32.
- [23] Lee, J.H. and D.L. Trimm, Catalytic combustion of methane. *Fuel Processing Technology* 1995; **42**(2): 339-359.
- [24] Otto, K., Methane oxidation over Pt on γ -alumina: kinetics and structure sensitivity. *Langmuir* 1989; **5**(6): 1364-1369.
- [25] Niwa, M., K. Awano, and Y. Murakami, Activity of supported platinum catalysts for methane oxidation. *Applied Catalysis* 1983; **7**(3): 317-325.
- [26] Yang, L., et al., Catalytic combustion of methane over PdO supported on Mg-modified alumina. *Applied Catalysis B: Environmental* 2002; **38**(2): 117-125.
- [27] Baldwin, T.R. and R. Burch, Catalytic combustion of methane over supported palladium catalysts: I. Alumina supported catalysts. *Applied Catalysis* 1990; **66**(1): 337-358.
- [28] Baldwin, T.R. and R. Burch, Catalytic combustion of methane over supported palladium catalysts: II. Support and possible morphological effects. *Applied Catalysis* 1990; **66**(1): 359-381.
- [29] Janbey, A., et al., Noble metal catalysts for methane removal. *Chemosphere* 2003; **52**(6): 1041-1046.

- [30] Gelin, P. and M. Primet, Complete oxidation of methane at low temperature over noble metal based catalysts: a review. *Applied Catalysis B: Environmental* 2002; **39**(1): 1-37.
- [31] Hayes, R.E., Catalytic solutions for fugitive methane emissions in the oil and gas sector. *Chemical Engineering Science* 2004; **59**(19): 4073-4080.
- [32] Yamamoto, H. and H. Uchida, Oxidation of methane over Pt and Pd supported on alumina in lean-burn natural-gas engine exhaust. *Catalysis Today* 1998; **45**(1-4): 147-151.
- [33] Sushil, S. and V.S. Batra, Catalytic applications of red mud, an aluminium industry waste: A review. *Applied Catalysis B: Environmental* 2008; **81**(1): 64-77.
- [34] Artizzu, P., et al., Catalytic combustion of methane on aluminate-supported copper oxide. *Catalysis Today* 1999; **47**(1): 83-93.
- [35] Paredes, J.R., et al., Combustion of Methane in Lean Mixtures over Bulk Transition-Metal Oxides: Evaluation of the Activity and Self-Deactivation. *Energy & Fuels* 2008; **23**(1): 86-93.
- [36] Arai, H., et al., Catalytic combustion of methane over various perovskite-type oxides. *Applied Catalysis* 1986; **26**(0): 265-276.
- [37] Berg, M. and S. Järås, Catalytic combustion of methane over magnesium oxide. *Applied Catalysis A: General* 1994; **114**(2): 227-241.
- [38] Bahlawane, N., Kinetics of methane combustion over CVD-made cobalt oxide catalysts. *Applied Catalysis B: Environmental* 2006; **67**(3-4): 168-176.
- [39] Cimino, S., et al., Transient behaviour of perovskite-based monolithic reactors in the catalytic combustion of methane. *Catalysis Today* 2001; **69**(1-4): 95-103.
- [40] Cimino, S., et al., Methane combustion on perovskites-based structured catalysts. *Catalysis Today* 2000; **59**(1-2): 19-31.
- [41] Barbosa, A.L., J. Herguido, and J. Santamaria, Methane combustion over unsupported iron oxide catalysts. *Catalysis Today* 2001; **64**(1-2): 43-50.
- [42] Spretz, R., et al., Fe/MgO Formulations for the Catalytic Combustion of Methane. *Journal of Catalysis* 2000; **194**(2): 167-174.
- [43] Liu, Z., et al., Effect of Fe₂O₃ Loading Amount on Catalytic Properties of Monolithic Fe₂O₃/Ce_{0.67}Zr_{0.33}O₂-Al₂O₃ Catalyst for Methane Combustion. *Journal of Rare Earths* 2007; **25**(5): 585-589.

- [44] Pecchi, G., et al., Catalytic Combustion of Methane on Fe-TiO₂ Catalysts Prepared by Sol-Gel Method. *Journal of Sol-Gel Science and Technology* 2003; **27**(2): 205-214.
- [45] Paredes, J.R., et al., Catalytic combustion of methane over red mud-based catalysts. *Applied Catalysis B: Environmental* 2004; **47**(1): 37-45.
- [46] Choudhary, V.R., et al., Nano-gold supported on Fe₂O₃: A highly active catalyst for low temperature oxidative destruction of methane green house gas from exhaust/waste gases. *Applied Catalysis A: General* 2008; **350**(2): 186-190.
- [47] Salomons, S., et al., Flow reversal reactor for the catalytic combustion of lean methane mixtures. *Catalysis Today* 2003; **83**(1-4): 59-69.
- [48] Marín, P., et al., Combustion of methane lean mixtures in reverse flow reactors: Comparison between packed and structured catalyst beds. *Catalysis Today* 2005; **105**(3-4): 701-708.
- [49] Aubé F. and H. Sapoundjiev, Mathematical model and numerical simulations of catalytic flow reversal reactors for industrial applications. *Computers & Chemical Engineering* 2000; **24**(12): 2623-2632.
- [50] Marín, P., S. Ordóñez, and F.V. Déz, Procedures for heat recovery in the catalytic combustion of lean methane-air mixtures in a reverse flow reactor. *Chemical Engineering Journal* 2009; **147**(2-3): 356-365.
- [51] Gosiewski, K., Efficiency of heat recovery versus maximum catalyst temperature in a reverse-flow combustion of methane. *Chemical Engineering Journal* 2005; **107**(1-3): 19-25.
- [52] You, C. and X. Xu, Utilization of Ventilation Air Methane as a Supplementary Fuel at a Circulating Fluidized Bed Combustion Boiler. *Environmental Science & Technology* 2008; **42**(7): 2590-2593.
- [53] Ishida, M., D. Zheng, and T. Akehata, Evaluation of a chemical-looping-combustion power-generation system by graphic exergy analysis. *Energy* 1987; **12**(2): 147-154.
- [54] Ishida, M. and H. Jin, A new advanced power-generation system using chemical-looping combustion. *Energy* 1994; **19**(4): 415-422.
- [55] Jin, H. and M. Ishida, A novel gas turbine cycle with hydrogen-fueled chemical-looping combustion. *International Journal of Hydrogen Energy* 2000; **25**(12): 1209-1215.
- [56] Anhedén, M. and G. Svedberg. Chemical-looping combustion in combination with integrated coal gasification-a way to avoid CO₂ emission from coal fired power plants

- without a significant decrease in net power efficiency. in Energy Conversion Engineering Conference, 1996. IECEC 96. Proceedings of the 31st Intersociety. 1996.
- [57] Anheden, M. and G. Svedberg, Exergy analysis of chemical-looping combustion systems. *Energy Conversion and Management* 1998; **39**(16-18): 1967-1980.
- [58] Rezvani, S., et al., Comparative assessment of coal fired IGCC systems with CO₂ capture using physical absorption, membrane reactors and chemical looping. *Fuel* 2009; **88**(12): 2463-2472.
- [59] Xiang and Chen, Hydrogen and Electricity from Coal with Carbon Dioxide Separation Using Chemical Looping Reactors. *Energy & Fuels* 2007; **21**(4): 2272-2277.
- [60] Xiang, W., et al., Investigation of coal gasification hydrogen and electricity co-production plant with three reactors chemical looping process. *International Journal of Hydrogen Energy* 2010; **35**(16): 8580-8591.
- [61] Chiesa, P., et al., Three-reactors chemical looping process for hydrogen production. *International Journal of Hydrogen Energy* 2008; **33**(9): 2233-2245.
- [62] Cleeton, J.P.E., et al., Clean hydrogen production and electricity from coal via chemical looping: Identifying a suitable operating regime. *International Journal of Hydrogen Energy* 2009; **34**(1): 1-12.
- [63] Gnanapragasam, N.V., B.V. Reddy, and M.A. Rosen, Hydrogen production from coal using coal direct chemical looping and syngas chemical looping combustion systems: Assessment of system operation and resource requirements. *International Journal of Hydrogen Energy* 2009; **34**(6): 2606-2615.
- [64] Li, F., L. Zeng, and L.-S. Fan, Biomass direct chemical looping process: Process simulation. *Fuel* 2010; **89**(12): 3773-3784.
- [65] Calin-Cristian, C., Evaluation of iron based chemical looping for hydrogen and electricity co-production by gasification process with carbon capture and storage. *International Journal of Hydrogen Energy* 2010; **35**(6): 2278-2289.
- [66] Calin-Cristian, C., Hydrogen production from fossil fuels with carbon capture and storage based on chemical looping systems. *International Journal of Hydrogen Energy* 2011; **36**(10): 5960-5971.
- [67] Moghtaderi, B., Application of Chemical Looping Concept for Air Separation at High Temperatures. *Energy & Fuels* 2010; **24**(1): 190-198.

- [68] Moghtaderi, B., Review of the Recent Chemical Looping Process Developments for Novel Energy and Fuel Applications. *Energy & Fuels* 2012; **26**(1): 15-40.
- [69] Song, H., et al., Reactivity of Al₂O₃- or SiO₂-Supported Cu-, Mn-, and Co-Based Oxygen Carriers for Chemical Looping Air Separation. *Energy & Fuels* 2014; **28**(2): 1284-1294.
- [70] Song, H., et al., Development of a Cu–Mg-Based Oxygen Carrier with SiO₂ as a Support for Chemical Looping Air Separation. *Energy & Fuels* 2013.
- [71] Jerndal, E., T. Mattisson, and A. Lyngfelt, Thermal Analysis of Chemical-Looping Combustion. *Chem. Eng. Res. Des.* 2006; **84**(9): 795-806.
- [72] Ishida, M., H. Jin, and T. Okamoto, Kinetic Behavior of Solid Particle in Chemical-Looping Combustion: Suppressing Carbon Deposition in Reduction. *Energy & Fuels* 1998; **12**(2): 223-229.
- [73] Abad, A., et al., Reduction Kinetics of Cu-, Ni-, and Fe-Based Oxygen Carriers Using Syngas (CO + H₂) for Chemical-Looping Combustion. *Energy & Fuels* 2007; **21**(4): 1843-1853.
- [74] Abad, A., et al., The use of iron oxide as oxygen carrier in a chemical-looping reactor. *Fuel* 2007; **86**(7-8): 1021-1035.
- [75] Leion, H., et al., The use of ilmenite as an oxygen carrier in chemical-looping combustion. *Chemical Engineering Research and Design* 2008; **86**(9): 1017-1026.
- [76] Adanez, J., et al., Ilmenite Activation during Consecutive Redox Cycles in Chemical-Looping Combustion. *Energy & Fuels* 2010; **24**(2): 1402-1413.
- [77] Mattisson, T., A. Lyngfelt, and P. Cho, The use of iron oxide as an oxygen carrier in chemical-looping combustion of methane with inherent separation of CO₂. *Fuel* 2001; **80**(13): 1953-62.
- [78] Cho, P., T. Mattisson, and A. Lyngfelt, Comparison of iron-, nickel-, copper- and manganese-based oxygen carriers for chemical-looping combustion. *Fuel* 2004; **83**(9): 1215-25.
- [79] Adáñez, J., et al., Selection of Oxygen Carriers for Chemical-Looping Combustion. *Energy Fuels* 2004; **18**(2): 371-77.

- [80] Mattisson, T., M. Johansson, and A. Lyngfelt, Multicycle Reduction and Oxidation of Different Types of Iron Oxide Particles Application to Chemical-Looping Combustion. *Energy Fuels* 2004; **18**(3): 628-37.
- [81] Johansson, M., T. Mattisson, and A. Lyngfelt, Investigation of Fe_2O_3 with MgAl_2O_4 for Chemical-Looping Combustion. *Ind. Eng. Chem. Res.* 2004; **43**(22): 6978-87.
- [82] Zafar, Q., T. Mattisson, and B. Gevert, Redox Investigation of Some Oxides of Transition-State Metals Ni, Cu, Fe, and Mn Supported on SiO_2 and MgAl_2O_4 . *Energy Fuels* 2006; **20**(1): 34-44
- [83] Corbella, B.M. and J.M. Palacios, Titania-supported iron oxide as oxygen carrier for chemical-looping combustion of methane. *Fuel* 2007; **86**(1-2): 113-22.
- [84] Ortiz, M., et al., Hydrogen production with CO_2 capture by coupling steam reforming of methane and chemical-looping combustion: Use of an iron-based waste product as oxygen carrier burning a PSA tail gas. *J. Power Sources* 2010; **196**(9): 4370-81.
- [85] Kang, K.-S., et al., Oxygen-carrier selection and thermal analysis of the chemical-looping process for hydrogen production. *International Journal of Hydrogen Energy* 2010; **35**(22): 12246-12254.
- [86] Yamaguchi, D., et al., Hydrogen production through methane-steam cyclic redox processes with iron-based metal oxides. *International Journal of Hydrogen Energy* 2011; **36**(11): 6646-6656.
- [87] Urasaki, K., et al., Hydrogen production via steam-iron reaction using iron oxide modified with very small amounts of palladium and zirconia. *Applied Catalysis A: General* 2005; **288**(1-2): 143-148.
- [88] Lorente, E., J.A. Pena, and J. Herguido, Separation and storage of hydrogen by steam-iron process: Effect of added metals upon hydrogen release and solid stability. *Journal of Power Sources* 2009; **192**(1): 224-229.
- [89] Takenaka, S., et al., Storage and formation of pure hydrogen mediated by the redox of modified iron oxides. *Applied Catalysis A: General* 2005; **282**(1-2): 333-341.
- [90] Takenaka, S., et al., Storage and supply of hydrogen by means of the redox of the iron oxides modified with Mo and Rh species. *Journal of Catalysis* 2004; **228**(1): 66-74.
- [91] Takenaka, S., V.T. Dinh Son, and K. Otsuka, Storage and Supply of Pure Hydrogen from Methane Mediated by Modified Iron Oxides. *Energy & Fuels* 2004; **18**(3): 820-829.

- [92] Chen, S., et al., Experimental investigation of chemical looping hydrogen generation using iron oxides in a batch fluidized bed. *Proceedings of the Combustion Institute* 2011; **33**(2): 2691-2699.
- [93] Chen, S., et al., Experimental investigation of chemical-looping hydrogen generation using Al₂O₃ or TiO₂-supported iron oxides in a batch fluidized bed. *International Journal of Hydrogen Energy* 2011; **36**: 8915-8926.
- [94] Gupta, P., L.G. Velazquez-Vargas, and L.S. Fan, Syngas redox (SGR) process to produce hydrogen from coal derived syngas. *Energy & Fuels* 2007; **21**(5): 2900-2908.
- [95] Bohn, C.D., et al., Production of Very Pure Hydrogen with Simultaneous Capture of Carbon Dioxide using the Redox Reactions of Iron Oxides in Packed Beds. *Industrial & Engineering Chemistry Research* 2008; **47**(20): 7623-7630.
- [96] Muller, C.R., et al., The production of separate streams of pure hydrogen and carbon dioxide from coal via an iron-oxide redox cycle. *Chemical Engineering Journal* 2011; **166**(3): 1052-1060.
- [97] Kierzkowska, A.M., et al., Development of iron oxide carriers for chemical looping combustion using sol-gel. *Industrial and Engineering Chemistry Research* 2010; **49**(11): 5383-5391.
- [98] Hacker, V., R. Vallant, and M. Thaler, Thermogravimetric Investigations of Modified Iron Ore Pellets for Hydrogen Storage and Purification: The First Charge and Discharge Cycle. *Industrial & Engineering Chemistry Research* 2007; **46**(26): 8993-8999.
- [99] Pineau, A., N. Kanari, and I. Gaballah, Kinetics of reduction of iron oxides by H₂: Part I: Low temperature reduction of hematite. *Thermochimica Acta* 2006; **447**(1): 89-100.
- [100] Pineau, A., N. Kanari, and I. Gaballah, Kinetics of reduction of iron oxides by H₂: Part II. Low temperature reduction of magnetite. *Thermochimica Acta* 2007; **456**(2): 75-88.
- [101] Monazam, E.R., et al., Kinetics of the reduction of hematite (Fe₂O₃) by methane (CH₄) during chemical looping combustion: A global mechanism. *Chemical Engineering Journal* 2013; **232**(0): 478-487.
- [102] Go, K.S., S.R. Son, and S.D. Kim, Reaction kinetics of reduction and oxidation of metal oxides for hydrogen production. *International Journal of Hydrogen Energy* 2008; **33**(21): 5986-5995.

- [103] Piotrowski, K., et al., Effect of gas composition on the kinetics of iron oxide reduction in a hydrogen production process. *International Journal of Hydrogen Energy* 2005; **30**(15): 1543-1554.
- [104] Piotrowski, K., et al., Topochemical approach of kinetics of the reduction of hematite to wustite. *Chemical Engineering Journal* 2007; **131**(1-3): 73-82.
- [105] Pope, S.B., Gibbs function continuation for the stable computation of chemical equilibrium. *Combustion and flame* 2004; **139**(3): 222-226.
- [106] Moghtaderi, B. and H. Song, Reduction Properties of Physically Mixed Metallic Oxide Oxygen Carriers in Chemical Looping Combustion. *Energy Fuels* 2010; **24**(10): 5359-68.
- [107] Ryu, H.-J., D.-H. Bae, and G.-T. Jin, Effect of temperature on reduction reactivity of oxygen carrier particles in a fixed bed chemical-looping combustor. *Korean Journal of Chemical Engineering* 2003; **20**(5): 960-966.
- [108] Gardner, R.A., The kinetics of silica reduction in hydrogen. *Journal of Solid State Chemistry* 1974; **9**(4): 336-344.
- [109] Nasr, M.I., et al., Carbon monoxide reduction and accompanying swelling of iron oxide compacts. *ISIJ International* 1996; **36**(2): 164-171.
- [110] Lin, H.-Y., Y.-W. Chen, and C. Li, The mechanism of reduction of iron oxide by hydrogen. *Thermochimica Acta* 2003; **400**(1-2): 61-67.
- [111] Mimura, K., et al., Brief review of oxidation kinetics of copper at 350 °C to 1050 °C. *Metallurgical and Materials Transactions A* 2006; **37**(4): 1231-1237.
- [112] Lenglet, M., et al., Low temperature oxidation of copper: The formation of CuO. *Materials Research Bulletin* 1995; **30**(4): 393-403.
- [113] Zhu, Y., K. Mimura, and M. Isshiki, Oxidation mechanism of copper at 623-1073K. *Materials transactions* 2002; **43**(9): 2173-2176.
- [114] Cocke, D., et al., Copper oxidation and surface copper oxide stability investigated by pulsed field desorption mass spectrometry. *Applied surface science* 1995; **84**(2): 153-161.
- [115] Zhang, Y., E. Doroodchi, and B. Moghtaderi, Thermodynamic Assessment of a Novel Concept for Integrated Gasification Chemical Looping Combustion of Solid Fuels. *Energy & Fuels* 2012; **26**(1): 287-295.

- [116] Castle, W.F., Air separation and liquefaction: recent developments and prospects for the beginning of the new millennium. *International Journal of Refrigeration* 2002; **25**(1): 158-172.
- [117] Yang, J.-b., N.-s. Cai, and Z.-s. Li, Hydrogen Production from the Steam-Iron Process with Direct Reduction of Iron Oxide by Chemical Looping Combustion of Coal Char. *Energy & Fuels* 2008; **22**(4): 2570-2579.
- [118] Panopoulos, K.D., et al., High temperature solid oxide fuel cell integrated with novel allothermal biomass gasification: Part I: Modelling and feasibility study. *Journal of Power Sources* 2006; **159**(1): 570-585.
- [119] Perdikaris, N., et al., Design and optimization of carbon-free power generation based on coal hydrogasification integrated with SOFC. *Fuel* 2009; **88**(8): 1365-1375.
- [120] Kalina, T. and R.E. Moore, *CATALYTIC COAL HYDROGASIFICATION PROCESS*, 1974, Exxon Research and Engineering Company (Linden, NJ): United States.
- [121] Wen C, Y., C. Abraham O, and T. Talwalkar A, A Kinetic Study of the Reaction of Coal Char with Hydrogen-Steam Mixtures, in *Fuel Gasification*. 1967, AMERICAN CHEMICAL SOCIETY. p. 253-272.
- [122] Shen, L., et al., Reactivity deterioration of NiO/Al₂O₃ oxygen carrier for chemical looping combustion of coal in a 10 kWth reactor. *Combustion and Flame* 2009; **156**(7): 1377-1385.
- [123] Xiang, W., S. Wang, and T. Di, Investigation of Gasification Chemical Looping Combustion Combined Cycle Performance. *Energy & Fuels* 2008; **22**(2): 961-966.
- [124] Gosiewski, K., et al., A study on thermal combustion of lean methane-air mixtures: Simplified reaction mechanism and kinetic equations. *Chemical Engineering Journal* 2009; **154**(1-3): 9-16.
- [125] Deshmukh, S.R. and D.G. Vlachos, A reduced mechanism for methane and one-step rate expressions for fuel-lean catalytic combustion of small alkanes on noble metals. *Combustion and Flame* 2007; **149**(4): 366-383.